The Madden-Julian Oscillation and the diurnal cycle over the Maritime Continent: scale interactions and modelling

A thesis submitted to the School of Mathematics
of the University of East Anglia in partial fulfilment
of the requirements for the degree of Doctor of Philosophy

Simon Christopher Peatman

May 2014

Abstract

The Maritime Continent archipelago, situated on the equator at 95°–165°E, has the strongest land-based precipitation on Earth. The latent heat release associated with the rainfall affects the atmospheric circulation throughout the tropics and into the extra-tropics.

The greatest source of variability in precipitation is the diurnal cycle. The archipelago is within the convective region of the Madden-Julian Oscillation (MJO), which provides the greatest variability on intra-seasonal time scales: large-scale (~10^7 km^2) active and suppressed convective envelopes propagate slowly (~5 m s^{-1}) eastwards between the Indian and Pacific Oceans. High-resolution satellite data show that a strong diurnal cycle is triggered to the east of the advancing MJO envelope, leading the active MJO by one-eighth of an MJO cycle (~6 days). Where the diurnal cycle is strong its modulation accounts for 81% of the variability in MJO precipitation. Over land this determines the structure of the diagnosed MJO. This is consistent with the equatorial wave dynamics in existing theories of MJO propagation. The MJO also affects the speed of gravity waves propagating offshore from the Maritime Continent islands. This is largely consistent with changes in static stability during the MJO cycle.

The MJO and its interaction with the diurnal cycle are investigated in HiGEM, a high-resolution coupled model. Unlike many models, HiGEM represents the MJO well with eastward-propagating variability on intra-seasonal time scales at the correct zonal wavenumber, although the inter-tropical convergence zone's precipitation peaks strongly at the wrong time, interrupting the MJO's spatial structure. However, the modelled diurnal cycle is too weak and its phase is too early over land. The modulation of the diurnal amplitude by the MJO is also too weak and accounts for only 51% of the variability in MJO precipitation.

Implications for forecasting and possible causes of the model errors are discussed, and further modelling studies are proposed.

Contents

List of figures

List of tables

Acknowledgements

I would like to thank my supervisors, Adrian Matthews and Dave Stevens, for all their assistance and support. Thank you both for being so generous with your time throughout my PhD. I have invariably come out of supervisory meetings with much more confidence in my work than when I went in, which is testament to how valuable your supervision has been. Thank you also to the Natural Environment Research Council for funding my PhD.

I am very grateful to the Fell Club and the Quiz Society for all the enjoyable times and welcome distractions from research they have provided during my time at UEA. Thank you also to everyone at the church of St Peter Mancroft. On moving to Norwich I hoped to find a faithful and friendly church, and Mancroft has proved to be exactly that. Finally, thank you to my family. I am so grateful for your love and support throughout all eight years of my university career.

S.C.P.
27/05/2014

The skies proclaim the work of His hands.
Psalm 19

The research in this thesis was carried out on the High Performance Computing Cluster supported by the Research and Specialist Computing Support service at the University of East Anglia.

Chapter 1

Introduction

1.1 Motivation

The Maritime Continent is the archipelago found on and around the equator between 95° and 160°E. It consists of many islands and shallow oceans (figure 1.1). Home to over 350 million people (5% of the world's population), it is also one of the wettest regions on Earth (figure 1.2) with annual rainfall, averaged over the region 95°–150°E, 10°S–10°N, of over 2600 mm.

However, the importance of precipitation over the Maritime Continent is not just local. The climatological mean rainfall of over 2600 mm across the region mentioned above has a mean associated latent heat release of ~16 MJ m^{-2} day^{-1} (over an area of ~14 $\times$ 10^6 km^2) when water vapour condenses to form rain clouds. This large amount of latent heat released into the surrounding atmosphere impacts on the circulation of air throughout the tropics and into the sub-tropics. It is for this reason that Charles Ramage (1968) termed the Maritime Continent a "boiler box" for the atmosphere, significant for the climate globally.

The greatest source of variability in precipitation over the Maritime Continent, particularly over the land, is the diurnal cycle (e.g. Yang and Slingo, 2001). Over the regions with the heaviest rainfall, the mean diurnal cycle during boreal winter (November to April) has an amplitude of ~15 mm day^{-1} or even more. This heavy rainfall does not necessarily occur every day, but when averaged over, say, a month or more the signal is clear. This raises the question of what factors may influence the occurrence of the diurnal cycle; for example, if another system of organised convection is in the vicinity, does this act to enhance

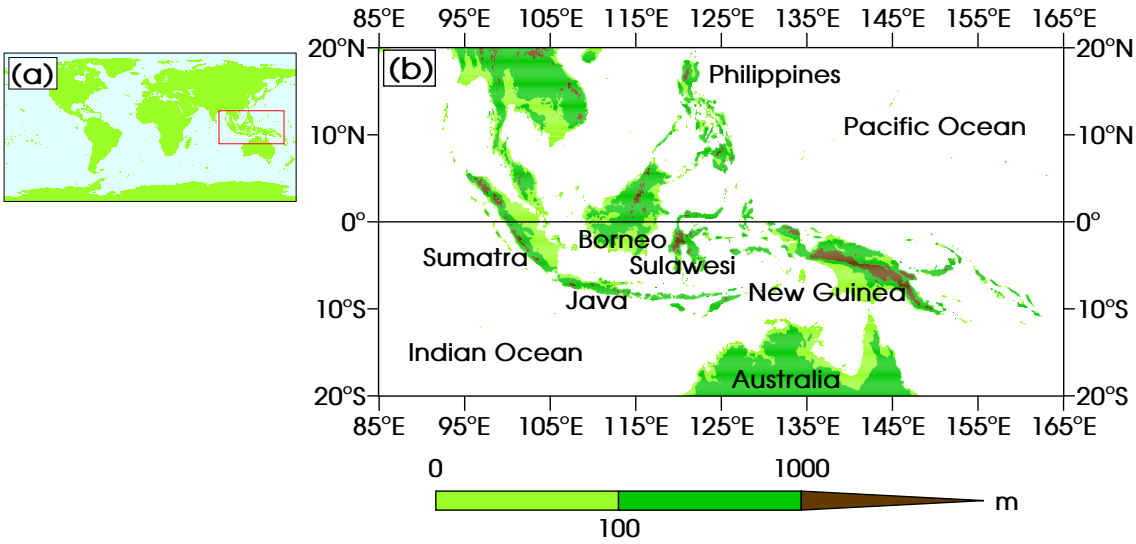

Figure 1.1: (a) Map of the world with the Maritime Continent indicated by the red box. (b) Topography of the Maritime Continent and its surroundings from the GLOBE data set, regridded to $0.11° \times 0.11°$ resolution.

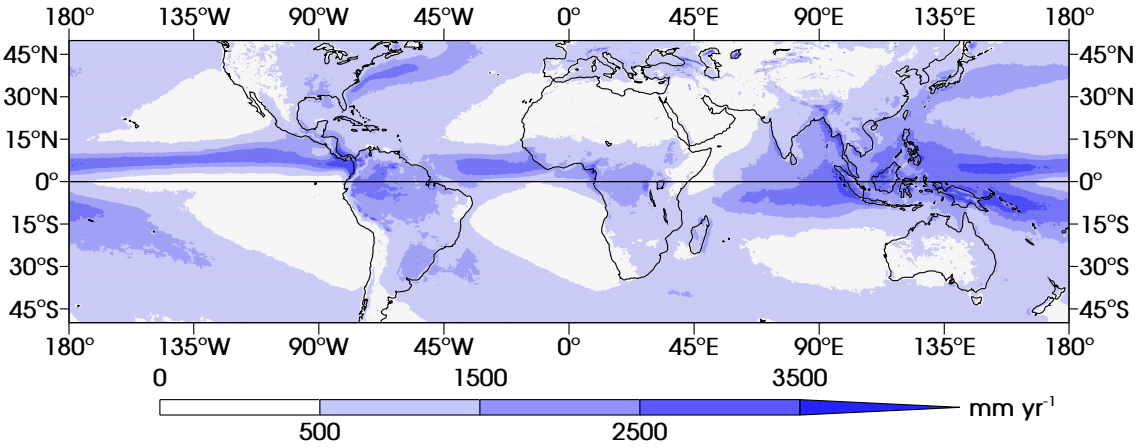

Figure 1.2: Annual mean precipitation from 3B42HQ, the "high quality" (microwave-only) part of the TRMM 3B42 dataset.

or suppress the diurnal cycle? In particular, how does the diurnal cycle interact with weather systems on different spatial or temporal scales?

One phenomenon that contributes to the large-scale environment, within which the diurnal cycle is embedded, is the Madden-Julian Oscillation (MJO; Madden and Julian 1971, 1972; reviews by Madden and Julian, 1994 and Zhang, 2005). On intra-seasonal time scales the MJO is the greatest source of variability in the tropics, and is known to affect weather patterns throughout the tropics and extra-tropics. For example, the MJO influences monsoons (e.g. Lorenz and Hartmann, 2006; Lavender and Matthews, 2009; Pai et al., 2011), interacts with tropical cyclones (e.g. Krishnamohan et al., 2012; Bessafi and Wheeler, 2006;

Hall et al., 2001), affects the extra-tropical circulation through Rossby wave forcing (Matthews et al., 2004) and interacts with the atmospheric circulation at the poles (Flatau and Kim, 2013). One of its key features is large-scale regions in which convection is alternately active and suppressed. A matter for consideration is whether the diurnal cycle varies as these phases of the MJO cycle evolve.

The Tropical Rainfall Measuring Mission (TRMM) has provided high-resolution meteorological data since the start of 1998. For example, gridded ($0.25° \times 0.25°$) estimates of precipitation rate throughout the tropics, every three hours, are available. This enables analysis of the Maritime Continent diurnal cycle of precipitation in unprecedented detail, whilst daily means of the same data product can be used to diagnose the convective aspect of the MJO.

Computer simulations of both the diurnal cycle over the Maritime Continent and the MJO have substantial shortcomings due to the coarseness of models' resolution and unrealistic convective parameterisation schemes. The associated errors lead to errors propagating globally in climate models. Therefore, it is important for global climate prediction that organised convection over the Maritime Continent be better understood and simulations improved. Any interaction that may exist between the diurnal cycle and the MJO needs to be simulated in climate models if convection over the Maritime Continent is to be well modelled.

The High-resolution Global Environmental Model (HiGEM; Shaffrey et al., 2009) is a coupled model with an atmospheric horizontal resolution of $0.83° \times 1.25°$. It has been developed as a higher-resolution version of the Met Office Hadley Centre model, and has many significant improvements in the simulation of various aspects of the climate system. The lack of accuracy of the MJO in many climate models means that there is limited scope for investigating the way in which the MJO interacts with other components of the climate. However, if it can be shown that the MJO is accurately represented, then a model's ability to simulate such interactions can be assessed.

1.2 Questions to investigate

The diurnal cycle and the MJO are two of the most important phenomena affecting rainfall over the highly populated Maritime Continent. The aim of this research is to further our understanding of how, if at all, they influence one

another. Given their importance to the climate of the Maritime Continent, any interaction between the two is also likely to have significant implications. An understanding of this could, in principle, inform short-term forecasting over the region and also be crucial in evaluating longer-term simulations. Any errors in the representation of convection over the Maritime Continent in a climate model is likely to introduce further errors. For example, clouds have a high albedo so an incorrect simulation of their location or timing could strongly affect the radiation budget.

The MJO evolves gradually, with convectively active and suppressed regions propagating slowly from the Indian Ocean to the Pacific Ocean, passing over the Maritime Continent. We wish to examine how the strength of the diurnal cycle of precipitation changes as the MJO moves through its cycle, and to consider the reason for any modulation which occurs, most likely in terms of the dynamics associated with the MJO's propagation. Most of the region over which the propagation of convection occurs is open ocean, with the Maritime Continent providing the only land in the path of the MJO, with the exception of a few very small, scattered islands (such as the Maldives, Cocos Islands and Kiribati). Therefore, it is possible that the MJO's propagation over the Maritime Continent is in some way different from the rest of the tropics. If so, the dynamics which affect the diurnal cycle could themselves be a special case of MJO propagation. Indeed, a chief component of the Maritime Continent diurnal cycle is the diurnal variation in the wind over and around the islands, and this may itself affect the MJO in a way which then feeds back onto the diurnal cycle. If there are other parts of the world in which both the MJO and diurnal cycle are significant, it would be of interest to note whether any interaction takes place there also. Such interactions could be similar to that over the Maritime Continent, or may be different entirely.

Given the important role played by both the Maritime Continent and the MJO in the climate throughout the tropics and extra-tropics, it is vital that both are well simulated by climate models. Output from HiGEM, a state-of-the-art model, will be studied. Many models struggle to simulate a realistic MJO, so a variety of diagnostics will first be used to establish whether MJO-like variability exists in the model and, if so, how accurate the structure and propagation are. However strong and accurate the intra-seasonal variability is, we wish to know whether it has any effect on the Maritime Continent diurnal cycle, and how this compares with any modulation seen in observations. The strength and timing of such interactions are of interest, as is the physical cause. Convection

is parameterised in the model, which often leads to errors (for example, in the timing of convection relative to the diurnal solar cycle). Therefore, this is likely to be a good test of the parameterisation scheme – for example, does the model manage to couple the convection to the dynamics realistically?

1.3 Thesis outline

This thesis begins with a review of existing literature on the Maritime Continent and the diurnal cycle (chapter 2) and the MJO (chapter 3). Satellite data are used in chapter 4 to composite the diurnal cycles of precipitation and wind, and the MJO. In this chapter also, new diagnostics are presented to show the nature of MJO propagation – for example, how likely it is, once MJO-like conditions appear, for the MJO to continue to propagate. Having presented observations of the MJO and the diurnal cycle, in chapter 5 the relationship between the two will be investigated. It will be shown that there exists a scale interaction between the two phenomena, and a possible physical mechanism behind this will be suggested.

The remainder of the thesis is concerned with how well HiGEM reproduces the results of the observational research. In chapter 6 it is demonstrated that an MJO exists in HiGEM, and different features of the MJO's structure and propagation are assessed for accuracy. The scale interaction between the MJO and the diurnal cycle in HiGEM is investigated in chapter 7. Finally, a summary and discussion of all findings is presented in chapter 8.

Chapter 2

The Maritime Continent and the diurnal cycle of precipitation

2.1 The Maritime Continent

The Maritime Continent was introduced in section 1.1 as the archipelago located just north of Australia, straddling the equator between 95° and 160°E, plus the surrounding seas. It is a complex system of islands of many sizes (figure 1.1b) and shallow seas. The largest islands, New Guinea and Borneo, are both in excess of 700,000 km^2 and are two of the world's three largest non-continental islands; the smallest are less than 1 km across (Love et al., 2011). Several of the islands have regions of high topography with peaks over 2000 m, for example the Barisan Mountains along the south-west coast of Sumatra (figure 2.1a), the New Guinea Highlands (2.1b), the mountains of northern and central Borneo (2.1c), mountains throughout Sulawesi (2.1d) and the range of peaks on Java (2.1e).

The climate of the Maritime Continent is of interest in meteorological research both *per se* and because of the impact it has on the rest of the tropics and on the extra-tropics. The Maritime Continent occupies a pivotal location in the warm pool – a region of sea with surface temperature greater than around 28–29°C (e.g., Yan et al., 1992; Weller and Anderson, 1996; Cravatte et al., 2009) – between the Indian and Pacific Oceans. It is thought that, before the emergence of the Maritime Continent islands during the past 5 million years, the Indian and Pacific may have acted as a single ocean basin with free transport of mass and heat between them (Dayem et al., 2007). Now, due to the presence of the

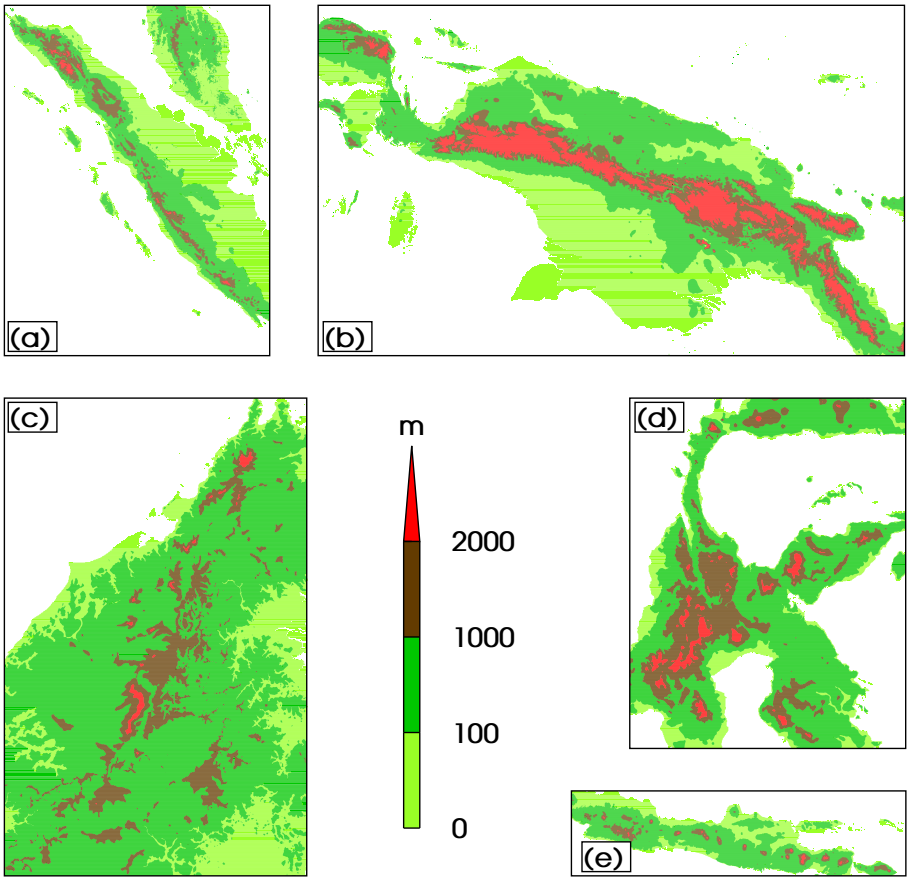

Figure 2.1: Orography of five major mountainous regions in the Maritime Continent: (a) Sumatra and Malay peninsula, (b) New Guinea, (c) Borneo, (d) Sulawesi and (e) Java. Data are from the GLOBE data set, at the original 1 km resolution. Note that the panels are not drawn to the same horizontal scale (cf. figure 1.1).

islands such transport is limited to the Indonesian throughflow (Godfrey, 1996), a current which flows from east to west along the Makassar Strait (between Borneo and Sulawesi) and past the Lesser Sunda Islands (the row of islands directly to the east of Java). This throughflow helps to control the sea surface temperature in the Indian and Pacific Oceans, thus affecting the location of atmospheric convection and atmospheric pressure throughout the tropics and, via teleconnections, at mid-latitudes (Schneider, 1998). Hence, the Indonesian throughflow is of major importance for the climate, particularly in the tropics.

Furthermore, the Maritime Continent forces the tropical climate through its effect on the atmosphere, as first identified by Ramage (1968). Ramage noted that tropical meteorologists used to focus on the ocean alone, but he argued that equatorial regions of land, including the Maritime Continent, transfer more heat to the atmosphere than the equatorial oceans do. The land provides sensible heating to the atmosphere, leading to ascent of air. Note that from

the following form of the Clausius-Clapeyron equation the saturation pressure of water vapour in air is a monotonically increasing function of temperature:

$$e_s = e_{s0} \exp\left[\frac{L}{R_v}\left(\frac{1}{T_0} - \frac{1}{T}\right)\right], \tag{2.1}$$

where e_s is the saturation pressure of water vapour, L is the specific latent heat of vaporisation = 2260 kJ kg^{-1} at 100°C under standard pressure, R_v is the specific gas constant for water vapour = 462 J kg^{-1} K^{-1}, T is the temperature of the air, and e_{s0} is the saturation pressure of water vapour at some reference temperature T_0 (Ambaum, 2010)[1]. Since the surrounding seas provide a ready source of water, the warm ascending air tends to be very moist, leading to the release of latent heat at the condensation level which then heats the surrounding atmosphere diabatically (Dayem et al., 2007). So strong is this heat source that the Maritime Continent has been labelled a "boiler box" for the atmosphere (e.g., Simpson et al., 1993; Saito et al., 2001; Teo et al., 2011).

The Maritime Continent has the planet's most intense convection and highest tropopause (Neale and Slingo, 2003). Not only does the latent heat associated with the convection force equatorial waves which affect the atmospheric circulation throughout the tropics, but also divergent outflow from the upper troposphere is a major forcing for wave generation globally. In a modelling experiment by Jin and Hoskins (1995), the outflow was shown to lead to planetary waves which propagate into the extra-tropics.

The Maritime Continent experiences heavy rainfall all year round, but the local circulations are complex due to the contrast between land and sea (Ichikawa and Yasunari, 2006). Most of the precipitation that falls originates in localised convective storms, and this convection is forced over a range of spatial and temporal scales. The large-scale organisation of such thunder storms is influenced by both the orography of the land and the sea-breeze patterns (Neale and Slingo, 2003).

The chief source of variability in the Maritime Continent climate is on the diurnal timescale, as discussed below (section 2.2). However, the Maritime Continent also acts as a "hub" where several other climatic features and sources of variability intersect and interact, including the Hadley circulation, Walker circulation, tropical cyclones, monsoon, El Niño–Southern Oscillation (ENSO)

[1]Strictly, equation 2.1 holds only if L is constant in T, which is an unrealistic assumption. However, a more rigorous derivation would not change our conclusion that e_s increases with increasing T.

and Madden-Julian Oscillation (MJO). While this research focuses on the interaction of just two sources of variability (the diurnal cycle and MJO), there is scope for investigating scale interactions between any of the afore-mentioned phenomena over this same region.

2.2 The diurnal cycle of precipitation

The Maritime Continent is a complex region in meteorological terms. There are several processes which force the spatial and temporal distribution of precipitation, the most important being the diurnal cycle of solar heating, the land-sea breeze circulation caused by the many coastlines, and the mountain-valley breeze circulation caused by regions of high topography. Such processes are important in various locations throughout the tropics, but especially over the Maritime Continent archipelago. What is common to nearly all tropical areas, however, is that these various mechanisms cause precipitation to obey a pronounced diurnal cycle, with sharp contrasts between land and ocean.

The diurnal cycle of precipitation has been studied for several decades. For example, Dexter (1944) and Riehl (1947) were among the earliest to study the concept of the diurnal cycle. Later studies began to investigate the diurnal cycle in the tropics specifically, such as in Charnock et al. (1956) and Pedgley (1969). In the 1970s, field campaigns such as the Barbados Oceanographic and Meteorological Experiment (BOMEX; 1 May to 28 July 1969), the Global Atmospheric Research Program (GARP) Atlantic Tropical Experiment (GATE; 15 June to 23 September 1974) and the Winter Monsoon Experiment (WMONEX; near Borneo, December 1978) allowed researchers to study the tropical diurnal cycle in ever increasing detail. This was followed in the 1990s by the Tropical Ocean Global Atmosphere Coupled Ocean Atmosphere Response Experiment (TOGA COARE; 1 November to 28 February 1993). However, such studies still tended to be confined to small regions, so that regional variations between the nature of the diurnal cycle complicated the search for the underlying mechanisms (Yang and Smith, 2006). For example, although it was generally accepted that the phase of the diurnal cycle of precipitation over land is linked to the diurnal cycle of solar radiation which destabilises the boundary layer in the afternoon, many studies discovered a maximum in precipitation over land during the small hours of the morning; although studies tended to find

that the maximum precipitation over ocean occurs in the morning, others (such as over the South Pacific Convergence Zone) found a peak in the afternoon (Nesbitt and Zipser, 2003). More recently, satellite missions such as the Tropical Rainfall Measuring Mission (TRMM; see section 4.2) have allowed coverage across the whole of the tropics in enough detail to investigate the diurnal cycle more rigorously. Thus, Yang and Slingo (2001) and Nesbitt and Zipser (2003) were able to provide tropics-wide climatologies of the diurnal cycle. Aside from observing the physics of the diurnal cycle, such climatologies are also much-needed when evaluating model simulations.

2.2.1 Diurnal cycle throughout the tropics

Gray and Jacobson (1977) reported that the existence of a diurnal cycle of deep convection over land in the tropics was already well established through observations, and showed that a diurnal cycle exists over tropical oceans also. Since then, many studies have shown a marked contrast between the land- and ocean-based cycles. For example, Yang and Slingo (2001) found that, throughout the tropics, where there is an ocean-based cycle of deep convection it tends to peak in early morning local time, whereas the land-based cycle peaks in the evening. However, they also noted that there are significant variations due to local differences in the land-sea and mountain-valley circulations. Many studies have shown that the oceanic diurnal cycle is weaker than that over land; Lindfors et al. (2011) found that the ocean-based cycle is so weak it is not identifiable everywhere, but that zonally averaging gives a robust oceanic diurnal cycle across the tropics. There is also some evidence that a double diurnal peak may exist over some regions. Yang and Smith (2006) found that the oceanic diurnal cycle tends to peak in late evening to early morning, but that a secondary peak appears in mid-to-late afternoon in regions where there is large-scale convergence. A similar observation was made by Liu and Zipser (2008), who found oceanic peaks during the night and the early afternoon. However, they stated that due to the timing of this second peak it could not be termed a "semi-diurnal cycle".

As well as land and ocean, Kikuchi and Wang (2008) identified coastlines as a third diurnal cycle regime. Using empirical orthogonal function (EOF) analysis of TRMM 3B42 (see section 4.2.2), they found 89% of the variability in tropical precipitation to be explained by the first two EOFs, which both account for the diurnal cycle. Agreeing with previous studies, they found the land regime to

have a strong diurnal cycle peaking in the afternoon and the ocean regime to have a relatively moderate diurnal cycle with a peak in the early morning. The third, coastal, regime also has a strong diurnal cycle with phase propagation onshore (with peaks in the afternoon and evening) and offshore (with peaks overnight and in the morning).

Other studies have focused on further aspects of the diurnal cycle. For example, Williams and Houze (1987) investigated the diurnal variability of cloud cluster size and found that large clusters over ocean peak in frequency during mid-morning. Takayabu (2002) compared the diurnal cycles of stratiform and convective precipitation and found that the two are synchronised over the ocean, but over land the convection peaks between 15:00 and 18:00 LT, whereas stratiform precipitation peaks between midnight and 03:00 LT. Sobel et al. (2011) considered the effect of island size, and found that it tends only to be over large islands that rainfall is enhanced relative to the surrounding ocean. According to their analysis, over small islands the enhancement is negligible compared with the surrounding ocean.

2.2.2 Diurnal cycle over the Maritime Continent

Over the Maritime Continent the diurnal cycle of precipitation tends to follow the pattern observed over the tropics as a whole, as described above – a strong cycle over land peaks later than a weak cycle over ocean. However, the Maritime Continent has many localised effects which must also be considered.

Biasutti et al. (2012) present the diurnal cycle of the rain frequency measured by the TRMM precipitation radar instrument (section 4.2.1), as reproduced in figure 2.2. The large islands such as Sumatra, Java, Borneo, Sulawesi and New Guinea are almost clear of rainfall in the morning (local time), with rainy conditions over the surrounding oceans. Conversely, during the evening there is rain over the land with almost no rain over the immediately surrounding oceans. Over the large islands the precipitation tends to start just inland of the coasts (e.g. Sulawesi and New Guinea in panel (b)) and over mountains (e.g. New Guinea in panel (b) and Sumatra in panel (c)). By late evening, the rainfall has spread to all parts of these islands (panel (e)). Although figure 2.2 shows rainfall frequency rather than rainfall amount, the diurnal cycle of rainfall amount is very similar, as found by numerous studies (e.g., Kubota and Nitta, 2001; Nesbitt and Zipser, 2003).

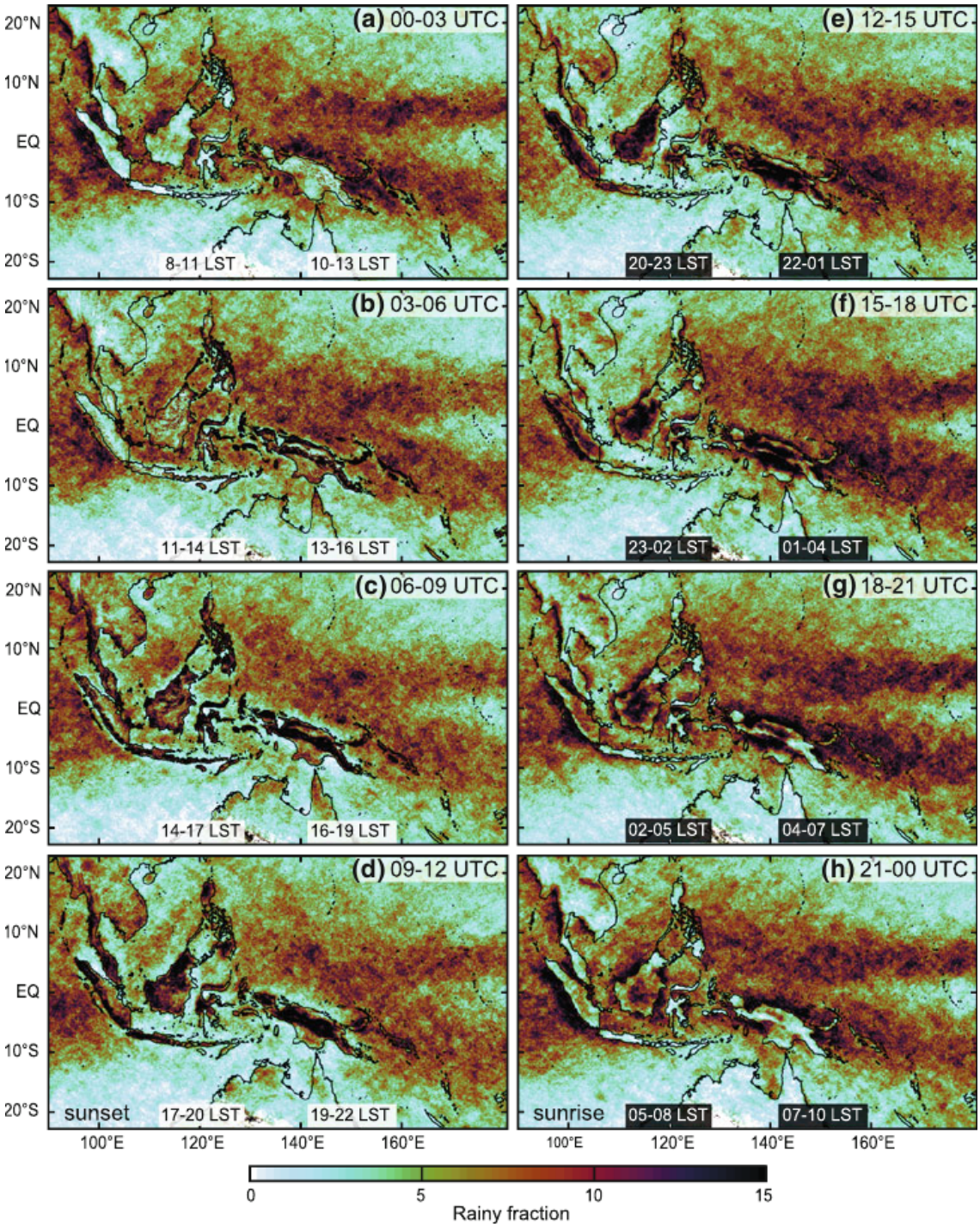

Figure 2.2: Diurnal cycle of rainy fraction (percentage of measurements in which rain rate is non-zero) over the Maritime Continent, measured by TRMM PR. Data are shown in three-hourly time bins in UTC (local solar times are written at the bottom of each panel for reference). *Image from Biasutti et al. (2012), figure 17.*

Research has identified three broad causes of the Maritime Continent diurnal cycle and its features: the diurnal cycle of insolation, the land-sea breeze circulation and the mountain-valley breeze circulation. Using EOF analysis of

TRMM data, Teo et al. (2011) found two modes associated with the diurnal cycle. The first EOF (which explains 57.2% of the variance) corresponds to the diurnal cycle of land-surface heat flux due to solar heating and long-wave radiative cooling, which leads to a diurnal cycle in convective instability. Thus, a diurnal cycle of convective precipitation occurs over the land. The second EOF (33.7% of the variance) corresponds to mesoscale dynamics interacting with gravity waves, density currents and the local circulation around coasts and mountains. Qian (2008) uses the existence of these mesoscale dynamics and currents to explain the fact that precipitation is strongly focused on the islands. He argues that this phenomenon is caused by the diurnal cycle itself, with the convergence of sea breezes (see below) causing moist air to be lifted and convection to be initiated (hence the bands of precipitation which form just inland of the coasts in figure 2.2b). He further argues that the convergence is reinforced by the mountain-valley circulation, before cumulus merger processes come to dominate and enhance the convection yet further.

The dynamics involved in this argument are summarised by figure 2.3 (figure 16 from Biasutti et al., 2012). During the day, the land and sea are heated at different rates since land has a smaller heat capacity, initiating sea breezes (onshore; panel (a)). These breezes converge over islands (panel (c)), especially near coastlines which curve outwards (panel (g)). Meanwhile, winds blowing up mountain slopes form strong rainfall over high orography (panel (e)). These all contribute to the day-time part of the diurnal cycle. Overnight, the land cools faster than the ocean so that land-breezes (offshore) are triggered (panel (b)). Now the reverse argument holds, with divergence over land where the coast curves outwards but convergence over ocean where the coast curves inwards (panel (h)), and downslope winds (panel (f)). This explains the facts that rainfall weakens overnight over land, and strengthens over ocean. Of the two modes of land-based rainfall which were identified by Teo et al. (2011), the first (convective instability caused by solar heating) does not occur over ocean during the night, but the second (relatively small-scale dynamics) does. This is why the ocean-based rainfall overnight is significantly weaker than the land-based rainfall during the day.

Studies of specific locations in the Maritime Continent are consistent with this dynamical scheme. Zhou and Wang (2006), for example, investigated the diurnal cycle over New Guinea using the TRMM precipitation radar. The observations showed bands of precipitation just inland from the coast forming between the early morning and late evening, which gradually propagate inland

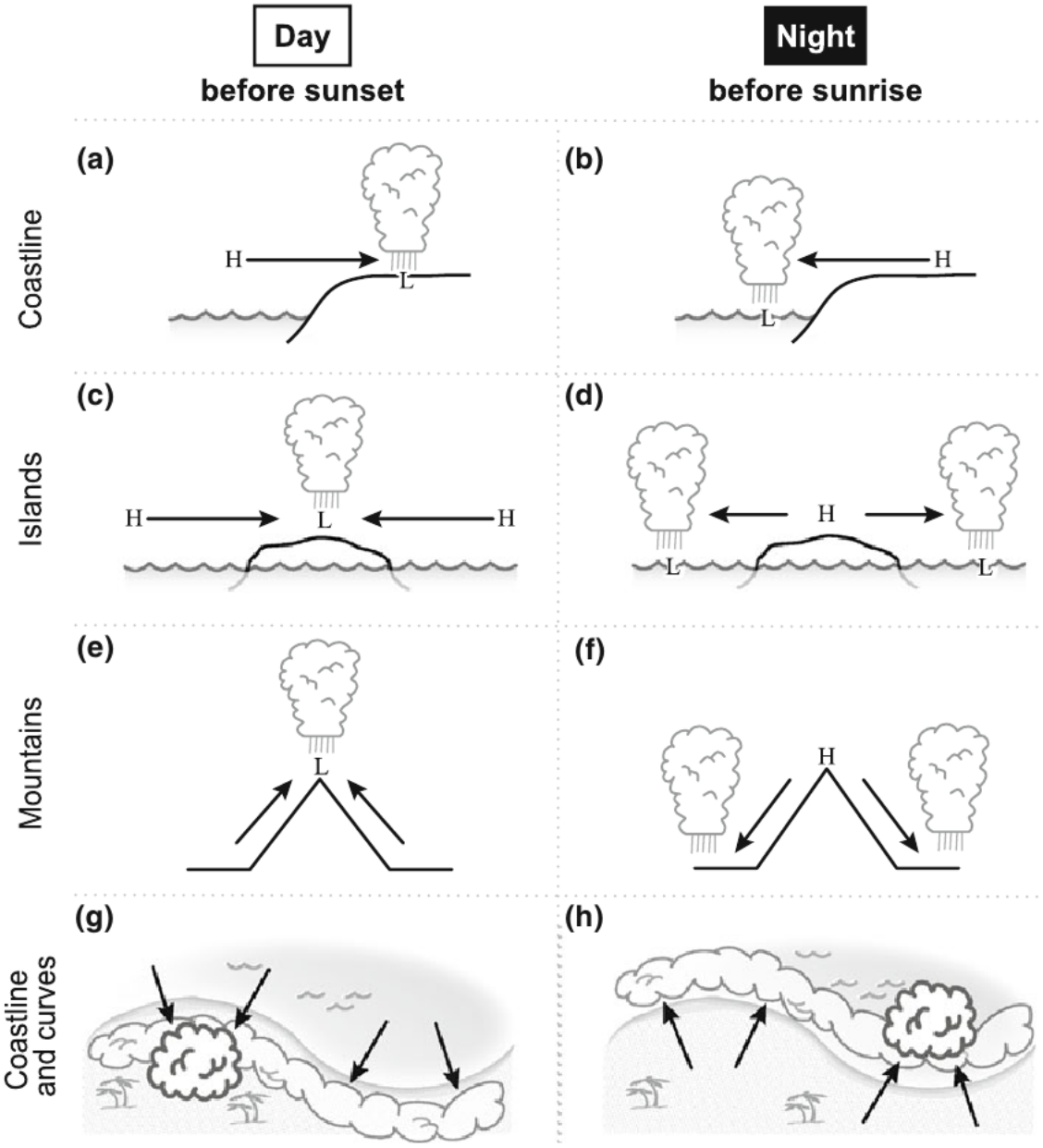

Figure 2.3: Schematic diagram of dynamics crucial to the Maritime Continent diurnal cycle. During the day sea breezes are triggered (a) which converge over islands (c). Similarly, at night land breezes blow offshore (b) leading to divergence over islands (d) and convergence over the straits and other seas of the Maritime Continent. Upslope (e) and downslope (f) winds blow during day and night respectively, creating the mountain-valley breeze circulation. The land-sea breeze circulation set up by the processes in (a) and (b) set up a convergence/divergence pattern just onshore and just offshore, due to the curvature of the coastlines (g and h). *Image from Biasutti et al. (2012), figure 16.*

and weaken. During the early afternoon, upslope winds create another band of precipitation over the mountains which intensifies and comes to dominate the precipitation field, before weakening overnight. Also overnight, bands of

precipitation form just offshore.

Of course, the daily breeze circulations mentioned above mean that there is also a diurnal cycle in the wind field. This has been observed, for example, by Gille et al. (2003; 2005) who used scatterometry data to detail the diurnal cycle of wind throughout the tropics. It is not a surprise to find that a diurnal cycle exists in other associated fields as well. For example, Liu and Zipser (2008), and Virts et al. (2013) have investigated the diurnal cycle of lightning flashes in the Maritime Continent area.

A further feature of the diurnal cycle consists of gravity waves triggered by the strong land-based convection, which propagate overnight and can produce further convection, especially offshore (Yang and Slingo, 2001). This has been studied off the south-west coast of Sumatra in particular, with strong rainfall forming during the day over the Barisan mountains which are very close to the coastline (figure 2.1a). Noting the offshore propagation of precipitation visible in TRMM observations, Love et al. (2011) showed that the Met Office Unified Model (UM) is able to simulate the gravity wave mode responsible; in a high-resolution run (4 km) with convection explicitly resolved, the convection produced a realistic response to the wave to give a propagating precipitation signal similar to that in observations. The wave propagates offshore through a region in which conditions are favourable for precipitation to form: Fujita et al. (2011) found, through observations made off the Sumatran coast, that precipitable water vapour (PWV) increases sharply overnight, with small amounts of PWV at around 22:00 LT but large amounts by 04:00 LT.

2.2.3 Modelling the Maritime Continent region

Neale and Slingo (2003) reported that the Maritime Continent presents a significant challenge for climate modelling because of the complex forcings and interactions mentioned above, and that models tend to exhibit a dry bias over the region. However, the Maritime Continent's global importance makes it vital that models are able to simulate its climate accurately in order to reproduce the global circulation faithfully.

In models the most frequent problem, which also tends to be the greatest source of inaccuracy, reported by researchers studying the diurnal cycle is that the diurnal phase is too early, especially for convective rainfall. A second, more minor, problem is that the diurnal cycle can have too large an amplitude. Often,

the diurnal phase of convection is found to be coupled directly to solar heating so that the maximum over land occurs around noon rather than in late afternoon or early evening. As well as giving an incorrect timing of the diurnal phase, this can lead to errors in the radiative balance since clouds appear at the wrong time relative to the cycle of solar radiation flux (and this itself will also feed back onto the convective diurnal cycle). Climate models tend to be unable to resolve cloud processes explicitly, and it is the parameterisation schemes that are believed to be responsible for the phase bias.

Such biases are reported across a range of climate models, both over the Maritime Continent and elsewhere in the tropics. For example, the Hadley Centre climate model HadAM3 has the diurnal cycle of convection peaking at about mid-day over the tropics in general, albeit with an accurate diurnal amplitude (Slingo et al., 2004). The International Pacific Research Center (IPRC) regional climate model (RegCM) has a very similar diurnal bias (Wang et al., 2007). Hara et al. (2009) found that the Meteorological Research Institute General Circulation Model (MRI-GCM), developed by the Japan Meteorological Agency, similarly simulates the phase of the diurnal cycle to be too early, but only over large islands (greater than around 200 km across). Over inland regions the phase bias was so large that the model was almost in anti-phase with observations. Over smaller islands, however, the phase was correctly modelled. Collier and Bowman (2004) quantified the error in diurnal phase in version 3 of the Community Climate Model (CCM3), including over Papua New Guinea (the eastern half of New Guinea island), where the diurnal cycle peaked about 5 hours before the peak in observations. Other errors found in models can include a lack of nocturnal offshore propagation from the Maritime Continent islands, such as in the Geophysical Fluid Dynamics Laboratory (GFDL) global atmospheric model (Ploshay and Lau, 2010). Models which exhibit an accurate tropical diurnal cycle include the Nonhydrostatic Icosahedral Atmospheric Model (NICAM), developed at the Center for Climate System Research (CCSR) in Tokyo, in which the Maritime Continent diurnal cycle of precipitation, rather than peaking with the cycle of solar heating, is strongly coupled with the diurnal breeze circulation (Sato et al. 2009).

While climate models are still too coarse in resolution to resolve convection explicitly, improvements in resolution appear to give little or no improvement in the models' ability to represent the diurnal cycle, especially when considering the diurnal phase. For example, Pearson et al. (2014) found a better representation of the diurnal cycle in higher-resolution (4 km) than

lower-resolution (12 km) runs of the UK Met Office Unified Model (UM), but attributed this to differences in the parameterisation scheme rather than the resolution itself. Sato et al. (2009) found that a higher resolution was able to improve the diurnal phase in NICAM, but only over land and not over ocean. Dirmeyer et al. (2012) found that higher resolution was not able to improve the diurnal phase in the operational Integrated Forecast System (IFS) from the European Centre for Medium-Range Weather Forecasting (ECMWF), although it did offer some improvement to the diurnal amplitude and daily mean of precipitation.

Many attempts have been made to improve the timing of convection by tuning the parameterisation schemes used in models. The main technique has been to alter the way in which entrainment is handled; specifically, researchers have experimented with the dependence of entrainment on the surrounding atmospheric conditions, with some success. Del Genio and Wu (2010) tried several parameterisation schemes in the Weather Research and Forecasting (WRF) model and found that the most successful at simulating the correct diurnal phase was a scheme in which entrainment varies with both buoyancy and updraft velocity (in a control run, entrainment was found to be too weak in general). Wang et al. (2007) increased the entrainment rate for shallow and deep convection in the IPRC RegCM, and found that each gave an improvement in both diurnal amplitude and phase. In an experiment with the UM, Stratton and Stirling (2012) also improved the diurnal amplitude and phase, by allowing entrainment rate to vary inversely with lifting condensation level (LCL), since LCL can be considered a proxy for cloud area early in the day. However, this did have the side effect of strengthening the Hadley circulation, which was already too strong in the model. An attempt was made by Slingo et al. (2004) to improve HadAM3 by calling the radiation scheme in full with every time step (usually it is called every sixth time step, for reasons of computational expense). They noted that the main effect of this was, over central Africa, to decouple the diurnal cycle of precipitation and outgoing longwave radiation (OLR), and speculated on whether this was indeed a real physical phenomenon.

2.3 Summary

The Maritime Continent archipelago is a complex region where many meteorological and oceanographical phenomena, on a variety of spatial and

temporal scales, interact. This means that there is much scope for studying scale interactions in observations, but it is a complex area to simulate accurately, and models tend to exhibit errors there. This is problematic because of the wide-ranging impacts that the Maritime Continent has on the rest of the tropics and the rest of the globe. The Maritime Continent is known as a atmospheric "boiler box" due to the latent heat release associated with the formation of convective clouds. This latent heat is enough to affect the atmospheric circulation well beyond the Maritime Continent itself.

The main component of patterns of precipitation over the Maritime Continent is the diurnal cycle, a phenomenon which occurs throughout the tropics. It arises from the diurnal cycle of solar heating, the land-sea breeze circulation and, in regions of high orography, the mountain-valley breeze circulation. A distinct contrast exists between the land and the sea, the land-based cycle being considerably stronger and peaking later in the day. During the morning there is almost no rain over the land of the Maritime Continent but there is rainfall over the surrounding oceans; in the evening the reverse is true. The strong convection over the land triggers gravity waves which propagate offshore overnight, triggering further convective rainfall as they do so.

Significant model errors in the Maritime Continent typically include a dry bias in the daily mean precipitation, and a diurnal cycle that peaks too early in the day over land (at noon rather than in late afternoon or the evening). The incorrect diurnal phase is caused by convection in the model being linked directly to the diurnal cycle of solar heating. This is due to failings in the convective parameterisation schemes used in the models. Improvements in model resolution have had little effect on the diurnal phase, but changes to parameterisation schemes, especially regarding the way in which entrainment rates are determined, has led to some improvement of the simulated diurnal cycle.

Chapter 3

Madden-Julian Oscillation

3.1 Introduction

The Madden-Julian Oscillation (MJO) is the mode of the tropical climate which has the greatest associated intra-seasonal variability. Discovered in the early 1970s (see section 3.2), by the end of the 20th century it had become one of the most studied tropical phenomena. In the 21st century the volume of research has continued to increase dramatically as it has become increasingly clear that the MJO is one of the most dominant and influential components of the tropical climate, and also affects the climate far into the extra-tropics. Indeed, Raymond (2001) described a full explanation of the MJO as the "holy grail" of tropical atmospheric dynamics.

The number of citations of the original MJO paper, Madden and Julian (1971; hereafter, MJ71), is plotted against time in figure 3.1. Since most papers on the MJO cite MJ71, the number of citations is a rough proxy for the amount of international MJO research activity. The number of citations is tending to increase over time, and in the last two years has accelerated rapidly.

A review of research into the MJO up to the early-to-mid 1990s was written by the initial discoverers (Madden and Julian, 1994) and a comprehensive account of MJO research up to the mid 2000s was written by Zhang (2005). This chapter describes the background of the MJO, its main features, theories of its propagation and its representation in climate models.

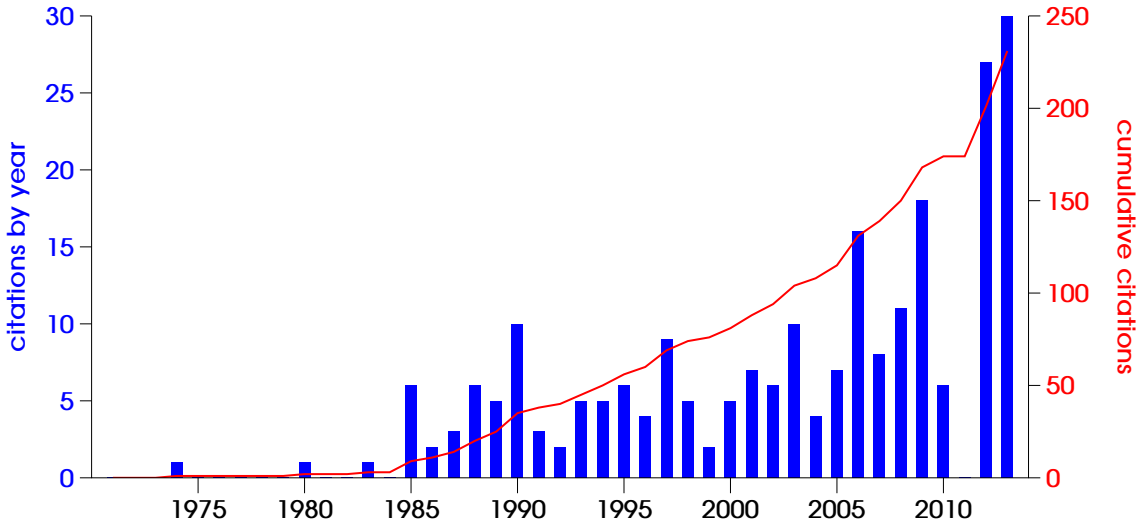

Figure 3.1: Number of citations[1] of Madden and Julian (1971): by year (blue) and cumulative (red).

3.2 Discovery and early work

The first sign of an especially strong signal in the tropics on intra-seasonal time scales was discovered by MJ71 when analysing rawinsonde data from Canton Island, an atoll in the Pacific Ocean near 3°S, 172°W. Rawinsondes are similar to radiosondes but measure wind only; thus, they provide a vertical profile of wind speed and direction at a particular location. MJ71 noticed a strong but broad spectral peak in zonal wind at upper and lower levels in the troposphere (150 and 850 hPa) in the period range 41–53 days. The spectral power at these time periods was minimal at intermediate levels (700–400 hPa), and there was no evidence of a similar feature in meridional wind. The researchers had no prior reason to expect such a signal, but it was shown to be statistically significant and could also be seen in pressure and tropospheric temperature data.

Figure 3.2 shows Figure 1 from the 1971 paper. The co-spectrum (real part of the cross-spectrum) between surface pressure (p_0) and zonal wind at 850 hPa (u_{850}) is positive for intra-seasonal time periods, peaking at around 1/45 cycles per day (cpd). Thus, there is an intra-seasonal oscillation in which low-level easterly (westerly) anomalies coincide with low (high) anomalies of p_0. The co-spectrum of u_{850} and u_{150} is negative over the same frequency range, again peaking around 1/45 cpd. Thus, the intra-seasonal oscillation gives rise to easterly (westerly) anomalies in the upper troposphere at the same time as westerly (easterly) anomalies at low levels. Given that the oscillation is not

[1]Source: http://journals.ametsoc.org/doi/abs/10.1175/1520-0469(1971)028<0702:DOADOI>2.0.CO;2

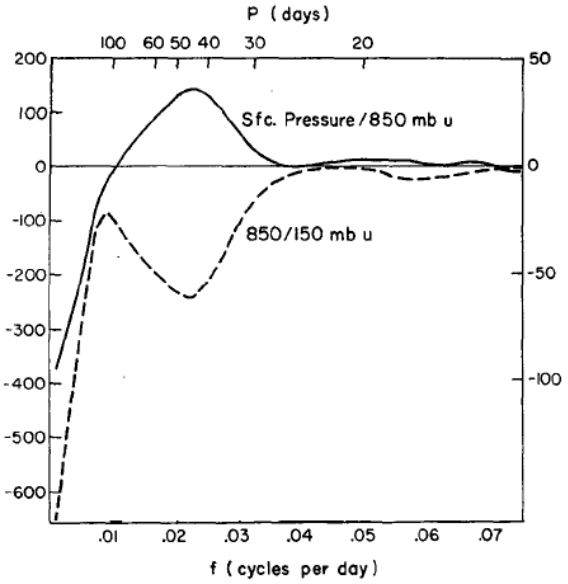

Figure 3.2: Co-spectra of: zonal wind at 850 hPa and zonal wind at 150 hPa (dashed line, left-hand axis), and zonal wind at 850 hPa and surface pressure (solid line, right-hand axis). *Image from Madden and Julian (1971), figure 1.*

visible in the meridional wind field, the authors assumed it to consist of some kind of circulation in the vertical-longitude plane (like a Walker cell). The relative phases of p_0, u_{850} and u_{150} suggest a similar structure to that of a first-baroclinic-mode equatorial Kelvin wave. MJ71 also suggested that deep convection may be part of the driving mechanism for the oscillation, since the vertical structure extends throughout the whole height of the troposphere.

The second paper on the MJO, Madden and Julian (1972; hereafer, MJ72), extended the investigation of the intra-seasonal oscillation to several other locations in the tropics. These extra data sets demonstrated that the oscillation is global in scale and allowed the authors to propose a speculative physical mechanism, shown schematically in figure 3.3. A negative pressure anomaly appears over the Indian Ocean, between Africa and Indonesia, in the latitude band 10°S–10°N (panel F). This anomaly propagates slowly eastward as far as the Pacific Ocean, where it weakens and dies away (panels G–C). Large-scale zonal circulation cells are also shown; where there is low-level convergence and upper-level divergence there is associated deep convection, as predicted by MJ71. The circulation cells and the convection also propagate slowly eastward, strengthening over the Indian Ocean (panel G) and weakening after passing over the Maritime Continent (panels B and C). Notice that, complementing the deep convection which coincides with regions of ascent, convection is suppressed in regions of descent, leading to alternating active and suppressed regions.

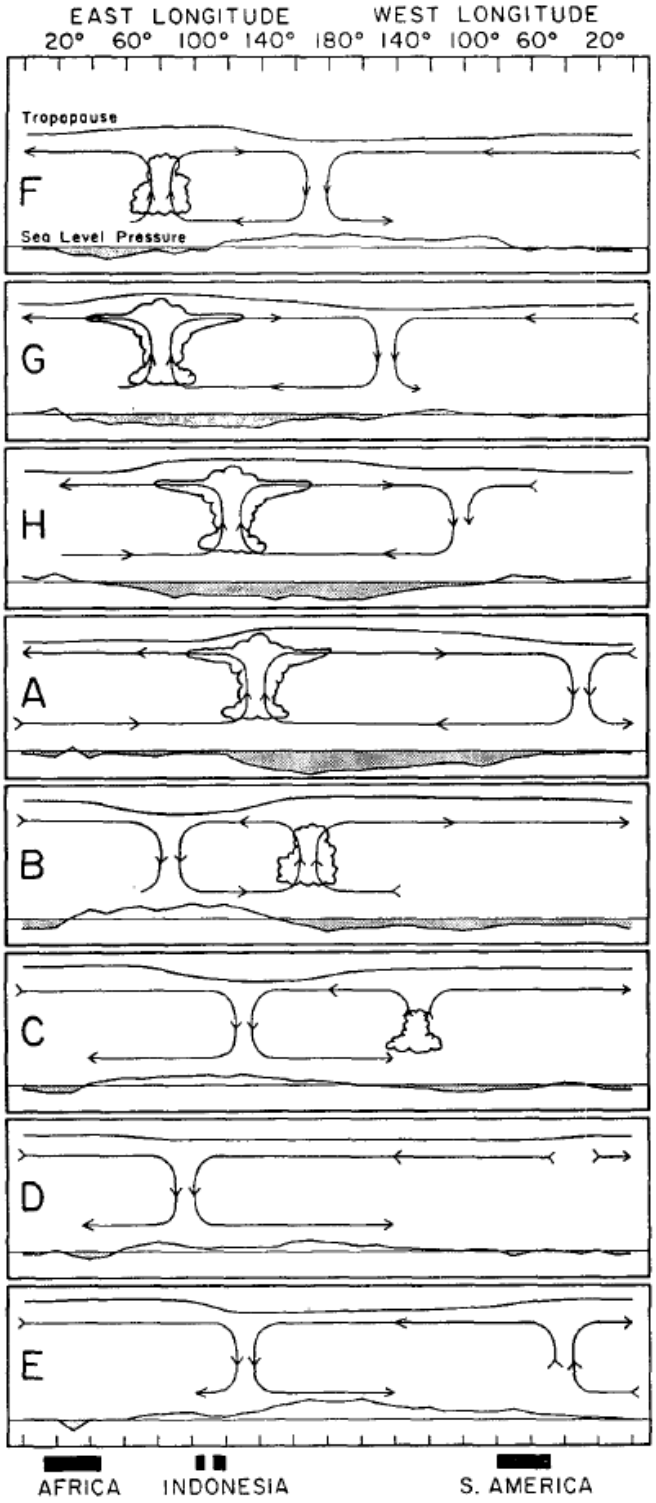

Figure 3.3: Speculative schematic diagram of the MJO, dating from 1972. Surface pressure anomaly is plotted at the bottom of each of the eight snapshots of the MJO, and relative tropopause height at the top of each. For surface pressure, negative anomalies are shaded. Zonal and vertical flow are indicated by the arrows, and large-scale convection anomalies are indicated by small (cumulus) or large (cumulonimbus) clouds. *Image from Madden and Julian (1972), figure 16.*

Although the MJ72 mechanism was based on little more than circumstantial evidence, and despite the large body of other research which has been carried out since, it is still used today to illustrate the MJO's propagation. Zhang (2005) reproduced this figure as an introduction to the main structure of the MJO.

Given the role of deep convective systems in the oscillation, it is possible to observe the eastward propagation in outgoing longwave radiation (OLR), which is a proxy for cloud top height and, therefore, for precipitation. Measurements of OLR by satellites in the 1970s and beyond allowed researchers to study this in detail. Lau and Chan (1983) described the pattern of OLR over the central equatorial Pacific Ocean as a dipole, alternating between wet and dry periods with a frequency of about 2 to 3 months. Moreover, wet periods over the Pacific Ocean were found to be accompanied by dry periods over the Maritime Continent, and *vice versa*. This is consistent with MJ72's mechanism. In panels H and A of figure 3.3 there are suppressed convective conditions (hence, clear skies) over the central Pacific Ocean whilst deep convection prevails over the Maritime Continent. Conversely, in panels B and C the convection is over the Pacific Ocean, with suppressed conditions over the Maritime Continent. A later study, Lau and Chan (1986), confirmed not only the wet/dry dipole over the Pacific Ocean but also demonstrated the eastward propagation of convection from the Indian Ocean to the Pacific, using OLR observations. The oscillation was shown to include this eastward OLR propagation in all seasons.

A major advancement in the understanding of the internal structure of the MJO was made by Nakazawa (1988), again using observations of OLR. It was known that tropical clouds tend to be organised into clusters on the order of 10^2 km across, consisting of a mixture of convective and stratiform precipitation. Furthermore, these clusters can form super clusters, on the order of 10^3 km across. Within an eastward-propagating convective region in the MJO there are several of these super clusters, which themselves also propagate eastwards. However, the clusters within them propagate westwards. These clusters have a lifetime of 1–2 days. The super clusters, with a lifetime of up to 10 days, propagate eastwards because new cloud clusters tend to form to the east of the most mature existing cluster. Thus, the super cluster envelope propagates to the east even though there is no advection, wave propagation or any other kind of motion in that direction. This eastward propagation of super clusters is consistent with the slow progression of the MJO from the Indian Ocean to the Pacific Ocean. Rather than there being a form of atmospheric circulation such as an equatorial Kelvin wave itself propagating at the MJO speed, the

rate of eastward propagation is instead controlled by the rate at which new cloud clusters form. Thus, Nakazawa (1988) had shown that the intra-seasonal oscillation is composed of a "hierarchy" of convection across a range of spatial scales.

MJ71 stated that the oscillation they had discovered was a broad-band phenomenon, not restricted to a small range of frequencies. In fact, the band of frequencies covered by the MJO is so broad that studies tend to differ widely on what counts as a "typical" MJO frequency. MJ71 stated that the spectral peak they had observed was in the range 41–53 days, but referred to the phenomenon as the 40–50-day oscillation. MJ72 also referred to the oscillation as having period 40–50 days, but pointed out that it can actually range from 22 to 79 days. Several researchers have referred to it as the 30–50-day oscillation (e.g., Krishnamurti and Subrahmanyam, 1982) and others as the 30–60-day oscillation (e.g., Weickmann et al., 1985). Zhang (2005) referred to the MJO as the 30–90-day oscillation but stated that the period can be as long as 100 days. The range of frequencies covered can be explained by the variability in both the speed of the eastward propagation and the interval between MJO events (Zhang, 2005). These both vary seasonally and inter-annually. In this thesis a "standard" MJO will generally be said to last about 48 days, but it should always be borne in mind that this can vary widely.

3.3 Features of the MJO

The previous section described the initial discovery of the MJO in the 1970s, and the discovery of some of its main features in the 1980s. This section gives a more detailed description of the MJO as it is currently understood. First we examine the MJO as diagnosed by the indices of Wheeler and Hendon (2004; hereafter, WH04), which will be used extensively in this thesis. There follows an overview of the existing literature on the nature of the MJO and its propagation.

WH04 introduced a system of MJO indices, used to track the progress of the MJO as it evolves through the stages of its life cycle, which are now popularly used in MJO studies. Prior to this, researchers had to decide for themselves how to diagnose the MJO for each study carried out, and the ensuing lack of consistency meant that comparing results from different papers was often inconvenient at best. We have seen that the MJO consists of a cycle of convection, mainly limited to the eastern hemisphere, and of a planetary-scale circulation

pattern. Other indices have been proposed (e.g., Kiladis et al., 2014; Ventrice et al., 2013), often with the intention of focusing on some particular feature of the MJO. The WH04 indices have the advantages of capturing both the convective and the circulatory features, and of being available in real time. Straub (2013) warned that using different indices can give an entirely different picture of the MJO. Events may appear to be initiated on different dates, and events identified by one set of indices may not appear to exist at all when using other indices. However, in this study the WH04 indices only will be used, given their advantage of being based on an overall picture of the MJO's structure and being so widely used in the existing literature. These indices divide the MJO into eight separate "phases". The WH04 methodology will be explained in detail in chapter 6 when it will be used to diagnose the MJO in the HiGEM model. Here, a brief description is given.

3.3.1 Wheeler and Hendon (2004) composites

By a process of trial and error, WH04 decided that OLR, u_{850} and u_{200} are the best three variables to use, in combination, to show the progression of MJO events from initiation to dissipation. Having first removed sources of variability not connected with the MJO, the first two empirical orthogonal functions (EOFs) were found from a single combined field of the three variables, averaged over 15°S–15°N. (These EOFs will be seen in figures 6.6a and b.) Data are then projected onto these EOFs to describe the state of the MJO in terms of just the two principal components (PCs). This process can be carried out in near-real-time, so the two PC time series are referred to as the Real-time Multivariate Indices (RMMs). If RMM2 is plotted against RMM1, a progression of the MJO with convection propagating eastwards is indicated by anti-clockwise rotation in the RMM plane. Instead of expressing the MJO in terms of the two RMMs (i.e., Cartesian co-ordinates), it is more useful to express it in polar co-ordinates. Then, the state of the MJO at any given time is described by its amplitude (strength) and phase (telling us the longitudinal positions of the active and suppressed convection).

WH04 divided the RMM plane into octants to define eight "MJO phases". An example is given in figure 3.4, for April to May 2002. Propagation is generally in the anti-clockwise direction. There is no strong MJO signal at the beginning of April, but an MJO event is initiated around the 12^{th} of the month. This is called a *primary* MJO event. During May the MJO propagates through phases 3

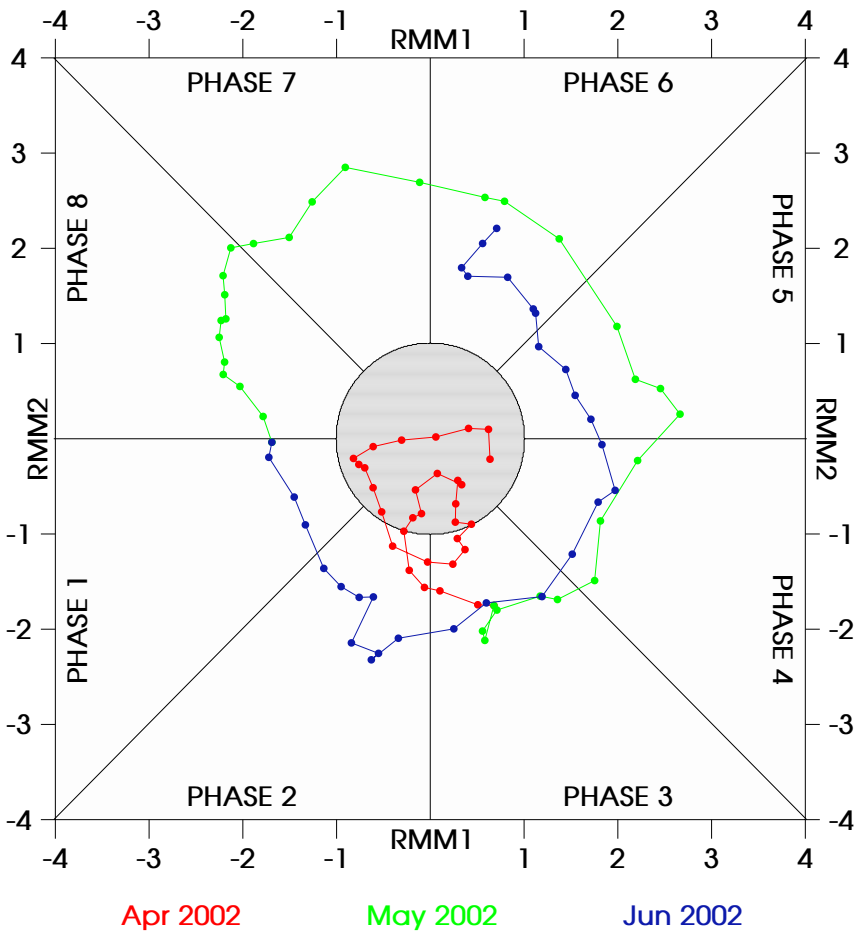

Figure 3.4: Example of a WH04 phase diagram, for April to June 2002. If the RMM amplitude is less than 1 (indicated by the shaded circle) then the MJO is considered to be "weak".

to 8. Moving into June, the MJO returns to phase 1 and continues to evolve through the phases. This cycle of the phase diagram is a *secondary* or *successive* (e.g., Matthews, 2008) MJO event, since it proceeds directly from the previous MJO.

Based on these eight WH04 phases it is possible to create composites showing each stage of the MJO during its evolution. Although this was done by many other researchers before WH04, the WH04 phases have become the most-used indices for diagnosing and investigating the MJO and they will be used throughout this thesis. The anomalies of OLR and 850 hPa wind for each of the eight composites are shown in figure 3.5. Negative OLR anomalies (shaded) indicate cold, high cloud tops and, therefore, are a sign of deep convection. As such, they are often taken to be a proxy for precipitation (e.g., Jury et al., 1993; Sandeep and Stordal, 2013).

The OLR anomalies confirm the finding of MJ72 and Lau and Chan (1986),

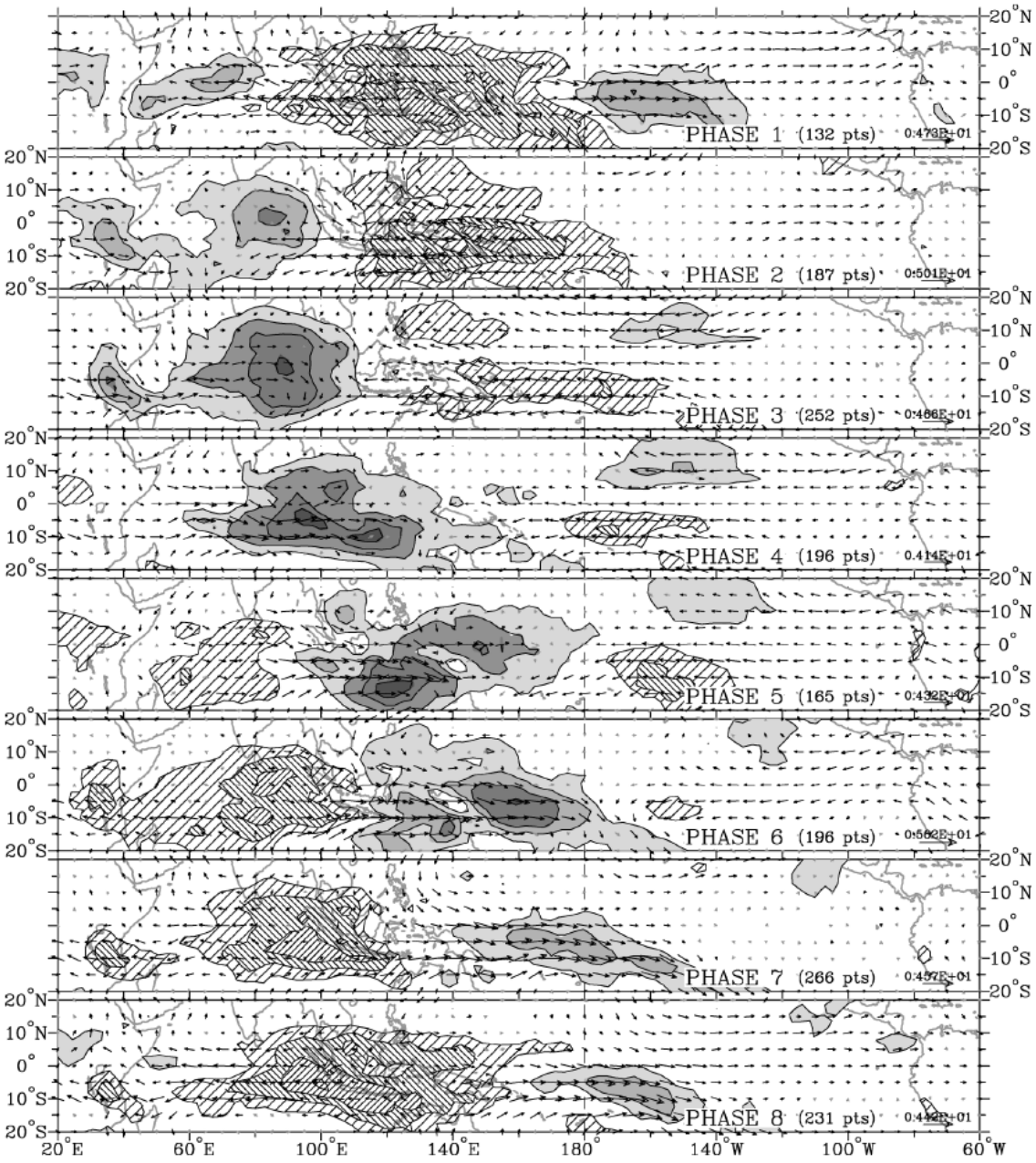

Figure 3.5: Anomalies of OLR (contours) and 850 hPa wind (arrows; black (grey) arrows are statistically significant (insignificant) at the 99% level) for composites of each of the eight WH04 phases. Shading (hatching) indicates negative (positive) OLR anomalies, with contours at ± 7.5, ± 15, ± 22.5 and -30 W m^2. Negative OLR anomalies indicate high, cold cloud tops associated with deep convection. The largest vector in each panel is reproduced in the bottom-right corner, next to the number of days used in the composite. *Image from Wheeler and Hendon (2004), figure 8.*

that a key feature of the MJO is convection propagating eastwards from the Indian Ocean, across the Maritime Continent, to the Pacific Ocean. MJ72's panel F very roughly corresponds to WH04's phase 1. As illustrated in figure 3.3 the convection is followed immediately afterwards by a suppressed region with no

convection. The WH04 composites show that these active and suppressed MJO "envelopes" are several thousand kilometres across.

3.3.2 The MJO life-cycle

We have seen that the MJO has two major components: convective anomalies which propagate eastwards from the Indian Ocean to the Pacific Ocean, and circulation anomalies on a planetary scale (zonal wavenumber 1), the structures of which also propagate eastwards. These two components are strongly coupled.

OLR anomalies in the MJO have zonal wavenumber ranging from 1 to 3, and are confined to the eastern hemisphere due to the cold sea surface temperature (SST) east of the date line (Hendon and Salby, 1994). The strong coupling between the MJO circulation and the convection arises from the fact that the circulation pattern is a response to the convection anomalies (both positive and negative), and this feeds back onto the convection signal by sustaining or suppressing convection in certain regions. The atmospheric response to diabatic heating on the equator was described theoretically by Matsuno (1966) and Gill (1980), and consists of an eastward-propagating equatorial Kelvin wave and a westward-propagating equatorial Rossby wave emanating from the heating region. The wind field associated with the MJO is consistent with such a forced response from regions of enhanced convection, and the same response but for a sign change from regions of suppressed convection. The two Rossby waves of opposite sign mean that the horizontal vorticity field consists of a distinctive quadrupole (e.g., Hendon and Liebmann, 1994). The Rossby gyres have been found to lag the convection (Hendon and Salby, 1994); the upper-level anti-cyclonic gyres associated with the enhanced convection appear 5 days after the peak convection, are still strengthening at a lag of 15 days when the convection has begun to decay, and persist even when the convection has decayed away entirely.

Matthews (2000) showed that the Kelvin wave to the east of an active MJO region and the Rossby wave to the west of the previous suppressed region, located further east, can combine to create a region of convergence on the equator between them. This convergence is able to sustain any convection in that region, thus extending the active envelope to the east and taking a "bite" out of the suppressed envelope. Thus, the whole MJO patterns move gradually eastwards. A similar result was established by Seo and Kim (2003). Also, the Rossby wave forced at the western edge of the active region generates divergence

which tends to shut off convection so that the whole active region propagates eastwards.

Hsu and Lee (2005) also explained MJO propagation in terms of this feedback between the convection and the atmospheric dynamics but argued that the propagation is not smooth and continuous. They noted that the low-level easterly wind anomaly associated with an active MJO envelope occurs to the east, as a result of the baroclinic Kelvin wave circulation, and the low-level easterly anomaly associated with the suppressed envelope is to the west, as a result of the two off-equatorial anti-cyclonic Rossby gyres. Thus, when there is an active envelope to the west of a suppressed envelope, a low-level easterly anomaly exists between them. Where there is topography, for example in the Maritime Continent, the flow impinges on it creating near-surface moisture convergence on the windward side. This results in quasi-static shallow heating anomalies which precede the deep heating anomalies inherent to the MJO. As the original active region decays away, the entire active envelope has propagated eastward. Thus, Hsu and Lee (2005) argue that the propagation of the MJO should be thought of as having discrete steps rather than being smooth and continuous. Wu and Hsu (2009) found that, specifically in the Maritime Continent, the MJO propagation is not at all smooth, with the topography holding up or even bifurcating the flow. Matthews (2000) identified similar effects outside the region of the tropics where convection is strong, in the propagation of the fast (~35 m s^{-1}) equatorial Kelvin wave which propagates eastward from the active MJO. It is held up by the Andes on the west coast of South America but propagates along the mountain range (both northwards and southwards, in the manner of a coastal Kelvin wave in the ocean). The northward-propagating wave is then able to propagate through the gap in the topography at Panama (~10°N). A similar blocking of the wave occurs due to the African Highlands before it finally reaches the Indian Ocean again where it may play a role in the generation of the next active envelope.

The initiation of MJO events is still not fully understood. Several studies have identified signals which tend to be a precursor to the genesis of an MJO event, in particular for primary events. For example, Ling et al. (2013) found that, around 20 days before the onset of MJO convection, there are low-level easterly anomalies propagating eastwards over the Indian Ocean, global-scale surface pressure anomalies propagating eastwards (with the low pressure region propagating from Africa to the Maritime Continent) and negative temperature anomalies in the mid-to-upper troposphere propagating eastwards from the

Indian Ocean. All three propagate at around the same speed of the MJO but appear to have no direct connection with the MJO convection; the signals are absent in the days before a successive MJO event. Straub (2013) similarly found slow eastward propagation of low-level easterly anomalies, and also of upper-level westerly anomalies, prior to the active MJO at a lead time of about 10 days. Positive anomalies in low-level convergence (Seo and Kim, 2003) and lower-tropospheric specific humidity and temperature (Zhao et al., 2013), both caused by the MJO wind field, have also been found at similar lead times. The wind field is due to the equatorial Kelvin and Rossby waves forced by the previous active and suppressed MJO envelopes respectively. The specific humidity and temperature anomalies act to destabilise the atmosphere, thus creating favourable conditions for the MJO to be initiated. The triggering of primary MJO events has also been linked to ocean processes. Webber et al. (2012) proposed a connection between MJO initiation and oceanic equatorial Rossby waves. An associated deepening of the ocean mixed layer results in the Rossby wave entraining less cold water from the thermocline so there is a positive SST anomaly of around 0.5–1.0°C which is able to prime the atmosphere for convection to occur. Matthews (2008) divided the MJO domain into four regions (Indian Ocean, Indonesia, Western Pacific and Africa) and found that the location over which the MJO is most frequently initiated is the Indian Ocean. However, the Indian Ocean still accounts for less than half of all MJO initiation, with the majority of events beginning anywhere from the Maritime Continent eastwards.

It has often been thought that the most important ingredient for the genesis of an MJO cycle is a region of suppressed convection which ultimately triggers the propagating active region. Convection may be present in the suppressed MJO, but only as isolated systems rather than being organised on a large-scale. The convection deepens during the onset of the MJO, and the population and degree of organisation of convective systems are at their largest at the MJO's peak (Guy and Jorgensen, 2014). Kim et al. (2014) studied examples of an active MJO envelope being present over the Indian Ocean while a suppressed envelope exists over the Maritime Continent and west Pacific Ocean. They found that the magnitude of the suppressed anomaly does not depend strongly on the magnitude of the corresponding active anomaly, but that the propagation of the active anomaly does have a strong dependence on the magnitude of the suppressed anomaly. Similarly, Hirata et al. (2013) claimed that the propagation of an active MJO envelope depends on the strength and lifetime of the equatorial

wave response to the previous suppressed envelope. When the response was weak or short-lived the active envelope decayed as it propagated eastwards, but if it was strong and long-lived it would propagate right through to the Pacific Ocean as a fully-fledged MJO event.

3.4 Modelling the MJO

Representing the MJO in general circulation models (GCMs) has been subject to many challenges, and the latest generation of GCMs still tend to struggle to simulate the MJO accurately if at all. However, given the importance of the MJO to the tropical climate it is important that models become able to represent it well. Inness and Slingo (2003) suggested that the accuracy of a model's simulation of the MJO is a "benchmark test" of the model's performance when it comes to the tropical climate. This section discusses the skill of some recent models at simulating the MJO, and gives an overview of the most common MJO modelling errors and their causes.

3.4.1 Accuracy of the MJO in current models

Zhang (2005) reported a number of common problems which arise in the simulation of the MJO, the most fundamental of which is a lack of eastward-propagating variability altogether between the Indian and Pacific Oceans. It was also reported that although early studies into the MJO in GCMs seemed promising, they mostly suffered from the propagation being too fast. Some models have tended to have MJO-like propagation occurring closer to the speed of an equatorial Kelvin wave than the relatively slow speed in the observed MJO. As explained in section 3.3.2 the MJO's propagation is a gradual progression as convection is initiated preferentially to the east of the existing active envelope, rather than arising simply from the propagation of a single wave, so it is likely that a range of processes need to be well represented in order to produce an accurate MJO. Therefore, the slow speed of the MJO's progress eastwards still tends to prove elusive to climate modellers. Further problems often encountered are a failure to couple convection to the atmospheric dynamics and an incorrect spatial distribution of convection. The latter error may occur even if the spectrum of eastward-propagating variability shows strong spectral power at the correct frequency. Hence, it must always

be remembered that an MJO-like spectrum does not necessarily imply a correct distribution of convection or a correct circulation pattern. Zhang (2005) stated that models were generally able to forecast the MJO up to about a quarter of an MJO cycle (~12 days). In terms of days this is longer than the forecasting times possible in the extra-tropics but it is usually possible to forecast the entire life time of extra-tropical weather systems, not just a quarter. Dynamical models were reported to have no more MJO forecasting skill than statistical models.

The Coupled Model Intercomparison Projects 3 (CMIP3) and 5 (CMIP5) were carried out in association with the Inter-governmental Panel on Climate Change (IPCC) Assessment Reports 4 (AR4) and 5 (AR5) respectively. Lin et al. (2006) studied the MJO in 14 CMIP3 models and Hung et al. (2013) studied the MJO in 20 CMIP5 models. As the GCMs which contributed to IPCC Assessment Reports these are state-of-the-art models of their day, and an appraisal of their ability to simulate the MJO gives a good overview of the skill of contemporary MJO simulation in general.

Lin et al. (2006) reported significant errors in the simulation of the MJO; Hung et al. (2013) reported significant improvements but still many major errors to be fixed. Across the 14 CMIP3 models studied there was a wide range of skill. Most of the models had intra-seasonal variability that was too weak, with the amount of MJO variability being close to the observed amount in only two of them. In the remaining 12, the amount of MJO variability was less than half that in observations. Only around half of the models exhibited convectively-coupled equatorial waves, and even these had variability that was too weak and propagation speeds that were too fast. Given that the structure and propagation of the MJO depend heavily on equatorial wave dynamics and the coupling of convection it is, therefore, unsurprising that the MJO is poorly represented by these models. The lack of coherent propagation resulted in most of the models having too small a ratio of eastward-propagating to westward-propagating MJO-like variability. Only one of the 14 models, the Météo-France/Centre National de Recherches Météorologiques Climate Model version 3 (CNRM-CM3), had a distinct spectral peak corresponding to the MJO. In the remaining 13 models, even where there was a reasonable amount of spectral power in the correct region of the spectrum for the MJO, this arose from an overreddened spectrum (i.e., skewed towards low frequencies) due to equatorial precipitation being too persistent, rather than a clear MJO-like feature.

In Hung et al. (2013) it was shown that significant problems remain in

the simulation of the MJO, but that definite progress has been made since CMIP3. Over the Indo-Pacific region the amount of MJO variability increased on average by 25% compared with the models in Lin et al. (2006). The ratio of eastward-propagating to westward-propagating MJO-like variability also increased, becoming more realistic. Still only around half the models exhibited convectively-coupled equatorial waves, but in those models where such waves were seen they had slower, more realistic propagation speeds. There was still the problem of the spectrum of precipitation being overreddened due to equatorial precipitation being too persistent (although this error was reduced compared with CMIP3). However, in stark to contrast to the CMIP3 models, around one-third of the CMIP5 models had an MJO-like feature that was a clear peak in the spectrum. This indicates a major improvement, although the phase speed of the MJO was generally too slow. Version 5 of the CNRM climate model was still the most skillful model studied, being the only GCM whose eastward propagation was realistic. CNRM-CM5 was the only CMIP5 model studied by Hung et al. (2013) to have a convection scheme closed on moisture convergence, leading to the suggestion that low-level moisture convergence may be crucial to the MJO's propagation.

3.4.2 Causes of model errors

Errors in simulations of the MJO were attributed by Zhang (2005) to four main causes, all of which have continued to be the focus of efforts to improve the MJO in GCMs. Firstly, and perhaps most importantly, is the convective parameterisation schemes. Ajayamohan et al. (2013), amongst others, have identified cumulus parameterisations as one of the key factors which hinder the accurate simulation of the MJO. Slingo et al. (1996) investigated the MJO in 15 GCMs and demonstrated that differences in the cumulus parameterisation schemes were responsible in part for the range of skill observed. Recent studies have led to improvements in the MJO through various alterations to parameterisations. For example, Zhou et al. (2012) were able to strengthen the amount of intra-seasonal variability in the NCAR Community Climate System Model (CCSM) and also improve the organisation of convection by altering the parameterisation scheme. Hirons et al. (2013) found that the European Centre for Medium-Range Weather Forecasting (ECMWF) model has a much more persistent MJO propagation signal when certain changes are made to the convection scheme. The model was able to maintain a realistic MJO

throughout an entire 21-month integration, a development which they described as "unprecedented" and attributed to changes in the cloud physics. One of the main modifications in this case was in the way entrainment is parameterised, so that it depends on the environmental relative humidity rather than local moisture convergence. Changes to the way in which the Hadley Centre Global Environmental Model (HadGEM) handles convective entrainment were also shown by Klingaman and Woolnough (in press *a*) to improve simulation of the MJO. By hindcasting 14 MJO event case studies they showed that the model's forecasting skill improved from 12 days to 22 days when increasing the amount of mixing entrainment and detrainment in deep and mid-level convection. This change allowed the model to build up instability over a longer period of time during the suppressed phase of the MJO, as opposed to a control run in which the model produced precipitation too readily. This longer build-up produced more realistic conditions for the active phase of the MJO when it arrived, improving the forecasting skill considerably. It is notable that changes to the representation of entrainment have been identified as one of the main ways to improve the diurnal phase of convection (section 2.2.3) and to improve the MJO.

However, other changes to parameterisation schemes have also improved MJO simulations. For example, Thual et al. (2014) chose to represent all unresolved convection in a model by a simple stochastic parameterisation. They incorporated this into the skeleton model of the MJO developed by Majda and Stechmann (2009), a simple model based on Matsuno-Gill dynamics with a neutrally buoyant atmosphere on planetary scales but with planetary-scale heating anomalies caused by modulations of synoptic-scale convectively-coupled waves. This model is able to produce intra-seasonal variability at the correct speed and with a horizontal quadrupole in the vorticity field. Incorporating the stochastic parameterisation allowed Thual et al. (2014) to represent the MJO's episodic nature and its organisation into growing and dissipating phases more accurately. Ajayamohan et al. (2013) carried out an experiment using a low-resolution aquaplanet simulation with fixed SSTs and no ocean dynamics. Even in this simple model it was shown that by coupling a model to a simple multicloud parameterisation which imitates observed tropical convection in terms of its dynamics and physical structure it was possible to produce a series of MJO events with realistic propagation speed and amplitude. A more novel approach to convection by Haertel et al. (in press) has also been shown to produce a realistic MJO. A Lagrangian atmospheric model was used, in which air parcels swap positions vertically whenever they are present in a

region of convective instability, although the reason why this produces such an accurate MJO is as yet not understood. Given the large number of studies which have found success through altering the parameterisation schemes in models, it is likely that this will continue to be the focus of further attempts to improve MJO simulation during the next few years.

The second cause of MJO errors in models identified by Zhang (2005) is resolution, although it can be difficult to separate out the effect of resolution *per se* from the effect of parameterisation schemes since they inherently depend on resolution anyway. Notwithstanding this, both horizontal and vertical resolution do seem to play some role. For example, Inness et al. (2001) showed that the upper-tropospheric zonal wind is improved in the MJO circulation in the Hadley Centre Atmospheric Model version 3 (HadAM3) as a result of doubling vertical resolution, due to a change in the distribution of cloud sizes. At higher resolution mid-level congestus clouds appeared in addition to the shallow cumulus and deep convective clouds which were present in the lower-resolution run. This is closer to the real-life distribution of cloud systems in the MJO, especially in the suppressed phase when it is these cumulus congestus clouds which dominate. Meanwhile, it was demonstrated by Crueger et al. (2013) that the effect of horizontal resolution in the ECMWF-Hamburg (ECHAM) model was to increase the strength of eastward propagation. Thus, the three-dimensional resolution can itself affect the representation of the MJO in a model, even though the effect of the convective parameterisation is likely to be more dominant.

Thirdly, the mean state in the model is known to affect the MJO, especially in terms of the dynamics of its propagation. For example, Inness et al. (2003) found that errors in the basic state (for example, in low-level wind) of the Hadley Centre Coupled Model version 3 (HadCM3) were responsible for the MJO failing to propagate beyond the Maritime Continent into the west Pacific Ocean. Slingo et al. (1996) found that the existence of MJO-like variability tends to be stronger in models with a more accurate climatology of precipitation and SST.

Finally, it has been shown that coupling between the atmosphere and ocean can affect the representation of the MJO. Zhang (2005) stated that the representation of feedback processes from intra-seasonal variability in SSTs can cause the accuracy of the MJO to be "obviously improved, improved only slightly, not affected, or even deteriorated", and even where it gives rise to an improvement it will not alone fix errors in the MJO. More recent studies have shown that these coupled processes are usually beneficial to the accuracy of

the MJO, possibly as ocean-atmosphere coupling in general has become more realistic in GCMs. A study by Kim et al. (2010) ran atmosphere-only and air-sea coupled versions of the Seoul National University GCM to show that the inclusion of coupling gave an MJO with a more realistic spatio-temporal structure, a more realistic amplitude and a more realistic lag between SST and OLR. The coupled version also increased the model's MJO forecasting skill. Similarly, Benedict and Randall (2011) compared two integrations of the super-parameterised Community Atmosphere Model (SP-CAM), one with prescribed SSTs and the other with a simplified slab ocean with SSTs coupled to the atmosphere. The latter version gave rise to several improvements in tropical intra-seasonal variability including in the spatio-temporal structure of the MJO, the strength of SST anomalies, the lag between SST and OLR, the low-level convergence field, the strength of equatorial Kelvin waves and the strength of convective heating to the east of the active MJO envelope, thus giving clearer eastward propagation of the MJO as a whole. Air-sea coupling was also found to strengthen convection in the ECHAM experiments of Crueger et al. (2013) mentioned above, and Klingaman and Woolnough (in press *b*) showed that in HadGEM, depending on the convective parameterisation used, coupling the atmosphere to the ocean can either strengthen the amplitude of the MJO or enhance its propagation.

3.5 Summary

The Madden-Julian Oscillation is the greatest source of variability in the tropics on intra-seasonal time scales. As its influence on the climate of the tropics and extra-tropics has become clearer over time, increasing amounts of research have focused on its initiation, propagation, interactions with other components of the climate and representation in GCMs. It has two main features: alternate large-scale regions (zonal wavenumber 1–3) of active and suppressed convection (giving rise to a dipole in OLR) which propagate slowly eastwards from the Indian Ocean to the Pacific, and planetary scale circulation anomalies which also propagate eastwards. The frequency of the oscillation is not consistent between MJO events, and has been known to vary from 22 day^{-1} to 100 day^{-1}. Whilst keeping in mind that the real MJO is a broad-band phenomenon, we take 48 days to be a typical MJO period.

Although aspects of the MJO circulation resemble an equatorial Kelvin wave,

the propagation speed of the MJO is considerably slower. The active convective envelope consists of cloud clusters around 10^2 km across which are organised into super clusters, each around 10^3 km across. The clusters themselves do not propagate eastwards but the super clusters do because each new cluster tends to form to the east of existing ones. Thus, the entire convective part of the MJO shifts eastwards with time. The circulation pattern consists of equatorial Rossby and Kelvin waves propagating westwards and eastwards respectively from the MJO's convective centre, and equivalent waves of the opposite sign from the MJO's suppressed phase. The Rossby gyres thus generated give the horizontal vorticity field of the MJO a distinctive quadrupole pattern. It has been shown that these equatorial wave dynamics are themselves responsible for new convection being formed at the eastern edge of the active MJO and suppressed at the western edge, giving rise to the eastward propagation. The initiation of MJO events is not fully understood, although it is generally thought that a suppressed phase of the MJO is required before an active phase can form (but not necessarily *vice versa*).

The most frequently used indices for tracking this propagation are those of Wheeler and Hendon (2004; WH04), who used EOF analysis of OLR and upper- and lower-level tropospheric zonal wind to divide the MJO into eight "phases". A WH04 phase diagram (figure 3.4) is often used to illustrate the evolution of an MJO event.

Modelling the MJO has proven to be a great challenge, and the current generation of climate models still struggles to simulate a propagating MJO realistically. The most frequent errors include a lack of eastward-propagation altogether in the MJO region, an incorrect spatial structure of either the convection or the circulation (or both), and a failure to couple convection to dynamical fields. The most frequent causes of model errors in the MJO are unrealistic convective parameterisation schemes, the model resolution being too coarse, an incorrect mean state and a failure to simulate air-sea coupled processes. The models which contributed to the fifth Assessment Report of the IPCC showed improvements compared with those contributing to the fourth Assessment Report, but still contained significant errors. Only one-third of the 20 models studied by Hung et al. (2013) had a spectral peak corresponding to the MJO, the MJO's propagation speed tended to be too slow, precipitation on the equator tended to be too persistent, only about half the models studied were able to represent convectively-coupled equatorial waves at all, and only one of the models exhibited realistic eastward-propagation in the MJO.

Chapter 4

Diurnal cycle and MJO in observations

4.1 Preface

In this chapter, data from the Tropical Rainfall Measuring Mission (TRMM) and the NASA Quick Scatterometer (QuikSCAT) will be used to analyse the diurnal cycle and Madden-Julian Oscillation over the Maritime Continent. Descriptions of the TRMM and QuikSCAT instruments and data sets are given in sections 4.2 and 4.3.

4.2 Tropical Rainfall Measuring Mission (TRMM)

This research makes much use of data from the Tropical Rainfall Measuring Mission (TRMM), a joint mission between the National Aeronautics and Space Administration (NASA) and the Japan Aerospace Exploration Agency (JAXA) which began with the launch of the TRMM satellite in 1997. Previously, tropical rainfall was not known to within a factor of two (Simpson et al., 1996). The aim of the mission is to provide precipitation estimates, in two- and three-dimensions, for the whole of the tropics at a high level of detail. The TRMM satellite carries three instruments: the Visible and Infra-Red Scanner, the TRMM Microwave Imager and the Precipitation Radar.

TRMM orbits the Earth approximately 16 times per day, at an inclination angle of 35°. The original intended lifetime for the mission was three years, but its life was extended in August 2001 by boosting the orbital altitude from

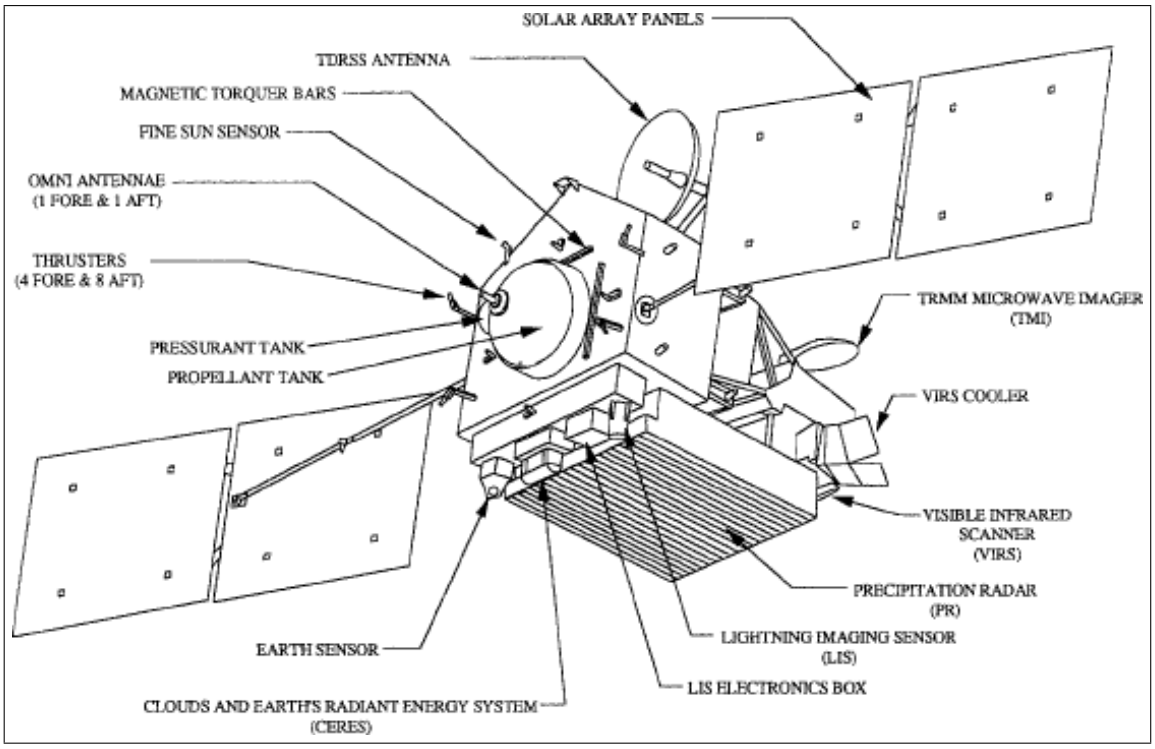

Figure 4.1: Arrangement of the instruments and main components on board the TRMM satellite. Relevant to this study are VIRS, TMI and PR (see main text for details). *Image from Simpson et al. (1996), figure 3.*

350 km to 402 km to conserve fuel by reducing the amount of nudging required to correct for atmospheric drag. This lengthened the orbital period from 91.5 minutes to 92.5 minutes. The cost of orbiting at a higher altitude is that ungridded raw data are now at a slightly lower resolution. However, they are still at a significantly higher resolution than the 0.25° gridded data used in this study (see section 4.2.2), so we can consider the 0.25° data before and after the orbital boost to form a consistent data set. It was thought that the boost would extend the mission to 2005–2007, but at the time of writing TRMM is still gathering data. There are currently plans to incorporate the satellite into the next NASA-JAXA precipitation measuring mission, Global Precipitation Measurement (GPM).

4.2.1 TRMM sensors

Kummerow et al. (1998) has details of the sensors on board the TRMM satellite; a summary is given here.

The Visible and Infra-Red Scanner (VIRS) is a passive sensor with five channels: channels 1 (visible; 0.623 μm) and 2 (infra-red; 1.610 μm) measure

reflected solar radiation, while channels 3–5 (infra-red; 3.784 μm, 10.826 μm and 12.028 μm respectively) measure thermal emitted radiation. The main optics consist of an 8.9 cm Cassegrain telescope and a scanning mirror on a paddle wheel with a scanning angle of $\pm 45°$, which gave a swath width of 720 km and horizontal resolution of 2.2 km before the orbital boost, and swath width of 833 km and horizontal resolution of 2.4 km ever since. Successive scan lines are contiguous at nadir and overlap during the rest of the scan, with a maximum overlap of about 0.9 km at the edges of the swath.

The two sets of channels (reflected solar and thermal) use separate calibration techniques. The reflected solar channels are calibrated by viewing solar radiation via an on-board diffuser and via radiation reflected by the Moon, whose surface reflectance is already known (Kieffer and Wildey, 1996). The thermal channels are calibrated using views of an on-board black body and out to space.

The TRMM Microwave Imager (TMI) and Precipitation Radar (PR) are both microwave instruments; TMI is passive and PR active. The signal detected by the passive TMI sensor is the end result of all radiative emission, absorption and scattering, integrated along its viewpath (i.e., through the precipitating cloud, if there is precipitation). The properties of clouds and hydrometeors are frequency-dependent so TMI has multiple spectral channels, ranging from 10.65 GHz (28 mm) to 85.5 GHz (3.5 mm), allowing it to sound several different depths within a cloud. The active PR sensor, meanwhile, measures the clouds' altitudes by measuring the travel-time of an emitted signal which is backscattered by precipitation.

The design of TMI is based on that of the American Defense Meteorological Satellite Program's (DMSP) Special Sensor Microwave/Imager (SSM/I). A major difference is the channel corresponding to the absorption line of water vapour. SSM/I has its channel at 22.235 GHz (13.5 mm), the exact centre of the water vapour absorption line, but since TMI measures exclusively tropical regions, where the air tends to be especially moist, such a channel would often be saturated. Therefore, TMI has its channel "off-centre" at 21.3 GHz (14.1 mm).

TMI's antenna rotates at a constant angular speed of 31.6 rpm, so a single rotation takes 1.90 s. During this time it sweeps out roughly a circle on the ground, but only the forward-most 130° are used for data collection. This gives a swath width of 760 km and horizontal resolution of 4.4 km pre-boost, and a swath width of 878 km and horizontal resolution of 5.1 km post-boost.

With the exception of the highest-frequency (85.5 GHz) channel, there are no gaps between scans, since successive footprints overlap. During the remaining 230° of each revolution of the antenna, the instrument is calibrated against two reference points of known temperature – an on-board "hot load" and the cosmic microwave background (2.73 K).

PR was the first ever space-based rain radar instrument. Its role is to determine the three-dimensional structure of precipitation, particularly the vertical profile, complementing the data found by the two passive sensors. The instrument scans an angle of $\pm 17°$ cross-track, within which are 49 angle bins of angular size 0.71°. The resulting swath width is 215 km (pre-boost) and 247 km (post-boost). 32 pairs of 1.6 μs pulses, at 13.796 GHz (21.73 mm) and 13.802 GHz (21.72 mm), are emitted per angle bin. In principle, the echo from each pulse has three components: direct reflection from precipitation; reflection from the surface of the Earth (which is used to determine the exact distance to the surface below, and the total path attenuation, which itself can be used to correct all microwave soundings); and a mirror image echo caused by reflection of the Earth's surface, followed by scattering off the underside of precipitation, followed by a second reflection off the Earth's surface (Li and Nakamura, 2002). However, reflections from the Earth's surface are very weak over land.

The PR instrument is calibrated both internally and externally; the latter, to correct for gradual degradation of the instrument, is carried out monthly using the Japanese ground-based Active Radar Calibrator (ARC).

4.2.2 Data product TRMM 3B42

The TRMM product used in this research is 3B42, a high-resolution ($0.25° \times 0.25°$) data set of precipitation estimates covering the latitude range 49.875°S–49.875°N at all longitudes, every three hours (0000 UTC, 0300 UTC, ..., 2100 UTC). The algorithm for producing 3B42, TRMM Multisatellite Precipitation Analysis (TMPA), is described in detail by Huffman et al. (2007) and is summarised here.

The TRMM satellite alone is unable to provide data coverage over such a large area so other instruments are also used. Data from microwave instruments on low-Earth orbit satellites are used as far as possible, with data from infra-red instruments on geostationary satellites used to fill any gaps. During the history of TRMM an increasing number of microwave instruments have been used,

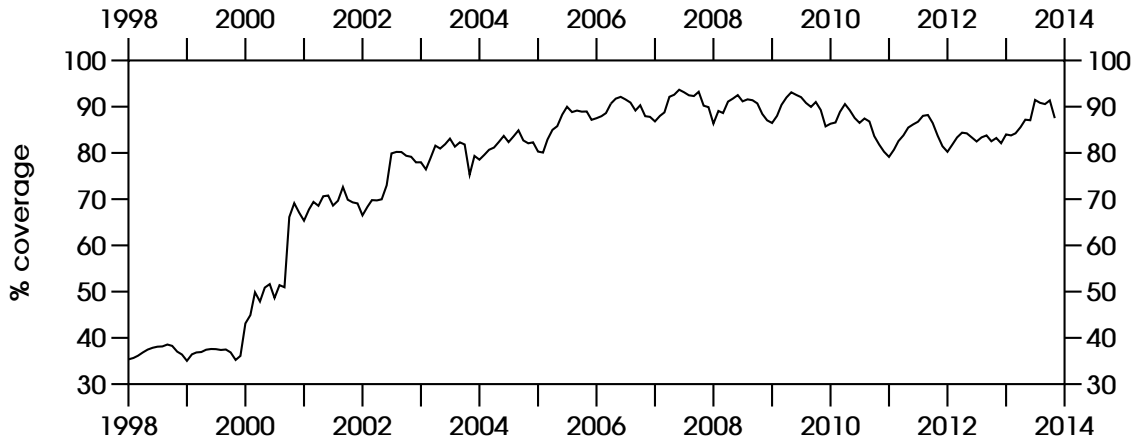

Figure 4.2: Monthly mean data coverage of the "high quality" (microwave data only) part of TRMM 3B42, calculated as the percentage of pixels in the 3B42HQ domain that are not flagged as missing.

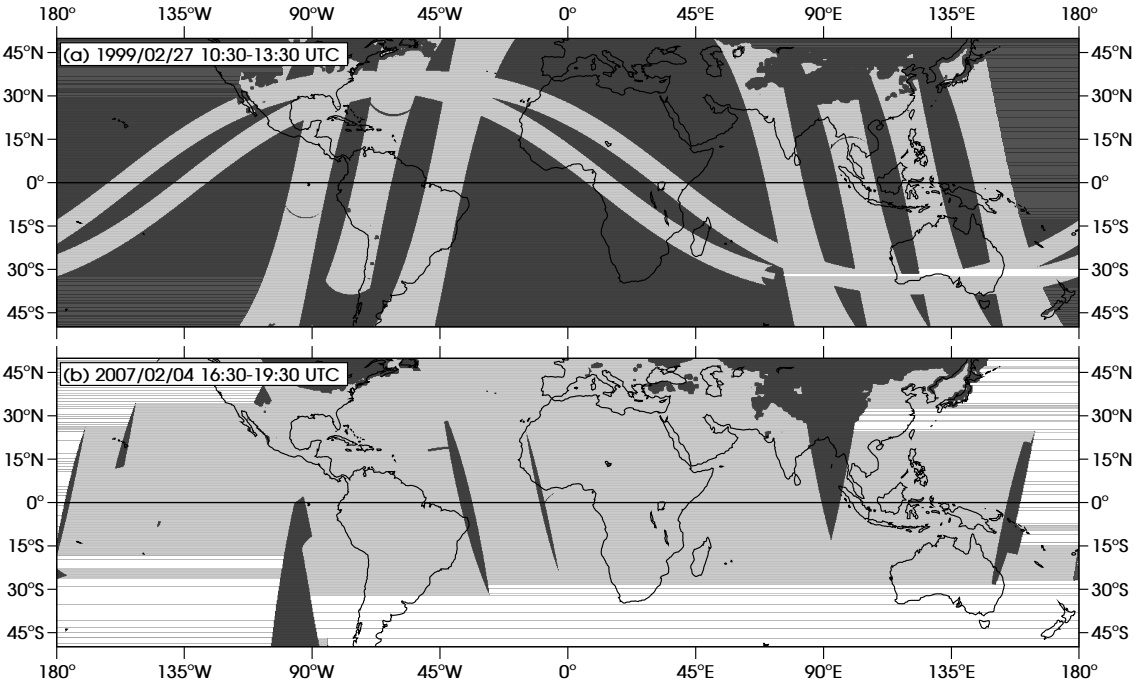

Figure 4.3: Coverage of TRMM 3B42HQ for two time steps, chosen as representative examples for the years 1999 (which had the worst annual mean data coverage) and 2007 (which had the best to date). Pixels with (without) coverage by microwave data are shown in white (grey).

so that the coverage of the "high quality" (i.e., microwave-only) estimates has improved considerably (figure 4.2). Figure 4.3 shows two typical examples of data coverage for (a) 1999 and (b) 2007, which were the years with the worst and best mean data coverage respectively. The two time steps chosen are those with percentage data coverage that was closest to that year's annual mean.

The microwave instruments used include SSM/I, the Advanced Microwave

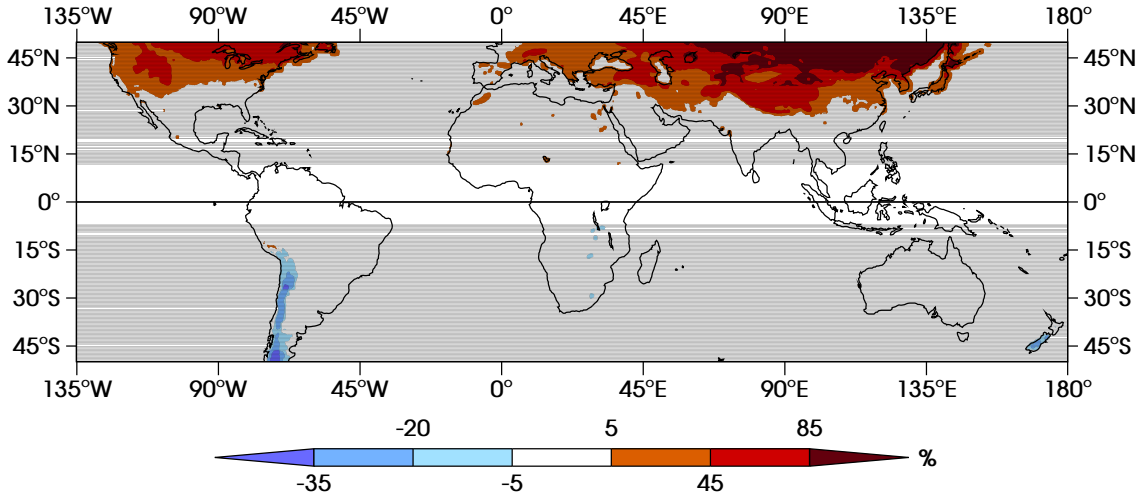

Figure 4.4: Difference between data coverage of 3B42HQ in July and January, averaged over the years 2006–2009 (see main text for details). Notice that data coverage is better in the summer hemisphere than the winter hemisphere.

Scanning Radiometer-Earth Observing System (AMSR-E) and the Advanced Microwave Sounding Unit-B (AMSU-B). Microwave data are converted to precipitation estimates on separate fields of view (FOVs), and all the FOVs are then averaged over the three-hour periods T-1.5 to T+1.5 (where T+0 are the three-hourly validity times 0000 UTC to 2100 UTC) onto a 0.25° grid. Forward gridding (the data value from the FOV contributes to the pixel in which the centre of the FOV lies) is used for all but AMSU-B, which uses backward gridding (the FOV contributes to each of the pixels over which it lies, in proportion to the area that lies over each pixel). A pixel is flagged as missing if more than 40% of the FOV lying over it are missing. If multiple overpasses occur within the same three-hour window then they are averaged together. The resulting data set from all the microwave instruments is the "high quality" part of 3B42, hereafter referred to as 3B42HQ.

It is very noticeable in figure 4.2 that the microwave data coverage exhibits a pronounced annual cycle, especially from 2002 onwards. This is due to large regions where data often tend to be flagged as missing in the winter hemisphere. Such regions are far larger in the northern hemisphere than the southern hemisphere (see figure 4.4), so global data coverage is better in northern hemisphere summer than northern hemisphere winter. In order to construct figure 4.4, mean maps of microwave coverage were produced for each January and each July in the years 2006–2009. Each of these monthly maps had the mean map for the whole year subtracted, and the four January anomalies were averaged together, as were the four July anomalies. The plot shows the

difference between the resulting maps (July minus January).

Areas in which data coverage diminishes in boreal winter include the Rocky mountains and other regions of Canada and northern USA; the Pyrenees, Alps and much of eastern Europe; the Himalayas and much of Kazakhstan, China and Mongolia; the Japanese islands of Hokkaido and, to a lesser extent, Honshu; and Lake Chad in Africa. In austral winter, data coverage diminishes over the southern Andes and New Zealand's South Island. With the exception of Lake Chad, these are all areas of significant snow coverage in the winter months. Therefore, it seems that the annual cycle of data coverage occurs because microwave instruments have difficulty performing retrievals over snow-covered ground. However, this does not affect the Maritime Continent so the annual cycle of data coverage is not a hindrance to this study.

Before missing pixels in 3B42HQ can be filled in with infra-red data to produce the full 3B42 data product, the infra-red radiances are calibrated against the microwave data. Infra-red radiances are accumulated into $1° \times 1°$ histograms for each calendar month, and similarly for the microwave precipitation estimates. These are both regridded to $3° \times 3°$ resolution and, where there is coverage of both, infra-red and microwave data are compared to derive calibration coefficients for converting infra-red radiance to precipitation. Above a particular infra-red radiance threshold, the rainfall rate is always taken to be zero. In any grid boxes still without data the precipitation rate is estimated by smooth filling from adjacent boxes.

The 3B42 files available from NASA contain 3B42, 3B42HQ and the infra-red part, 3B42IR.

4.3 Quick Scatterometer (QuikSCAT)

The NASA Quick Scatterometer (QuikSCAT), which measures surface-level wind over the sea, was launched in June 1999 as a quick recovery mission to replace the NASA Scatterometer (NSCAT) instrument on board the Advanced Earth Observing Satellite 1 (ADEOS-1), which lost power in June 1997 after less than a year in orbit. Although originally intended to last for only three years, QuikSCAT gathered approximately a decade of data until its antenna malfunctioned in November 2009.

The principle of measuring surface-level winds over the ocean (and other

regions of water) is based on the fact that such winds create ripples and small waves on the water's surface, modulating the surface roughness. This itself modulates the radar cross-section σ_0 of the surface. QuikSCAT emits microwave pulses which are backscattered by the surface; an estimate of σ_0 can be found from the backscattered power received by the detector. From this, the surface wind speed and direction are calculated. This technique can be used under all weather and cloud conditions.

The QuikSCAT satellite is in a sun-synchronous orbit at an altitude of 803 km with an angle of incidence of 98.616°. The orbital period is 101 minutes, resulting in around 14.3 orbits per day, with a recurrence period of 4 days (57 orbits). QuikSCAT passes over the equator at 6am and 6pm, local solar time. The instrument consists of a dish antenna which rotates conically at 18 rpm, sweeping out a circle on the Earth's surface of 1800 km diameter. Two spot beams ($\nu = 13.4$ GHz) are used; one is polarised horizontally and the other vertically, and they impinge on the Earth at angles of incidence 46° and 54° respectively. Pencil beams are used as opposed to fan beams, since they provide a higher signal-to-noise ratio and greater coverage, and are smaller in size. Approximately 90% coverage of the planet's ice-free oceans is achieved.

Estimates of σ_0 for each measurement are grouped into wind vector cells (WVCs), each of which typically contains forward- and backward-looking data from both beams. The maximum-likelihood estimates of wind speed and direction are found for each WVC individually, using a predetermined geophysical model function (GMF). This typically produces 2 to 4 ambiguous solutions, the best of which is chosen using a median filter.

4.4 Data in this study

In this research it will be desirable to compare precipitation data with outgoing longwave radiation (OLR; i.e., infra-red radiance). It would not be reasonable to use the full 3B42 data set for such comparisons, because of the infra-red data that are used to fill the gaps in 3B42HQ. Therefore, 3B42HQ[1] only will be used to analyse precipitation. At any given time step in the data there will be missing values, but the location of these missing values is not the same in all time steps so when producing composites over a long period of time there will be no gaps. Although the early part of the data set (1998–1999) suffered

[1]Downloaded from NASA-Goddard (http://mirador.gsfc.nasa.gov)

from poor microwave coverage (figure 4.2), compositing over all years means that this is not a problem. Composites will often be made for boreal winter only (November to April) since this is when the MJO is strongest and does not include the complicating factor of northward-propagating variability. Figure 4.2 showed that data coverage is often worst in boreal winter, but this does not present a problem since the Maritime Continent region is unaffected (figure 4.4).

As explained in section 4.2.1, the TRMM satellite carries the Visible and Infra-Red Scanner (VIRS), a five-channel radiometer. Radiance from channel 4 (central wavelength 10.826 μm, bandwidth 1.045 μm), gridded to a 0.5° grid and converted to brightness temperature (T_b) via a lookup table, is available as TRMM product 3G01. This study uses daily means of this data set.

QuikSCAT sea winds[2] were converted from polar (speed, direction) to cartesian (u, v) form and gridded to $0.11° \times 0.11°$ resolution (which corresponds closely to the nominal 12.5 km spacing of QuikSCAT data), in one-hourly bins (23:30–00:30 UTC, 00:30–01:30 UTC, ...). The data were then converted from UTC to LST as described below (section 4.5.1). Data centred on 06:00 and 18:00 LST will be used here, since that is when QuikSCAT passes over the tropics.

The state of the MJO on any given day is established using the analysis of Wheeler and Hendon (2004; hereafter WH04)[3]. WH04 projected OLR, and zonal wind at 850 hPa and 200 hPa onto the first two EOFs of the combined field of those variables to find the principal components (which they term "Real-time Multivariate MJO series", RMM1 and RMM2). RMM2 is then plotted against RMM1, and the octant of the plane in which the data for a given day fall determines which of the 8 "phases" the MJO is in. For a detailed explanation of the WH04 method, see section 6.2.3.

4.5 Observed Maritime Continent diurnal cycle

This section uses composites and harmonic analysis to diagnose the diurnal cycle of precipitation over the Maritime Continent region, and of surface-level wind over the surrounding seas.

[2]Downloaded from the Jet Propulsion Laboratory Physical Oceanography Distributed Active Archive Center (http://podaac.jpl.nasa.gov)

[3]Downloaded from the Centre for Australian Weather and Climate Research (http://www.cawcr.gov.au/staff/mwheeler/maproom)

4.5.1 Diurnal cycle of precipitation

3B42HQ precipitation data from the whole of 1998 to 2012 were averaged together, separately at each time step (00:00, 03:00, ..., 21:00 UTC), to create a climatology of the diurnal cycle. Since the phase of the diurnal cycle is partially determined by the diurnal cycle of insolation, it makes more sense to consider the precipitation at a given local solar time (LST). LST varies with longitude as

$$\mathrm{LST} = \left(\mathrm{UTC} + \frac{\lambda}{360} \times 24\right) \bmod 24, \tag{4.1}$$

where λ is longitude measured in degrees, and UTC and LST are times of day measured in hours after midnight. Hence, to convert a map from UTC to LST, data must be transformed separately at each longitude column on the latitude/longitude grid.

The data were transformed to 00:00, 03:00, ..., 21:00 LST. To create the eight new maps, the corresponding UTC time was calculated from the LST for each longitude. If this happened to coincide exactly with one of the eight time steps, the data from that UTC time step was used at that longitude. Otherwise, the data were linearly interpolated from the two nearest time steps. For example, if the local solar time is 06:00 at 60°E, the time in UTC is 02:00. Hence, for this longitude the data r would be found by linearly interpolating between the data at 00:00 and 03:00:

$$r_{\mathrm{LST}}(06{:}00) \;=\; \frac{1}{3} r_{\mathrm{UTC}}(00{:}00) \;+\; \frac{2}{3} r_{\mathrm{UTC}}(03{:}00). \tag{4.2}$$

Hereafter in this chapter, all times are given in LST unless otherwise stated.

The resulting climatology is shown in figure 4.5. Times of day move clockwise round the diagram, with midnight in the bottom-right corner. At each grid point in the domain a single sine wave was fitted to the eight precipitation values for the eight times of day. (In other words, the diurnal harmonic was computed at each grid point.) The amplitude and phase of this harmonic are shown in figure 4.6.

Features of the 3B42HQ diurnal cycle confirm findings from previous research (see section 2.2.2). Of the land and the ocean, the land has by far the stronger diurnal cycle (with the exception of regions very close to the land, associated with nocturnal gravity wave propagation, the oceanic diurnal amplitude is less than 3 mm day^{-1}). In section 2.2.2 we saw that this effect,

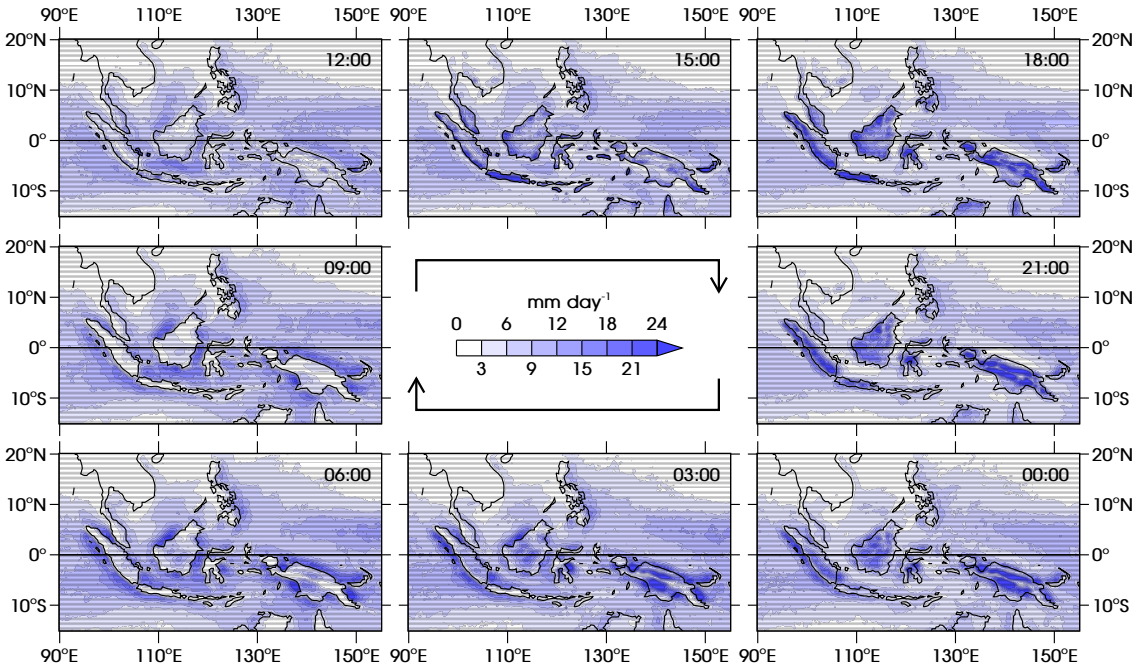

Figure 4.5: Climatology of the diurnal cycle of precipitation over the Maritime Continent from TRMM 3B42HQ, for boreal winters (November to April) 1998/9 to 2012/3. Times of day are shown in local solar time (see main text), moving clockwise round the diagram.

of Maritime Continent precipitation being confined mainly to the land, was explored in detail by Qian (2008). The land-based cycle peaks much later than that over ocean, during the late afternoon and early evening. The diurnal maximum over land is at 15:00–03:00 (mostly 18:00–00:00), whereas over ocean it is in the morning, mainly 06:00–12:00 in the Maritime Continent region and 00:00–09:00 further afield (figure 4.6b).

Around 09:00, the islands of Sumatra, Java, Borneo, Sulawesi and New Guinea are almost dry, as found by Biasutti et al. (2012) which used TRMM PR data only. That study also found that over immediately surrounding regions of ocean at the same time, there is stronger precipitation; again, this is confirmed by these observations (figure 4.5). By 15:00 in the same figure, regions of fairly strong precipitation have started to appear just inland of the coasts of large islands. Notice that these regions are not uniformly distributed around the coast, but occur where the coastline is convex. This is consistent with the mechanism of Biasutti et al. (2012) in figure 2.3g, in which convergence of onshore breezes causes convection and, therefore, precipitation. Note that this effect, whereby precipitation forms near the coasts earlier than over the centre of the large islands, is shown by figure 4.6b, with the earliest land-based diurnal phase almost exclusively occurring in coastal regions. Also at 15:00,

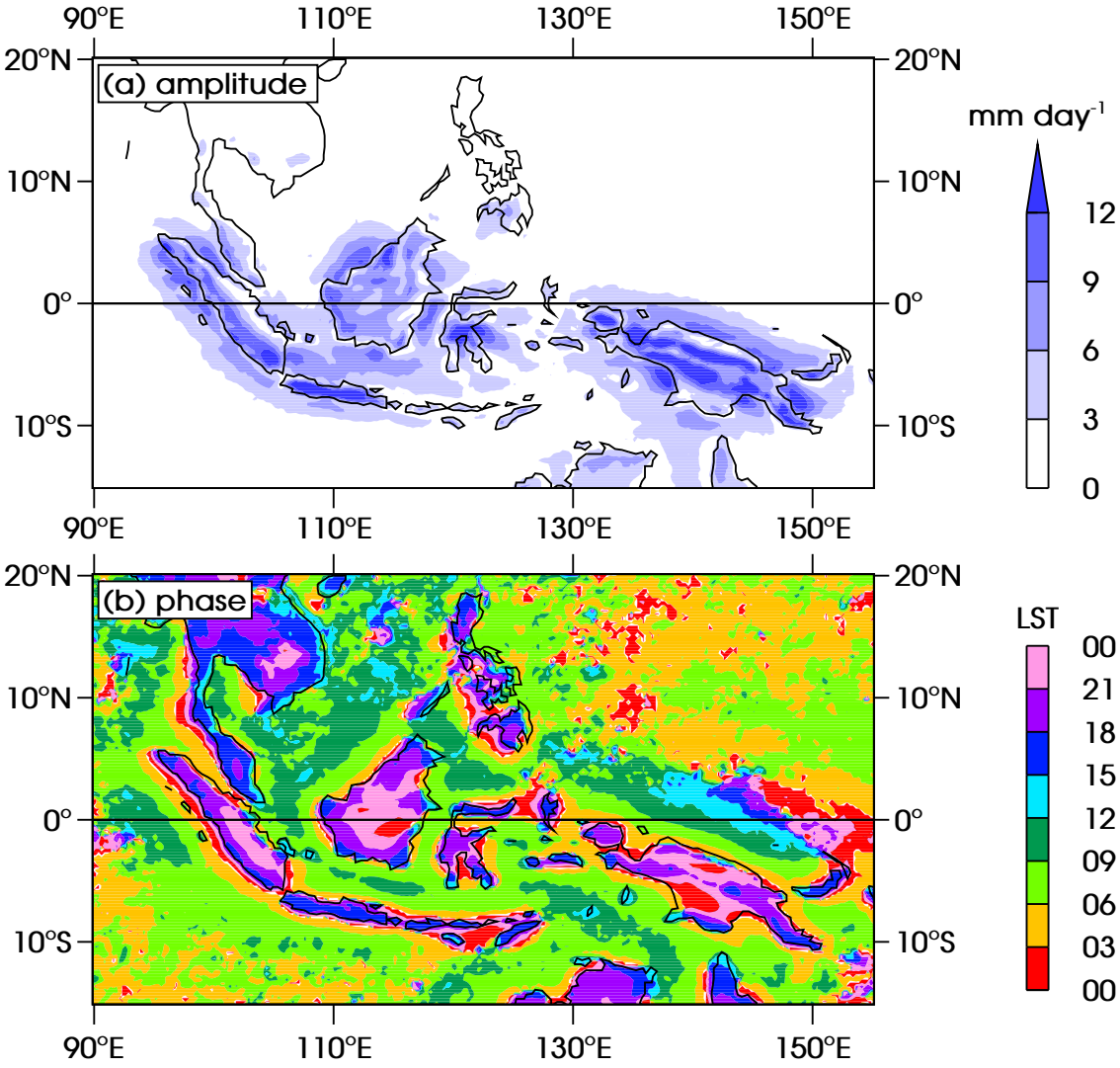

Figure 4.6: (a) Amplitude and (b) phase of the diurnal harmonic of precipitation from TRMM 3B42HQ, for boreal winters (November to April) 1998/9 to 2012/3.

precipitation starts to form over regions of high orography (cf. figure 2.1) and has strengthened by 18:00, in particular over south-west Sumatra, Java and New Guinea, including the Bird's Head Peninsula at the north-west corner of New Guinea. Again, this is consistent with the Biasutti et al. (2012) mechanism, with upslope winds causing convergence over mountains (figure 2.3e).

The findings of Zhou and Wang (2006), who also used TRMM PR only, are also mostly confirmed by this composite of 3B42HQ. They found bands of precipitation forming just inland of the New Guinea coast, which can be seen along the north coast at 15:00. They found also that precipitation forms over the mountains due to upslope winds in the morning, which then intensifies and comes to dominate during the day. By 12:00 precipitation has indeed started to form over the New Guinea Highlands which run west-north-west

to east-south-east across the centre of the island. This precipitation has strengthened slightly by 15:00 and greatly by 18:00 such that it dominates for the rest of the day. Figure 4.6a clearly confirms that it is this orographic rainfall that is the dominant feature of the New Guinea diurnal cycle.

By evening (18:00–21:00), precipitation covers much of the islands as rainfall spreads inland from the coasts due to propagating gravity currents, and from the mountains. Complementing the day-time precipitation just inland of the coasts, the mechanism of Biasutti et al. (2012) also has nocturnal rainfall just offshore as land breezes converge where the coast is concave. This is especially noticeable in figure 4.5 over Cenderawasih Bay off north-west New Guinea (just south-east of the Bird's Head Peninsula), where the precipitation begins at around 21:00, and strengthens and spreads around midnight and 03:00. Zhou and Wang (2006) note that precipitation over the New Guinea Highlands splits overnight, with half spreading northwards and half southwards, as can be seen here at 00:00 and 03:00. By 06:00 this rainfall has weakened so much that the signal is barely visible.

Zhou and Wang (2006) also noted propagation of precipitation offshore during the night, a phenomenon which occurs throughout the Maritime Continent (Love et al., 2011) and, as described by Yang and Slingo (2001), throughout the whole tropics. This is why the strong diurnal amplitude (figure 4.6a) is not confined to the land alone but is also present over certain ocean regions adjacent to the land. This effect is tied strongly to the land-based diurnal cycle and is caused when gravity waves propagate (Love et al., 2011) over an oceanic region with a large amount of precipitable water vapour in the atmosphere (Fujita et al., 2011). Such regions can be identified clearly by bands over ocean running parallel to coastlines in figure 4.6b. For example, bands can be seen moving away from the south-west coast of Sumatra, the north and south coasts of Java, the north-west coast of Borneo, the north-west coast of Palawan (the long thin island of the Philippines that lies north of Borneo at 10°N, 119°E), all around Sulawesi and, with the greatest extent into the ocean, the north coast of New Guinea. Off the coasts of Palawan the offshore propagation is weak (it cannot be seen in figure 4.6a), but the phase propagation is coherent nonetheless. Off the coasts of Sumatra, Borneo, Sulawesi and New Guinea the nocturnal propagation offshore is particularly strong, and can be seen explicitly in figure 4.5 from around 21:00 through to 09:00 or even 12:00.

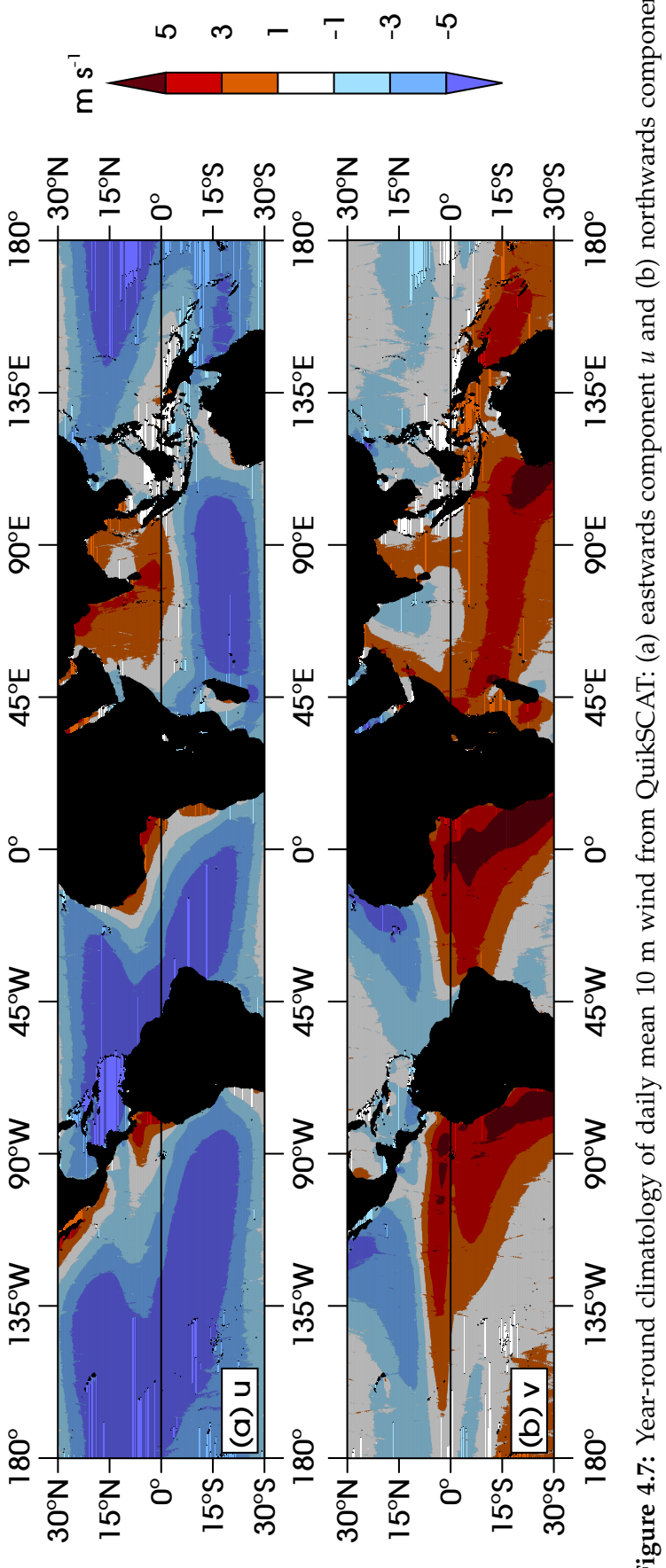

Figure 4.7: Year-round climatology of daily mean 10 m wind from QuikSCAT: (a) eastwards component u and (b) northwards component v. Missing data are shown in black.

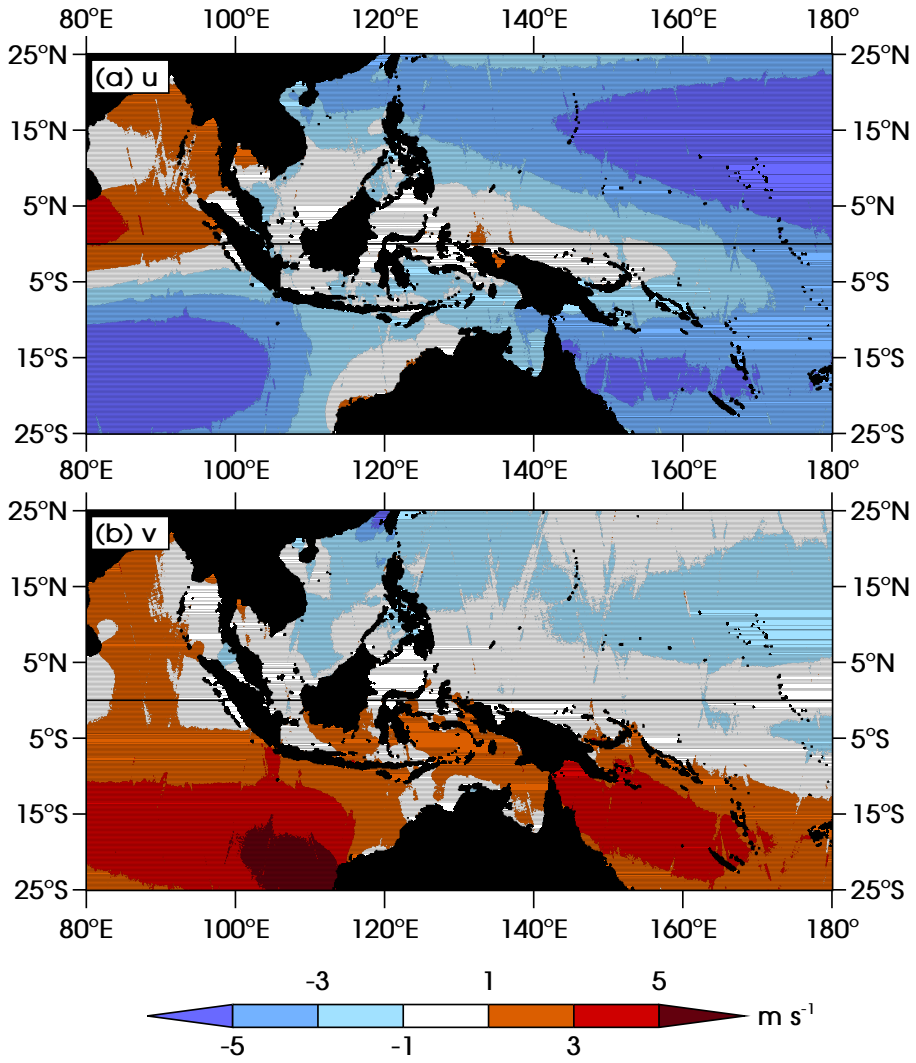

Figure 4.8: As figure 4.7, but for the Maritime Continent region only.

4.5.2 Daily mean and diurnal cycle of ocean surface wind

The climatology of daily mean wind from QuikSCAT is shown in figure 4.7 for the entire tropics, and for the Maritime Continent region only in figure 4.8. The streaks visible in these plots are artefacts of the QuikSCAT swath patterns. They are probably caused by the fact that the accuracy of pixels at the edges of each scan can be unreliable (e.g., Hoffman and Leidner, 2005), partly because there are fewer pixels on which the median filter can act to resolve ambiguities. Although referred to as the "daily mean" wind, around the equator this is, in fact, just the average of the 06:00LST and 18:00LST wind since these are the times when the satellite passes over. A representation of the diurnal cycle can be found by plotting the difference between these two times of day. The 6am data were subtracted from the 6pm data to create figures 4.9 (all longitudes)

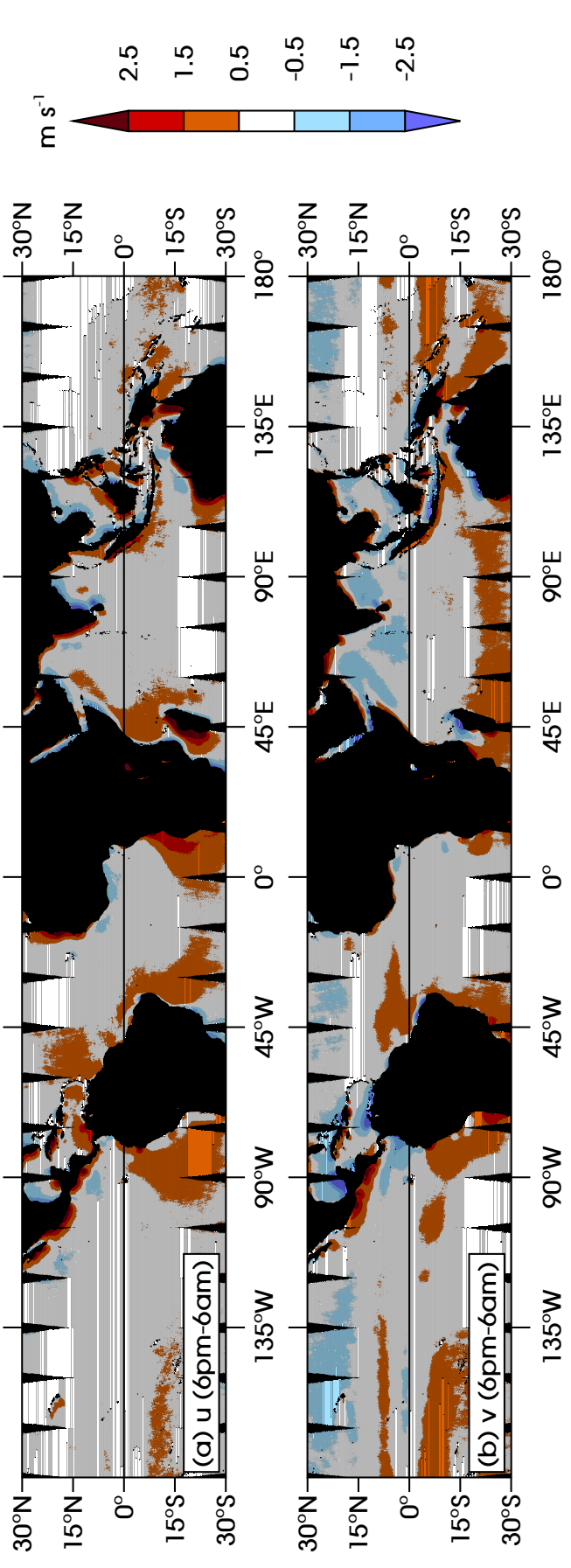

Figure 4.9: Year-round climatology of the diurnal difference of 10 m wind from QuikSCAT, found by subtracting the 06:00 from the 18:00 data: (a) eastwards component u and (b) northwards component v. Missing data are shown in black.

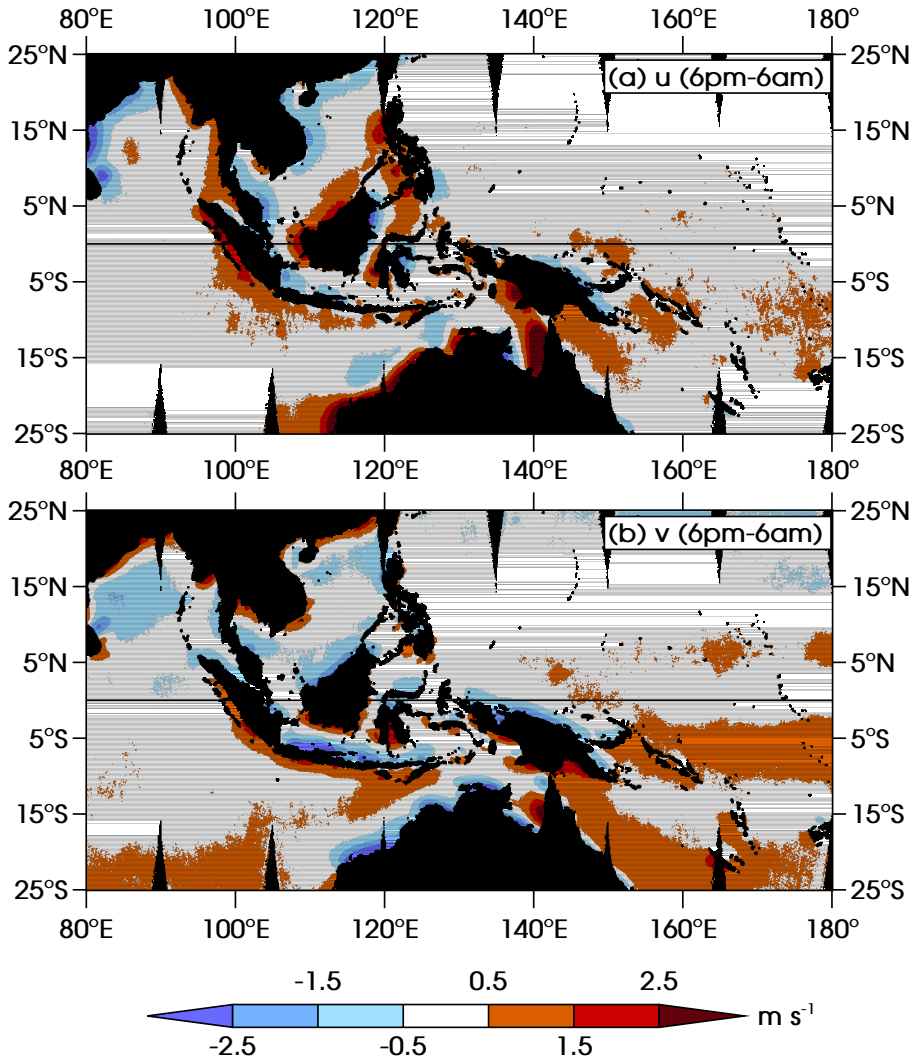

Figure 4.10: As figure 4.9, but for the Maritime Continent region only.

and 4.10 (Maritime Continent).

In figure 4.7 the Trade Winds are clearly seen over the Atlantic and Pacific Oceans, converging at the Inter-Tropical Convergence Zone (ITCZ) which lies slightly north of the equator. These winds are the main large-scale feature of the surface-level atmospheric circulation. Since year-round data have been used, seasonal variations – notably the monsoon circulations – are averaged out here.

Zooming in on the Maritime Continent and Indo-Pacific warm pool (figure 4.8), we see that the mean flow around the warm pool is mostly easterly, with a reasonably strong southerly component in the southern hemisphere. As well as the seasonal variation associated with the monsoon, the intra-seasonal variation associated with the MJO and the diurnal variation associated with sea breezes are also averaged out here. This is why the mean wind is lower around

the equator than away from the equator, and especially in between the Maritime Continent islands.

In figure 4.9 we refer to the quantity plotted as the "diurnal difference". This is characteristic of the diurnal amplitude, although of course there is no guarantee that the maximum and minimum winds do occur around 06:00 and 18:00. This plot is similar to that by Gille et al. (2003), also from QuikSCAT data. For zonal wind u, positive values (shown here in red) imply a tendency for winds to be more westerly in the evening and/or more easterly in the morning; for meridional wind v, positive values imply a tendency for winds to be more southerly in the evening and/or more northerly in the morning. The diurnal difference is generally very small away from land, implying that there is little diurnal variation over open ocean. Near to coasts, however, there is a consistent pattern. The diurnal difference of u tends to be positive on the western coasts of land masses and negative on the eastern coasts. For v it tends to be positive on the southern coasts of land masses and negative on the northern coasts. This implies that flow tends to be onshore in the evening and offshore in the morning. This is consistent with the accepted view of the land-sea breeze circulation due to differential solar heating of land and ocean.

Figure 4.10 shows in detail the structure of the diurnal cycle around the Maritime Continent islands. Almost all the coastlines have an associated diurnal cycle of surface-level wind, including the major islands of Sumatra, Java, Borneo, Sulawesi and New Guinea. The region in which the diurnal difference is greater than 0.5 ms^{-1} can be taken as a rough measure of the area over which the diurnal cycle has an influence. For much of the Maritime Continent this area extends, very approximately, 200 ± 50 km offshore from the coast.

4.6 Observed Madden-Julian Oscillation

The Madden-Julian Oscillation (MJO) was described in detail in chapter 3. It was explained that successive envelopes of active and suppressed convective conditions propagate slowly eastwards from the Indian Ocean, over the Maritime Continent, to the Pacific Ocean.

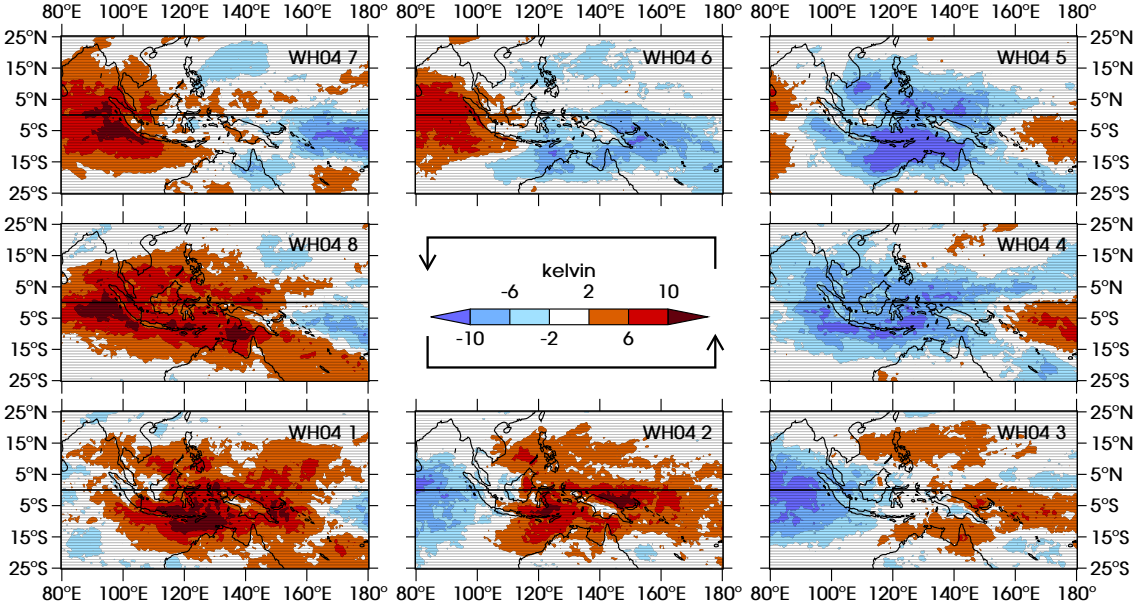

Figure 4.11: Anomaly of TRMM 3G01 brightness temperature (derived from outgoing longwave radiation) in each phase of the MJO, for boreal winters (November to April) 1998/9 to 2012/3. Blue regions indicate high, cold cloud tops, which are generally considered a good proxy for increased precipitation.

4.6.1 Composites

In section 3.3.1 composites of outgoing longwave radiation (OLR) were shown from the paper by Wheeler and Hendon (2004; WH04) in which the eight phases of the MJO, which have become the *de facto* standard, were defined. Data from TRMM allow us to produce similar composites in much higher resolution. Brightness temperature measurements, derived from infra-red radiances (i.e., outgoing longwave radiation, OLR) measured by the TRMM VIRS instrument, are available as TRMM product 3G01 on a $0.5° \times 0.5°$ grid.

Composites are created for each day in boreal winters (November to April) 1998/9–2012/3 on which the MJO is in WH04 phase 1, each day on which it is in phase 2, and so on, ignoring days on which the MJO is weak. A "weak" MJO is defined as a day on which the RMM amplitude is less than 1:

$$\sqrt{(\mathrm{RMM1})^2 + (\mathrm{RMM2})^2} < 1. \tag{4.3}$$

In figure 4.11 these composites are plotted with the boreal winter climatology subtracted. (This climatology does include both weak and non-weak MJO days.) Phase 1 is shown in the bottom-left corner and successive phases move anti-clockwise around the diagram. Boreal winters are used because

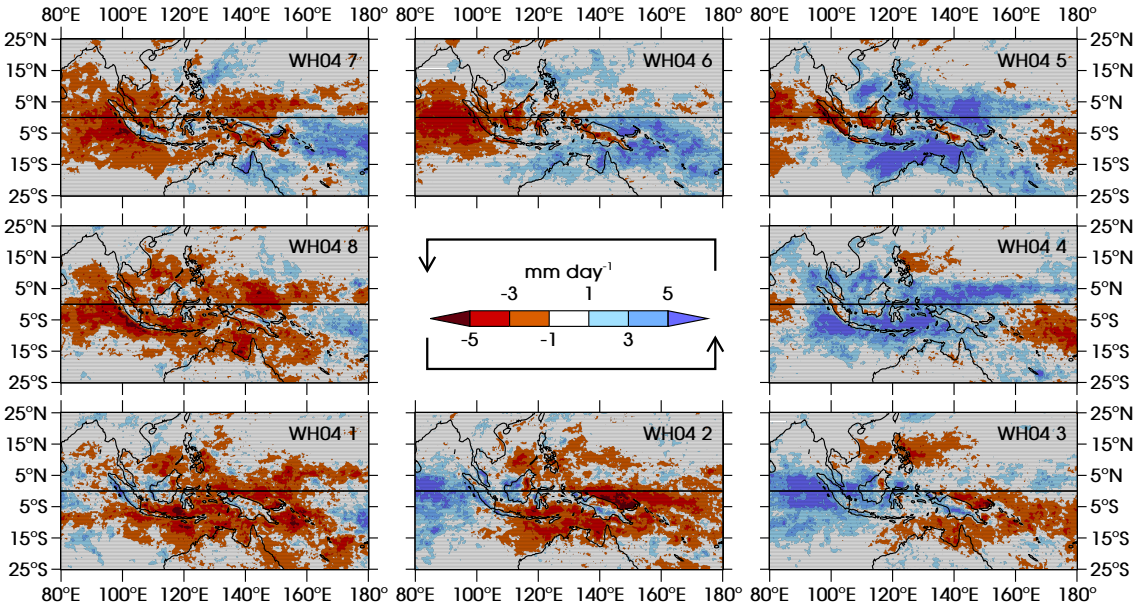

Figure 4.12: Anomaly of daily mean precipitation from TRMM 3B42HQ in each phase of the MJO, for boreal winters (November to April) 1998/9 to 2012/3.

in boreal summer the MJO tends to be weaker and it can obey a different pattern with northward-propagating elements, so the WH04 indices are less useful as a diagnostic tool. Blue regions indicate anomalously cold temperatures which are caused by high, cold cloud tops. These tend to be the tops of tall columns of cumulonimbus, caused by deep convection. As such, cold brightness temperatures are generally taken to be a proxy for precipitation. Warmer temperatures, shown in red, indicate lower cloud tops or clear skies, with little or no precipitation.

As expected we see large-scale envelopes propagating eastwards across the domain. An active envelope can be seen approaching the Maritime Continent from the west in phase 2, reaching Sumatra and the west of Borneo in phase 3, and covering the whole Maritime Continent in phases 4 and 5. Similarly, a suppressed envelope reaches the Maritime Continent at phase 6, and by phases 8 and 1 is entirely covering the archipelago.

The inhomogeneous nature of these plots show that, as mentioned in section 3.3, an MJO event does not consist of one large storm which propagates along the equator, but a large number of storms on a range of length scales which are organised into a large region. Similarly, the suppressed MJO does not consist of entirely clear skies. Furthermore, the islands of the Maritime Continent sometimes interrupt the large-scale MJO pattern. For example, in phases 2 and 3 the MJO is clearly suppressed over the area surrounding New

Guinea, but over New Guinea itself the brightness temperature anomaly is very small or even negative. Similarly, in phases 4 and 5 there is a part of New Guinea with a very small anomaly even though all the surroundings are clearly experiencing an active MJO, and in phase 5 the same can be said for parts of Borneo and Sumatra.

Figure 4.12 is similar to figure 4.11 but for daily mean precipitation instead of brightness temperature. Here, blue is used for positive anomalies so again blue denotes a wet anomaly. We again see MJO envelopes propagating slowly eastwards, arriving at the Maritime Continent and passing over it in the same phases as the brightness temperature envelopes. Again the envelopes are inhomogeneous, and the coherence is less here than it was for brightness temperature. This is explained by the fact that the brightness temperature data show large clouds that often spread out over a large area, whereas precipitation tends to be be more localised. Again we see that the anomalies over Maritime Continent islands do not always match the anomalies in the surrounding area. Especially clear examples of this include Sumatra, Borneo, Sulawesi and New Guinea in phase 1, where the anomaly over land tends to be wet in the heart of the suppressed envelope; New Guinea in phases 2 and 3, again with an incongruous wet anomaly; and Borneo in phase 5, where there is a dry anomaly in amongst the active envelope. At present these effects over land are merely noted; they will be investigated further in chapter 5.

4.6.2 Wheeler-Kiladis diagrams

It should be noted that the MJO cycle does not occur continuously. There may be a period of many days or even weeks in which the RMM amplitude is weak and there is no intra-seasonal propagation of large-scale anomalies. Therefore, it is useful to consider how much intra-seasonal variability does exist. This can be achieved using wavenumber-frequency diagrams known as Wheeler-Kiladis diagrams (Wheeler and Kiladis, 1999).

To create the diagrams, data on a time-longitude grid, with the first three harmonics of the annual cycle removed, are divided into 96-day segments (since we are interested in variability up to intra-seasonal time scales) with an overlap of about two months (here, an overlap of 65 days will be used). From each segment, the mean and a linear trend, found by least-squares fitting, are removed, and the ends of the data are tapered to zero in order to prevent spectral leakage. The 65-day overlap between segments ensures that there is minimal

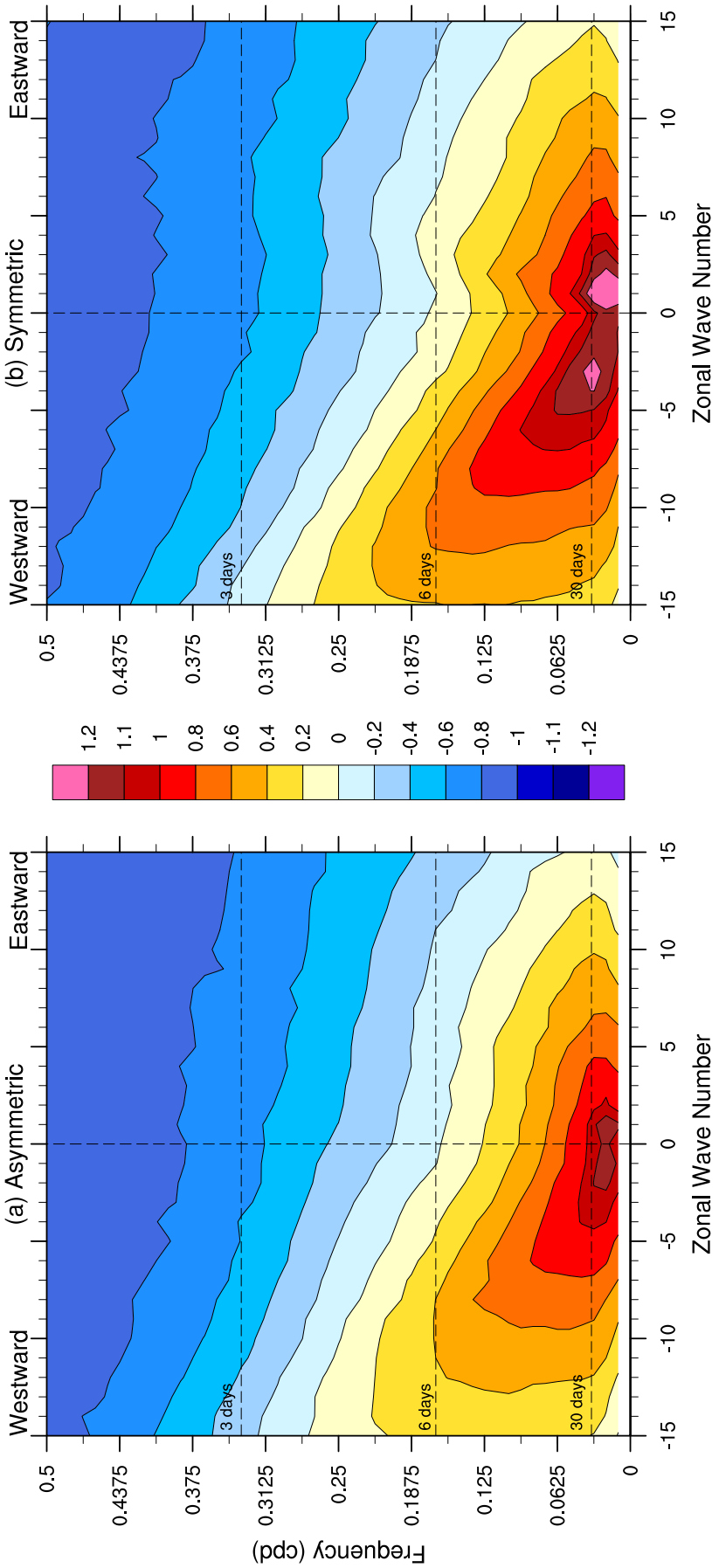

Figure 4.13: $\log_{10}$ of the spectral power of OLR from NCEP-DOE Reanalysis 2, summed over the range 15°S–15°N. The two panels are for the (a) equatorially-asymmetric, (b) equatorially-symmetric parts of the OLR field. This is the equivalent of figure 1 in Wheeler and Kiladis (1999). See main text for more details.

data loss due to this tapering. A fast Fourier transform (FFT) is performed along the longitude direction to obtain Fourier coefficients in zonal wavenumber space for each time. A subsequent FFT is performed on these coefficients along the time direction to obtain spectral power in wavenumber-frequency space. The power in each of the 96-day segments is then averaged together. This entire process is performed at every latitude on the data grid from 15°S to 15°N, and the results are summed together.

The above process is performed separately for the symmetric and asymmetric components of the data. For some variable $X(\phi)$, where ϕ is latitude, these components are found by

$$X_{\text{sym}} = \frac{1}{2}\left[X(\phi) + X(-\phi)\right], \tag{4.4a}$$

$$X_{\text{asym}} = \frac{1}{2}\left[X(\phi) - X(-\phi)\right]. \tag{4.4b}$$

The wavenumber-frequency diagrams calculated from OLR, from the National Center for Environmental Prediction-Department of the Environment (NCEP-DOE) Reanalysis 2 (Kanamitsu et al., 2002)[4], are shown in figure 4.13 for the years 1980 to 2012 (cf. figure 1 in Wheeler and Kiladis, 1999). OLR_{asym} was used for figure 4.13a and OLR_{sym} for figure 4.13b; in both panels, $\log_{10}$ of the field is plotted. The spectra are both heavily dominated by a red component (i.e., skewed towards low frequencies) which obscures most of the features in them. It is preferable to show the spectral power normalised by some background spectrum. This background is found by averaging together the two fields in figure 4.13 then repeatedly smoothing (not shown). Figure 4.14 (cf. figure 3b in Wheeler and Kiladis, 1999) shows the spectral power for OLR_{sym} (10 to the power of the quantity in figure 4.13b) divided by the background spectrum. The asymmetric field is not shown because the structure of the MJO, the object of our interest here, is chiefly symmetric about the equator. Hypothetical dispersion curves are superimposed on figure 4.14 for equatorial Kelvin waves (which are non-dispersive, hence their linear dispersion relation), equatorial Rossby waves (ER) and inertio-gravity waves (IG).

The MJO appears in figure 4.14 as a strong but small region of spectral power centred on zonal wavenumber 1, in the approximate frequency range 1/30 to 1/75 cycles per day (cpd). This is by far the strongest region of spectral power so, although MJO conditions do not exist continuously, they are still by far the

[4]Downloaded from the National Oceanic and Atmospheric Administration, Earth System Research Laboratory, Physical Sciences Division (http://www.esrl.noaa.gov/psd)

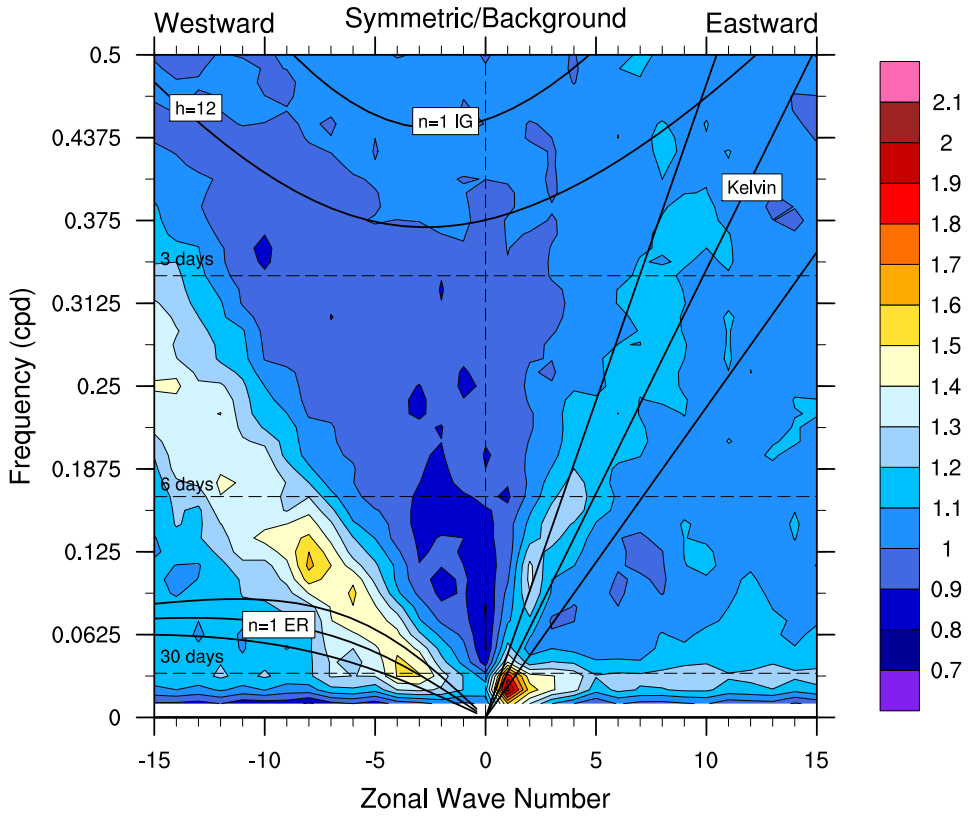

Figure 4.14: Spectral power of the equatorially-symmetric part of the OLR field from NCEP-DOE Reanalysis 2, summed over the range 15°S–15°N (10 to the power of the quantity in figure 4.13b), divided by the background spectrum (not shown). Hypothetical dispersion curves for families of equatorial waves are superimposed (ER = equatorial Rossby, IG = inertio-gravity, n = mode number, h = equivalent depth; see Kiladis et al., 2009). This is the equivalent of figure 3b in Wheeler and Kiladis (1999). See main text for more details.

most significant form of tropical variability in the Wheeler-Kiladis diagram. (As we know, the diurnal cycle is an even more significant source of variability but it is not seen here because daily data are used. The highest frequency shown is the Nyquist frequency of 0.5 cpd.)

4.6.3 New WH04-based diagnostics

As well as the fact that the MJO phases do not necessarily form a continuous cycle, we must also consider the fact that the tropical atmosphere does not necessarily spend the same number of days in each WH04 phase. This is because the propagation speed of the MJO can vary, and also because isolated days or a run of a few days can have conditions which look similar to a particular stage of the MJO (enough to project strongly onto at least one of the WH04 EOFs)

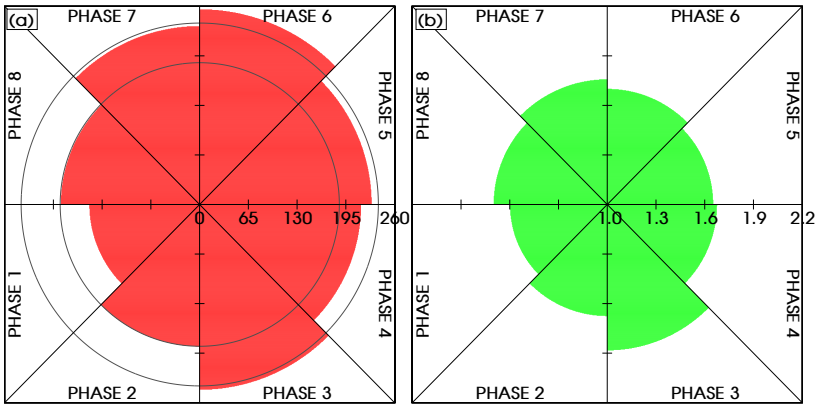

Figure 4.15: (a) Number of days and (b) mean RMM amplitude in each phase of the MJO, for boreal winters (November to April) 1998/9 to 2012/3. Days in which the RMM amplitude is less than 1 have been neglected from both plots. Red regions which lie entirely within the inner grey circle (186 days) or extend beyond the outer grey circle (238 days) are statistically significant (95% confidence).

without there being a real MJO event. New diagnostics will now be presented to show the nature of the distribution of MJO events and MJO-like days.

First, we show the number of days on which the MJO is in each phase during boreal winters, and the mean RMM amplitude on those same days (figure 4.15). For both panels (a) and (b), all days on which the RMM amplitude was less than 1 are ignored. (Note that in panel (b) the axis is drawn from 1, not from 0.) If such weak days were included then the number of days in panel (a) would increase roughly equally for all phases and, of course, the amplitudes in panel (b) would be much smaller for all phases. Given a null hypothesis that the MJO is equally likely to be in any of the eight phases, the grey circles in panel (a) indicate the 2.5^{th} and 97.5^{th} percentiles (186 and 238 days respectively). Thus, if the red sector for any given phase does not extend as far as the inner circle then there is a significant tendency for the MJO not to be in that phase, and if it extends beyond the outer circle then there is a significant tendency for the MJO to be in that phase.

Although some small variation between the phases is always to be expected, in panel (a) there is a clear difference between the phases with the fewest and the most days. Only 147 days were in phase 1, as opposed to 256 days in phase 6; phase 8 also has significantly few days (and phase 2 has exactly 186 days), and phase 3 has significantly many. In panel (b) there is very little variation between the phases, except for phase 3 which has a much larger mean amplitude than any of the others. Why the MJO should be so much stronger in that phase than any other is unclear.

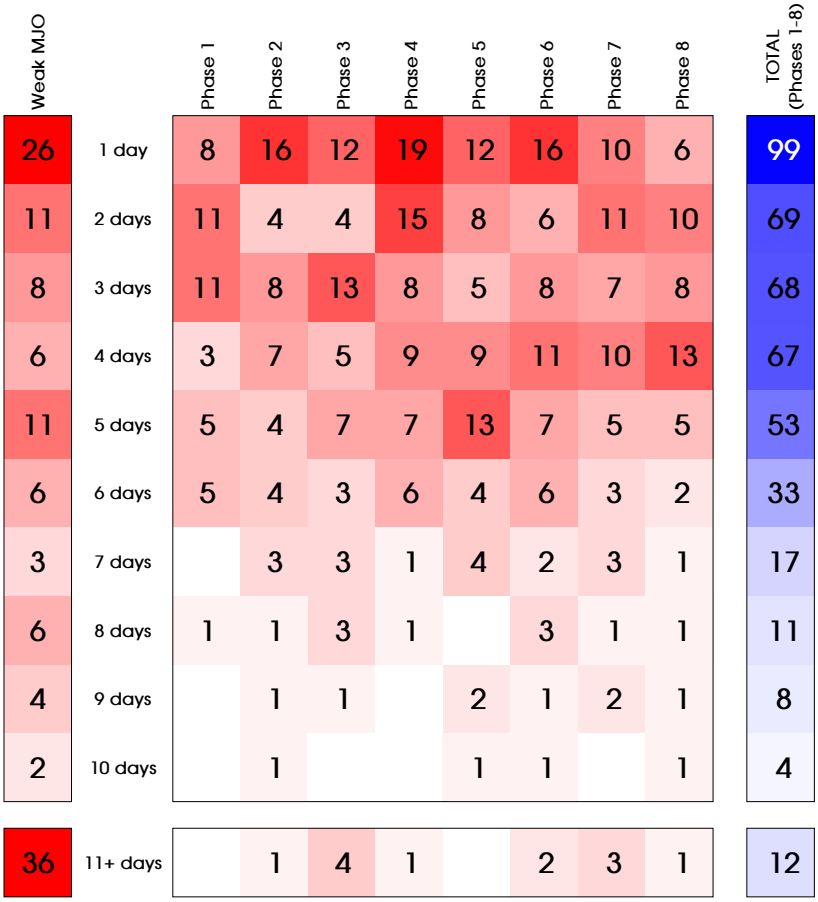

Figure 4.16: Histogram showing the number of occurrences of strings of successive days of the same phase, for boreal winters (November to April) 1998/9 to 2012/3. For example, there were 15 instances of phase 4 occurring on exactly 2 successive days.

The results of figure 4.15a may suggest that the initiation and decline phases of the MJO (8 to 2) occur relatively rapidly compared with the propagation phases (3 to 7), or that there are a lot of days which look like phases 3 to 7 but are not part of real MJO events. Figures 4.16 and 4.17 suggest a combination of these two explanations. For figure 4.16, all instances of the same phase occurring on successive days were found, as were all instances of a phase occurring in isolation (for just one day). (Days on which the RMM amplitude was less than 1 had been relabelled as phase "0".) The histogram shows the number of times that a string of any given number of successive days were all in the same phase (with phase 0 shown on the left-hand side, labelled "Weak MJO"). For example, to find the number of times that exactly two days in a row were in phase 4, see the second row of the fourth column in the main grid; there were 15 such occasions. For phase 1 the frequency distribution is skewed towards the top of the histogram, suggesting that the MJO does tend to move through that phase quite rapidly. On only one occasion was the MJO in phase 1 for more than

6 successive days, and even then it was for only 8 days. In contrast, the MJO remained in phase 3 for more than 6 successive days on 11 occasions, the longest being 13 (not shown). The longest string of days in the same phase was 17 (phase 7; not shown).

The analysis above considers WH04 phases in isolation. However, a crucial element of the MJO is phase propagation. To diagnose this, a modified technique was used (figure 4.17). Days with an RMM amplitude of less than 1 were again relabelled as being in phase "0". Then, inspired by the method of Matthews (2008), any duplicate phases on successive days were removed; for example, any number of successive 4s would be replaced by a single 4. All instances were then found of at least two consecutive phases occurring successively. For example, if a 1 is followed by a 2, a 5 followed by a 6, an 8 followed by a 1, and so on, then there is an MJO "event". It is emphasised that these are not necessarily MJO events in the conventional sense, which are often thought of as a complete cycle through all the WH04 phases. A large proportion of the "events" in this analysis are only two phases long, but even these are of interest because they help us to identify the phases during which the MJO tends to continue propagating or to die out. All instances were also found of "standalone" phases – that is, a phase neither following nor followed by a phase in sequence. Figure 4.17 is a histogram of all these events. In the notation used in the diagram, a letter x denotes a phase out of sequence. Thus, an "x345x" event means an instance of phase 3 followed by phase 4 followed by phase 5, with the whole thing preceded by any phase other than 2 and succeeded by any phase other than 6. (In practice, an x is often phase 0.) In the histogram, events are sorted by their end phase (the phase at which the MJO propagation dies out or in some other way ceases) and by their length. xNNx events – which are only two phases long, so it could not be said that MJO propagation has become established – do tend to occur more for the middle phases 3 to 7 than for the initiation and decline phases 8 to 2. This suggests that phases 3 to 7 do occur outside of anything that could be called a genuine MJO event more frequently than phases 8 to 2 do.

The composites in figures 4.11 and 4.12 can be used to validate the simulation of the MJO in a model, by comparing the spatial structure and amplitude of the anomalies in the equivalent composites. The diagnostics in figures 4.14–4.17 are also useful, since we can use them to verify the sporadic and inconsistent nature of the MJO; if a model produces MJO composites that look very similar to those in observations but, for example, this MJO occurs repeatedly without breaks

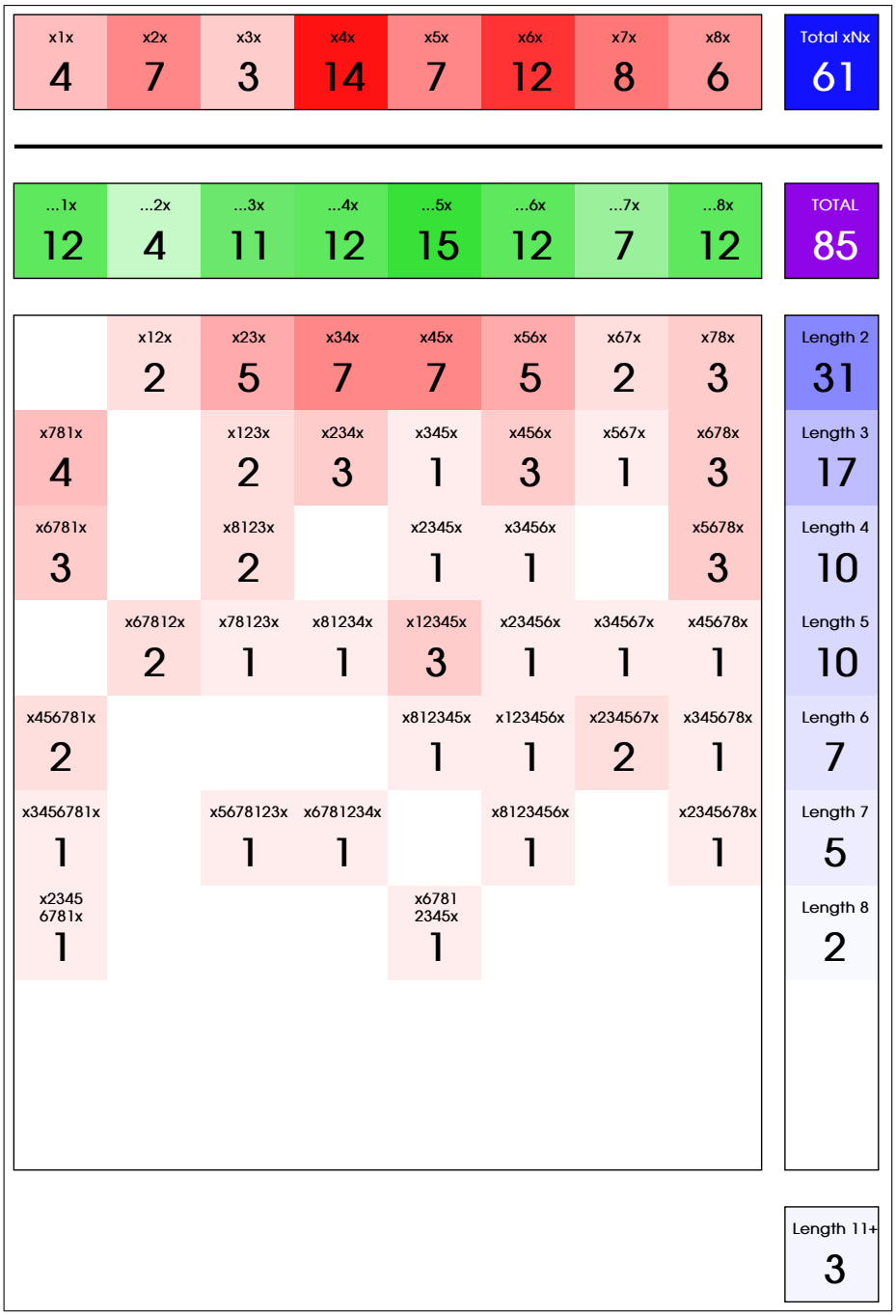

Figure 4.17: Histogram of MJO "events" in boreal winters (November to April) 1998/9 to 2012/3. An N denotes any phase; an x denotes any phase that does not continue the numerical sequence. An ellipsis denotes any sequence of phases, so "...4x" means any event ending with 4x. The top row shows the number of one-phase "events" (i.e., no propagation whatsoever). The large red grid shows the number of each type of event; they are summed by end phase (above in green) and by length (to the right in blue). The purple box shows the total number of events of length 2 or more. See main text for full details.

between any of the events, or always occurs with exactly the same frequency, there would still be major MJO errors in the model. These diagnostics will all

be used in chapter 6 for verification of the MJO in a high-resolution GCM.

4.7 Conclusions

The advent of high-resolution data sets provided by satellites has allowed us to study phenomena such as the diurnal cycle and the MJO in unprecedented detail. TRMM 3B42HQ provides precipitation data eight times per day throughout the tropics; although there are missing data due to gaps between swaths, these do not present a problem when compositing over a long period of time. Daily mean brightness temperature data are provided by TRMM 3G01. QuikSCAT data provides measurements of surface level wind over the ocean. The satellite is in a sun-synchronous orbit crossing the equator at 6am and 6pm local solar time, so we have a snapshot of the tropical diurnal cycle around these two times.

Composites of the data from these sources are able to show us features of the MJO and the diurnal cycles of precipitation and wind over the Maritime Continent. Wheeler-Kiladis diagrams are able to show us the strength of MJO variability relative to other forms of variability. The MJO is analysed using the index invented by Wheeler and Hendon (2004); the eight phases they defined are used for composites of the MJO cycle. New diagnostics have been devised to investigate how often these phases occur, how often the state of the atmosphere really does evolve from one phase to the next, and how long it spends in each phase. These diagnostics can also be used with model output to compare simulations of the MJO to reality.

Chapter 5

Scale interaction between diurnal cycle and MJO

5.1 Preface

This chapter is based heavily on a paper, *Peatman, Matthews and Stevens (2014)*, published in the Quarterly Journal of the Royal Meteorological Society. Some alterations have been made here, mainly to the introductory and concluding sections of the text in order to avoid repetition of material in chapters 2, 3, 4 and 8, and extra details have been added to some sections. Additionally, the sections on offshore propagation (5.4.3) and global analysis (5.7) did not appear in the paper.

5.2 Results of previous studies

We have seen (section 4.5.1) that the precipitation over the Maritime Continent exhibits a strong diurnal cycle, with a sharp contrast between the cycles over land and ocean. Section 1.2 posed the question of whether the synoptic large-scale environment, in which the relatively small-scale, short-timescale diurnal cycle is embedded, can affect the properties of the diurnal cycle. In particular, does the amplitude of the diurnal cycle change depending on whether the active MJO envelope is overhead, or whether the MJO conditions are suppressed?

Many studies have suggested that the MJO does indeed act to modulate both the amplitude and phase of the diurnal cycle. For example, Sui and Lau (1992)

found that the diurnal cycle is diminished during the active phase of the MJO and enhanced during the suppressed phase, while Sui et al. (1997) found that diurnal cycles of atmospheric variations are more pronounced during the wet phase. Chen and Houze (1997) investigated the diurnal cycle of deep convection and found the suppressed MJO to be associated with small, short-lived cloud systems which form and decay in the afternoon, and the active MJO to be characterised by larger, longer-lived systems which form during the afternoon but do not peak until the early hours of the following morning, before decaying. Tian et al. (2006) and Suzuki (2009) found the diurnal cycle of deep convection over both land and ocean areas to be enhanced during the active MJO compared with the suppressed MJO, but the diurnal phase to be similar under both regimes. However, Rauniyar and Walsh (2011) suggested that the mean and diurnal maximum of rainfall rate is greatest during the suppressed MJO over land, but greatest during the active MJO over ocean. Oh et al. (2012) found in the western Maritime Continent that precipitation amount over land is the most suppressed and over ocean is the most active during the active phase of the MJO, in particular finding the precipitation to be more intense over the Java Sea in the morning and less intense over Borneo and Sumatra in the evening, relative to other stages of the MJO cycle. During the decaying phase of the MJO they found the precipitation to be significantly weakened over ocean but weakened only slightly over land.

The differences between the above studies suggest that further work is required before a consensus can be reached on the effects of the MJO on the diurnal cycle. It should be noted that some of these studies suffered from a lack of data (covering a fairly short range of time), or from compositing the diurnal cycle using data at a fairly coarse resolution. For example, Sui and Lau (1992) used data from the First GARP (Global Atmospheric Research Program) Global Experiment, which ran from 5th January to 5th March 1979 and included only two MJO events. Similarly, both Sui et al. (1997) and Chen and Houze (1997) used data from TOGA COARE (Tropical Ocean Global Atmosphere Coupled Ocean Atmosphere Response Experiment), which ran from 1st November 1992 to 28th February 1993 and mainly covered the ocean only. All three of these studies investigated the diurnal cycle of cloudiness, not that of precipitation.

Tian et al. (2006) investigated the diurnal cycle over both land and ocean during a 7.5-year period, but although they used the high-resolution TRMM 3B42 data set (see section 4.2.2) to diagnose the MJO, they used low-resolution ($2.5° \times 2.5°$) deep convective cloud data to diagnose the diurnal cycle. Rauniyar

and Walsh (2011) used TRMM data to diagnose the diurnal cycle over the whole of the Maritime Continent, but did not compare the diurnal cycle in each of the WH04 MJO phases. Rather, they divided the domain into four longitude bands in each of which they defined certain WH04 phases to be "active" and certain phases to be "suppressed". This allowed composites to be constructed for active and suppressed conditions. In reality, however, the MJO conditions are never active or suppressed throughout the entire Maritime Continent simultaneously; moreover, the approach led to unrealistic discontinuities in the composited fields at the interface of each longitude band, and did not allow an analysis into how the diurnal cycle changes at each stage of the MJO cycle (i.e., in each WH04 phase).

Finally, Oh et al. (2012) uses TRMM 3B42 and the Japanese 25-year Reanalysis from the Japan Meteorological Agency and the Central Research Institute of Electric Power Industry (JMA-CRIEPI). They considered the diurnal cycle over both land and ocean in separate WH04 phases, although the region of study did not include the entire Maritime Continent, focusing only on the region 100°–120°E, 10°S–5°N.

5.3 Research parameters and data

Here we use fifteen boreal winters (November to April) of high-resolution data to investigate how the diurnal cycle of precipitation changes throughout an MJO cycle, how synchronous certain variations are during the evolution of the MJO, and how these indicate scale interactions between the two cycles. We also consider the changes which occur as the atmospheric state evolves through each successive phase of the MJO, as opposed to simply comparing two separate regimes, "active MJO" and "suppressed MJO". We wish to compare precipitation with infra-red brightness temperature data from TRMM 3G01, so we use only the microwave ("high quality") part of 3B42, denoted 3B42HQ.

Daily means of wind at 1000 hPa and mean sea level pressure, both at 2.5° horizontal resolution, are used from the NCEP-DOE Reanalysis 2.

All climatologies presented here are based on boreal winters (November to April) from 1998/9 to 2012/3. As in section 4.6, composites for each WH04 phase exclude days on which the MJO was "weak", defined as the RMM amplitude being less than 1.

5.4 Interaction between the diurnal cycle and the MJO

5.4.1 Diurnal cycle and MJO in observations

Figure 4.5 showed the climatology of the diurnal cycle of precipitation from TRMM 3B42HQ precipitation rate estimates, with the time of day moving clockwise around the diagram, and figure 4.6a showed the climatological amplitude of the diurnal harmonic (r_d) of precipitation rate, calculated for each grid point from the eight maps in figure 4.5. It was explained in section 2.2 how the strong land-based diurnal cycle arises from the relative effects of insolation over land and sea. It was also noted that land-based precipitation is enhanced by orography (Qian, 2008) and there is, accordingly, an especially strong diurnal cycle over mountainous regions such as along the islands of Sumatra and Java, in central Sulawesi and north-west Borneo, and along both sides of the high mountain range running east-west along New Guinea.

In section 4.6 composites were shown for each WH04 phase of daily mean brightness temperature $\overline{T}_b$ (figure 4.11, from TRMM 3G01, which is derived from OLR) and daily mean precipitation rate $\bar{r}$ (figure 4.12, from TRMM 3B42HQ). Figure 4.11 showed an active convective envelope in blue propagating slowly eastwards, with a corresponding suppressed envelope in red propagating behind it. The active MJO envelope as measured with $\overline{T}_b$ appears over the Maritime Continent region during WH04 phases 3 to 6, especially in phases 4 and 5.

Even though an MJO event consists of many convective systems across a range of scales which are merely organised into a large-scale envelope, it is common in the scientific literature for MJO envelopes to be treated as effectively homogeneous regions. Here we shall consider the internal spatial structure of the MJO envelopes. As noted in section 4.6, during certain WH04 phases in figure 4.11 there are some regions within the MJO envelope where the $\overline{T}_b$ anomaly is small or even of the opposite sign from its immediate surroundings. These regions are often, but not exclusively, over land. For example, over west Borneo in phases 1 and 5, and over New Guinea in phases 1–2 and 4–6 the anomaly is small; and over south New Guinea in phase 3 the anomaly is of the opposite sign to the rest of the envelope. For $\bar{r}$ in figure 4.12 the synoptic picture is similar to that for $\overline{T}_b$, with a clear eastward propagation

of successive active and suppressed envelopes, but there is more variability on small spatial scales. In particular, during WH04 phase 1 the large-scale MJO envelope over the Maritime Continent shows suppressed conditions, but there are near-zero or even positive precipitation anomalies over Sumatra, western Borneo and New Guinea. In phase 2, the active MJO has now reached the western Maritime Continent and subsumed the existing wet conditions over Sumatra into the large-scale envelope. However, western Borneo, Sulawesi and southern New Guinea show active convection, whilst being embedded in the large-scale envelope of suppressed conditions. Later in the MJO cycle these islands experience negative rainfall anomalies while the surrounding envelope is in its active phases (5–6). Each of these regions is a case of a vanguard of the propagating MJO precipitation "leaping ahead" of the main MJO envelope. This leaping ahead is a characteristic of the MJO propagation which is peculiar to the archipelago of the Maritime Continent.

5.4.2 Modulation of the diurnal cycle by the MJO

We now consider the effect of the MJO on the diurnal cycle of precipitation rate

$$r = \bar{r} + r_d \cos\left\{\frac{2\pi}{\tau}(t - t_0)\right\}, \tag{5.1}$$

where $\tau = 24$ hours is the time period of the diurnal harmonic and t_0 is a time offset. We are especially interested in whether it is only the daily mean precipitation $\bar{r}$ which is dependent on the phase of the MJO, or whether the amplitude of the diurnal harmonic r_d is also modulated.

As an example, the diurnal cycle averaged over the land area of Borneo is plotted in figure 5.1; the climatology is shown by the thick black line, and composites for each WH04 phase are shown by the thin coloured lines (as indicated by the key). Comparing, say, the opposing phases 3 and 7, we see that the daily mean is higher for phase 3 than phase 7. This is as we expect from figure 4.12 – the MJO is active over Borneo in phase 3 so conditions are wetter, and *vice versa* for phase 7. However, it is also evident that in the wetter phases (2–4), the amplitude of the diurnal cycle is enhanced compared with the drier phases (5–7). Hence, there is an interaction by which the small-scale diurnal cycle is modulated by the state of the large-scale MJO envelope.

The climatological mean amplitude r_d of the diurnal harmonic, averaged over all days in the study period, calculated for each grid point was shown in

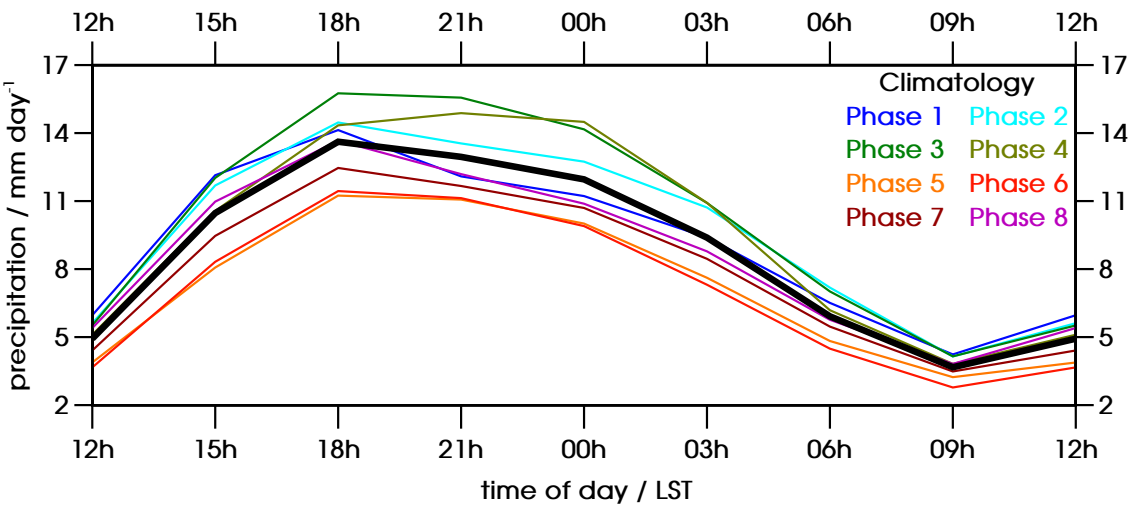

Figure 5.1: Diurnal cycle of precipitation from TRMM 3B42HQ, averaged over the land of Borneo. The thick black line is the climatology; thinner coloured lines are for each of the eight WH04 phases, as indicated.

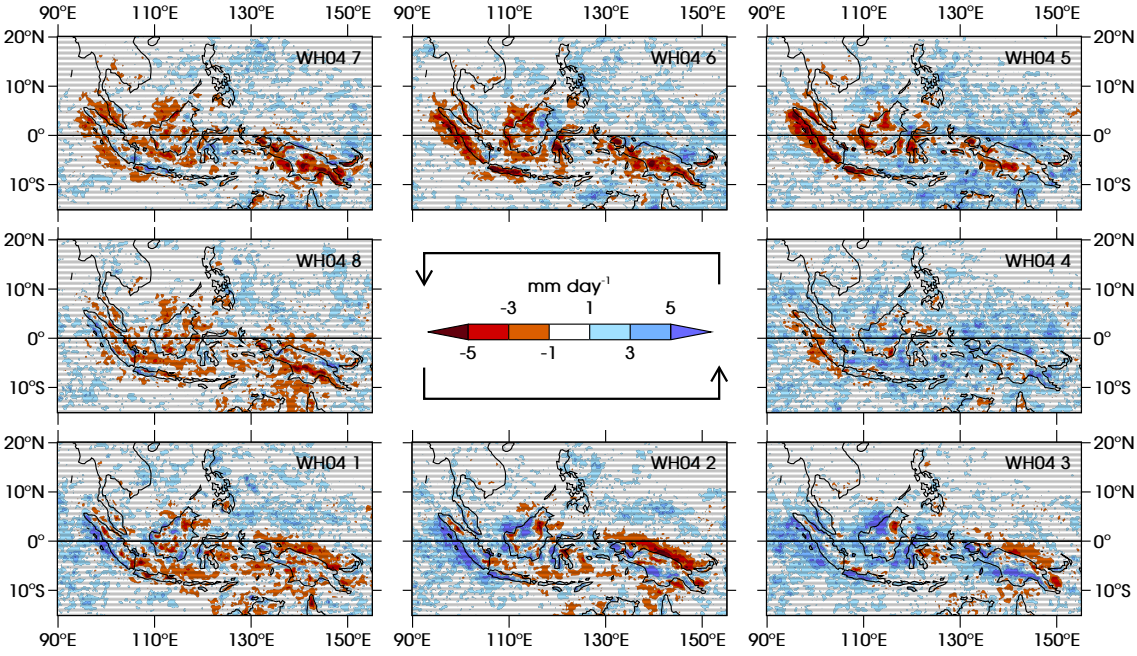

Figure 5.2: Anomaly of the amplitude r_d of the diurnal harmonic of precipitation from TRMM 3B42HQ in each phase of the MJO. Blue (red) regions indicate an enhanced (suppressed) diurnal amplitude. The amplitude of the climatological diurnal cycle is shown in figure 4.6a.

figure 4.6a. The mean amplitude at each grid point is also calculated using just the days in each WH04 phase; a map of the anomalous amplitude of the diurnal harmonic is then calculated for each WH04 phase (figure 5.2) by subtracting the mean over all WH04 phases. These r_d anomalies are of the same order of magnitude as the $\bar{r}$ anomalies in figure 4.12 (note that both figures use the same colour scale). There is not a smooth eastward propagation over the Maritime

Continent, but r_d exhibits strong anomalies which are confined to the islands and immediately-surrounding ocean. This notably includes but is not confined to those ocean regions where there is strong offshore propagation (as described in sections 2.2.2 and 4.5.1), such as south-west of Sumatra and north of New Guinea. The negative anomalies off the north coast of New Guinea in phases 1–3 and off the south coast in phases 5–7 confirm the findings of Ichikawa and Yasunari (2008), who showed how the propagation of precipitation is altered by the wind anomaly associated with the MJO.

The r_d anomalies differ by as much as 10 mm day^{-1} in opposing MJO phases over some regions. There is spatial coherence, but on a scale smaller than the MJO envelope, unlike in the $\overline{T}_b$ and $\bar{r}$ anomalies; the MJO envelope appears not to modulate the diurnal cycle in a simple, linear way. Although we saw in figure 4.6a that the diurnal cycle tends to be strongest near to high topography, there is not a clear correlation between topography (figure 1.1b) and r_d anomaly (figure 5.2), so it appears that while topography is important in determining the strength of the diurnal cycle it has little effect on the degree to which the diurnal cycle is modulated by the MJO.

5.4.3 Modulation of nocturnal offshore propagation by the MJO

In section 4.5.1 it was noted that, over certain regions of the Maritime Continent, there is strong offshore propagation of precipitation overnight. It was stated that this is caused by the triggering of gravity waves (Love et al., 2011), which themselves trigger convection as they propagate. We now consider the effect of the MJO on this offshore propagation. Given the differences in the large-scale dynamical fields between different phases of the MJO, it is reasonable to expect differences in, for example, the speed and extent of the convectively-coupled gravity waves. It is even possible that, under some circumstances, the gravity waves may not be triggered at all.

In order to investigate the effect of the MJO, three regions of strong offshore propagation were chosen (see figure 5.3): (a) the south-west coast of Sumatra, (b) the north-west coast of Borneo and (c) the north coast of New Guinea. The dashed boxes indicate the regions in which the offshore propagation is investigated. The solid axis with tick marks runs in the direction of the propagation, from the land out into the ocean. The tick marks denote integer

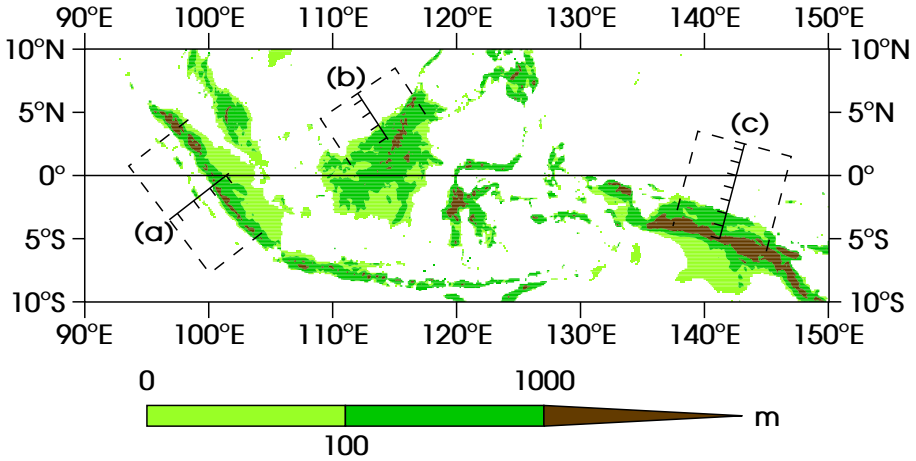

Figure 5.3: Orography of the Maritime Continent from GLOBE, with offshore propagation case study regions indicated by the dashed boxes: (a) south-west of Sumatra, (b) north-west of Borneo and (c) north-north-east of New Guinea. The solid axes are the horizontal axes in the Hovmöller diagrams in figure 5.4; the tick marks indicate integer values of degrees latitude.

values of degrees latitude. Precipitation from 3B42HQ is averaged across the width of the box at each time of day, to give a field of time versus distance along the solid axis. These fields are shown in figure 5.4. In this figure the horizontal axes are the same as the solid axes in figure 5.3. The bottom horizontal axis for each panel shows latitude (so the tick marks are the same as those in figure 5.3) and the top horizontal axis shows longitude. At the top of figure 5.4 is the climatological offshore propagation in each of the the three regions. Beneath these is plotted the average orography (from GLOBE), again averaged over the width of the dashed boxes. Then the diurnal cycle in each propagation region is plotted for each of the eight WH04 phases.

Overlaid is a line showing the propagation of the convectively-coupled gravity wave; in the top-right corner of each diurnal cycle is the speed of propagation in m s^{-1}. The positioning of this line is determined objectively, using an algorithm based on that developed by Webber et al. (2012). By looking at the Hovmöller diagrams, the gravity wave propagation was defined to start and end at 18:00 and 09:00 respectively for region (a), 18:00 and 12:00 for region (b), and 00:00 and 12:00 for region (c). The latitude co-ordinate at which the propagation line starts and finishes was determined by interpolating the precipitation field onto the line, and calculating the mean of the precipitation values over all the times along it. The start and end positions that give the maximum value of this quantity were chosen. For example, in phase 1 off the coast of Sumatra, some of the calculated values are shown in table 5.1. The line is drawn from 0.6°S to

		end latitude co-ordinate						
		··· 1.25°S	1.30°S	1.35°S	1.40°S	1.45°S	1.50°S	1.55°S ···
start latitude co-ordinate	⋮							
	0.45°S	19.475	19.724	19.973	20.222	20.503	20.756	20.822
	0.50°S	19.914	20.163	20.412	20.661	20.931	21.067	21.101
	0.55°S	20.353	20.602	20.851	21.100	21.312	21.317	21.304
	0.60°S	20.687	20.937	21.186	21.390	21.359	21.310	21.260
	0.65°S	20.743	20.956	21.132	21.172	21.107	21.058	21.008
	0.70°S	20.718	20.875	20.985	20.920	20.855	20.806	20.757
	0.75°S	20.617	20.774	20.743	20.669	20.604	20.554	20.505
	⋮							

Table 5.1: Excerpt from the matrix of values used to find the propagation line for offshore propagation area (a), south-west of Sumatra, in MJO phase 1. The maximum value (outlined) occurs for the line that starts at 0.6°S and ends at 1.4°S.

1.4°S since this gives the maximum value along the line of 21.390 mm day^{-1}.

The propagation lines found by this objective method are only approximate, but do tend to fit the Hovmöller diagrams reasonably well. One significant problem is in plots such as phase 4 for Borneo, in which the gravity wave appears to speed up as it propagates. This change in phase speed is, of course, not accounted for by the linear fit. Other methods were also tried in order to achieve a better fit (not shown) but they caused further problems to arise. Designing an approach for finding the best fit is complicated by factors such as, in the top-left corner of the plots, non-propagating signals (Borneo and New Guinea) and signals propagating in the wrong direction (Sumatra). Also, in some cases it is difficult to distinguish the propagation at all (e.g., New Guinea in phase 2). An alternative approach was to find the location of the maximum precipitation at each time step in the Hovmöller diagram and to fit a curve through these points. This gives each time step an equal weighting in the fitting process, whereas the approach used in figure 5.4 effectively weights each time of day according to the strength of precipitation. Each method has advantages and disadvantages, and both give some propagation lines which do not appear quite accurate. The method of finding the straight line with the maximum average precipitation rate along it was chosen, but it must be noted that the results presented here are approximate and are sensitive to the fitting algorithm used.

The offshore propagation is seen in the climatology in all three regions, and although it weakens and strengthens significantly as the MJO evolves it is also present in all WH04 phases. The dispersion relation for gravity waves (in the

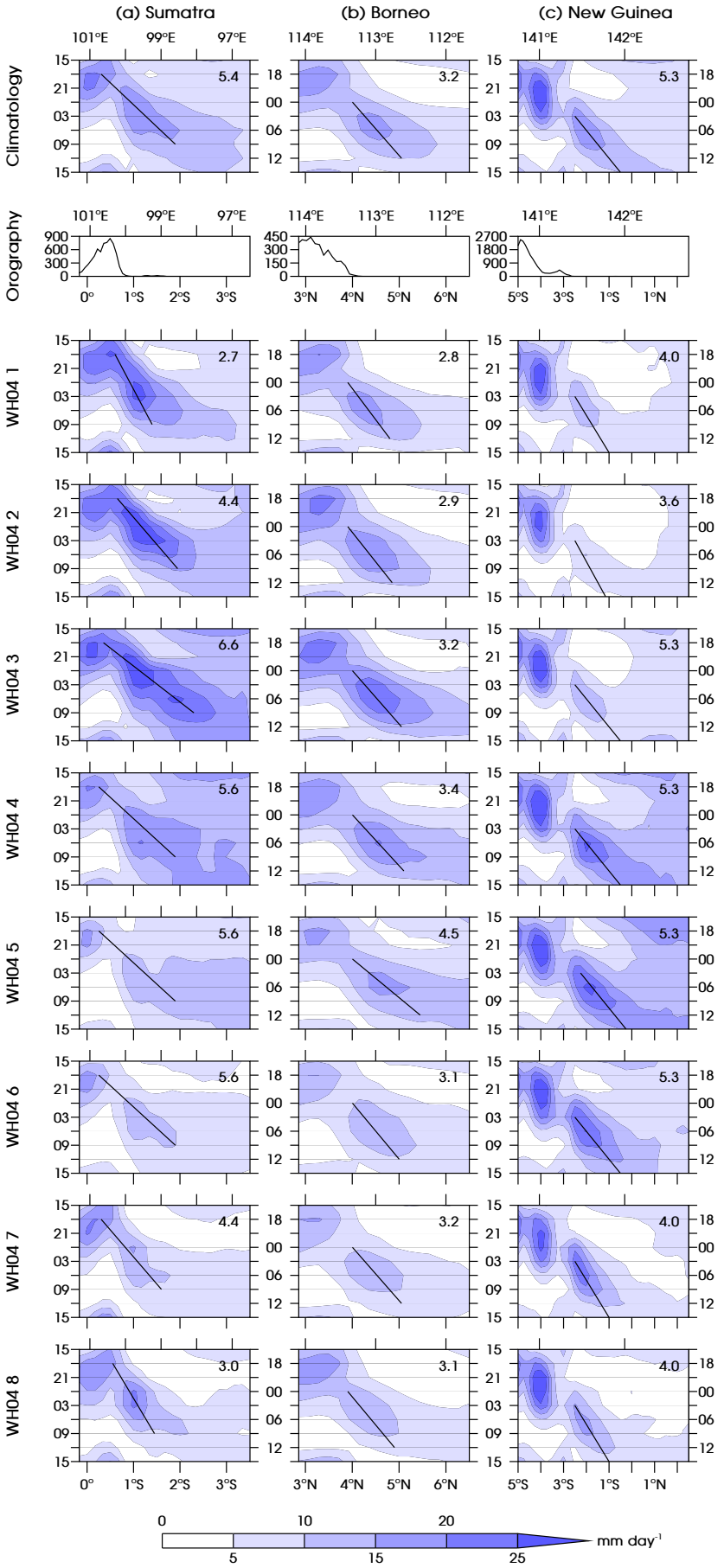

Figure 5.4: Hovmöller diagrams of precipitation (TRMM 3B4HQ) over the regions shown in figure 5.3: (a) south-west of Sumatra, (b) north-west of Borneo and (c) north-north-east of New Guinea. Diurnal cycle composites are shown for the climatology (top) and for each of the 8 MJO phases. Time of day moves downwards and is labelled in LST. The mean cross-section of orography (GLOBE) is also shown for each region (note the different vertical scales for each). The horizontal axes of all panels correspond to the solid axes in figure 5.3, and are labelled in latitude at the bottom of the plots and longitude at the top.

hydrostatic limit) is

$$\omega^2 = \frac{N^2k^2 + f^2m^2}{m^2}, \tag{5.2}$$

where ω is the angular frequency, N is the Brunt-Väisälä frequency, f is the Coriolis parameter, k is the horizonal wavenumber and m is the vertical wavenumber (Gill, 1982). At the equator $f = 0$, so the phase speed is given by

$$c_p = \frac{\omega}{k} = \pm\frac{N}{m} = \pm\frac{N\lambda_z}{2\pi}, \tag{5.3}$$

where λ_z is the vertical wavelength. From figure 5.4 the mean of the three climatological propagation speeds is 4.6 m s^{-1}, and a typical value for N is 10^{-2} s^{-1}. Hence, the vertical wavelength λ_z is about 2.9 km (or slightly smaller for non-zero but small f, near the equator). This is notably around the same height as the mountains of New Guinea, but on Sumatra and Borneo the peaks are much lower so it is unlikely that the vertical structure of these waves is being determined by the orography. In a 40 km resolution model with convective parameterisation, Love et al. (2011) found gravity waves of considerably faster speed (the fastest being around 60 m s^{-1}), so the waves found by this analysis are of a relatively high order. It is quite possible, however, that multiple gravity wave modes are being generated at the same time over the Maritime Continent so the real picture may be more complicated than this methodology suggests.

The speed (and, therefore, the horizontal extent) of the propagation varies throughout the MJO, especially off the coast of Sumatra. The range there is from 2.7 m s^{-1} in phase 1 to 6.6 m s^{-1} in phase 3, a difference of a factor of almost 2.5. Off New Guinea the variation is less but there is still a clear MJO cycle, with the speed varying between 3.6 m s^{-1} in phase 2 and 5.3 m s^{-1} in phases 3–6. Off Borneo the speed is generally around 3 m s^{-1}, except in phase 5 when it increases to 4.5 m s^{-1}. Thus, the fastest propagation occurs later during the MJO cycle off Borneo than off Sumatra, whereas off New Guinea the propagation is at a consistent speed throughout the more active half of the MJO.

Three factors which may be contributing to the change in propagation speed in different WH04 phases are the changing heating profiles and the changing static stability, both due to the MJO's cycle of active and suppressed convection, and the background wind caused by the MJO circulation. Figure 5.5 shows the propagation speed of the gravity waves plotted against WH04 phase for each of the three case study regions, along with the brightness temperature anomaly (left-hand column) and daily mean precipitation anomaly (right-hand

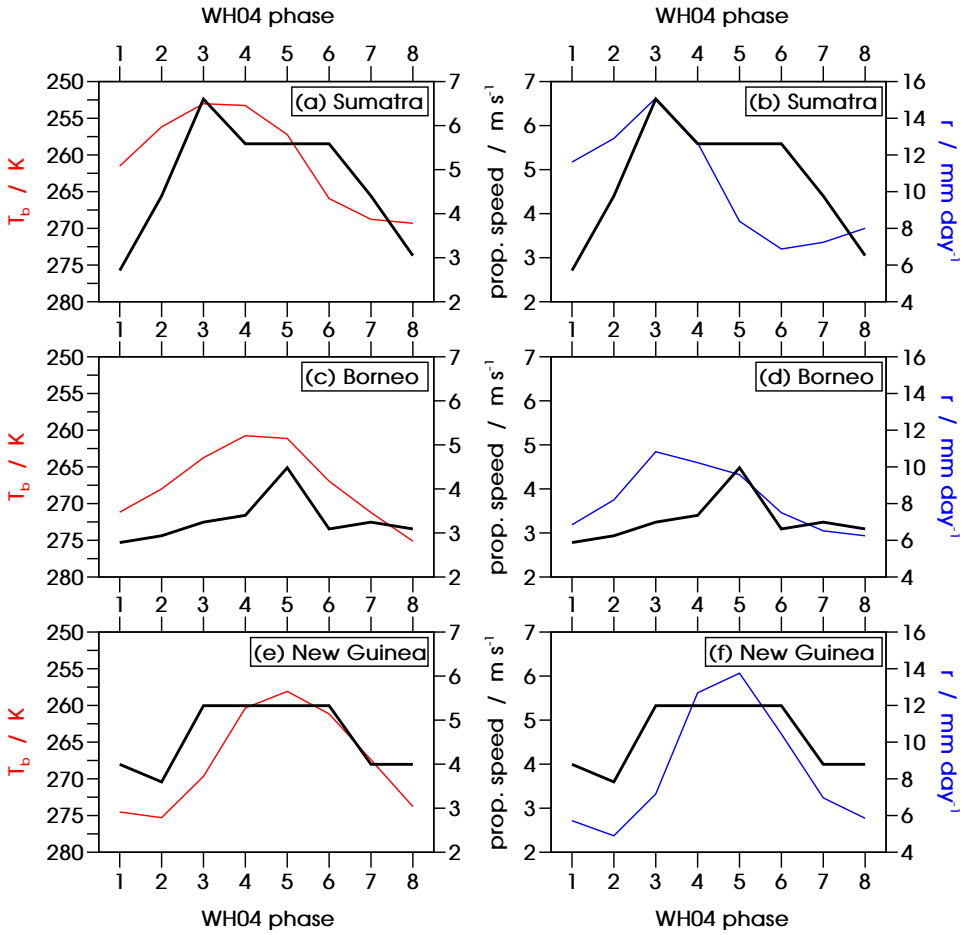

Figure 5.5: Speed of gravity wave propagation (black lines) against WH04 phase for (a,b) Sumatra, (c,d) Borneo and (e,f) New Guinea (domains defined in figure 5.3), along with daily mean brightness temperature $\overline{T}_b$ (left-hand column, red lines) and daily mean precipitation $\overline{r}$ (right-hand column, blue lines). Note that the $\overline{T}_b$ axis is inverted.

column), both averaged over ocean within the dashed boxes in figure 5.3. Note that the $\overline{T}_b$ axes on the left are inverted, since lower values of $\overline{T}_b$ indicate more active convection. In general the speed of the convectively-coupled waves is faster during the more active phases of the MJO and slower during the more suppressed phases.

Ling and Zhang (2011) computed heating profiles for each phase of the MJO. Positive heating anomalies exist throughout the troposphere during the active phases of the MJO and negative anomalies during suppressed phases. Love et al. (2011) showed that different gravity wave modes are triggered during the day depending on the vertical heating profile present. Deeper vertical modes are associated with deeper (convective) heating whereas higher-order modes occur for heating profiles associated with stratiform cloud. The results presented here suggest that a similar change in gravity wave modes may occur throughout the

MJO cycle, since the wave speed tends to increase during active phases when there is a deep, positive heating profile. In the suppressed phases, when heating anomalies are negative and there is no such deep convection, slower gravity waves may be triggered.

As shown in equation 5.3 the speed of a gravity wave depends on N, where

$$N^2 = \frac{g}{\theta}\frac{\mathrm{d}\theta}{\mathrm{d}z}, \tag{5.4}$$

where g is the acceleration due to gravity, θ is potential temperature and z is height. By definition a stable atmosphere has positive $\partial\theta/\partial z$, so greater static stability means that the waves have a higher frequency and, therefore, a higher phase speed. During the suppressed phase of the MJO there are clear skies, allowing the ground to heat up and thus reducing the stability of the atmosphere. Hence, brightness temperature and precipitation can be considered a rough proxy for static stability. This is consistent with the observed propagation speeds, since reduced static stability reduces the value of N^2, thus reducing the gravity wave speed during the suppressed MJO. In the active phase the moist convection acts to return the atmosphere to a more stable state so N^2 increases, which is consistent with the faster gravity wave speeds during phases of more active brightness temperature and precipitation.

The background wind field may also affect the speed of gravity wave propagation; this process is known as Doppler shifting. For example, off the coast of Sumatra, given the orientation of the gravity waves, we would expect easterly winds to result in faster waves and westerly winds to result in slower waves. During the phases exhibiting faster propagation (3 to 6), easterly wind anomalies exist in the upper troposphere; during the phases when propagation is slower (7 to 2) there are westerly wind anomalies in the upper troposphere. Off the coast of Borneo the fastest propagation is in phase 5, which again is consistent with upper-level easterlies. Off the coast of New Guinea, where the propagation is roughly northwards, it is unlikely that the speed is affected by the background wind field since the meridional MJO anomalies are very small. There is also some evidence to suggest that the influence of the wind may be stronger when there is a lack of vertical wind shear. As shown in figure 5.6, off the coast of Sumatra in phase 1 (panels a and b, when the propagation is slowest) there is strong vertical wind shear, but in phase 3 (panels c and d, when the propagation is fastest) the wind field close to the Sumatran coast is almost barotropic throughout the troposphere. It is possible that this consistent

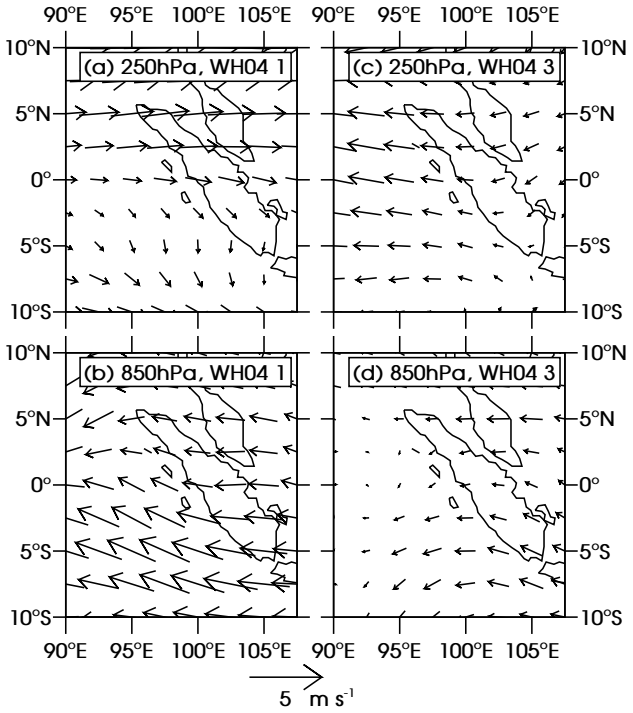

Figure 5.6: Wind anomalies (NCEP-DOE Reanalysis 2) over the offshore propagation region near Sumatra, in (a,b) WH04 phase 1 (slowest propagation, 2.7 m s^{-1}) and (c,d) WH04 phase 3 (fastest propagation, 6.6 m s^{-1}). Anomalies are shown for the upper (250 hPa) and lower (850 hPa) troposphere.

direction throughout the height of the troposphere in the phase 3 anomaly may allow it to contribute to the gravity wave speed, whereas when the direction of the wind anomaly varies with height it has less of an effect, or may even act to slow the wave down.

To summarise, the offshore propagation of precipitation due to gravity waves from the coasts of Sumatra, Borneo and New Guinea has been shown to be modulated by the evolution of the MJO as the phase speed depends on MJO phase. A typical propagation speed for the convectively coupled gravity waves in the climatology is around 4.6 m s^{-1} and a typical vertical wavelength is up to about 2.9 km. The greatest variation in propagation speed during the MJO is south-west of Sumatra, with a range from 2.7 m s^{-1} (phase 1) to 6.6 m s^{-1} (phase 3), although significant variations are also seen north-west of Borneo and north-north-east of New Guinea. In general, the faster propagation speeds occur when the MJO is most active. Three possible reasons for this were suggested. First, the deep convective heating profile associated with the active MJO may allow faster gravity wave modes to be triggered. Second, the active MJO tends to restore stability to the atmosphere, increasing the Brunt-Väisälä frequency and, therefore, the phase speed of the waves. And third, the changes

in the background wind in the upper troposphere are consistent with a Doppler shifting of the gravity waves. Also, for the Sumatra case study region there is a suggestion that the wind may play a more significant role when there is a lack of vertical wind shear.

5.4.4 Relationship between daily mean and diurnal amplitude of precipitation

For each grid point in figures 4.12 and 5.2 there is a notional scatter plot with one point for each WH04 phase, with the daily mean precipitation rate as the abscissa and the diurnal amplitude of precipitation rate as the ordinate. The scatterplots for three arbitrary points, chosen as examples, are shown in figure 5.7. Linear regression was computed for each grid point; the linear fit is also shown in figure 5.7. The gradient and correlation coefficient R for all grid points are shown in figures 5.8a and b respectively.

Statistical significance of the correlation is calculated using a Fisher Z transform of the correlation coefficient (Wilks, 2011). Given the sample correlation coefficient R, the quantity

$$Z = \frac{1}{2}\ln\left(\frac{1+R}{1-R}\right) \equiv \tanh^{-1}(R) \tag{5.5}$$

follows a Student's t distribution with mean

$$\overline{Z} = \frac{1}{2}\ln\left(\frac{1+\rho}{1-\rho}\right), \tag{5.6}$$

where ρ is the population correlation coefficient, and variance

$$\sigma_Z = \frac{1}{\sqrt{N-3}}, \tag{5.7}$$

where N is the number of pairs of data points (in this case $N = 8$, for the 8 WH04 phases). Given the hypotheses

$$H_0 : \rho = 0 \tag{5.8a}$$

$$H_1 : \rho \neq 0 \tag{5.8b}$$

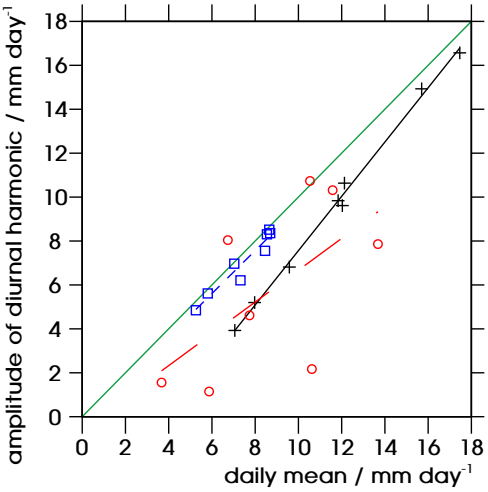

Figure 5.7: Scatterplot of the amplitude of the diurnal harmonic (r_d) against daily mean precipitation ($\bar{r}$) for the eight WH04 phases, for the three sample points 2.125°N 113.125°E (Borneo, solid black), 5.125°S 142.125°E (New Guinea, short-dashed blue) and 0.125°N 103.125°E (Sumatra, long-dashed red). Each data point represents one WH04 phase. Straight lines show the best fit according to linear regression; the gradient and correlation coefficient for all grid points are shown in figure 5.8. The line $r_d = \bar{r}$ is shown in green.

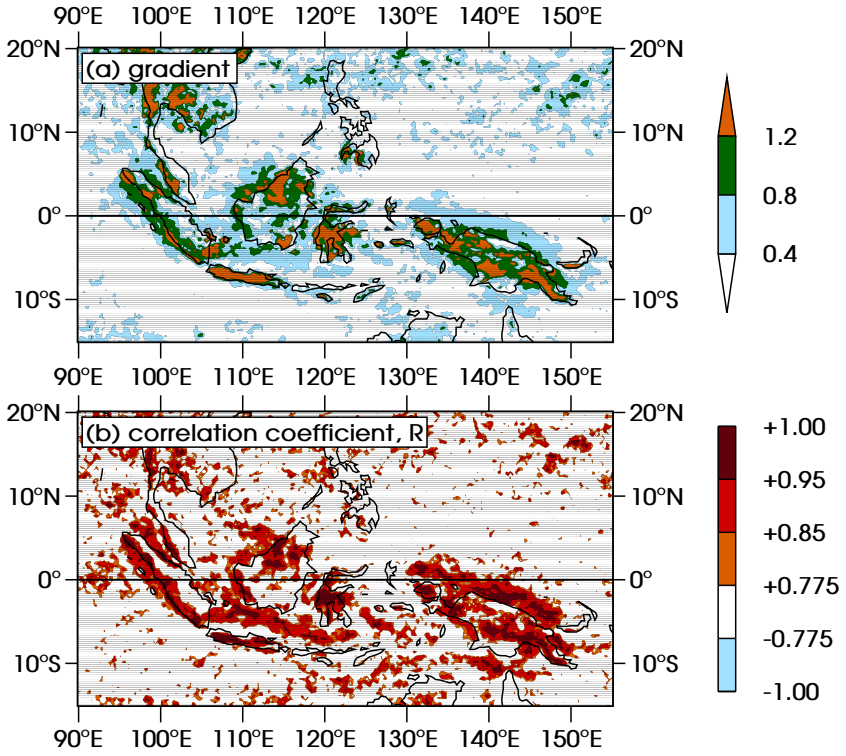

Figure 5.8: (a) Gradient and (b) correlation coefficient R of the linear relationship between the amplitude of the diurnal harmonic of precipitation for each WH04 phase, and the daily mean in the corresponding phase (both from TRMM 3B42HQ). (See figure 5.7 for three example grid points.) In (b), regions in white are below the 95% confidence threshold of $|R| = 0.775$.

under the null hypothesis H_0 the mean reduces to

$$\overline{Z} = 0. \tag{5.9}$$

To reject H_0 and accept the alternative hypothesis H_1 at the 95% confidence level, for a two-tailed test we require

$$C_8(Z) = 0.975 \tag{5.10}$$

$$\Rightarrow \quad Z_{95\%} = 2.31\sigma_Z \tag{5.11}$$

$$\Rightarrow \quad Z_{95\%} = \frac{2.31}{\sqrt{8-3}}, \tag{5.12}$$

where C_N is the cumulative probability function for the Student's t distribution with N degrees of freedom. Hence, the critical value of R is

$$R_{95\%} = \tanh\left(\frac{2.31}{\sqrt{5}}\right) = 0.775. \tag{5.13}$$

In figure 5.8b, regions where there is a statistically significant correlation are shaded and regions where the correlation is insignificant are left white.

Over regions where the diurnal cycle is strong (where the amplitude of the diurnal harmonic exceeds 10 mm day^{-1} – see figure 4.6a), the mean of R is 0.899, which is above the 95% significance threshold of 0.775. $R = 0.899$ corresponds to a correlation with 99% confidence and $R^2 = 81\%$ of the variance in the MJO daily mean precipitation anomaly being accounted for by the change in the diurnal cycle. Over these same regions the mean of the gradient between r_d and $\overline{r}$ is 1.18 (≈ 1), so they are of similar magnitude. We know from figure 4.12 that the MJO causes the variation in daily mean precipitation. Therefore, we suggest that where there is a strong diurnal cycle, the change in the amplitude of the diurnal cycle is the dominant contributor to the daily mean MJO precipitation. Thus, the MJO precipitation in those regions is largely due to the diurnal cycle. This hypothesis will be examined further in section 5.5 below.

Having found a 1:1 relationship between $\overline{r}$ and r_d over regions of strong diurnal cycle, we now briefly consider those regions and MJO phases which depart from such a relationship – that is, those data points which lie far from the green line $\overline{r} = r_d$ in figure 5.7, such as the red data points for the location 0.125°N 103.125°E in Sumatra. If data points lie on the line then, in each MJO phase, we presumably have a diurnal cycle with the same structure but differing

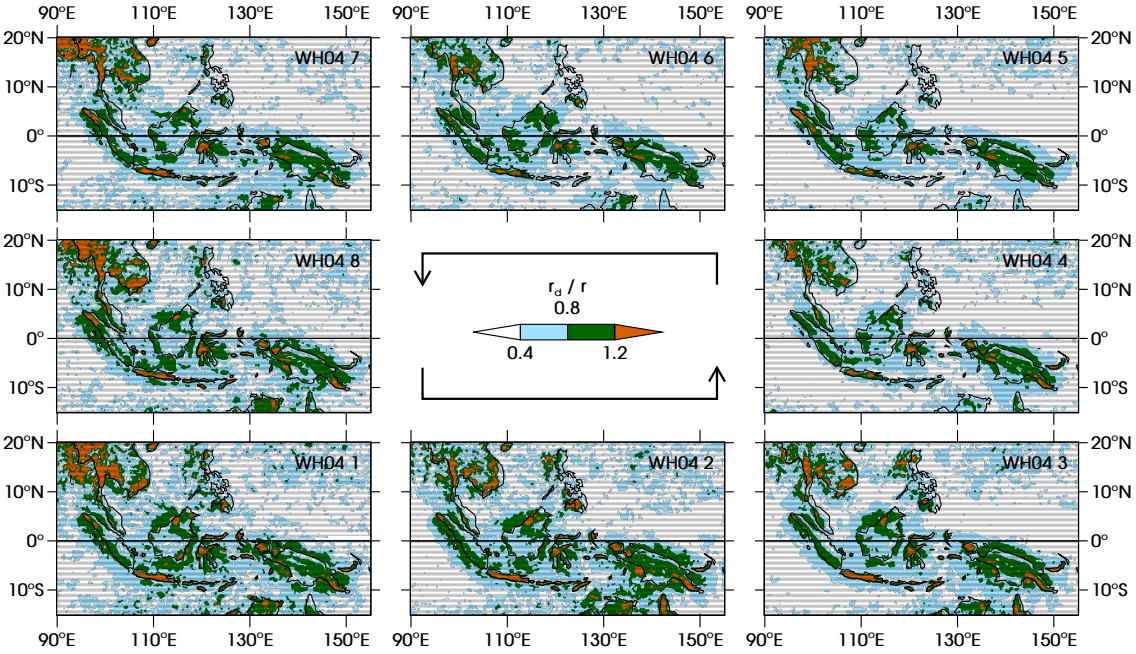

Figure 5.9: Ratio of the amplitude r_d of the diurnal harmonic of precipitation to the daily mean precipitation $\bar{r}$, from TRMM 3B42HQ in each phase of the MJO.

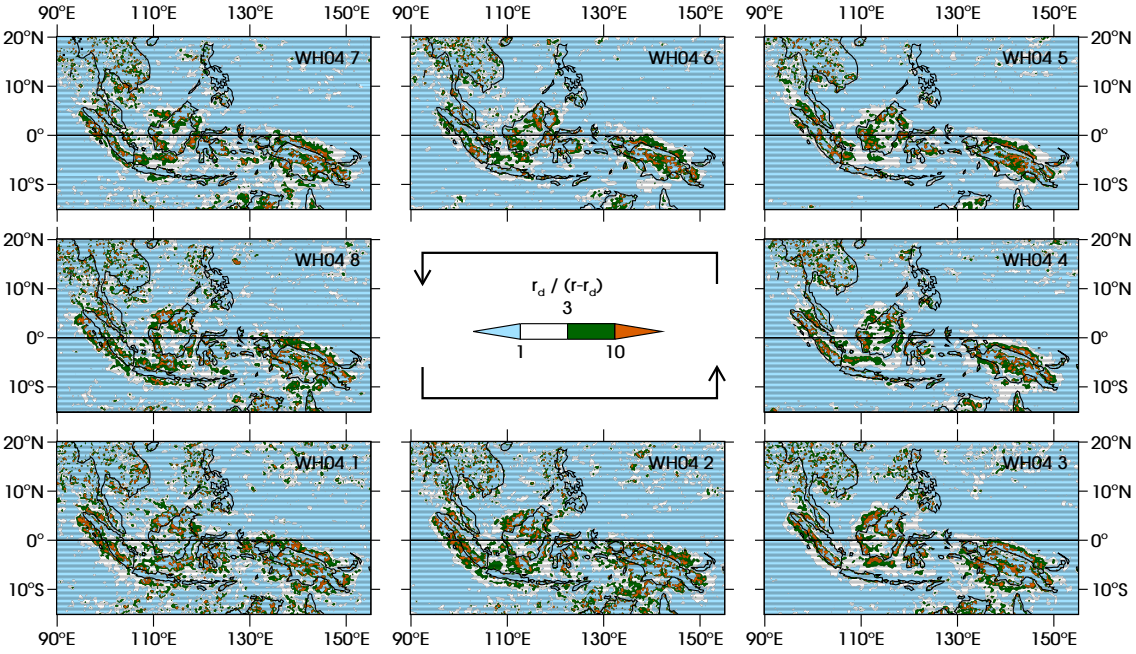

Figure 5.10: Ratio of the amplitude r_d of the diurnal harmonic of precipitation to persistent precipitation (defined as the daily mean precipitation $\bar{r}$ minus r_d), from TRMM 3B42HQ in each phase of the MJO.

in magnitude. If points lie to the bottom-right of the line, however, then rainfall must occur which is not accounted for by the diurnal cycle, and instead of a simple change in magnitude we may have a change in the very structure of the diurnal cycle at different stages of the MJO. For example, certain phases may

see different types of convective system forming, with longer lifetimes than the diurnal systems.

The ratio $r_d/\overline{r}$ is plotted in figure 5.9 for each phase of the MJO. Precipitation which is not part of the diurnal cycle will predominantly be due to more persistent convective systems, so we can estimate "persistent rainfall" by subtracting r_d from $\overline{r}$. The ratio of diurnal to persistent rainfall, $r_d/(\overline{r} - r_d)$, is plotted for each MJO phase in figure 5.10. The ratio $r_d/\overline{r}$ is very similar to the gradient in figure 5.8a and does not vary much from phase to phase. Similarly, on large scales the ratio of diurnal to persistent precipitation does not vary much from phase to phase. Although on small scales there are regions which do vary strongly throughout the MJO, this occurs close to the grid point scale only, rather than in any spatially coherent manner. This suggests that there are no large-scale regions which behave like the red data points over Sumatra in figure 5.7, with some points close to the $\overline{r} = r_d$ line but others far from it. Therefore, where the diurnal cycle is strong, the dominant effect of the MJO is to leave the structure of the diurnal cycle roughly unchanged and just to change its magnitude.

5.5 Relative MJO phases

We now consider the extent to which daily mean brightness temperature $\overline{T}_b$, daily mean precipitation $\overline{r}$ and the amplitude of the diurnal cycle r_d lead or lag each other during an MJO cycle. We take two approaches: first (section 5.5.1) we examine when the maxima in $\overline{r}$ and r_d occur relative to the large-scale $\overline{T}_b$ envelope; second (section 5.5.2) we construct "MJO harmonics" and use them to compare locally (i.e., at each grid point) the timings of the maxima in $\overline{T}_b$, $\overline{r}$ and r_d.

5.5.1 MJO phase relative to the large-scale envelope

Figure 5.11 shows (panels (c) and (d)) the land-means and ocean-means of $\overline{T}_b$, $\overline{r}$ and r_d over the regions 7°S–10°N, 100°–120°E (Borneo and most of Sumatra; see panel (a)) and 12°S–3°N, 130°–153°E (New Guinea; see panel (b)). The thick solid black line indicates the $\overline{T}_b$ signal over ocean, which may be thought of as the large-scale MJO envelope unaltered by the presence of the Maritime Continent islands. The thin solid black line ($\overline{T}_b$ over land) follows roughly the same shape

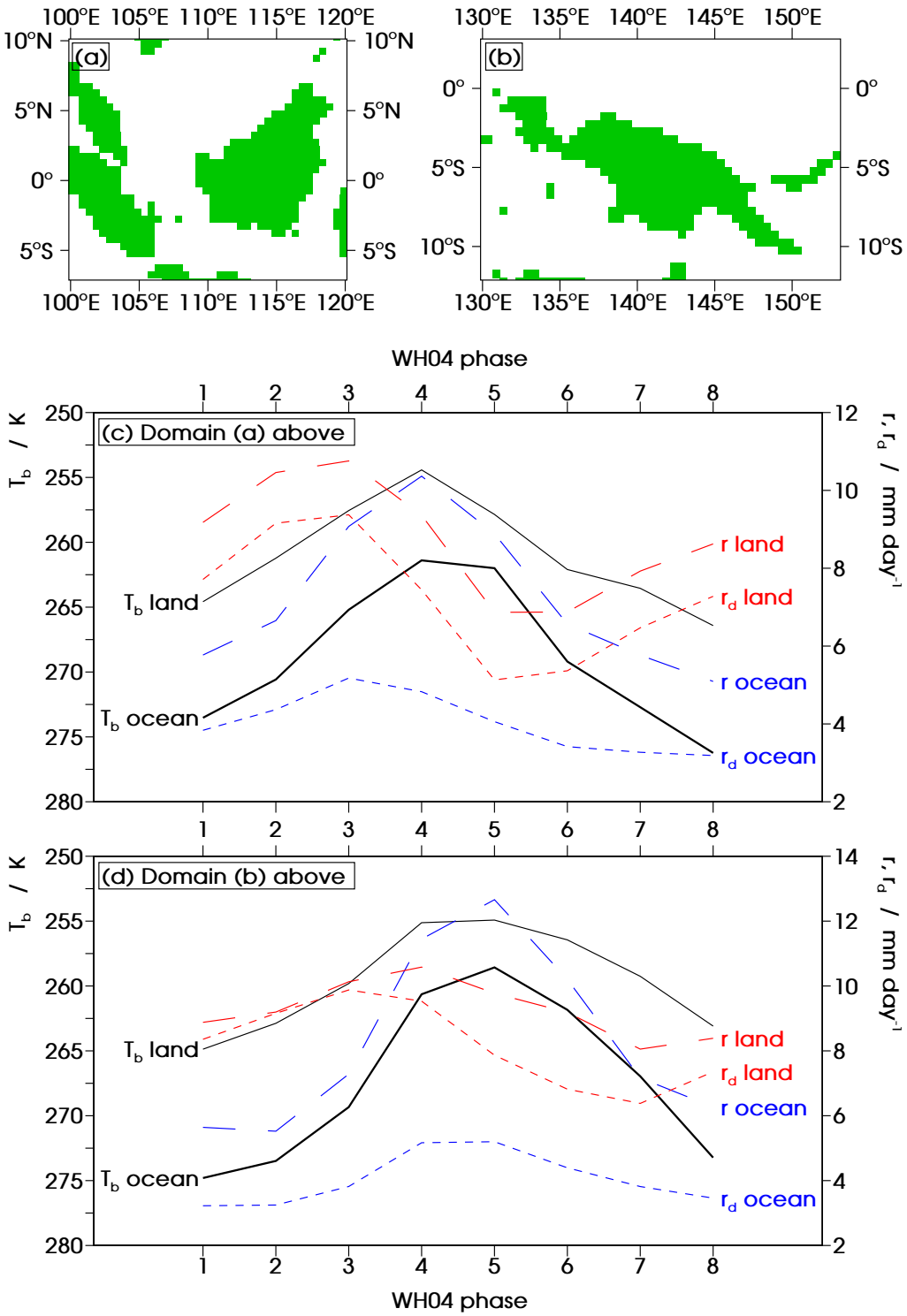

Figure 5.11: Land masks for the regions (a) 7°S–10°N, 100°–120°E and (b) 12°S–3°N, 130°–153°E, created by regridding GLOBE orography to the TRMM 3B42HQ grid. (c) and (d): means of daily mean brightness temperature ($\overline{T}_b$), daily mean precipitation (r) and amplitude of the diurnal harmonic of precipitation (r_d), averaged separately over land and ocean for the domains shown in (a) and (b) respectively. Note that the $\overline{T}_b$ axes are inverted.

as the ocean-mean line but at a colder brightness temperature, as expected since convective precipitation is focused over the islands.

The $\overline{T}_b$ signal over ocean peaks in WH04 phase 4 over domain (a) and in phase 5 over domain (b), as expected since this is when the MJO is most active. We consider the Sumatra-Borneo domain first (panel (c)). As well as the ocean $\overline{T}_b$ signal, the land $\overline{T}_b$ signal also peaks in phase 4 (although it could be argued that the land signal is slightly earlier, since the ocean signal appears to peak between phases 4 and 5). However, the daily mean precipitation $\bar{r}$ over land (red long-dashed) peaks earlier in phase 3. The diurnal amplitude of precipitation r_d over the land (red short-dashed) also peaks in phase 3 and follows the shape of the $\bar{r}$ signal throughout the whole MJO. Hence, the $\bar{r}$ and r_d signals associated with the MJO peak ahead of the large-scale $\overline{T}_b$ envelope by approximately 1 WH04 phase, or 1/8 of a cycle. We have already seen in figure 5.8a that there is an approximate 1:1 relationship between $\bar{r}$ and r_d, and in 5.8b that most of the MJO-variance in $\bar{r}$ may be attributed to the changes in r_d. This suggests that the strong diurnal cycle, leading the large-scale MJO envelope, is mostly responsible for the daily mean signal also leading the envelope.

In contrast, over the ocean $\bar{r}$ (blue long-dashed) is roughly in phase with $\overline{T}_b$. This may be attributed to the fact that the ocean-based diurnal cycle is weak (see figure 4.6a), so even though it does peak (blue short-dashed) ahead of $\overline{T}_b$ its contribution to the daily main precipitation is insufficient to cause $\bar{r}$ to leap ahead of the MJO envelope.

The situation over New Guinea (panel (d)) is quite similar. Again, $\overline{T}_b$ peaks in the same phase over land as over ocean, although again it could be argued that the peak over land is slightly earlier than over ocean, because $\overline{T}_b$ over land appears to peak between phases 4 and 5. Over ocean the diurnal cycle peaks in phase 4 or 5, which is not so far ahead of the $\overline{T}_b$ envelope as in the other domain, but again we see that $\bar{r}$ has a clear peak in phase with $\overline{T}_b$. The ocean-based diurnal cycle is too weak to cause the daily mean precipitation to precede the MJO's OLR envelope. Over land the diurnal cycle does peak well ahead of $\overline{T}_b$, in phase 3, and $\bar{r}$ also precedes $\overline{T}_b$, clearly peaking in phase 4. Again, the strength of the diurnal cycle is enough to cause the daily mean precipitation to lead the OLR envelope, but in this case not to the extent that $\bar{r}$ and r_d are in phase. However, the same phenomenon as over domain (a) is still apparent here.

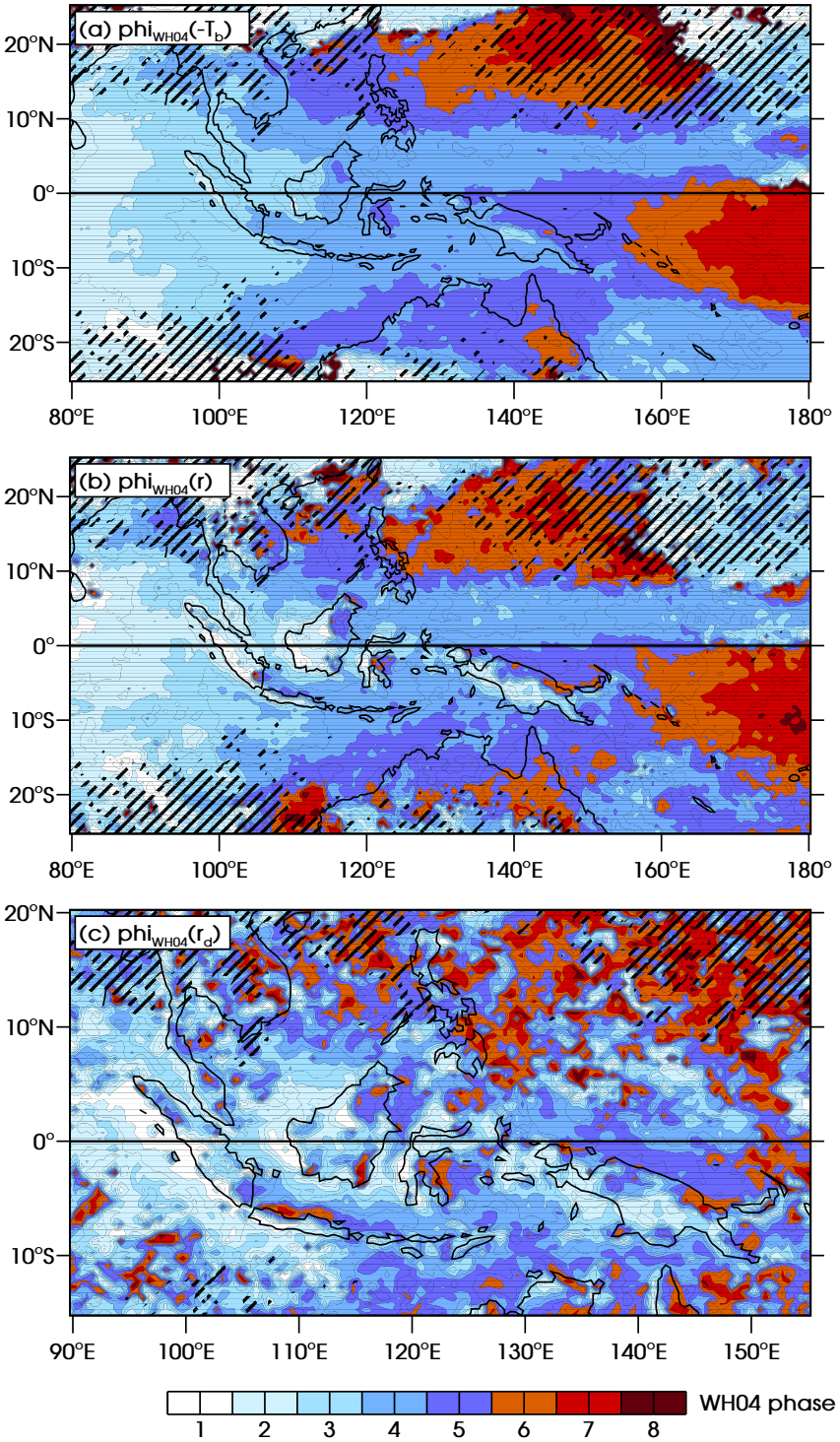

Figure 5.12: Phase of the "MJO harmonic" (see section 5.5.2) of: (a) daily mean negative brightness temperature $-\overline{T}_b$ (from TRMM 3G01); (b) daily mean precipitation $\overline{r}$ (from TRMM 3B42HQ); (c) diurnal amplitude of precipitation r_d (also from TRMM 3B42HQ). The phase is measured in MJO phases as defined by WH04. Black hatching indicates regions of low variability of the diurnal cycle during the MJO, defined as the anomaly in figure 5.2 being below 1 mm day^{-1} for all eight WH04 phases.

5.5.2 Phase of the MJO harmonics

We now introduce *MJO harmonics*, which will be used to quantify MJO phase lags at each grid point. We create separate climatologies for each of the eight WH04 phases for some variable, just as in figures 4.11, 4.12 and 5.2. These eight maps form a time series, since they describe successive phases of the MJO cycle. We compute harmonics of this time series for each grid point, referring to the fundamental harmonic as the "MJO harmonic". The amplitude of the MJO harmonic describes how much the variable in question changes as the MJO evolves while the phase of the MJO harmonic (ϕ_{WH04}, measured in WH04 phases) tells us the stage of the MJO at which the maximum value of the variable occurs, where the MJO is now modelled as a single, pure sine wave. The phase of the MJO harmonic is not required to be an integer value; it varies continuously in the range $0.5 \leq \phi_{\mathrm{WH04}} \leq 8.5$, and the phase is periodic so these end points are equivalent. The amplitudes of the semi-MJO and higher-frequency harmonics were always found to be much smaller than the amplitude of the MJO harmonic (not shown here). This technique is an alternative to the approach of Sperber et al. (1997), in which the eastward propagation of the active MJO was plotted by picking out for each grid point, from lagged correlation maps, the day on which there is the strongest correlation between the data and a previously-computed MJO index.

For example, the phase of the MJO harmonic of negative brightness temperature ($\phi_{\mathrm{WH04}}(-\overline{T}_b)$; figure 5.12a) shows when the MJO is most active, since negative $\overline{T}_b$ anomalies correspond to enhanced convection. There is a progression of the active MJO envelope from west to east, as seen earlier in figure 4.11. The MJO is most active over the Maritime Continent during phases 3 to 5. The inter-tropical convergence zone (ITCZ) and South Pacific convergence zone (SPCZ) extend eastwards and south-eastwards respectively from the centre of the Maritime Continent region, and are visible here since they are most active ahead of when their immediate surroundings are most active.

The amplitude of the MJO harmonic of $\bar{r}$ is shown in figure 5.13b and the phase of the harmonic in figure 5.12b. The amplitude of the variation in $\bar{r}$ is generally large over the ocean within the Maritime Continent; over land it tends to be small except for regions where the diurnal cycle is strong (see figure 4.6a). $\bar{r}$ generally has the same WH04 phase as $-\overline{T}_b$ to the west of the Maritime Continent, but over the major islands such as Sumatra, Borneo and New Guinea $\bar{r}$ tends to peak earlier than $-\overline{T}_b$ in the MJO. Thus, the precipitation appears

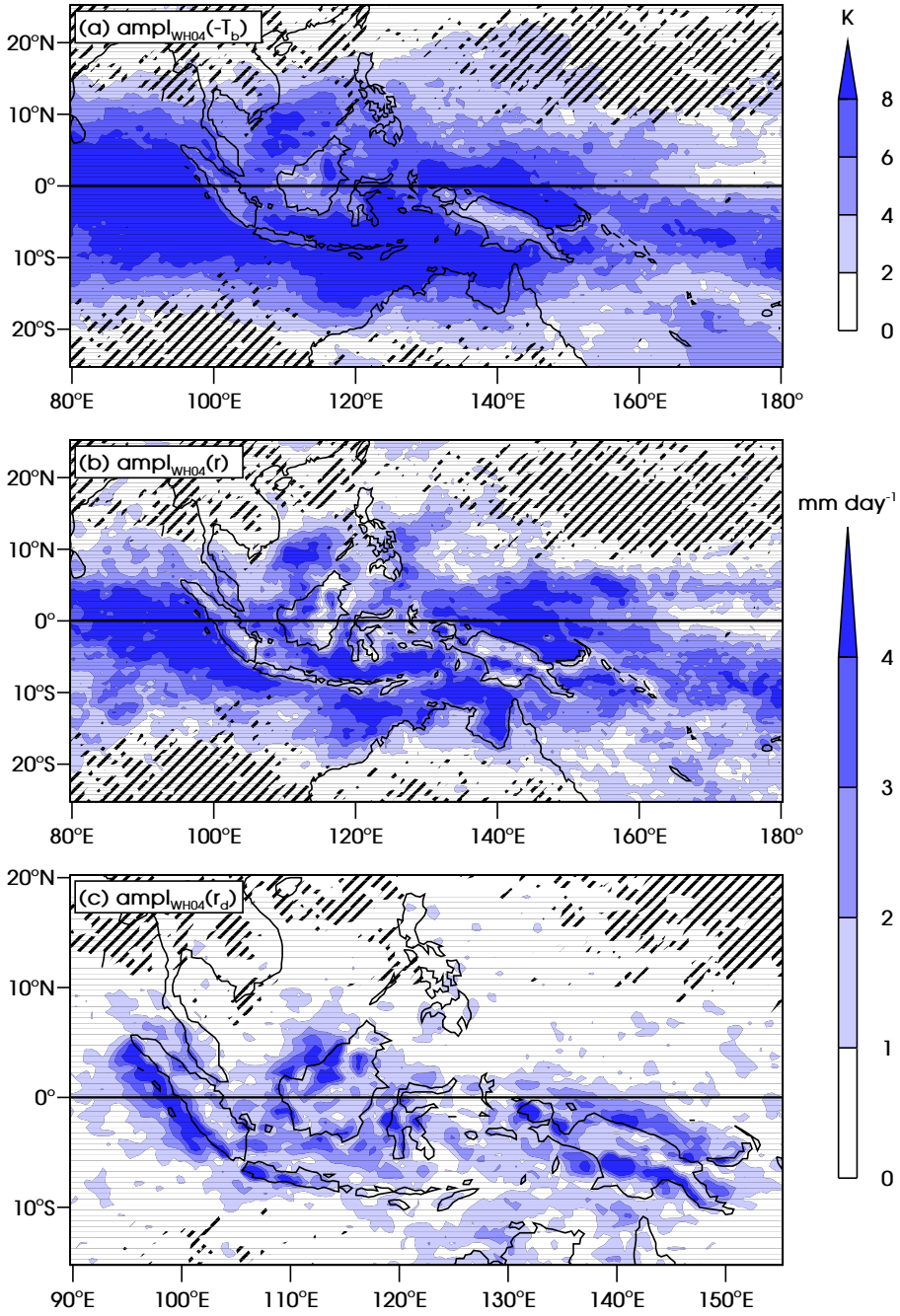

Figure 5.13: Amplitude of the MJO harmonic of: (a) daily mean brightness temperature $\overline{T}_b$ (from TRMM 3G01); (b) daily mean precipitation $\overline{r}$ (from TRMM 3B42HQ); (c) diurnal amplitude of precipitation r_d (also from TRMM 3B42HQ). Black hatching is used as in figure 5.12.

to leap ahead of the brightness temperature signal, and has already begun to diminish again by the time the most active $-\overline{T}_b$ does arrive.

Figure 5.13c shows the amplitude of the MJO harmonic of r_d and figure 5.12c shows the phase $\phi_{\mathrm{WH04}}(r_d)$. Note that the amplitude is small over most of the ocean, but over land and regions where nocturnal offshore propagation is

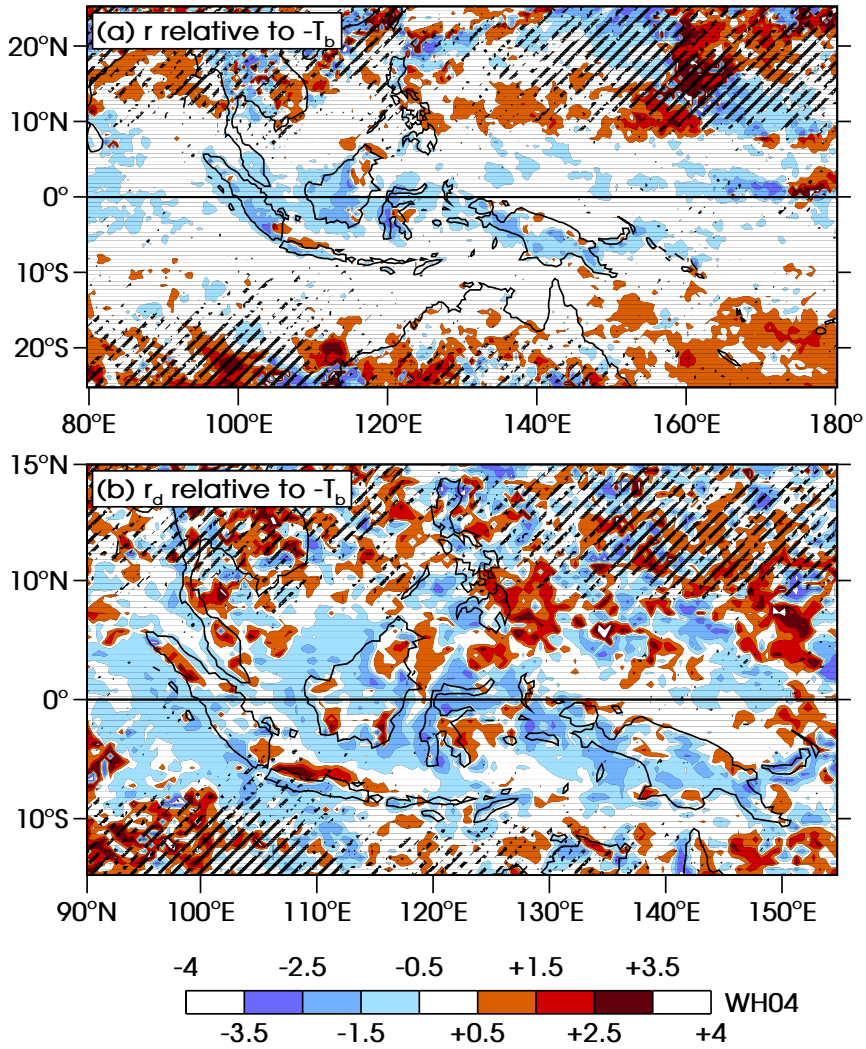

Figure 5.14: MJO phase lags (see section 5.5.2): (a) $\Delta\phi\left(-\overline{T}_b, \bar{r}\right)$ (i.e., figure 5.12b minus 5.12a); and (b) $\Delta\phi\left(-\overline{T}_b, r_d\right)$ (5.12c minus 5.12a). As in figure 5.12, the scale is measured in MJO phases as defined by WH04. If $\Delta\phi\left(-\overline{T}_b, \bar{r}\right)$ is positive (negative) then the maximum in $\bar{r}$ lags (leads) the maximum in $-\overline{T}_b$, and similarly for $\Delta\phi\left(-\overline{T}_b, r_d\right)$. Black hatching is used as in figure 5.12.

strong the amplitude is very similar to that of $\bar{r}$. As suggested in section 5.4.2 in reference to figure 5.2, there is no clear eastward propagation, as there is for $\phi_{\mathrm{WH04}}(-\overline{T}_b)$ and $\phi_{\mathrm{WH04}}(\bar{r})$. A visual comparison of figures 5.12b and c shows that $\bar{r}$ and r_d tend to have the same WH04 phase over the land of the Maritime Continent. Although $\phi_{\mathrm{WH04}}(r_d)$ shows much less spatial coherence than figures 5.12a and b in some regions, the spatial coherence is still strong over and around the land, which is where the diurnal cycle is strongest (see figure 4.6a).

As an improvement on the qualitative comparisons of ϕ_{WH04} made above, we can quantify relative MJO phases. For example, if variable X has its maximum at

WH04 phase 4.0 and variable Y has its maximum at WH04 phase 6.0, we define the MJO phase lag of Y relative to X as $\Delta\phi(X,Y) = \phi_{\mathrm{WH04}}(Y) - \phi_{\mathrm{WH04}}(X) = +2.0$. That is, Y lags X by 2.0 WH04 phases or a quarter of an MJO cycle.

Over most of the ocean, $-\overline{T}_b$ and $\bar{r}$ are in phase through the MJO cycle, since $\Delta\phi\left(-\overline{T}_b, \bar{r}\right) \approx 0$ (figure 5.14a). This supports the canonical view, that OLR is a good proxy for precipitation. The exception over ocean is the ITCZ at about 5°N, extending from 135°E to the eastern edge of the domain, where $\Delta\phi \approx -1$ so $\bar{r}$ leads $-\overline{T}_b$ by about 1 WH04 phase. Over the islands of the Maritime Continent, $\Delta\phi\left(-\overline{T}_b, \bar{r}\right)$ is also approximately -1 almost everywhere. Hence, over the land, where the diurnal cycle is strong, the view that OLR is a good proxy for precipitation breaks down. The daily mean precipitation occurs about 1 WH04 phase (one eighth of an MJO cycle, typically about 6 days) ahead of when the most active MJO envelope arrives as observed in infra-red brightness temperature.

We now compare this picture with that of $\Delta\phi\left(-\overline{T}_b, r_d\right)$ in figure 5.14b. As suggested in the discussion above of figures 5.12b and c, there is a strong similarity between the WH04 phase of $\bar{r}$ and r_d over the land of the Maritime Continent; we see here that both tend to lead $-\overline{T}_b$ by about 1 WH04 phase, for example over the south-west coast of Sumatra and the whole southern half of that island, all but the east of Borneo, and most of New Guinea. Over ocean, far from land, the diurnal cycle is weak and any changes to it during the MJO tend to be incoherent.

5.6 Discussion

In the previous section we compared the relative MJO phases of $\overline{T}_b$, $\bar{r}$ and r_d, and found that in the Maritime Continent the land-based precipitation signals jump ahead of the normal large-scale MJO envelope (section 5.5.1); and that the precipitation signals over land jump ahead of the OLR signal over land, so that OLR can no longer be considered a good proxy for rainfall (section 5.5.2). We now consider possible mechanisms for these phenomena.

5.6.1 Why does the diurnal cycle lead the main MJO envelope?

We have seen that the diurnal cycle is strongest over land about 1/8 of an MJO cycle (about six days – or, equivalently, 2000 km) ahead of the arrival of the active MJO envelope. The land diurnal cycle is set up by a land-sea temperature contrast as insolation heats the land and water at unequal rates (section 2.2). It is during the active phase of the MJO that the sky is the most cloudy, so incoming solar radiation flux at the surface is at a minimum. One possible mechanism which suggests itself for the observed MJO phase lag is that during the active phase of the MJO the diurnal cycle is suppressed slightly by the low level of insolation, and that the diurnal cycle precedes the most active part of the MJO because that is when the balance between convective activity and cloudiness allows the strongest over-land convection to occur. However, were this the case we would expect to see a double-peak in the diurnal amplitude, with one peak before the most active MJO and one after it. Note that evidence for such a double-peak exists for other variables, for example latent heat flux from the ocean (Batstone et al., 2005). There is no evidence for such a double-peak in the diurnal amplitude anomalies in figure 5.2, and the fact that the semi-MJO harmonic and all higher-frequency harmonics have relatively small amplitudes (as mentioned in section 5.5.2) suggests that the diurnal amplitude anomalies are roughly sinusoidal with only one peak and one trough per MJO cycle. Therefore, this simple scheme fails to predict the observed MJO phase lags between $-\overline{T}_b$, $\bar{r}$ and r_d.

The regions of anomalous convection in the MJO propagate eastwards not by advection of the numerous convective systems therein but by priming the atmosphere to the east for further convection and shutting off convection to the west. The fact that the land-based Maritime Continent diurnal cycle peaks just to the east of the active MJO envelope but not to the west of it suggests that the diurnal cycle is being excited as part of the eastward-propagation mechanism of the MJO. There are existing theories of the propagation of the MJO based on large-scale equatorial wave dynamics (e.g., Hendon and Salby, 1994; Maloney and Hartmann, 1998; Matthews, 2000). We now propose a mechanism that is consistent with both our observations and these previously-proposed mechanisms.

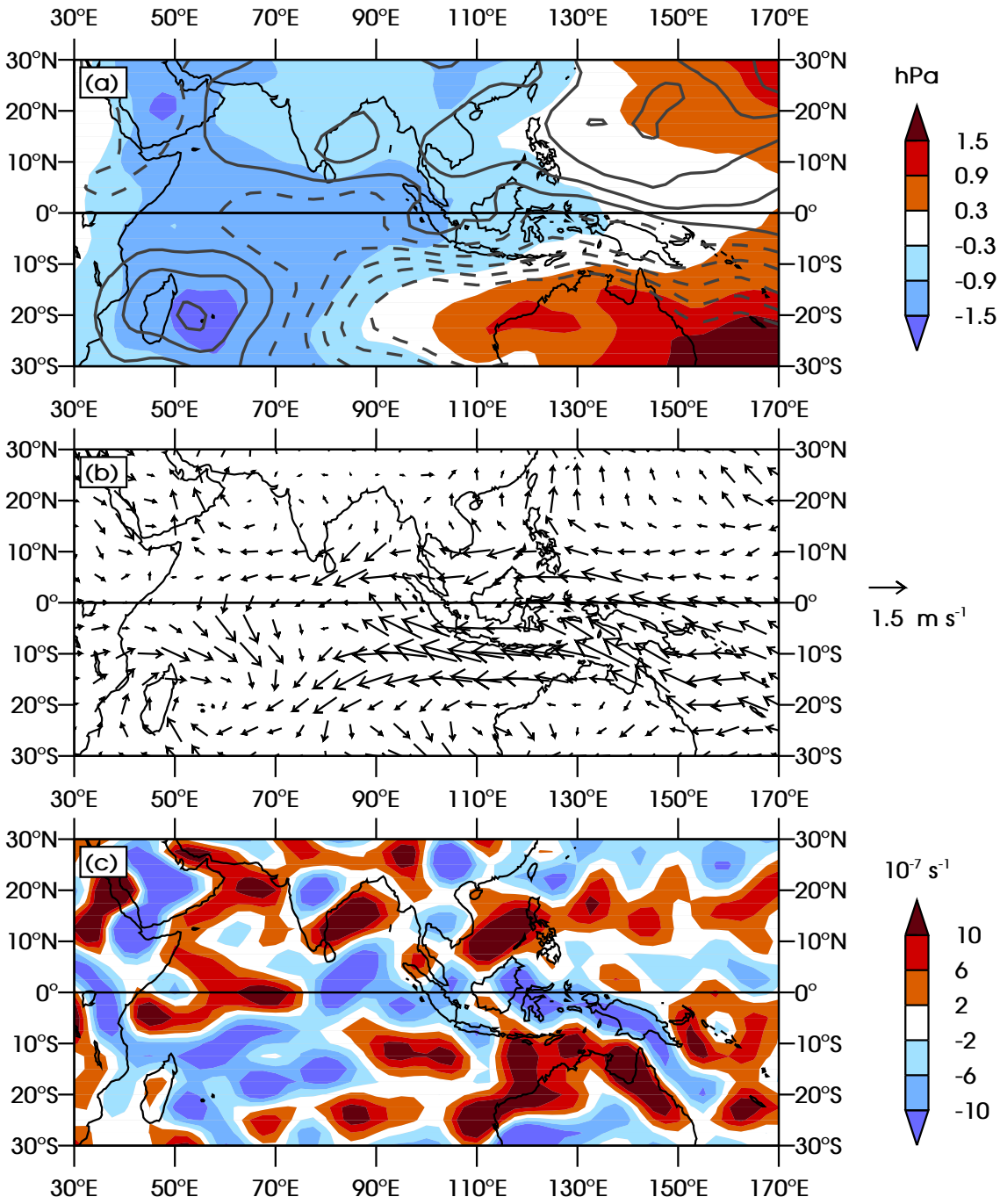

Figure 5.15: MJO phase 2 anomalies of: (a) mean sea level pressure with stream function contours at 1000 hPa; contours are drawn every 4×10^5 m^2 s^{-1} with the smallest contours at $\pm 2 \times 10^5$ m^2 s^{-1}; positive (negative) contours are solid (dashed); (b) wind at 1000 hPa (regridded to 5° resolution for clarity); (c) divergence at 1000 hPa. All data are from the NCEP-DOE Reanalysis 2.

5.6.2 MJO propagation and diurnal cycle excitation by equatorial wave dynamics

Figure 5.15 shows the anomalies in WH04 phase 2 of (a) mean sea level pressure, (b) wind at 1000 hPa and (c) horizontal divergence at 1000 hPa. The first panel also shows contours of stream function anomaly, ψ, at 1000 hPa. Wind and pressure data are taken from the National Center for Environmental Prediction-Department of the Environment (NCEP-DOE) Reanalysis 2. Horizontal divergence and ψ were calculated directly from the wind field at the full 2.5° resolution, but for clarity wind was regridded to 5° resolution before plotting.

The Matsuno-Gill model (Matsuno, 1966; Gill, 1980) of the dynamical atmospheric response to diabatic heating in the tropics has a solution in the form of equatorial Kelvin and Rossby waves, propagating eastwards and westwards respectively. These waves are bound by the equatorial waveguide – that is, their amplitude decays with meridional distance from the Equator;

$$\text{amplitude} \propto \exp\left[-\left(\frac{y}{y_0}\right)^2\right], \tag{5.14}$$

where y_0 is the e-folding width. For example, for an equatorial Kelvin wave $y_0 \approx 17°$ latitude either side of the Equator; note that the islands of the Maritime Continent are within this waveguide.

In phase 2 the active MJO envelope is over the Indian Ocean; its eastern edge is just reaching the Maritime Continent (see figure 4.11). Figure 5.15a shows a tongue of low pressure extending eastwards along the Equator from the region of anomalous heating, weakening to the east. This is consistent with an eastward-propagating equatorial Kelvin wave. There are also regions of low pressure extending north-westwards and south-westwards from the Equator, consistent with a westward-propagating equatorial Rossby wave. This matches the predicted pressure perturbation field in figure 1b of Gill (1980). The off-equatorial pressure troughs associated with the Rossby wave response to the active convection have a corresponding pair of ridges in pressure to the east, arising from the Rossby wave response to the previous suppressed MJO envelope, which in phase 2 is over the west Pacific Ocean (see Matthews, 2000). The anti-cyclonic flow associated with these regions of high pressure is seen around 120–140°E in the northern hemisphere and 80–100°E in the southern

hemisphere (figures 5.15a and b).

A reduction in the Coriolis force due to surface friction results in an ageostrophic component of the wind field into the equatorial pressure trough associated with the Kelvin wave. This results in a negative contribution to divergence from the meridional wind. Since the air is guaranteed to be moist over the warm oceans, this is an example of frictional moisture convergence (Hendon and Salby, 1994; Maloney and Hartmann, 1998). This occurs throughout the propagation of the MJO envelope. Furthermore there is an easterly wind anomaly on and around the Equator, due in part to the wind flowing down the pressure gradient associated with the Kelvin wave and in part to the anti-cyclonic vorticity associated with the Rossby wave extending from the west Pacific. Over the Maritime Continent this leads to horizontal convergence of air on the eastern flanks of mountains, for example in east Borneo and north-east New Guinea, as the flow is blocked by topography. Thus, the effect of topography enhances the effect of frictional moisture convergence to give particularly strong convergence over the islands, as seen in figure 5.15c.

We saw in figure 4.11 that over the Maritime Continent itself the OLR anomaly in phase 2 is positive, indicating relatively clear skies. Therefore, the amount of shortwave radiation reaching the ground is enhanced, destabilising the atmosphere; the low thermal inertia of the land allows the usual diurnal cycle to occur. The result of the strong convergence of moist air due to the wave dynamics described in the previous paragraph is a tendency to sustain this diurnal cycle convection, so that on average over the land this phase of the MJO is more convectively active than climatology. It may be speculated that the Kelvin wave response to the oncoming active convection is more dominant in this effect than the Rossby wave from the departing suppressed convection, since the peak in the diurnal cycle is just 1 WH04 phase ahead of the active envelope but 3 phases behind the suppressed envelope.

This mechanism also explains why there is no double-peak in the amplitude of the diurnal cycle, as was suggested in section 5.6.1. Once the active envelope of the MJO has moved away from the Maritime Continent there are clear skies over the islands, causing the atmosphere to destabilise, but there is no longer the frictional moisture convergence to sustain any convection, because the wave dynamics argument presented above applies but with a sign change (not shown). A peak of high pressure extends eastwards along the equator, associated with a Kelvin wave forced by the negative heating anomaly over the Indian Ocean, and there are regions of off-equatorial low pressure associated

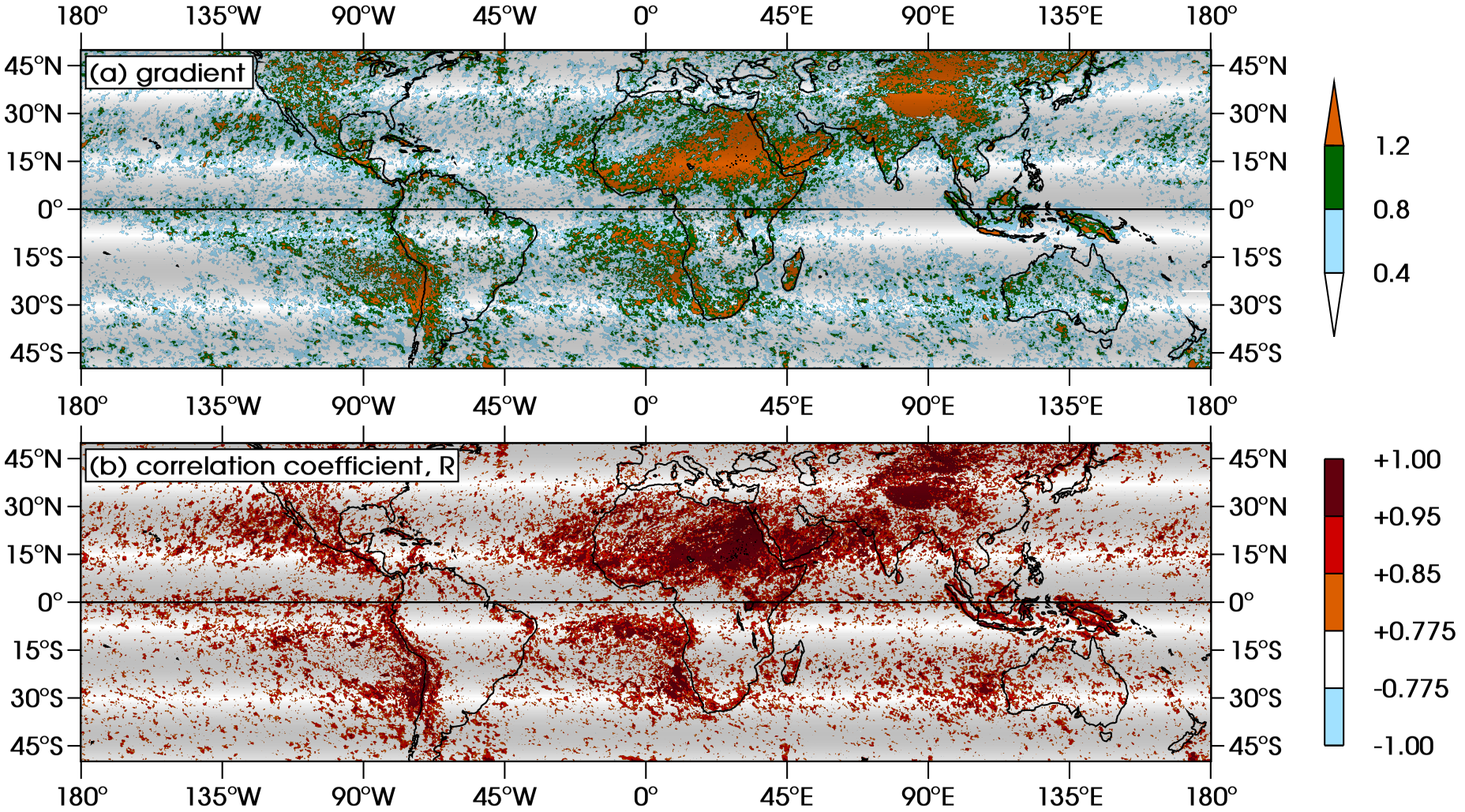

Figure 5.16: As figure 5.8 but for the whole of the TRMM 3B42HQ domain.

with the active envelope which is now over the west Pacific Ocean. These result in anomalous westerly flow near the Equator, and frictional moisture divergence as a reduction in Coriolis force causes air to flow out of the equatorial pressure peak, giving rise to a positive contribution to divergence from the meridional winds. Hence, the wave dynamics act to suppress the diurnal cycle when the active convection has passed through.

5.7 Extension to the whole tropics

In section 5.4.4 we investigated the relationship between the daily mean and diurnal cycle of precipitation over the Maritime Continent area by performing linear regression between the two. We now investigate whether similar relationships occur elsewhere in the tropics. Figure 5.8 shows the gradient and correlation coefficient for diurnal amplitude against daily mean precipitation, over the whole domain covered by the TRMM 3B42HQ data set. It is immediately clear that the strong relationship between the two variables is not confined to the Maritime Continent. Over the Sahara and the northern part of sub-Saharan Africa, off the west coast of southern Africa, the Andes and off the west coast of South America are all examples of regions where there is a very strong correlation, suggesting that a diurnal cycle accounts for almost all the daily mean precipitation.

However, it must be remembered that over some of these regions the daily mean and diurnal cycle are extremely small. For example, over the Sahara the mean daily precipitation is only around 0.15 mm day^{-1}, and rain events are both infrequent and sporadic. The amplitude of the diurnal cycle is shown in figure 5.17a, and compared with the Maritime Continent and other parts of the world where the diurnal cycle is prominent, the diurnal cycle over the Sahara is negligible. Therefore, not every region of high gradient and/or correlation in figure 5.16 can be considered significant. Indeed, the Maritime Continent is one of very few locations indeed where the diurnal amplitude and daily mean are correlated, and the diurnal amplitude is non-negligible. Other such locations include Madagascar which, notably, is a tropical island similar in size to the largest Maritime Continent islands; Sri Lanka, also a tropical island; Lake Victoria (centred on 1°S, 33°E) which is large enough that the land-lake temperature contrast sets up an onshore-offshore breeze circulation, as seen in figure 4.9; the southern coast of western Africa (Liberia, Côte d'Ivoire and

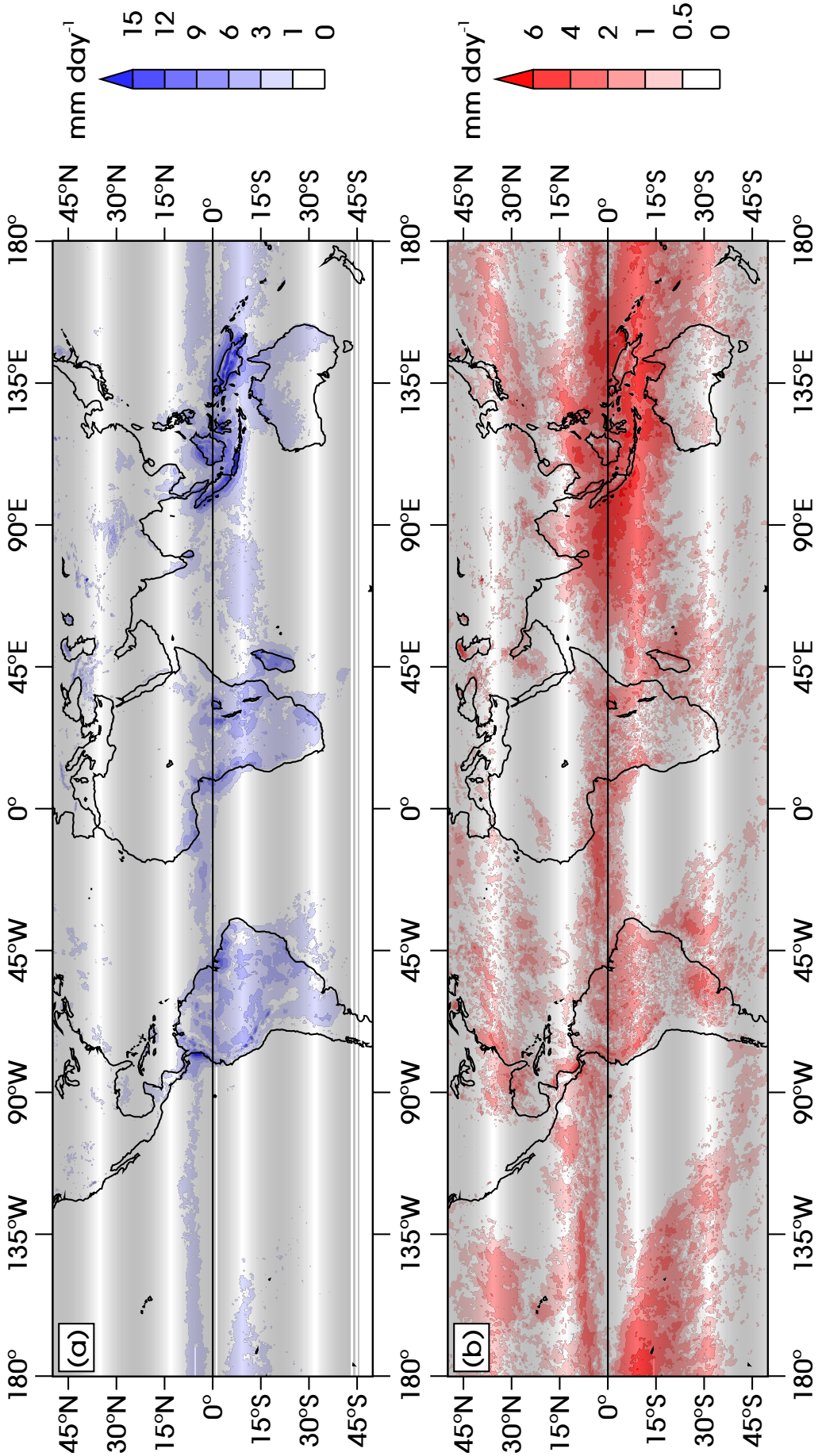

Figure 5.17: Amplitude of (a) the diurnal harmonic of precipitation (r_d; as figure 4.6a) and (b) the MJO harmonic of daily mean precipitation ($\bar{r}$; as figure 5.13b), but for the whole of the TRMM 3B42HQ domain.

Ghana); and the western coast of Africa around 5°–15°S (Angola). The linear regression was performed for composites of each of the eight WH04 phases, but it is very important to note that this does not necessarily mean the MJO is responsible for the differences in daily mean and diurnal amplitude across the eight composites. Due to the inherent variability in the precipitation data the eight composites will not be exactly the same, even if the MJO has no systematic effect on precipitation. Even if a correlation between daily mean and diurnal amplitude shows up in figure 5.16b, we can make a connection with the MJO only if the variability is strong among the eight composites. Therefore, we must also consider the correlation in conjunction with figure 5.17b, the amplitude of the MJO harmonic of daily mean precipitation. Over the Maritime Continent, as we know, the MJO variability is strong so we were justified throughout this chapter in attributing the diurnal cycle interaction to the MJO. To find objectively those regions where both the diurnal cycle and MJO variability are strong, we reproduce figure 5.16 but mask out those regions where the diurnal cycle amplitude is less than 3 mm day^{-1} in figure 5.17a and where the MJO amplitude is less than 2 mm day^{-1} in figure 5.17b. This ensures that the Maritime Continent is retained, and any other regions where the magnitude of the diurnal cycle and MJO are at least as strong as they are over the Maritime Continent. The result is shown in figure 5.18, with masked regions plotted in grey. Lake Victoria and Sri Lanka are unmasked, and both (especially Lake Victoria) have a strong correlation and gradient. Hence, these locations appear to exhibit a similar scale interaction to that observed over the Maritime Continent in this chapter. This may be of particular importance for the forecasting of storms over Lake Victoria. Recent model studies have attempted to forecast dangerous conditions for fishermen there (Chamberlain et al., 2014), since frequent storms over the lake are often life-threatening.

5.8 Conclusions

In this chapter, 15 boreal winters of high-resolution brightness temperature and precipitation data were used along with the WH04 MJO index and harmonic analysis to investigate the state of the diurnal cycle during each phase of the MJO. It was found that the amplitude r_d of the diurnal cycle changes by as much as 10 mm day^{-1} over the land in opposite phases of the MJO cycle. The offshore propagation of convectively-coupled gravity waves was also investigated in each MJO phase. There is significant variability in the speed of the propagating waves

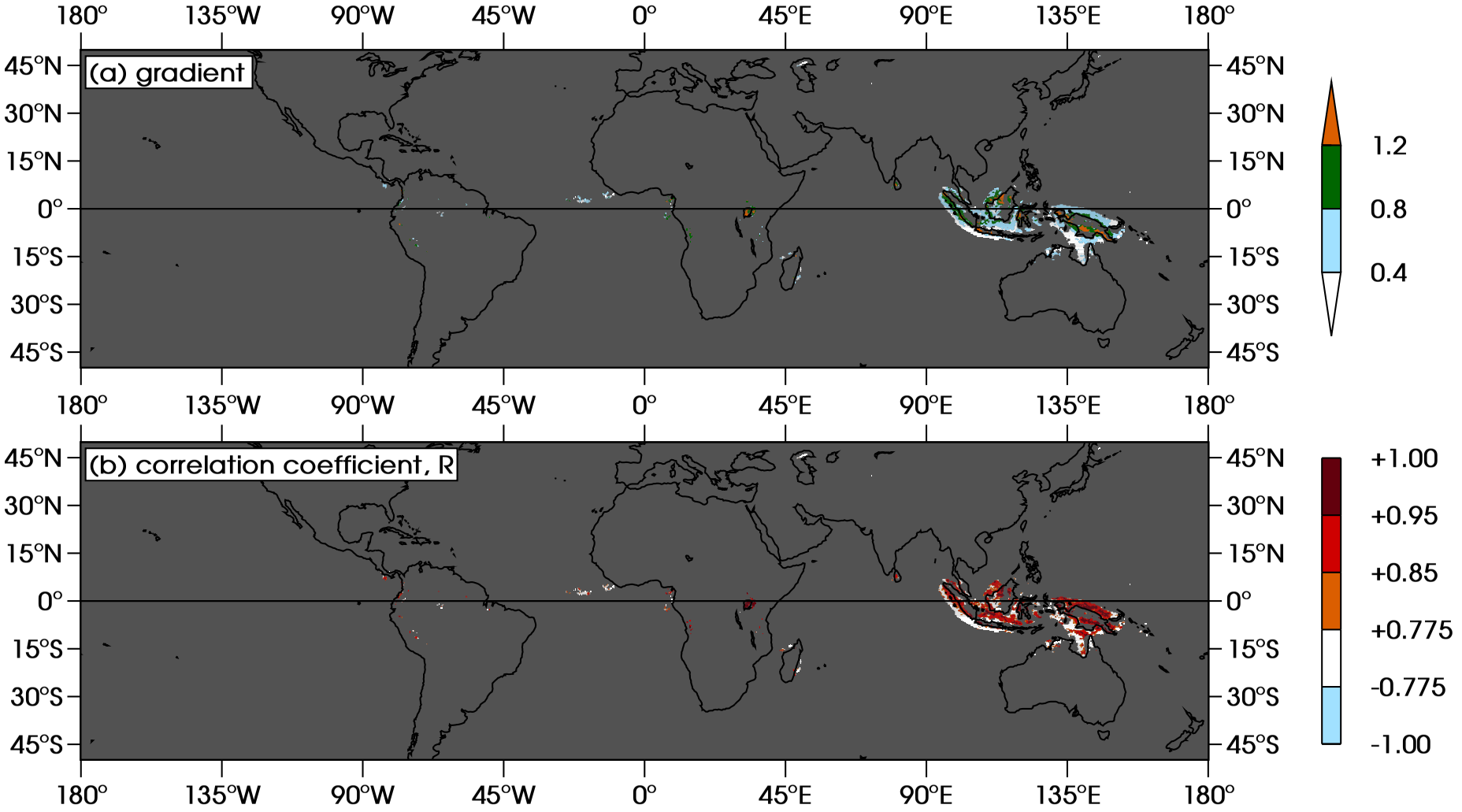

Figure 5.18: As figure 5.16 but with regions of weak diurnal cycle (< 3 mm day^{-1}) or weak MJO (< 2 mm day^{-1}) masked out in grey (see figure 5.17).

throughout the MJO off the north-west of Borneo, the north of New Guinea and, especially, off the south-west of Sumatra (where the range in propagation speeds is 2.7 m s^{-1} to 6.6 m s^{-1}). This is consistent with the changes in heating profiles, static stability and background wind field during the MJO's life cycle. In the active phase the gravity wave modes triggered may be of lower order and, therefore, faster. Also in the active phase, convection restores stability to the atmosphere, which is consistent with faster propagation. In the suppressed phase the atmosphere goes through a process of becoming less stable, consistent with the gravity wave speed being slower. Off the coasts of Sumatra and Borneo, where there is a sizeable westwards component to the horizontal propagation, the propagation speeds tend to be faster when there are easterly anomalies in the upper troposphere, consistent with Doppler shifting of the waves. It was also observed that off the coast of Borneo, when the propagation extends a long way over the ocean, the waves appear to speed up as they propagate.

It was found that the diurnal amplitude r_d over the Maritime Continent is greatest shortly before the large-scale active MJO envelope arrives, with a lead time of a single WH04 phase or one-eighth of an MJO cycle, approximately six days (see figure 5.11). Furthermore, by computing *MJO harmonics* it was shown that OLR does not act as a good proxy for the precipitation over the land; the brightness temperature does not peak until the large-scale MJO envelope arrives, even though the precipitation over the land is strongest 1 WH04 phase before that (see figure 5.14). This could be because the large-scale precipitation tends to be longer-lived than diurnal precipitation, so the convection is deeper, associated with a stronger OLR signal. It is possible that the effect is accentuated by the absence of extensive cirrus anvils from the diurnal cloud systems, which are present in the large-scale systems. In section 2.2.3 it was stated that Slingo et al. (2004) found a decoupling between OLR and precipitation over Africa in a climate model, and the authors of that study speculated as to whether this was a real phenomenon. Here, the same effect has been found in observations over the Maritime Continent, suggesting that this decoupling may not have been just an artefact of the model convection scheme.

When the diurnal amplitude peaks, over land it is so strong that the diurnal cycle almost entirely accounts for the daily mean precipitation; in regions where there is a strong diurnal cycle about 80% of the MJO precipitation signal is accounted for by changes in the diurnal amplitude. Therefore, over the land to the east of the main MJO envelope the MJO precipitation signal is just the diurnal cycle of precipitation. Hence, there is a scale interaction in which the

large-scale environment provided by the MJO modulates the diurnal cycle, and the strength of the diurnal cycle determines the structure of the diagnosed MJO. A mechanism was proposed that is consistent with previous theories that describe the propagation of the MJO in terms of the equatorial wave response to diabatic convective heating. As the active MJO envelope just reaches the Maritime Continent the eastward-propagating equatorial Kelvin wave from the active region and the westward-propagating equatorial Rossby wave from the previous suppressed region combine to induce near-equatorial easterly anomalous flow. The influence of topography enhances the effect of frictional inflow to the pressure trough associated with the Kelvin wave. Together they provide frictional moisture convergence which is able to sustain a strong diurnal cycle over the land just to the east of the oncoming convection. When the MJO suppressed envelope is just reaching the Maritime Continent the reverse is true, and frictional moisture divergence acts to suppress the diurnal cycle. This is all in contrast to MJO propagation over open ocean, where the absence of land means there is no strong diurnal cycle to excite, and the MJO propagation is smoother.

It is emphasised that what we have shown here is that the MJO dynamics modulate the diurnal cycle, and that this modulation is responsible for a particular feature of the diagnosed MJO. It may be that this modulation of the diurnal cycle somehow feeds back onto the MJO dynamics themselves, perhaps affecting the mechanism of the MJO's propagation over the Maritime Continent, but any such effect is beyond the scope of this observational study and could better be investigated in modelling experiments.

The two-way scale interaction between the diurnal cycle and the MJO has consequences for forecasting precipitation in the region and for the simulation of the MJO in GCMs. In principle the organised structure and predictable propagation of the MJO give us a rare opportunity in numerical weather prediction to forecast, for example, precipitation and the large-scale wind field several weeks ahead. This compares with the theoretical limit for synoptic systems of one or two weeks, arising from the chaotic nature of the solutions to the governing equations. In chapter 7 we investigate whether the land-based diurnal cycle of precipitation is excited at the correct stage of the MJO in a GCM.

By extending the analysis to the whole of the tropics, we have seen that a similar scale interaction occurs over a small number of other regions, namely over Lake Victoria, Madagascar, and parts of the coastlines of Angola and Brazil. Of course, the physical mechanism over those regions may well differ from that

proposed for the Maritime Continent, but this is not investigated here.

Chapter 6

Representation of the MJO in HiGEM

6.1 HiGEM

Having considered the scale interaction between the MJO and the diurnal cycle in observations (chapter 5), we now wish to investigate whether the same interaction is well simulated in a state-of-the-art model. We have seen that the interaction is sufficiently strong to have a major effect on precipitation over the Maritime Continent and the propagation of the MJO itself. Given that model biases over the Maritime Continent can lead to further errors elsewhere, it is important that models represent the scale interaction accurately.

The model used for this investigation will be the High-resolution Global Environmental Model (HiGEM). First, in this chapter, we ascertain whether HiGEM simulates a realistic MJO before investigating the scale interaction with the diurnal cycle in chapter 7.

HiGEM1.2, the version of the model used in this study (hereafter referred to as just HiGEM), is described in detail by Shaffrey et al. (2009). Some key details

Resolution	HadGEM1	HiGEM1.2
Horizontal (atmos.)	1.25° lat × 1.875° lon	0.83° lat × 1.25° lon
Vertical (atmos.)	38 levels up to 39 km	38 levels up to 39 km
Horizontal (ocean)	1° lat × 1° lon	$\frac{1}{3}$° lat × $\frac{1}{3}$° lon
Vertical (ocean)	40 levels down to 5.5 km	40 levels down to 5.5 km
Temporal	30 minutes	20 minutes

Table 6.1: Spatial and temporal resolutions of HadGEM1 and HiGEM1.2.

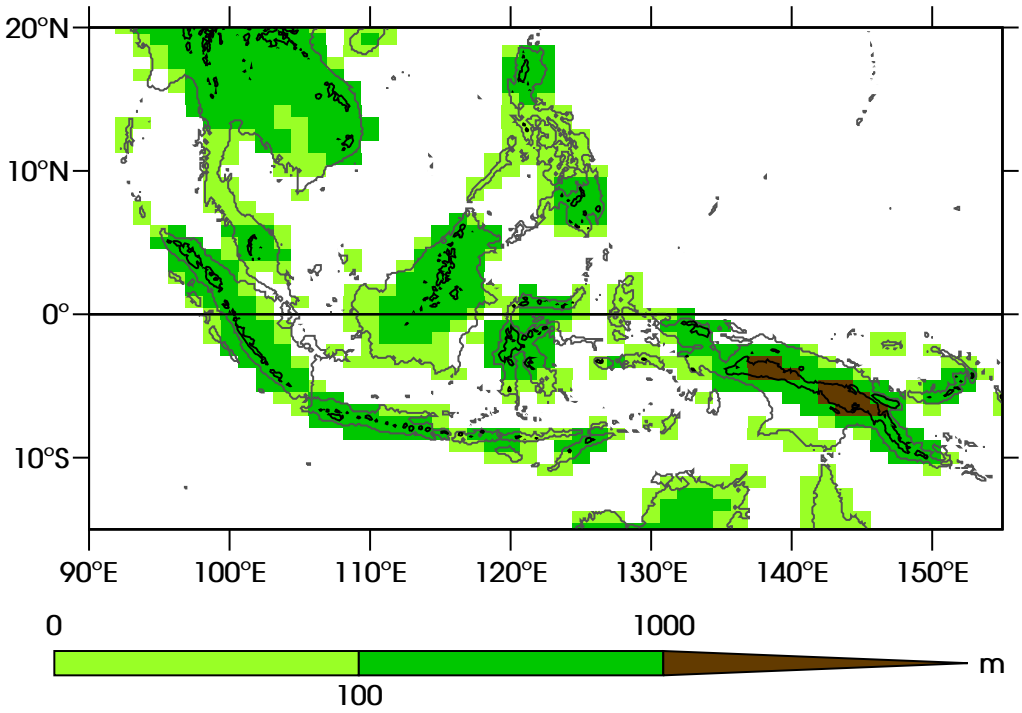

Figure 6.1: Orography of the Maritime Continent in HiGEM, in metres (coloured pixels). Orography from the GLOBE data set is overlaid for comparison (0 m contour in grey, 1000 m contour in black).

are summarised here. HiGEM is based on version 1 of the UK Met Office Hadley Centre model (HadGEM1; Martin et al., 2006; Ringer et al., 2006) with improved horizontal and temporal resolution (see table 6.1) and alterations to, amongst other things, the moisture diffusion scheme, surface flux calculations, snow-free sea ice albedo, and the treatment of run-off on frozen soil. Integrations of HiGEM show many improvements compared with HadGEM1, including the sea surface temperature and representation of air-sea coupled processes in the tropical Pacific Ocean.

The orography used in HiGEM is plotted for the Maritime Continent domain in figure 6.1. Although the resolution is high by the standards of climate models, it is still very coarse compared with the scale of coastal features of the Maritime Continent islands. In section 2.2.2 it was explained that diurnal convection can be triggered as a result of convergence forming onshore of a convex coastline during the day and offshore of a concave coastline overnight. These coastal features are almost entirely unresolved by HiGEM. Also, many of the islands are joined together in HiGEM because the narrow straits between them cannot be resolved, so the land-sea breeze circulation is likely to be unrealistic. Although mountains over 1000 m above sea level exist throughout the Maritime Continent, HiGEM has land over 1000 m on New Guinea only. Elsewhere, this may

contribute to errors in the mountain-valley breeze circulation and, therefore, orographic rainfall. The representation of the diurnal cycle in the model will be shown in chapter 7.

The integration used for this study was a contribution to the decadal prediction part of the Coupled Model Intercomparison Project Phase 5 (CMIP5; Taylor et al., 2012), which appears in the Fifth Assessment Report (AR5) of the Intergovernmental Panel on Climate Change (IPCC). The run lasts from 1957 to 2016, initialised from a control run (a 120-year run using 1990s forcing throughout). Historical greenhouse gas and aerosol forcings were used up to the model year 2005, and representative concentration pathway 4.5 (RCP4.5; Moss et al., 2010) thereafter. RCP4.5 gives a change in radiative forcing relative to pre-industrial levels of +4.5 W m^{-2} in the year 2100; this is near the middle of the range of RCPs used in CMIP5 (the other pathways being RCP2.6, RCP6 and RCP8.5).

Since results will be compared with observations, we wish to use model output from the same era as TRMM. Hence, output from the model year 2000 onwards is used.

6.2 Existence of MJO-like variability

6.2.1 Hovmöller diagrams

By way of exploratory data analysis, we first consider a Hovmöller diagram of daily mean outgoing longwave radiation (OLR) in order to search for MJO-like events, in which positive and/or negative anomalies propagate eastwards over the warm pool on intra-seasonal time scales. The date range 1st May 2008 to 1st May 2009 is chosen as an example.

Figure 6.2a shows a Hovmöller diagram of OLR which has had the mean and first three harmonics of the annual cycle removed at each grid point, then has been averaged over the range 15°S–15°N. It is clear that the dominant variability is westward-propagating, occurring in particular to the east of the 120°E meridian. These anomalies, propagating in the wrong direction for the MJO and with a much higher frequency (a period of only a few days), are consistent with equatorial Rossby waves. There are, however, signs of eastward-propagating anomalies from December 2008 onwards which cover the entire domain, at a much slower speed. These positive and negative anomalies

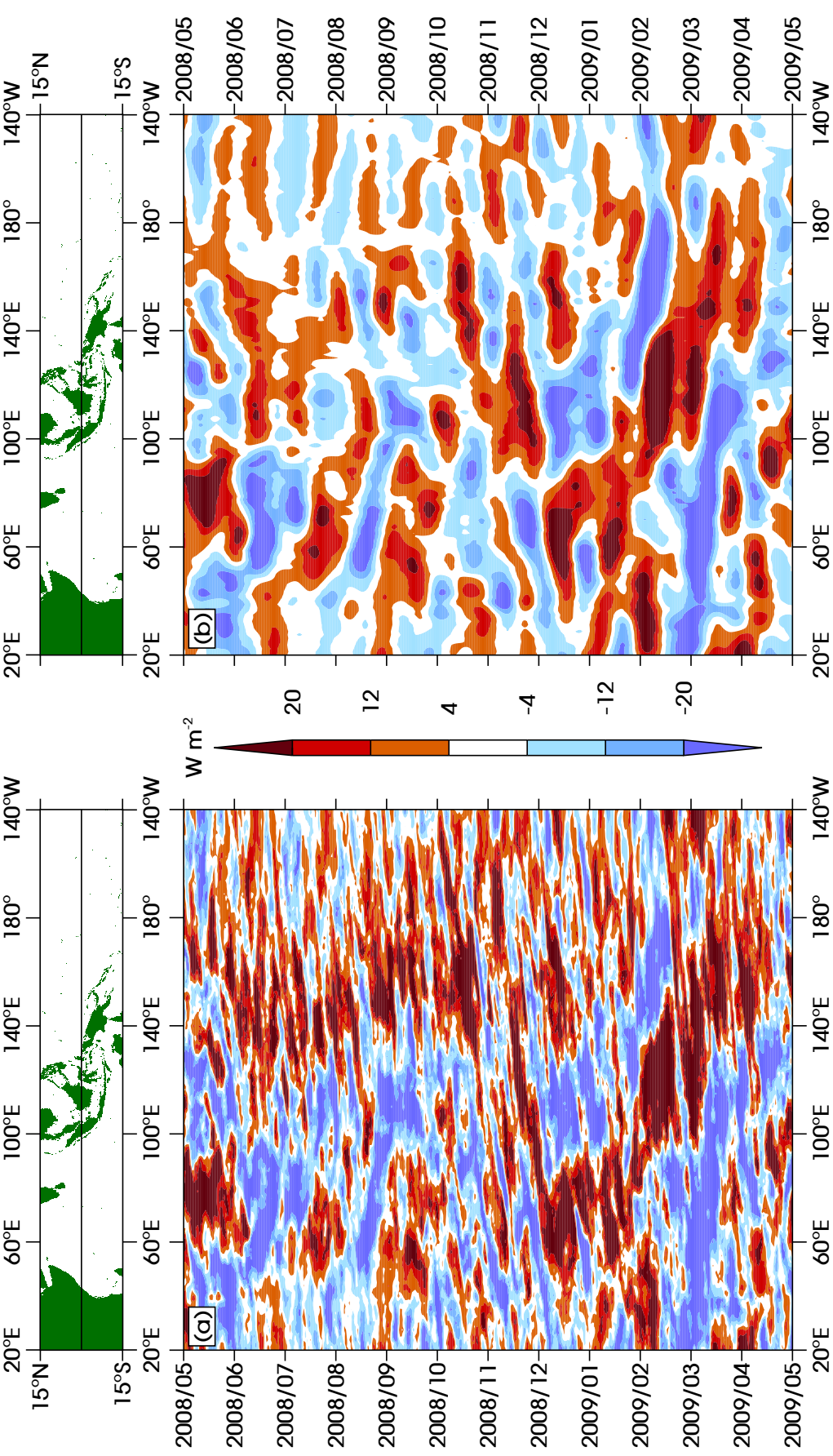

Figure 6.2: Hovmöller diagrams of OLR from HiGEM experiment xgwvg, for May 2008 to April 2009. (a) Mean and first three harmonics of the annual cycle removed; (b) as for (a), then passed through a 20–200-day bandpass Lanczos filter. In each case, the data were averaged over the latitude range 15°N to 15°S before plotting. A land mask, generated using the GLOBE topography data set at $0.11° \times 0.11°$ resolution, is shown for information.

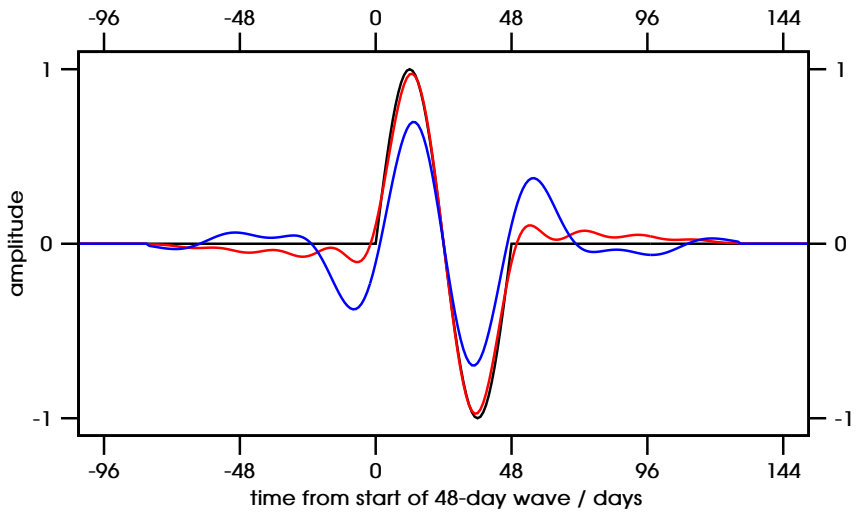

Figure 6.3: Single wavelength of a pure sine wave with period 48 days (black line) starting at t=0; result of passing this sine wave through a 30–70-day (blue) or 20–200-day (red) bandpass Lanczos filter with order $n = 120$. (After figure 1 of Matthews, 2000.)

have a period of around 40–50 days so the variability is on an intra-seasonal time scale, making them strong candidates for MJO-like events. There also appear to be eastward-propagating anomalies from May to about September or October 2008 with a period of about 30 days, although they tend to die out at about 130°E.

In order to make it easier to look for features like the MJO, a bandpass filter can be applied to remove variability that is not intra-seasonal. A 20–200-day bandpass Lanczos filter (Duchon, 1979) was used with order $n = 120$ (that is, 241 weights). Cut-off frequencies of 1/200 and 1/20 day^{-1} were chosen since they introduce far smaller errors than the 1/70 to 1/30 day^{-1} window that is often used in MJO analysis. This was demonstrated by Matthews (2000) by passing a single pure sine wave of period 48 days (a typical MJO period) through 20–200-day and 30–70-day bandpass Lanczos filters separately. The result is reproduced here in figure 6.3. The 30–70-day filter (blue line) introduces large spurious oscillations before and after the unfiltered wave (black); the corresponding errors in the 20–200-day filtered wave (red) are much smaller. Furthermore, the amplitude of the 30–70-day filtered wave is considerably smaller than the pre-filtered wave during its 48-day period, whereas the 20–200-day filtered wave loses almost no amplitude at all.

A Hovmöller diagram of the bandpass filtered OLR data is shown in figure 6.2b. The MJO-like variability beginning around the start of December 2008 is now much clearer. Clearly defined active and suppressed MJO envelopes propagate from the east coast of Africa right across the Indian

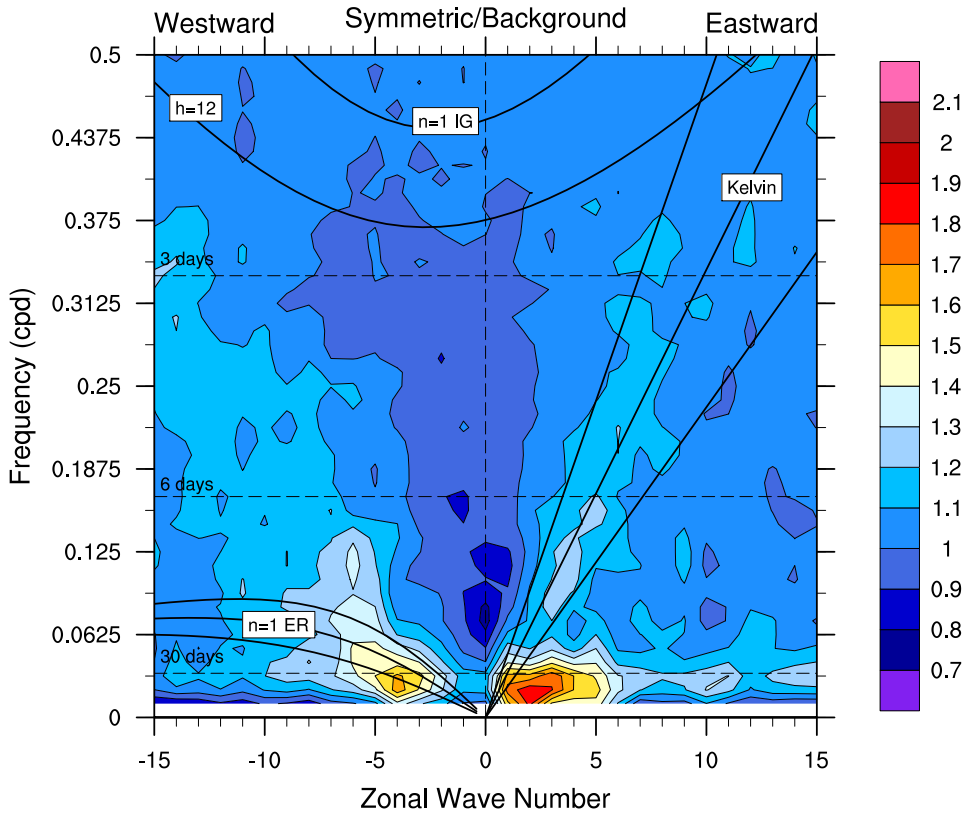

Figure 6.4: As figure 4.14 but for HiGEM: Wheeler-Kiladis diagram of the equatorially-symmetric part of daily mean OLR (wavenumber-frequency field summed over 15°S–15°N, divided by a background spectrum). See main text for more details of this plot, and section 4.6.2 for details of Wheeler-Kiladis diagrams.

Ocean and warm pool, into the western Pacific Ocean. There are also signs of eastward-propagating intra-seasonal variability, at roughly the same propagation speed, from May 2008 until around September or October of the same year. These anomalies tend to be weaker than in the propagating event starting in December, and they die out whilst propagating over the Maritime Continent, at around 120°–130°E. Their frequency is about 1/30 day^{-1}, which is higher than the frequency of the December event but still just within the frequency range that may be considered an MJO.

6.2.2 Wheeler-Kiladis diagram

The above case study indicates that HiGEM produces MJO-like OLR events, propagating eastwards along the equator on intra-seasonal time scales, but to know whether the model consistently produces such features we need to know how prevalent such variability is. Therefore, we consider a Wheeler-Kiladis diagram (see section 4.6.2) of the HiGEM output. As in figure 4.14b we consider

OLR_{sym}, the equatorially-symmetric component of the OLR field; spectral power is summed over the range 15°S–15°N and divided by a background spectrum. Data are used for the years 2000 to 2015. The power was averaged over 96-day windows which overlap by 65 days. The resulting wavenumber-frequency field is plotted in figure 6.4.

As in the reanalysis data there are equatorial Kelvin waves and equatorial Rossby waves clearly present. The spectral power associated with these waves has roughly the same strength as that in the reanalysis data. There is also a clear signal in the region representing the MJO, with frequency of less than about 1/30 cycles per day (cpd) and small zonal wavenumber propagating eastwards. However, this peak in spectral power is slightly lower than that in the reanalysis data. This is explained by the fact that the spectral power is more spread out, in a peak which has greater width in the wavenumber direction. In the reanalysis the peak ranged from about 0 to 2, and was centred on zonal wavenumber 1; in the model the peak ranges from close to 0 to about 5, and is centred on zonal wavenumber 2. Hence, the zonal structure tends to vary too much in the model, and on average the wavenumber tends to be too high. The frequency range covered by the MJO spectral peak is very nearly the same as in the reanalysis, but does extend slightly into higher frequencies (up to around 1/25 cpd in the model as opposed to 1/30 cpd in the reanalysis).

6.2.3 Wheeler-Hendon analysis

The Hovmöller and Wheeler-Kiladis diagrams above show that HiGEM does simulate eastward-propagating anomalies of OLR along the equator on the correct time scales, over the correct longitude domain and with roughly the correct zonal wavenumber. However, we have not yet seen the spatial structure of these anomalies. Do they look like the real-life MJO envelopes as they propagate? To investigate this, we now carry out the same analysis used by Wheeler and Hendon (2004; WH04) for generating their Real-time Multivariate MJO (RMM) indices (see section 4.4). The WH04 analysis is based on empirical orthogonal functions (EOFs), an analysis technique frequently used in meteorology and oceanography. The principle is to generate a small number of functions (in this case, two) onto which data can be projected, so that the data set can be expressed in terms of just two variables (known as the principal components (PCs) of the EOFs) whilst retaining as much variability as possible. Not only does this allow the data to be expressed in an efficient,

compact manner, but the EOFs are often found to correspond to modes of the system so they can also give valuable physical insights into the phenomena under investigation.

The WH04 analysis uses daily means of OLR, and zonal wind u at the 850 hPa and 200 hPa pressure levels (denoted here as u_{850} and u_{200}). To remove seasonal biases, for each of the three variables the mean and first three harmonics are removed at each grid point. Then, WH04 remove inter-annual variability (especially that due to ENSO) by a two-stage process. The first stage is to remove variability based on a particular measure of SST (known as SST1; Drosdowsky and Chambers, 2001). For simplicity, this step is neglected here; applying the WH04 analysis to reanalysis data without this step produced RMM time series which were very close to those found by WH04 (not shown), so this does not cause any significant errors. The second stage is to subtract, for each day, the mean of the previous 120 days. Although the removal of unwanted variability could be better achieved using a conventional filtering technique, WH04 wished their indices to be available in real time. (Filtering involves computing a weighted mean at each time-step t_0 using data from the time range $t_0 - n$ to $t_0 + n$, where the number of time steps n is the order of the filter, so the indices could not be computed until n days after t_0.) In order to recreate WH04's analysis as closely as possible we use the method of removing the 120-day mean, although the indices derived using the filtering approach will also be shown for comparison.

The three fields are now averaged over the latitude range 15°S to 15°N, and each is then normalised by its standard deviation, creating a dimensionless field. The three variables, which are two-dimensional (time and longitude), are now concatenated along the longitude axis in the order OLR, u_{850}, u_{200}. Thus, the combined field, which we denote $\mathbf{x}$, has a "longitude" axis of length $L = 864$ which runs from 0° to 360° three times over. The RMM time series are the PCs of the first two EOFs. In order to find the EOFs of the combined field, the covariance matrix $\mathbf{C}$ must be computed as follows:

$$\mathbf{C} = \frac{(\mathbf{x} - \overline{\mathbf{x}})^{\mathrm{T}} \cdot (\mathbf{x} - \overline{\mathbf{x}})}{N - 1}, \tag{6.1}$$

where $^{\mathrm{T}}$ denotes the transpose of a matrix, $\overline{\mathbf{x}}$ is the time-mean of $\mathbf{x}$, and N is the number of times in $\mathbf{x}$. If we number each point along the "longitude" axis of $\mathbf{x}$

as 1, 2, 3, ..., L then the elements of $\mathbf{C}$ are given by

$$\mathbf{C}_{ij} = \rho(i,j)\sigma_i\sigma_j \tag{6.2}$$

for $i, j \in \{1, \ldots, L\}$, where $\rho(i,j)$ is the correlation between i and j, and σ_i is the standard deviation at co-ordinate i. The quantity on the right-hand side of equation 6.2 is known as the covariance of i and j, or $\mathrm{cov}(i,j)$. Note that the matrix is symmetrical since $\rho(i,j) \equiv \rho(j,i)$ by definition; and that for $i = j$, $\mathrm{cov}(i,j)$ reduces to σ_i^2 since $\rho(i,i) \equiv 1$ by definition. Therefore, the covariance matrix has the form

$$\mathbf{C} = \begin{pmatrix} \sigma_1^2 & \rho(1,2)\sigma_1\sigma_2 & \rho(1,3)\sigma_1\sigma_3 & \cdots & \rho(1,L)\sigma_1\sigma_L \\ \rho(2,1)\sigma_2\sigma_1 & \sigma_2^2 & \rho(2,3)\sigma_2\sigma_3 & \cdots & \rho(2,L)\sigma_2\sigma_L \\ \rho(3,1)\sigma_3\sigma_1 & \rho(3,2)\sigma_3\sigma_2 & \sigma_3^2 & \cdots & \rho(3,L)\sigma_3\sigma_L \\ \vdots & \vdots & \vdots & \ddots & \vdots \\ \rho(L,1)\sigma_L\sigma_1 & \rho(L,2)\sigma_L\sigma_2 & \rho(L,3)\sigma_L\sigma_3 & \cdots & \sigma_L^2 \end{pmatrix}. \tag{6.3}$$

The covariance matrix is plotted in figure 6.5. As shown in equation 6.3, the leading diagonal contains the variance at each "longitude" point. The greatest variance of OLR is between around 45°E and 180°E, as expected since this is where the MJO convective envelopes propagate. The covariance between OLR around, say, 90°E and 135°E is negative due to the anti-correlation between them. This is the MJO dipole structure, which consists of one active envelope and one suppressed envelope. The variance of u_{850} is strong from about 45°E to about 270°E, and of u_{200} is strong from about 225°E to about 60°E. The covariance between u_{850} at some longitude and u_{200} at the same longitude is always negative since the upper- and lower-level winds at the equator blow in opposite directions, mainly due to the baroclinic Kelvin wave associated with the MJO's propagation.

The EOFs are the eigenfunctions of $\mathbf{C}$, and the eigenvalues are proportional to the variance described by their associated EOFs (Wilks, 2011). The first two EOFs describe 13.4% and 10.3% of the total variance respectively (table 6.2), which is significantly larger than the proportion described by the third (6.2%). Hence, we retain only the first two EOFs as the new basis for our time series. These are plotted in figures 6.6d and c respectively. Figures 6.6a and b show the first two EOFs, in order, found by WH04 from reanalysis data. WH04's EOF1 and HiGEM's EOF2 exhibit very similar spatial structures, as do WH04's EOF2 and HiGEM's EOF1. The WH04 EOFs account for 12.8% and 12.2% of the total

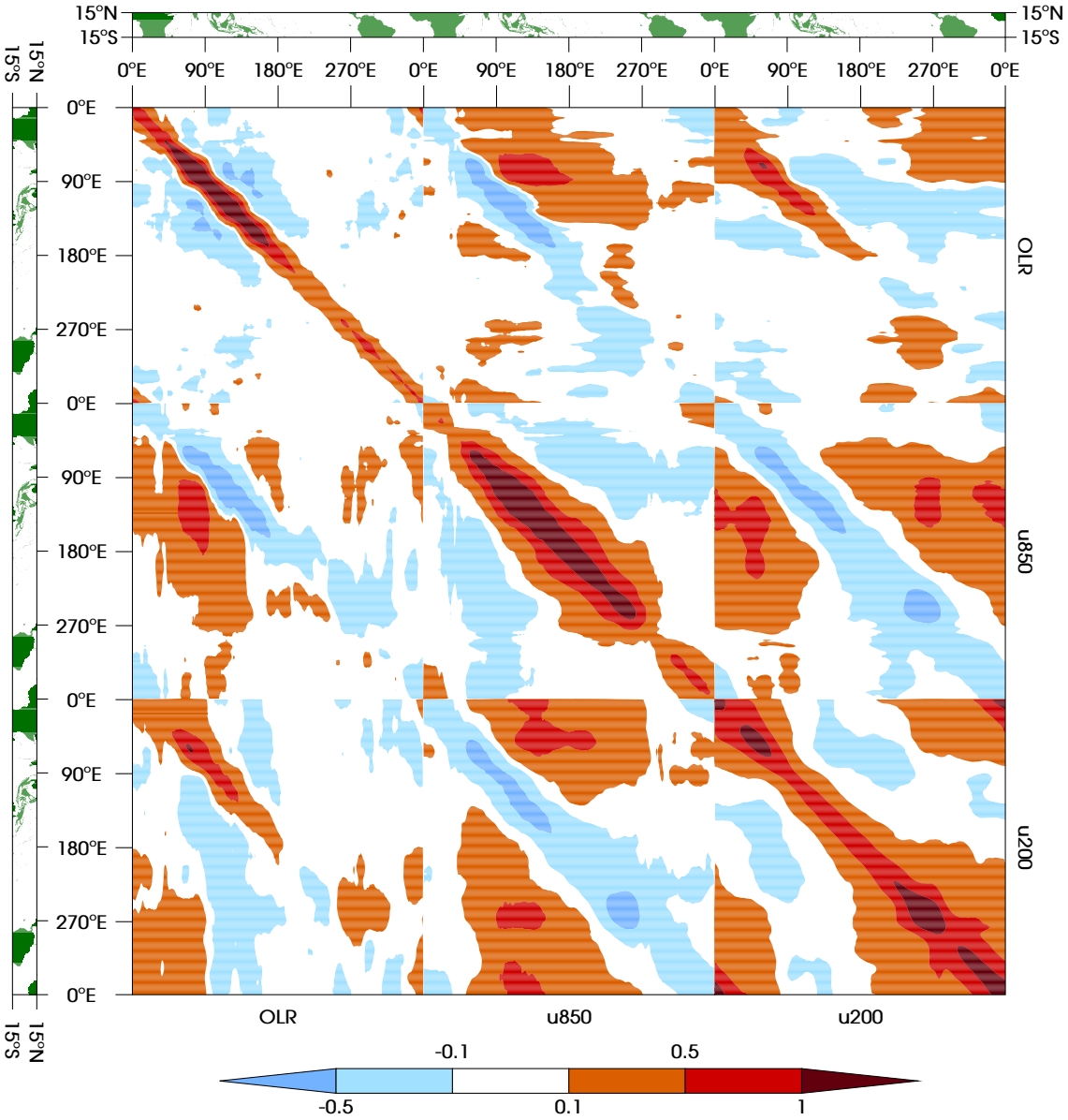

Figure 6.5: Covariance matrix **C** (see equation 6.3) of the combined field of OLR, u_{850} and u_{200} from HiGEM. A land mask, generated using the GLOBE topography data set at $0.11° \times 0.11°$ resolution and covering the same longitude range as was used to generate the matrix, is shown for information.

variance respectively. From North et al. (1982), the error in an eigenvalue λ is

$$\delta\lambda \sim \lambda\sqrt{\frac{2}{N}}, \tag{6.4}$$

where N is the number of independent realisations of the MJO and is given by the ratio of the length of the data series to the MJO decorrelation time. WH04 used 8401 days of data to generate their EOFs; the decorrelation time is

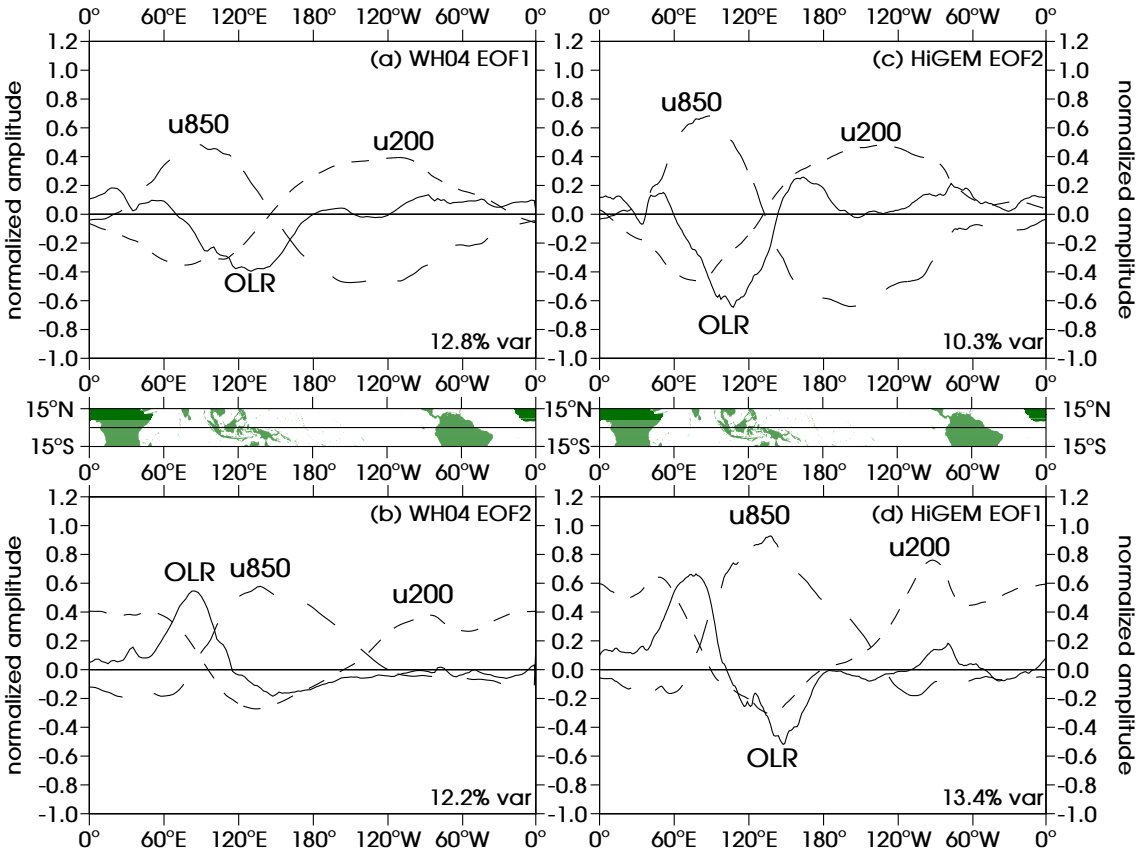

Figure 6.6: EOFs computed from the combined field **x**, from reanalysis data (WH04; (a) EOF1 and (b) EOF2) and HiGEM ((c) EOF2 and (d) EOF1). The percentage of the total variance explained by each EOF is printed in the bottom right of the panel. A land mask, generated using the GLOBE topography data set at $0.11° \times 0.11°$ resolution and covering the same longitude range as was used to generate the EOFs, is shown for information.

approximately a quarter of an MJO cycle, so we take a typical value of 12 days. Hence, measured in percent of the total variance,

$$\delta\lambda_1 \sim 12.8\% \times \sqrt{\frac{2 \times 12}{8401}} = 0.68\% \tag{6.5}$$

$$\delta\lambda_2 \sim 12.2\% \times \sqrt{\frac{2 \times 12}{8401}} = 0.65\%. \tag{6.6}$$

Therefore, the uncertainty ranges of WH04's leading two eigenvalues overlap, so the EOFs are degenerate. Hence, there is no inconsistency between the WH04 EOFs and the HiGEM EOFs, even though they are ordered differently.

The similarity between WH04's EOFs and those generated from HiGEM is remarkable. Nearly all the same local maxima and minima, for all three variables and for both EOFs, are present in both WH04 and HiGEM. The

EOF	1	2	3	4	5	6	7	8	9	10
% variance	13.4	10.3	6.2	5.8	3.8	3.7	3.4	2.8	2.7	2.2
cumulative	13.4	23.7	29.9	35.7	39.5	43.2	46.5	49.3	52.0	54.2

Table 6.2: Percentage of the variance associated with each of the first 10 EOFs in the WH04-like analysis of the MJO in HiGEM; cumulative percentage variance of the same.

differences which exist are mainly in amplitude, or a shift in longitude. For example, the chief minimum in OLR in WH04 EOF1 is quite broad and centred around 130°E, whereas the corresponding minimum in HiGEM EOF2 is sharper and centred around 105°E. Also, there is only a very shallow minimum in OLR in WH04 EOF2 at around 145°E, whereas HiGEM EOF1 has a far more pronounced minimum at the same longitude.

Although EOFs have now been computed from HiGEM according to WH04's method, henceforth we use the WH04's own EOFs generated from observations. This is to ensure consistency with other studies of the MJO. The WH04 EOFs were generated not only as a means of producing the real-time MJO indices product; they are also intended as a standard definition of the MJO against which models can be tested. The fact that the EOFs in HiGEM are so similar to those from WH04 justifies the use of WH04's EOFs in analysing the HiGEM output, since the model is clearly able to reproduce the same modes in its atmosphere as occur in reality.

The combined time series of OLR, u_{850} and u_{200} from HiGEM was projected onto the HiGEM EOFs. Figures 6.7a and b show WH04-style phase diagrams (plots of RMM2 against RMM1) for May–October 2008 and November 2008–April 2009 respectively. Note that these cover the same date range that was used for the Hovmöller diagrams in figure 6.2. Figures 6.8a and b show WH04-style phase diagrams for the same time periods but in producing the RMM time series the data were 20–200-day bandpass Lanczos filtered rather than having the mean of the previous 120 days removed. The diagrams in figure 6.7 are exactly as the WH04 method produces, but figure 6.8 makes it easier to see the long-term pattern of propagation. Table 6.3 indicates the approximate geographical region over which the MJO is active for each of the WH04 phases.

In section 6.2.1 it was suggested that there might be an MJO from May to around September or October 2008, albeit rather weak and dying out over the Maritime Continent. (Recall, however, that figure 6.2 showed OLR only whereas the RMM time series also depend on zonal wind.) In figures 6.7a

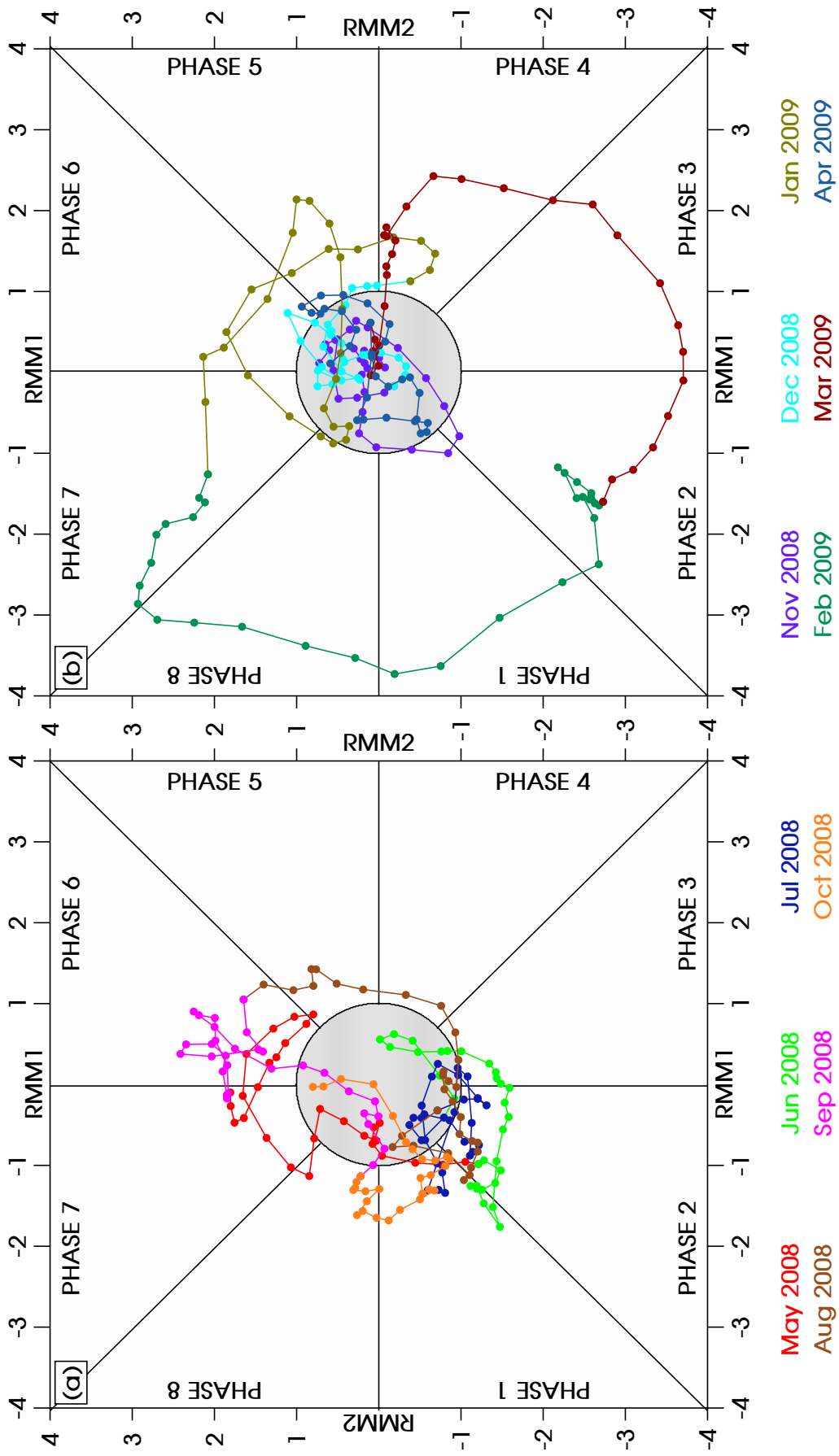

Figure 6.7: WH04 phase diagrams for (a) May to October 2008 and (b) November 2008 to April 2009. RMM time series were computed using the real WH04 EOFs; data projected onto the EOFs have had the mean, first three harmonics of the annual cycle and mean of the previous 120 days removed. Data points within the shaded unit circle are considered to have a weak amplitude. Note that the time range of these diagrams corresponds to that of the Hovmöller diagrams in figure 6.2.

Phases	Active region
1	Western hemisphere and Africa
2–3	Indian Ocean
4–5	Maritime Continent
6–7	Western Pacific Ocean
8	Western hemisphere

Table 6.3: The approximate region over which the MJO is active in each WH04 phase.

and 6.8a we see the MJO evolving from phase 1 to 2 around the end of May and start of June, which corresponds to the eastward-propagating negative OLR (active MJO) anomaly at the top left of figure 6.2b. However, the RMM amplitude is weak for much of the time, especially when in phase 1. During June the anomaly propagates to about 100°E (just reaching Sumatra, the start of the Maritime Continent) before dying out; in the phase diagrams we see the MJO phase evolving through phase 3 weakly and almost completely dying in phase 4. During July a positive OLR (suppressed MJO) anomaly propagates along the same path as the negative anomaly before it, extending slightly further into the Maritime Continent. However, the phase diagrams shows the amplitude to be extremely weak, possibly because there is no clear active envelope complementing the suppressed envelope during this time. The MJO strengthens in August and the start of September due to an active envelope which propagates from about 50°E (phase 2) to about 125°E (phase 6). The active anomaly briefly propagates westward again, explaining the clockwise evolution from around the 11th September onwards, before the MJO dies away again as the active anomaly dies out.

It was also suggested in section 6.2.1 that a much stronger and clearer signal, resembling a real-life complete MJO event, occurs from December 2008 to March 2009. The event is initiated over the Maritime Continent in phase 4, with the active anomaly which appears at around 90°E–120°E. Although the MJO briefly weakens during January as the active anomaly weakens (figures 6.7b and 6.8b), it quickly strengthens again as a strong active-suppressed dipole structure emerges from the end of January onwards. The MJO evolves from phase 6 to 8, at which point a secondary active envelope forms so it continues to evolve through phases 1 to 4. The event finally dies away over the Maritime Continent near the end of March.

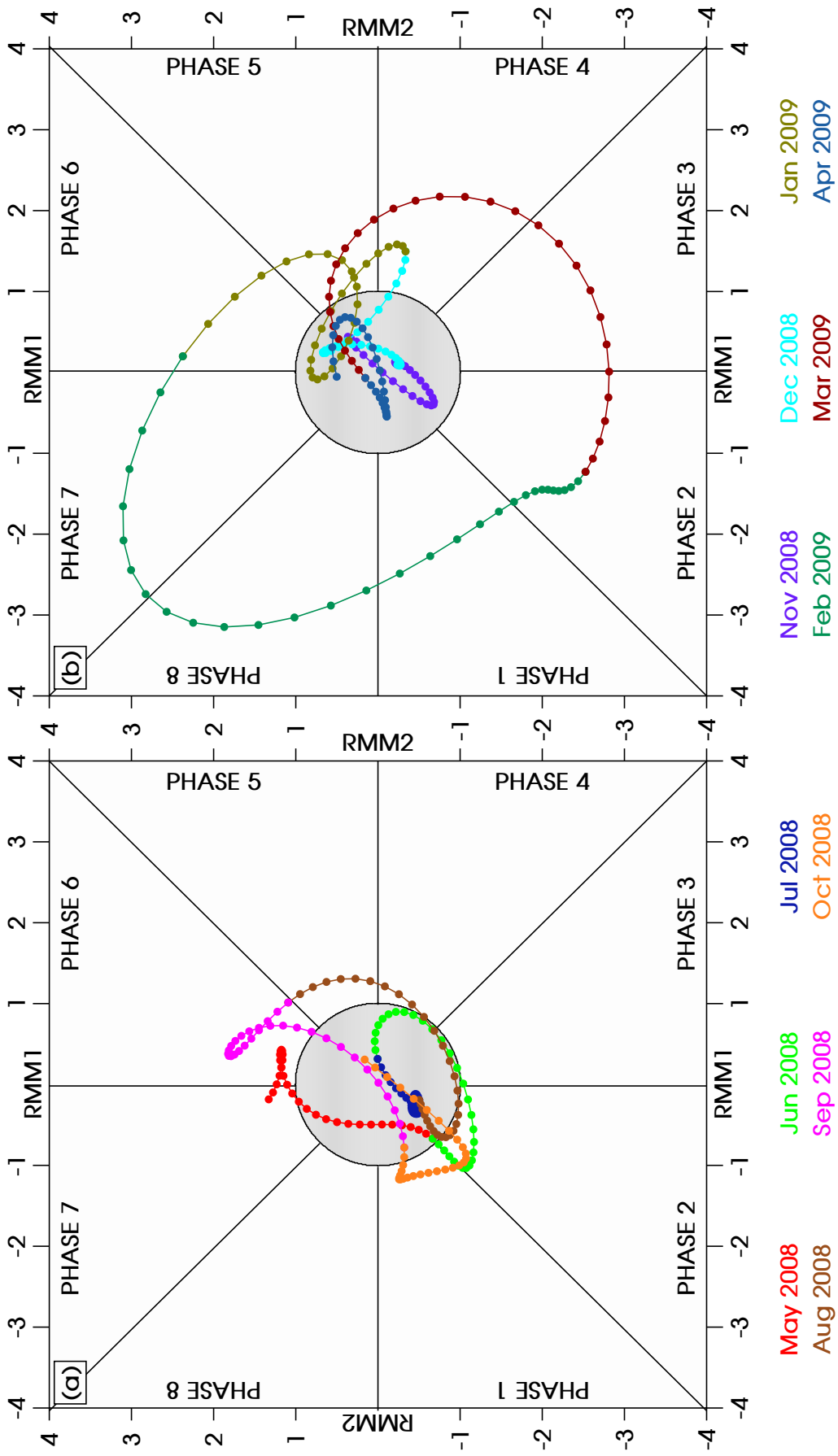

Figure 6.8: As for figure 6.7 but the data projected onto the EOFs have been 20–200-day bandpass Lanczos filtered instead of having the mean of the previous 120 days removed.

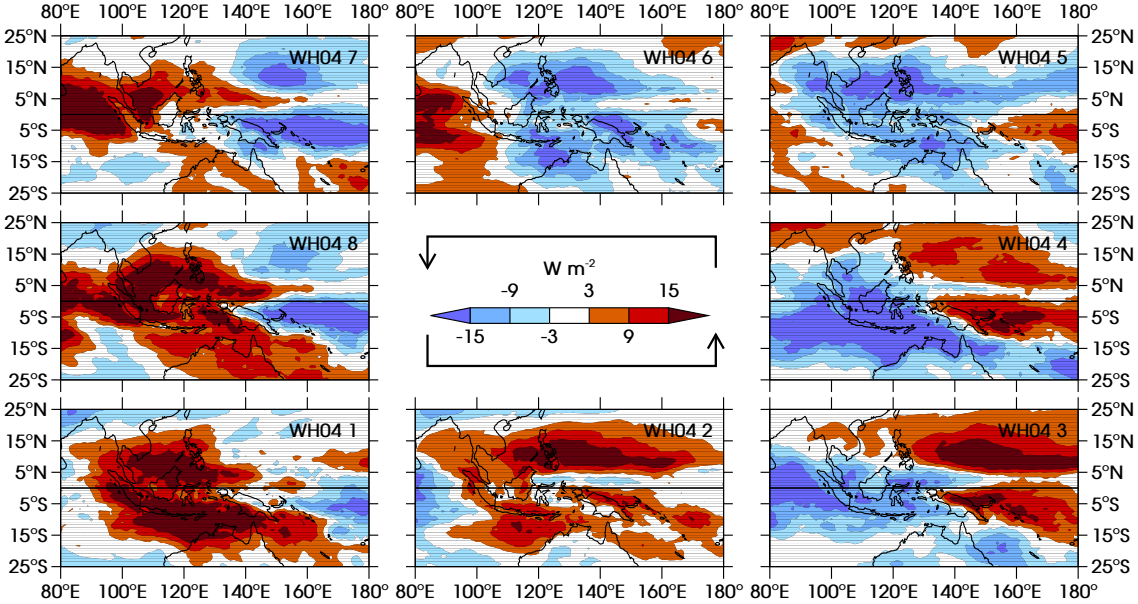

Figure 6.9: Anomaly of daily mean OLR in each phase of the MJO in HiGEM, for boreal winters (November to April) 2000/1 to 2014/5. The equivalent plot for observed brightness temperature is shown in figure 4.11 (page 63).

6.3 Spatial structure of the MJO

It has been shown in section 6.2 that eastward-propagating variability does exist around the equator on intra-seasonal time scales, which projects onto WH04's EOFs in a manner similar to that of the real-life MJO. However, all of the analysis so far has involved averaging or summing over latitude, so we have not yet seen whether the full structures in latitude-longitude space being produced by the model do look like the MJO. Therefore, we now produce composites for the WH04 phases for daily mean OLR and precipitation, as we did for observations in section 4.6. As for observations, data from November to April only are used, for 15 boreal winters (for HiGEM, this was 2000/1 to 2014/5).

The anomaly of daily mean OLR is shown in figure 6.9; this is the equivalent of figure 4.11 (page 63) which used TRMM 3G01 observations, except that here we have radiance in W m^{-2} whereas in observations we had brightness temperature in K. The anomalies show envelopes propagating from west to east, as we know they must because the WH04 indices are found by projecting data onto EOFs which correspond to such propagation. However, we are now seeing the composites without latitude averaging, and it can be seen that there are some major differences between the model and observations.

In phase 1, HiGEM produces a suppressed envelope which has strong

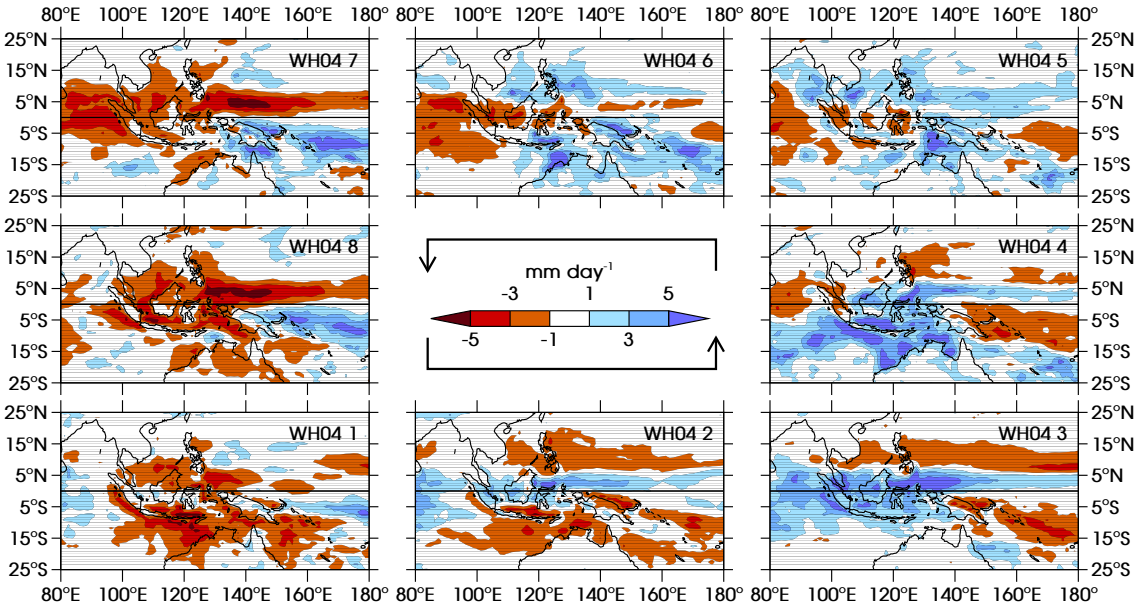

Figure 6.10: Anomaly of daily mean precipitation in each phase of the MJO in HiGEM, for boreal winters (November to April) 2000/1 to 2014/5. The equivalent plot for observations is shown in figure 4.12 (page 64).

positive (clear sky) anomalies in two regions, north and south of the equator. This bifurcation of the envelope, which is not seen in observations, is even clearer in phases 2 to 4, in which a negative anomaly appears to shoot through from the west between about 0° and 5°N. As a result, a persistently strong inter-tropical convergence zone (ITCZ) occurs whilst the surroundings are in the suppressed MJO phase. It could be argued that this does also occur in observations (figure 4.11, phases 3 and 4) but the effect is not nearly as clear or prolonged as in the HiGEM run. The manner in which the anomaly in the model appears to move through quickly from the west is consistent with this being an unrealistically fast, strong equatorial Kelvin wave. A similar effect occurs but for a sign change in phases 6 to 8, with a suppressed (positive OLR) anomaly along the ITCZ splitting the active envelope into two, although this is not as strong as the active anomaly splitting the suppressed envelope.

Figure 6.10 shows the anomaly of daily mean precipitation in HiGEM, the equivalent of the TRMM 3B42HQ plot in figure 4.12 (page 64). As with observations, the precipitation anomalies tend to be less spatially coherent than those for OLR. There is definite eastward propagation as expected, but the dominant feature is, again, the ITCZ which peaks well out of phase with its surroundings. In phases 2 and 3 the suppressed envelope as a single large-scale region is barely discernible as the ITCZ runs right through the Maritime Continent. The strong ITCZ is still present in phase 4, and the suppressed

ITCZ appears again in phases 7 and 8.

In section 4.6 it was noted that the OLR and precipitation anomalies in observations sometimes have gaps in the large-scale envelopes over the Maritime Continent islands. There is some sign of a similar effect occurring in HiGEM. For example, over northern New Guinea in phase 1 and southern New Guinea in phase 2 there is a positive anomaly in amongst the suppressed envelope; and in phases 5 and 6 the suppressed anomaly extends beyond the main suppressed envelope to Sumatra, Java and Sulawesi (phase 5), and to Borneo, Sulawesi and the Bird's Head Peninsula at the north-west corner of New Guinea (phase 6). This "leaping ahead", and any connection with the diurnal cycle, will be investigated in chapter 7.

6.4 Lifetime and recurrence of MJO events

In section 4.6 diagnostics were presented which indicated the sporadic nature of MJO propagation. The same diagnostics are presented here for the HiGEM run. First, in figure 6.11, is (a) the number of days in each WH04 phase and (b) the mean RMM amplitude in each of those phases, with weak days (RMM amplitude less than 1) ignored for both plots. For panel (a), as in figure 4.15, two grey circles indicate the 95% confidence region for a two-tailed statistical significance test; if the number of days in a phase lies outside this region then the probability of any strong-MJO day being in that phase is statistically significantly different from one-eighth. The number of days is skewed towards phases 2, 3, 6 and 7 (when the magnitude of RMM2 is larger than that of RMM1), with all of these phases having a statistically significantly large number of days. There is no such significant pattern for observations, although in both the observations and the model it is phase 1 in which the fewest days fall (147 for observations, 135 for HiGEM; both are statistically significantly small). The mean amplitude (panel (b)) of each phase is roughly similar for the model as for the observations, with the clear exception of phase 3 which on average is the strongest in observations (amplitude 1.88) but the weakest in the model (amplitude 1.56).

Figure 6.12 is a histogram showing the number of times that the atmosphere remains in the same phase for a given number of days in a row, with days on which the MJO is weak counted separately (labelled "Weak MJO"). This is the HiGEM equivalent of figure 4.16 (page 70). For observations the distribution

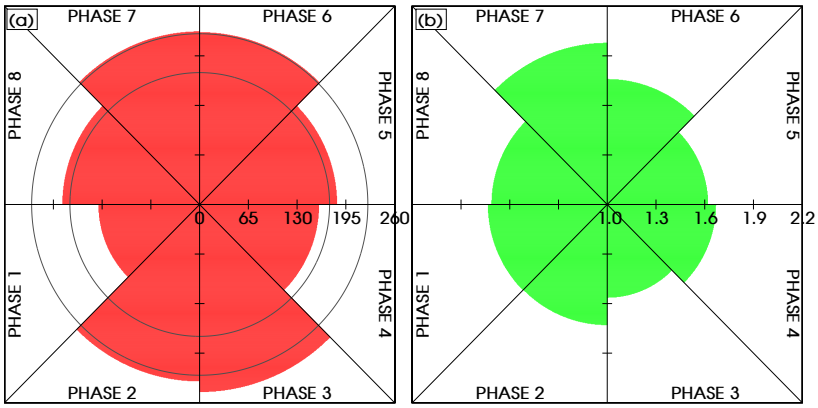

Figure 6.11: (a) Number of days and (b) mean RMM amplitude in each phase of the MJO, for boreal winters (November to April) 2000/1 to 2014/5. Days in which the RMM amplitude is less than 1 have been neglected from both plots. Red regions which lie entirely within the inner grey circle (173 days) or extend beyond the outer grey circle (224 days) are statistically significant (95% confidence). The equivalent plots for observations are shown in figure 4.15 (page 69).

Weak MJO		Phase 1	Phase 2	Phase 3	Phase 4	Phase 5	Phase 6	Phase 7	Phase 8	TOTAL (Phases 1-8)
9	1 day	5	9	6	2	13	9	2	2	48
13	2 days	9	9	5	9	6	7	8	7	60
12	3 days	7	9	8	9	11	8	7	12	71
9	4 days	8	6	15	3	8	3	8	3	54
10	5 days	1	5	6	5	6	5	4	7	39
10	6 days	3	4	5	3	3	8	3	3	32
3	7 days	1	2	4	3	1		2	4	17
9	8 days	2	3	1	2	2	3		1	14
8	9 days		2	2		1	1		1	7
4	10 days						3	5		8
29	11+ days	1	3	2	1	1	2	3	1	14

Figure 6.12: Histogram showing the number of occurrences of strings of successive days of the same phase, for boreal winters (November to April) 2000/1 to 2014/5. For example, there were 15 instances of phase 3 occurring on exactly 4 successive days. The equivalent plot for observations is shown in figure 4.16 (page 70).

in the histogram was clearly skewed towards length 1; that is, the atmosphere tended not to remain in the same phase for more than one day at a time. Indeed, the column on the right showing totals across all phases was monotonically decreasing with increasing length. However, in HiGEM these totals peak at length 3 days, with only 48 1-day 'events' but 71 3-day 'events'. Hence, the modelled atmosphere appears to have more 'inertia' with respect to the MJO, with a tendency for it to remain in the same phase for a longer period of time than occurs in reality.

6.4.1 Propagation events

The equivalent of the histogram in figure 4.17 (page 72) is shown in figure 6.13. As explained in section 4.6, with all days on which the MJO was weak first relabelled to "phase 0", all consecutive duplicate phases were removed from the times series of WH04 indices. Then all instances of MJO propagation were found, along with all instances of standalone phases. An "x" denotes any phase that does not continue the numerical sequence. Broadly, the distributions in the histograms for observations and for HiGEM are very similar. There are 85 and 86 events respectively of length 2 or more, and the distribution of phases by length are similar (both are monotonically decreasing with increasing length, at roughly the same rate). This suggests that the number of propagating MJO events is very realistic in the model. In addition, the number of events of length 1 (61 in observations, 54 in HiGEM) and length 2 (31 in observations, 36 in HiGEM) are similar, so the frequency with which non-propagating MJO-like conditions appear is realistic in the model.

The red row of data at the top of the histogram shows the number of times that an MJO-like signal appears but never propagates into the next phase. If we take as a null hypothesis that this is equally likely to occur for any of the eight phases (so the probability of it being any given phase is $p = 0.125$) then the phase of an xNx event has a binomial distribution with $n = 61$ (in observations) or $n = 54$ (in HiGEM). Using a two-tailed statistical significance test with a 95% confidence interval we reject the null hypothesis – and conclude that there is a bias towards or against an xNx event occurring for a particular phase – if there are fewer than 3 or more than 13 (for observations) or fewer than 2 or more than 11 events (for HiGEM) for any given phase. Thus, the only phase for which there is statistical significance is phase 4, with 14 x4x events in observations but only 1 in the model. In observations, this means that

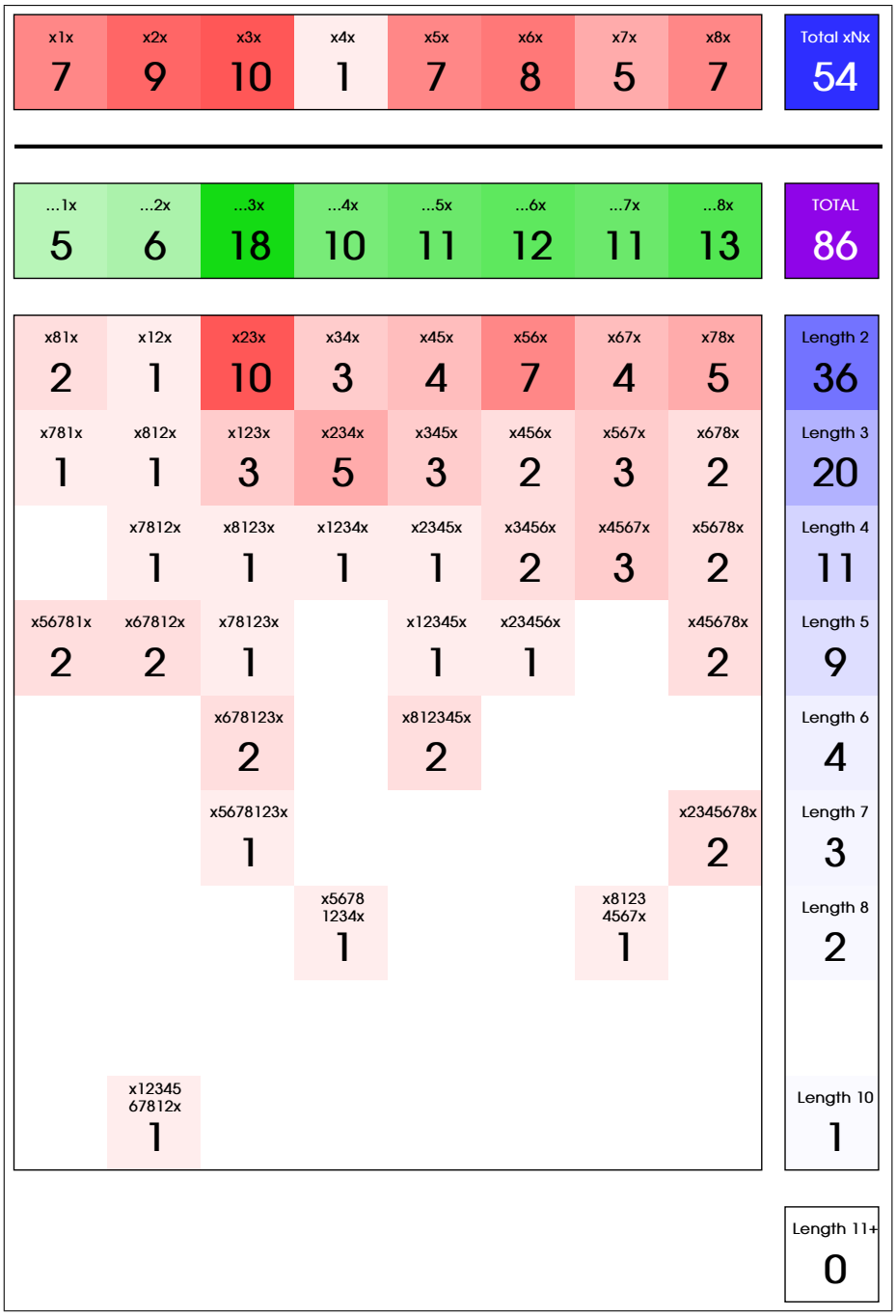

Figure 6.13: Histogram of MJO "events" in boreal winters (November to April) 2000/1 to 2014/5. An N denotes any phase; an x denotes any phase that does not continue the numerical sequence. An ellipsis denotes any sequence of phases, so "...4x" means any event of length 2 or more, ending with 4x. The top row shows the number of one-phase events (i.e., no propagation whatsoever). The large red grid shows the number of each type of event; they are summed by end phase (above in green) and by length (to the right in blue). The purple box shows the total number of events of length 2 or more. See section 4.6.3 for full details. The equivalent plot for observations is shown in figure 4.17 (page 72).

there is a significant tendency for OLR and zonal wind patterns which look like phase 4 to appear, not propagating from phase 3 first, and not to propagate into phase 5. However, in the model we cannot conclude the opposite – that there is a significant tendency for phase 4 to propagate into phase 5 – because, as we have seen in figure 6.11, a significantly small number of phase 4 days occur in the first place.

The green row of data shows the frequency with which the MJO was in each of the eight WH04 phases immediately before dying out or switching to some other non-consecutive phase. If we take as a null hypothesis that MJO propagation is equally likely to end in any of the eight phases (so $p = 0.125$ as before) then the end phase of an event of length 2 or more also follows a binomial distribution, with $n = 85$ (in observations) or $n = 86$ (in HiGEM). Using a two-tailed statistical significance test with a 95% confidence interval we reject the null hypothesis – and conclude that there is a bias towards or against ending in a particular phase – if there are fewer than 5 or more than 16 events which end in any given phase. Thus, the only phase for which there is statistical significance in HiGEM is phase 3, since there are 18 examples of "...3x" events. The model has a tendency for the MJO to cease propagating immediately after it has been in phase 3, which is consistent with the fact that the mean amplitude is weaker in this phase than in any other (figure 6.11). Looking at the "...3x" column in figure 6.13, 10 of the 18 events ending in phase 3 were only two phases long, suggesting that the model quite frequently initiates MJO-like convection over the Indian Ocean which may begin to propagate but never reaches the Maritime Continent. There is no statistically significant evidence for this occurring in observations (figure 4.17). In observations there are, however, only 4 events ending in phase 2, which is statistically significant. Thus, in the real atmosphere, if MJO-like convection is formed over the Indian Ocean there is a definite tendency for it to begin propagating over the ocean, whether it goes on to reach the Maritime Continent or not. In the model, the number of "...2x" events is small, with only 6 such events occurring, so there is a sign of the same effect occurring, but it is not statistically significant to the level of the confidence interval chosen here.

6.5 Conclusions

HiGEM is a high-resolution model based on the Met Office Hadley Centre's HadGEM1 model. It is shown here that eastward-propagating intra-seasonal variability at a similar frequency to the real-life MJO is present in OLR in the model, with a realistic amount of associated spectral power. However, this variability does not always have a realistic zonal wavenumber; its wavenumber varies over a wider range and is centred on wavenumber 2 rather than 1. Despite this, repeating the analysis of WH04 produces EOFs which are very similar to those found by WH04, suggesting that the structure of the MJO, at least when averaged over latitude, is broadly correct. OLR and zonal wind data from the model were projected onto WH04's EOFs to find the RMM time series. When plotted on an MJO phase diagram, the MJO in HiGEM was shown to propagate in a realistic manner, and the propagation was easily seen to be consistent with OLR envelopes which can be picked out visually from Hovmöller diagrams.

Composites of OLR and precipitation based on the WH04 phase analysis show the full structure of the model's MJO, not just that averaged over latitude. Although there is clear propagation of active and suppressed envelopes of a realistic spatial extent, there are significant errors caused by the ITCZ peaking in the wrong WH04 phase, completely out of phase with the rest of the MJO. This is especially visible in the composites of precipitation. This error has the effect of unrealistically bifurcating the MJO envelopes, and is consistent with a fast Kelvin wave shooting through the Maritime Continent region, disrupting the MJO.

Diagnostics showing the tendency of the modelled MJO to remain in a given phase, or to propagate or die out altogether, were compared with those from the real-life MJO. Statistical significance tests reveal certain aspects of the model's ability to simulate such features of the MJO's evolution. Unlike in real life, the model has a significant tendency for the magnitude of RMM2 to be larger than that of RMM1 (phases 2–3 and 6–7), so the model is more likely to have active MJO envelopes existing either side of the Maritime Continent (over the Indian and Pacific Oceans – see table 6.3). This is consistent with the fact that over the Maritime Continent the ITCZ interrupts the MJO structure, so when the active and suppressed envelopes are over the Maritime Continent the data project less strongly onto the EOFs. The model also has an unrealistic level of MJO 'inertia', with a tendency for the MJO to remain in the same phase for a greater number of successive days than in reality.

The frequency with which the MJO shows any propagation from one phase to the next is overall realistic, but within this there are variations. In observations there is a significant tendency for the MJO to continue propagating when it is in phase 2, with an active envelope over the central Indian Ocean, but there is no significant evidence for the same in the model. Conversely, in the model there is a significant tendency for the MJO to cease propagating when it is in phase 3, with an active envelope over the eastern Indian Ocean, but there is no significant evidence for the same in observations. This is consistent with the fact that phase 3 has on average the weakest amplitude of any phase in the model, but in observations it does not (indeed it has the strongest). In turn, this may explain why there are significantly few phase 4 days in the model, when the active envelope is over the western Maritime Continent.

Having explored the nature of the MJO in HiGEM in this chapter, we next investigate whether it interacts with the Maritime Continent diurnal cycle.

Chapter 7

Scale interaction between the diurnal cycle and MJO in HiGEM

7.1 Introduction

In chapter 4 diagnostics were used to illustrate the nature of the diurnal cycle over the Maritime Continent and of the Madden-Julian Oscillation. The findings from these observations were used in chapter 5 to show that there is a scale interaction between the two over the Maritime Continent, whereby the diurnal cycle of precipitation is triggered ahead of the advancing active MJO envelope and is strong enough over land to contribute significantly to the MJO signal. Having shown in chapter 6 that HiGEM has MJO-like variability that is very realistic (but for a problem with a strong ITCZ peaking in the wrong phase), the intention in this chapter is to examine whether a similar scale interaction to that seen in observations exists in the model.

7.2 The diurnal cycle in HiGEM

As in section 4.5, this section diagnoses the diurnal cycle using composites and harmonic analysis.

7.2.1 Climatological diurnal cycle of precipitation

The TRMM 3B42HQ data set provides observations of precipitation at 00:00, 03:00, ..., 21:00 UTC, but in HiGEM the precipitation is output at 01:30, 04:30,

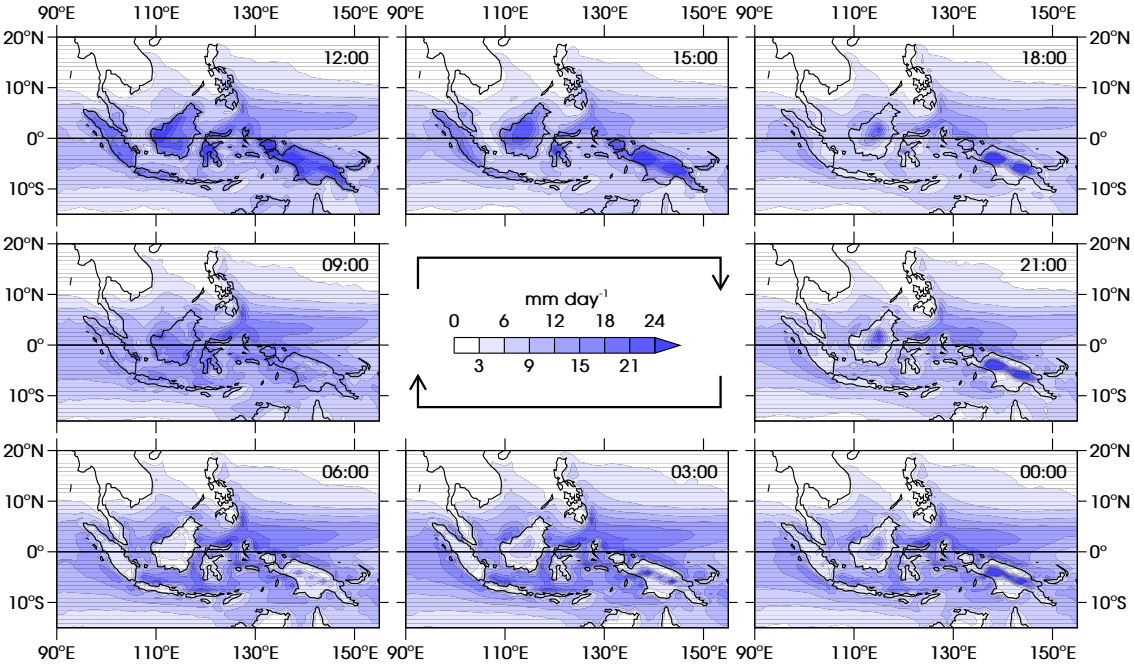

Figure 7.1: Climatology of the diurnal cycle of precipitation over the Maritime Continent, from HiGEM. Times of day are shown in local solar time (see main text), moving clockwise round the diagram. The equivalent plot for observations is shown in figure 4.5 (page 55).

. . . , 22:30 UTC. However, since we wish to interpolate to local solar time (LST) anyway, we can find the composited diurnal cycle for 00:00, 03:00, . . . , 21:00 LST so that the observations and model output are directly comparable. Composites of precipitation for each time of day during boreal winters (November to April) are shown in figure 7.1; the observed diurnal cycle from 3B42HQ is shown in figure 4.5 (page 55). As in section 4.5.1 the diurnal harmonic was found at each grid point, and the amplitude and phase are plotted in figure 7.2; the equivalent plot for observations is figure 4.6 (page 56). All times referred to below are given in LST.

The clearest difference between the observed and simulated diurnal cycle is the phase. As explained in section 2.2.3, this is a very common error in the tropical diurnal cycle in climate models. The observed diurnal cycle shows that the land of the Maritime Continent is almost clear of rain during the morning, with precipitation starting around the edges of the islands around 15:00 and spreading inland, and becoming stronger, through the evening. In HiGEM, however, precipitation over the land has begun by 09:00, peaks at 12:00 and decays in the afternoon. Thus, it appears that the phase of the parameterised convection is locked to that of the incoming solar radiation. The phase of the diurnal harmonic (figure 7.2b) confirms that the precipitation tends to peak

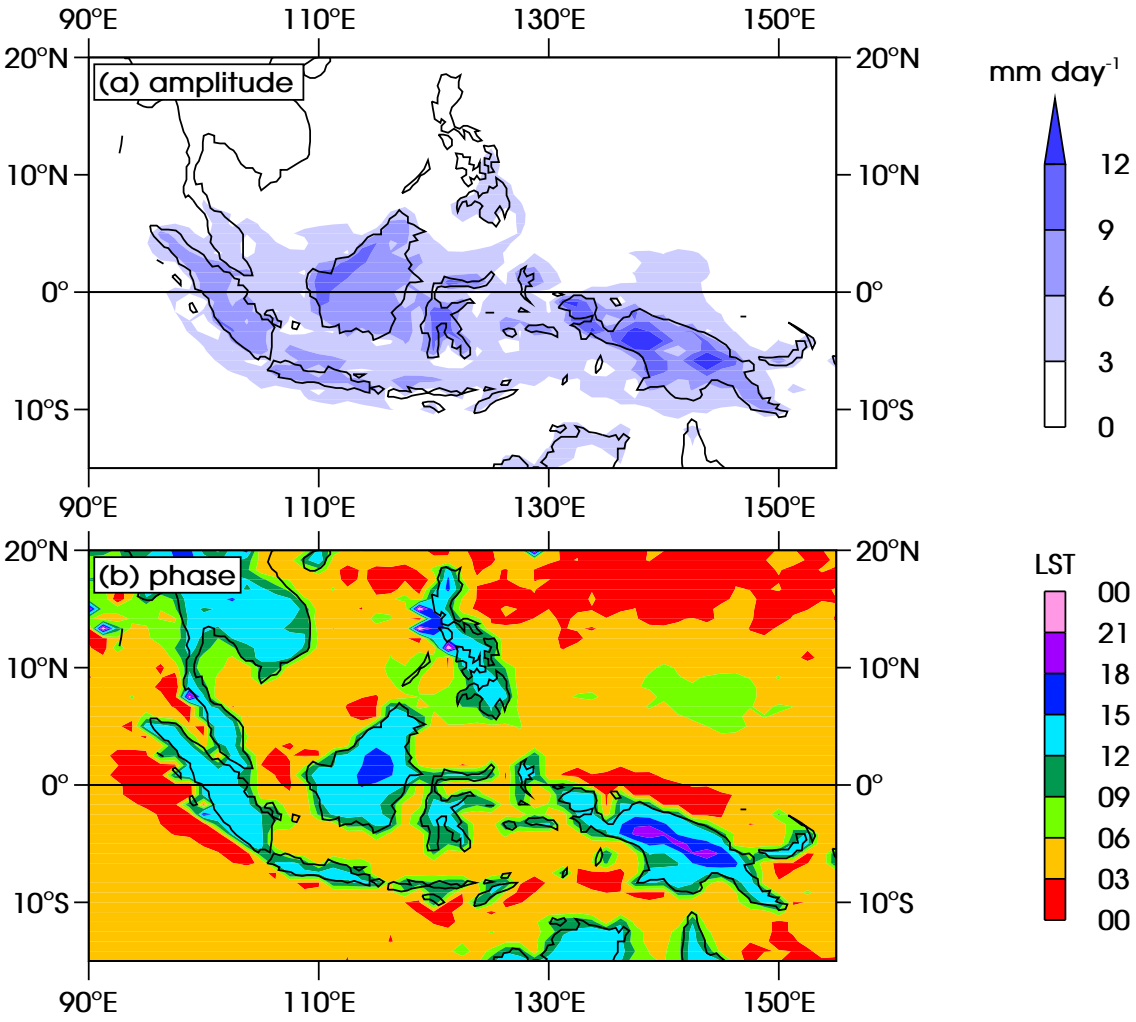

Figure 7.2: (a) Amplitude and (b) phase of the diurnal harmonic of precipitation, from HiGEM. The equivalent plot for observations is shown in figure 4.6 (page 56).

around the middle of the day over much of the land. It also shows that the peak progresses from the coast to the centre of the islands, with the harmonic peaking just before midday at the coasts, just after midday over most of the land, and in the late afternoon or evening in the middle of the larger islands (Borneo and New Guinea). However, a close examination of figure 7.1 (see below) will show that this is not due to the initiation of precipitation moving inland, as in observations. Over ocean the diurnal phase is much more spatially coherent in HiGEM than in 3B42HQ, but (away from the islands) it is at roughly the correct time of day; in the model the ocean diurnal cycle generally peaks between 03:00 and 06:00 and in observations it is generally between 03:00 and 09:00.

The amplitude of the diurnal cycle (figure 7.2a) is much weaker in the model than in reality, which is the opposite of the problem often reported in climate models (section 2.2.3). The spatial structure of the diurnal amplitude is

otherwise realistic, with the strongest amplitudes limited to the land, and the diurnal cycle over the ocean being small (generally 3–6 mm day^{-1}) close to the land and even smaller a long way from it. However, the precipitation in HiGEM does not show such fine spatial details as are present in the observations, because of the difference in resolution. In 3B42HQ the precipitation spreads inwards on the islands, beginning over convex regions of the coast where onshore breezes converge as described in sections 2.2.2 and 4.5.1. The relatively coarse resolution of HiGEM means that the orography, shown in figure 6.1, does not resolve the convex and concave shapes of the coastlines. Therefore, precipitation is not triggered where there are converging sea breezes at the coasts. Rather, the convective parameterisation causes precipitation to start and then strengthen almost uniformly across all land areas. At 06:00 there is almost no precipitation over the land (and what precipitation is present is due to rainfall from the previous day which has not quite decayed away). At 09:00 there is precipitation over almost all of the land of the Maritime Continent, and this strengthens almost homogeneously between 09:00 and 12:00.

In the afternoon and evening precipitation weakens, but inhomogeneously. Under the model's parameterisation the decay of the diurnal rainfall occurs more rapidly over areas of low orography. At 15:00 there is already a visible difference between highlands and lowlands. Over Sumatra there are drier conditions along the plains of the north-east than the mountains of the south-west; over Borneo and, in particular, New Guinea the precipitation is clearly strongest over those regions where orography is highest. Over Borneo and New Guinea this is true right through the evening and into the following morning. By 21:00 there is almost no rainfall except over the mountains; over New Guinea there is still a very strong mountain-based signal at midnight and even 03:00. Hence, the fact that the diurnal phase in figure 7.2b spreads during the afternoon from the coasts to the centre of the islands is due to the way in which the precipitation dies away. In observations this does also occur, but the more important cause is that precipitation is initiated at the coasts earlier and inland later. Thus, the convective parameterisation scheme is unsuccessful at timing the start of the diurnal cycle, but the way in which the diurnal rainfall dissipates is reasonably accurate.

A notable feature of the diurnal cycle in observations is the two separate bands of rainfall on the north and south flanks of the New Guinea Highlands, running along the length of the mountain range (roughly east-west). There is no such north-south split in the model but there is an east-west split, with

regions of strong diurnal cycle at either end of the mountain range. Hence, the parameterisation scheme is not able to produce convection responding to the mountain-valley breeze circulation.

A further feature of the observed diurnal cycle is the offshore propagation of precipitation due to gravity waves. There are signs of this occurring in HiGEM, but to a much lesser extent than in observations. In section 4.5.1, several offshore propagation regions were identified, distinguished by bands of successively later diurnal phase moving away from coastlines over the ocean. Of the regions identified, the observed propagation is strong (diurnal amplitude exceeding 6 mm day^{-1}) south-west of Sumatra, north of Java, north-west of Borneo, east of Sulawesi and north of New Guinea. In HiGEM the diurnal amplitude exceeds 3 mm day^{-1} offshore of these coastlines, but only north of Java does it exceed 6 mm day^{-1}. This is consistent with the land-based diurnal cycle, which triggers the gravity waves, also being weak in the model. Propagation was also observed south of Java and north-west of Palawan (10°N, 119°E). Of all these propagation regions, there are distinct signs of offshore propagation in the model in only two locations: south-west of Sumatra and north of New Guinea.

7.2.2 Climatological diurnal cycle of wind

In section 4.5.2 QuikSCAT was used to show the daily mean and diurnal cycle of wind. The equator crossing times of the QuikSCAT satellite are 06:00 and 18:00 LST; HiGEM outputs the 10 m wind eight times per day, at the same times as precipitation. The daily mean wind, found by averaging together all times of day, is shown in figure 7.3 for all longitudes and in figure 7.4 for the Maritime Continent only. Of course, in the model we have 10 m wind over land as well as over ocean.

The mean flow is very similar in the model and in observations. All the large-scale features of the circulation present in QuikSCAT also appear in HiGEM, and the winds blow at a very similar speed. This is especially true over the Maritime Continent, where there is very little difference between the two.

A characteristic diurnal cycle amplitude, referred to as the "diurnal difference", was shown in figures 4.9 (page 60) and 4.10 (page 61) by subtracting the 06:00 observations from the 18:00 observations. For HiGEM, four different diurnal differences were computed (not all shown here): 12:00 minus 00:00, 15:00 minus 03:00, 18:00 minus 06:00, and 21:00 minus 09:00. Over most coastlines the

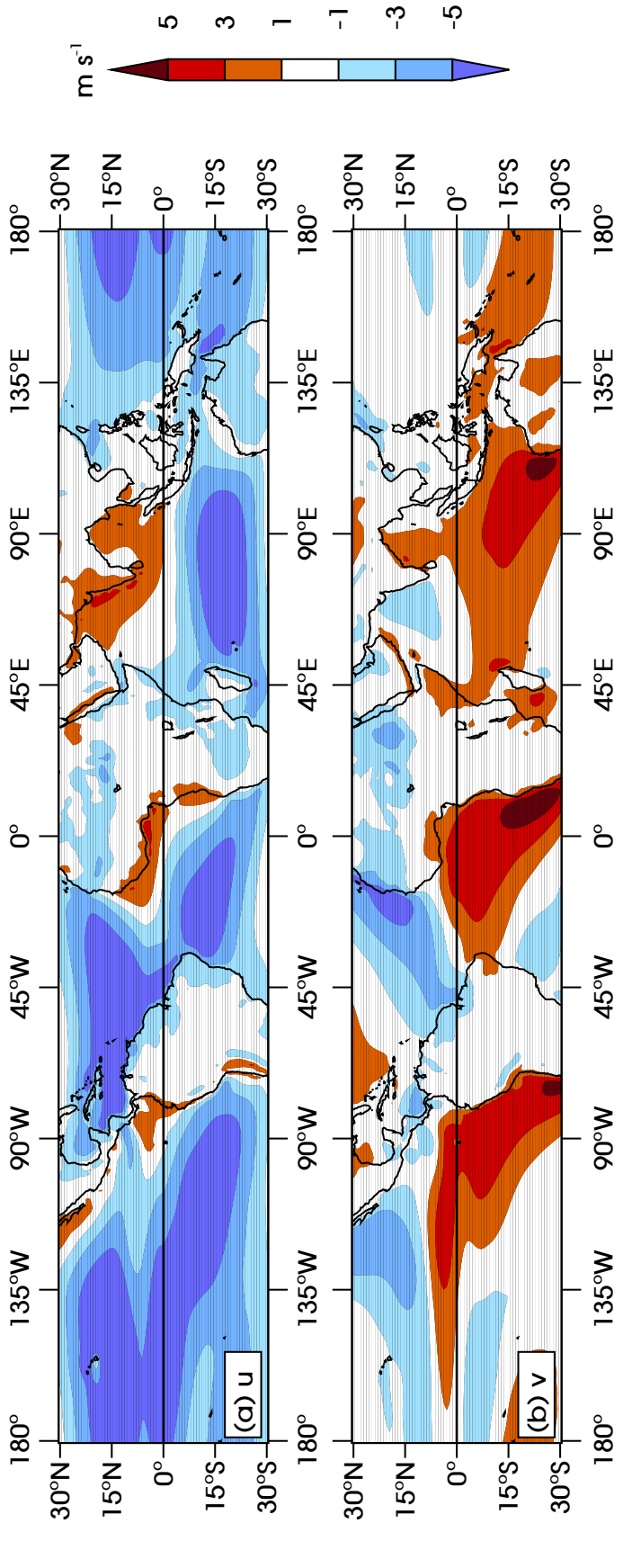

Figure 7.3: Year-round climatology of daily mean 10 m wind from HiGEM: (a) eastwards component u and (b) northwards component v. The equivalent plot for observations is shown in figure 4.7 (page 58).

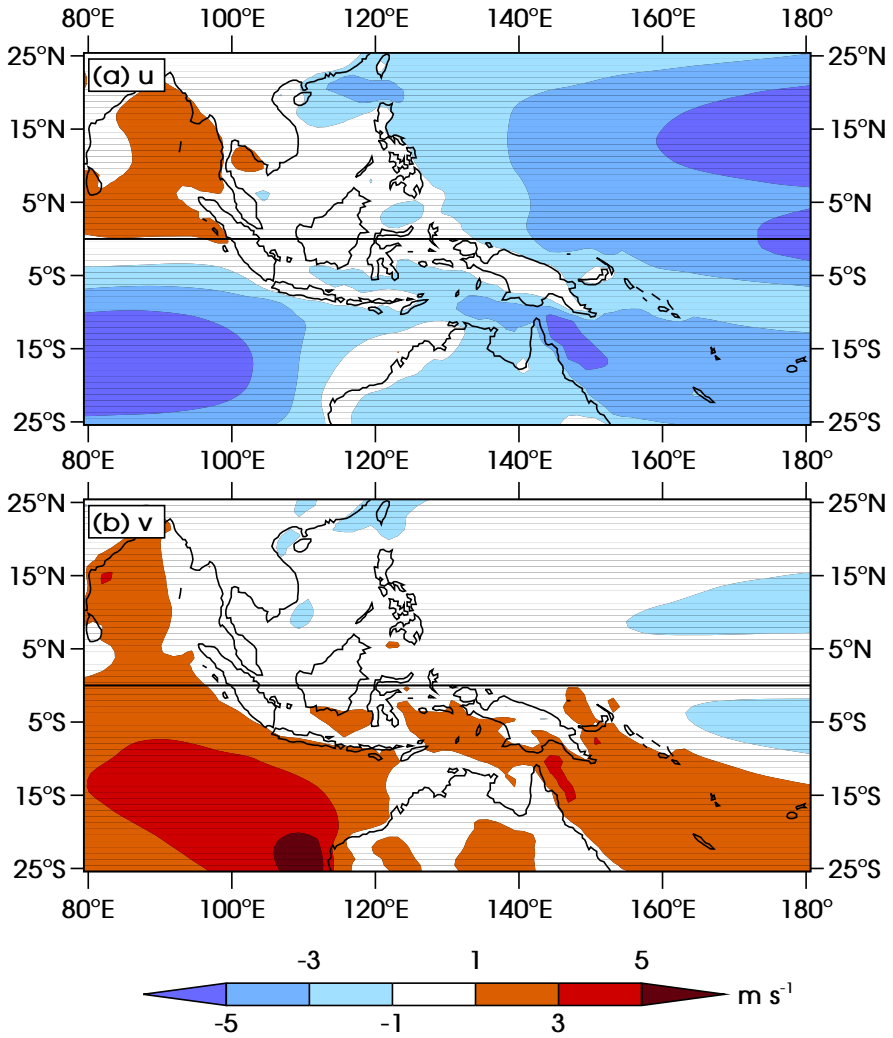

Figure 7.4: As figure 7.3, but for the Maritime Continent region only. The equivalent plot for observations is shown in figure 4.8 (page 59).

strongest diurnal difference turned out to be 18:00 minus 06:00, so these times will be used in the plots shown here. This has the advantage of allowing a direct comparison with QuikSCAT. The maximum diurnal difference being at 6am and 6pm is broadly in line with findings from previous observational studies (e.g., Deser and Smith, 1998), suggesting that the phase of the diurnal cycle of wind is accurate in the model, unlike that of the diurnal cycle of precipitation. The 6pm-6am diurnal difference is shown for the whole tropics in figure 7.5, and for the Maritime Continent only in figure 7.6.

Again, globally, most of the features in the plot from observations are also present in that from the model. Over the Maritime Continent, however, there are a few small model errors to note. In particular, the strength and extent of the diurnal cycle just offshore of the land are incorrectly simulated in several regions. For example, north of Java the difference in wind between 06:00 and

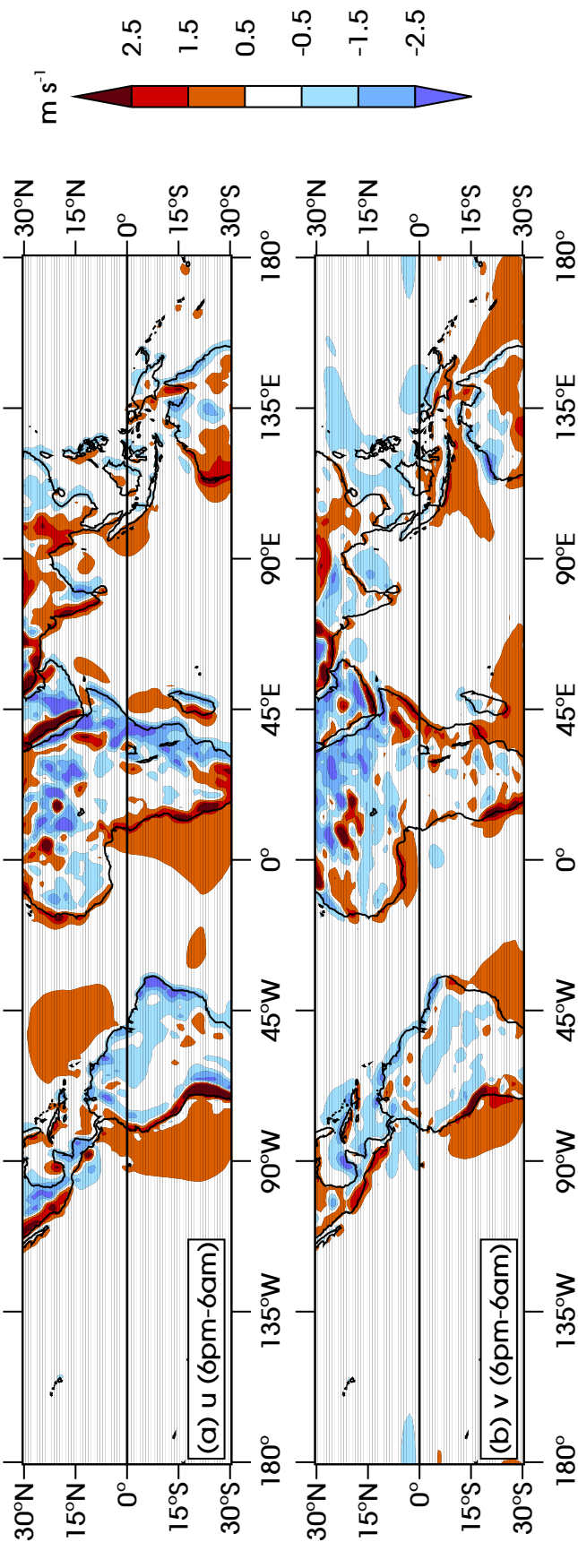

Figure 7.5: Year-round climatology of the diurnal difference of 10 m wind from HiGEM, found by subtracting the 06:00 from the 18:00 data: (a) eastwards component u and (b) northwards component v. The equivalent plot for observations is shown in figure 4.9 (page 60).

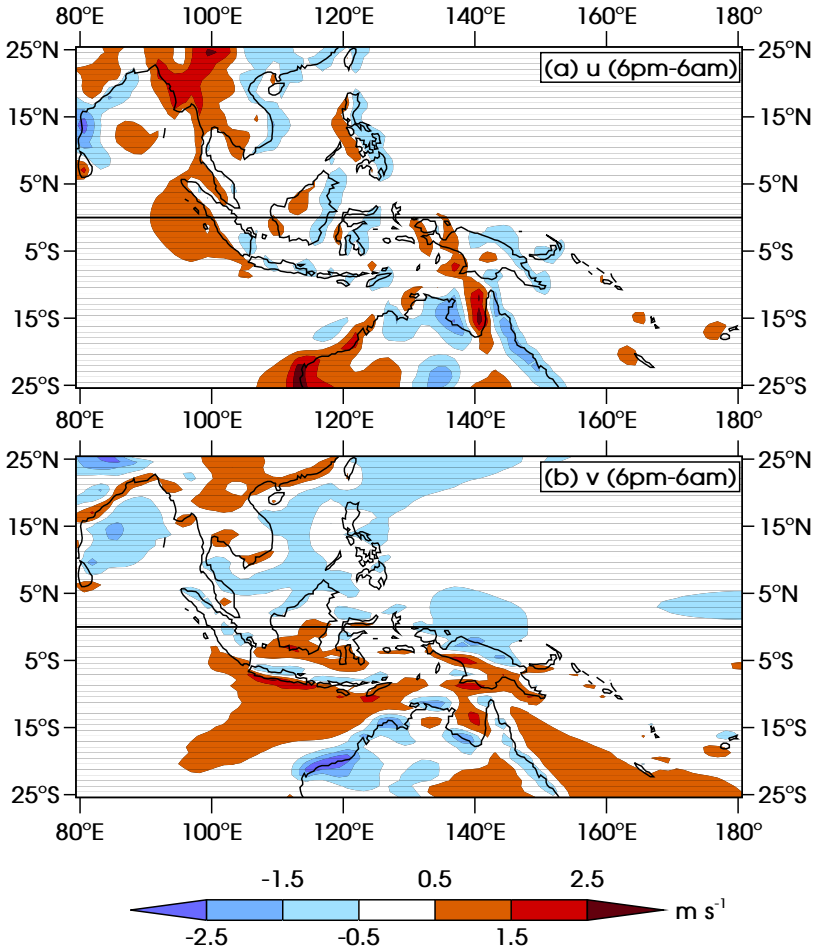

Figure 7.6: As figure 7.5, but for the Maritime Continent region only. The equivalent plot for observations is shown in figure 4.10 (page 61).

18:00 exceeds 2.5 m s^{-1}, but in the model it is less than 1.5 m s^{-1}. Off the south-west coast of Sumatra, the region in observations over which both u and v have a diurnal difference of greater than 0.5 m s^{-1} extends only as far as the Mentawai Islands, about 140 km off the Sumatran coast. The regions for u and v cover almost exactly the same area and have a similar magnitude of diurnal difference, suggesting that the diurnal land-sea breezes blow at 45° to the equator. In the model the diurnal difference in v is close to zero, suggesting that the change in land-sea breeze during the day lies almost entirely in the zonal direction. The diurnal difference in u exceeds 0.5 m s^{-1} right out to ~1000 km from the Sumatran coast. Similarly, north of New Guinea the region over which the diurnal difference in v exceeds 0.5 m s^{-1} extends approximately 900 km off the coast in the model, but only around 200 km in observations. Hence, HiGEM does not consistently reproduce the correct spatial structure of the diurnal cycle. Overall, however, its simulation of the diurnal cycle is very good, with more onshore flow in the evening and more offshore flow in the morning around

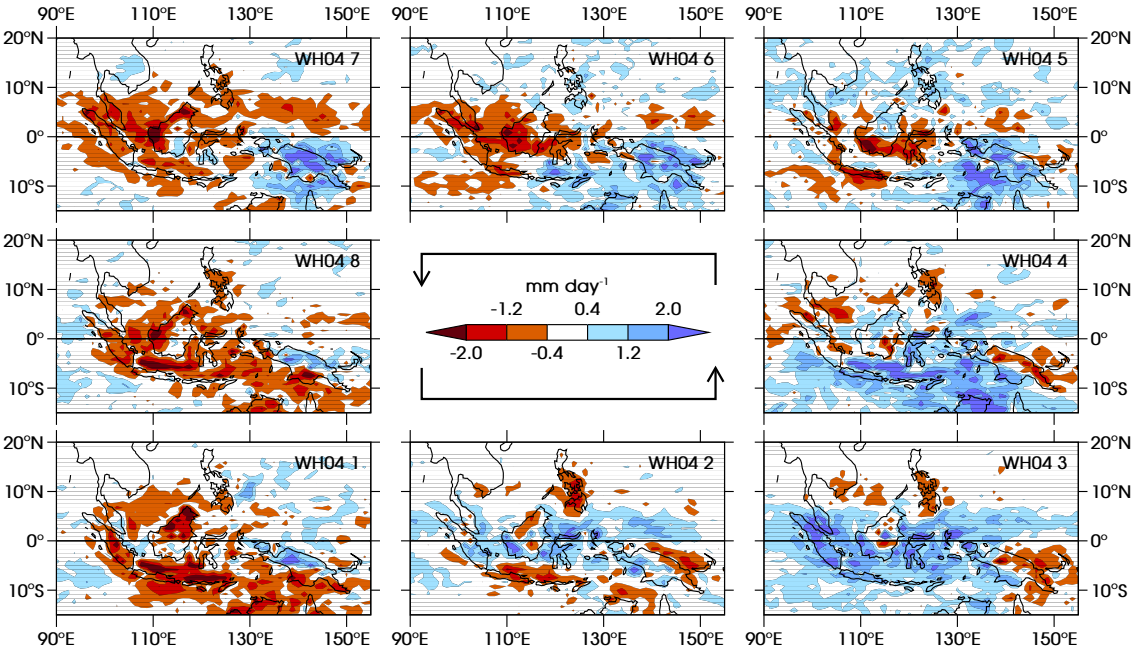

Figure 7.7: Anomaly of the amplitude r_d of the diurnal harmonic of precipitation in HiGEM in each phase of the MJO. Blue (red) regions indicate an enhanced (suppressed) diurnal amplitude. The equivalent plot for observations is shown in figure 5.2 (page 80; note the different colour scale).

almost all coastlines.

7.3 Scale interaction between the diurnal cycle and the MJO

The previous section showed that, over the Maritime Continent, HiGEM has an accurate diurnal cycle of wind but for some small errors, and a diurnal cycle of precipitation over mostly the correct areas but with the wrong phase and slightly too weak an amplitude. We now investigate whether the diurnal cycle is modulated by the MJO, and whether any modulation is similar to that seen in observations (chapter 5).

7.3.1 Modulation of the diurnal cycle by the MJO

We begin by considering the amplitude r_d of the diurnal harmonic of precipitation in each phase of the MJO. Phases of the MJO are determined using WH04's EOFs, as in chapter 6. The anomaly of the diurnal amplitude in each WH04 phase is shown in figure 7.7. Note that the colour scale is different

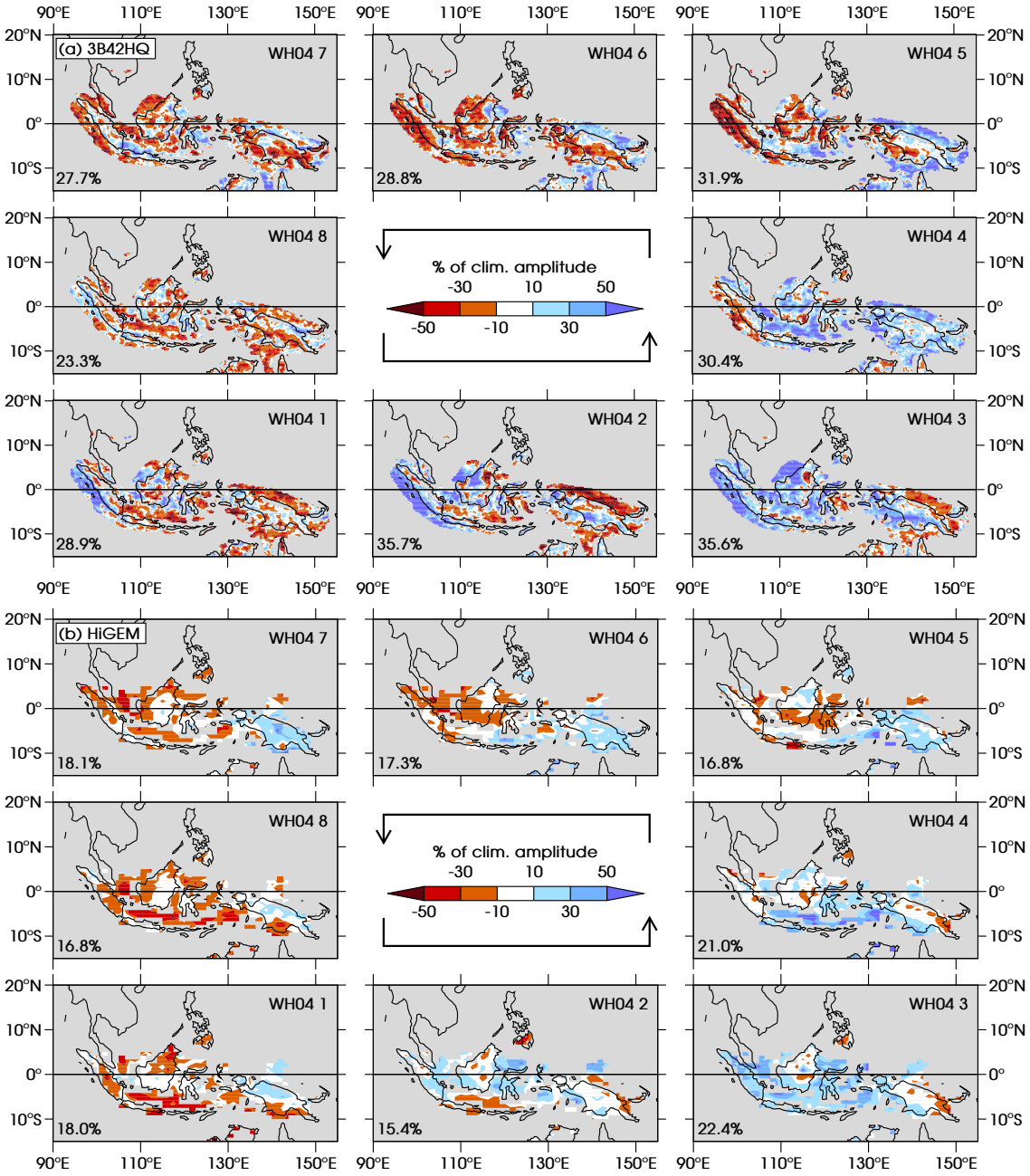

Figure 7.8: Anomaly of the amplitude r_d of the diurnal harmonic of precipitation in each phase of the MJO, as a percentage of the climatological r_d: (a) TRMM 3B42HQ and (b) HiGEM. Regions where the climatological r_d is less than 3 mm day^{-1} are masked out in grey. The figure in the bottom-left corner of each plot is the mean of the absolute value for that plot.

from that used for observations (figure 5.2, page 80). The anomalies in HiGEM tend to have the correct sign but are smaller than those in TRMM 3B42HQ by a factor of about 2 or 3. Even when we take account of the fact that the climatological diurnal amplitude is weaker in the model, the modulation is still relatively weak. Figure 7.8 shows the MJO anomalies of the diurnal amplitude

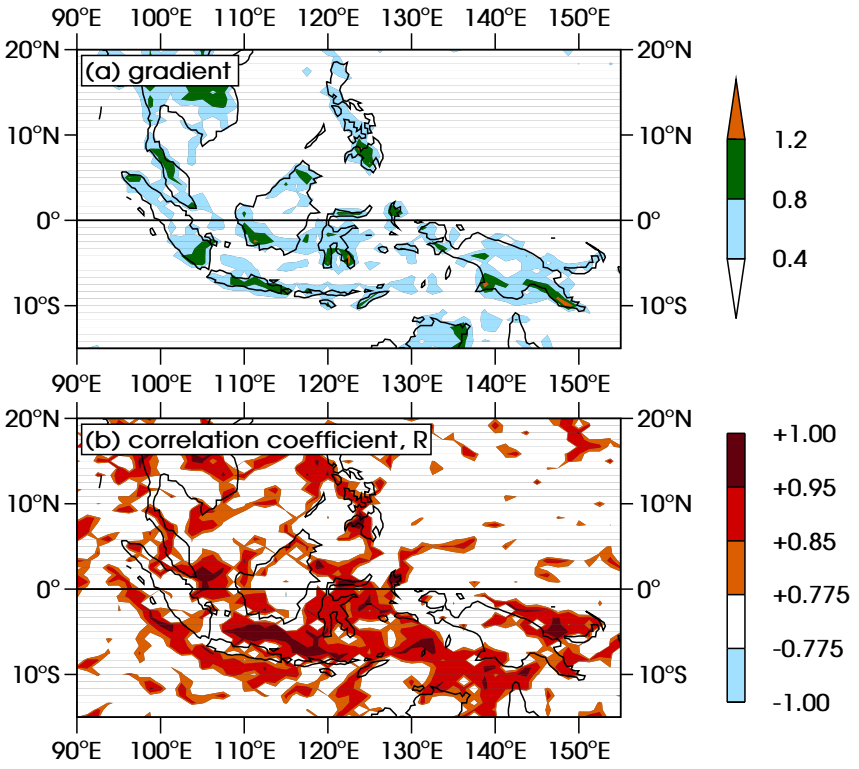

Figure 7.9: (a) Gradient and (b) correlation coefficient R of the linear relationship between the amplitude of the diurnal harmonic of precipitation for each WH04 phase, and the daily mean in the corresponding phase. In (b), regions in white are below the 95% confidence threshold of $|R| = 0.775$. The equivalent plot for observations is shown in figure 5.8 (page 90).

for both TRMM 3B42HQ and HiGEM, each as a percentage of the climatological amplitude at each grid point. Regions where the climatological diurnal cycle is weak ($r_d < 3$ mm day^{-1}) are masked out in grey. The mean of the absolute value of the data was found for each plot, and is shown in the bottom-left corner of each panel. The mean of these values is 30.3% for 3B42HQ and 18.2% for HiGEM. Thus, even when normalised by the climatological amplitude the model has a considerably weaker modulation of the diurnal cycle than exists in observations. However, there is a coherent structure to the regions of enhanced and suppressed diurnal cycle in HiGEM so the modulation of the diurnal amplitude in the model, despite being weak, is consistent.

In observations there were many localised effects meaning that the diurnal amplitude anomaly was very noisy. In figure 7.7 there is far greater spatial coherence, suggesting that the convective parameterisation responds to the MJO in a relatively consistent manner rather than being sensitive to location. As in observations, there is no clear relationship between orography and the modulation of the diurnal cycle. In many locations the anomaly is of the same

sign in 3B42HQ and HiGEM in particular MJO phases, but in some it is of the opposite sign. For example, over New Guinea in phases 6 and 7 the simulated diurnal cycle is enhanced whereas the observed diurnal cycle is suppressed. There is only a very weak correlation between the numbers in the bottom-left corners in figure 7.8 for 3B42HQ and for HiGEM, so there is little or no skill in simulating the varying strength of the diurnal cycle's modulation through the MJO cycle.

It was shown in chapter 5 that in observations the diurnal cycle is so strong that it almost entirely accounts for the daily mean precipitation, and that the "leaping ahead" of the daily mean precipitation with respect to the advancing MJO envelope could be explained in terms of a two-way interaction with the diurnal cycle. The starting point for this argument was to find the best linear fit between diurnal amplitude and daily mean precipitation through the eight MJO phases, the gradient and correlation coefficient R being plotted in figure 5.8 (page 90). This is repeated for HiGEM in figure 7.9. In observations there was a strong gradient (about 1 or even more) and a strong correlation (around 0.9 or even more) over those land areas where the diurnal cycle is strong. However, in the model the gradient is much less than 1 almost everywhere so the diurnal cycle is not strongly triggered at the same time as the daily mean MJO rainfall being strong. Furthermore, there does not tend to be a strong correlation over those regions where there is a strong diurnal cycle. Where the diurnal amplitude exceeds 10 mm day^{-1} the mean value of R is 0.714, which is below the 95% statistical significance threshold of 0.775 (the significance level is still quite high, however, at 92%). In observations the mean value of R where the diurnal cycle is strong was 0.899, statistically significant at a confidence level of 99%. In the model the diurnal cycle explains $R^2 = 51\%$ of the MJO variance in daily mean precipitation, as opposed to 81% in observations. The smaller gradient in HiGEM is consistent with the fact that the diurnal cycle is only weakly modulated as the daily mean rainfall changes in the MJO (figure 7.7). The daily mean precipitation is shown in figure 7.10 for both TRMM 3B42HQ and HiGEM. Although the model has a clear wet bias over ocean, over land the daily mean has a very similar magnitude in observations and the simulation with the exception of Java, where the modelled daily mean is too dry. The fact that the correlation coefficient R is weaker in the model than in observations is consistent with the fact that the climatological diurnal cycle is weak to begin with (figure 7.2a) but the daily mean is the same. Unlike in reality, in HiGEM there is no 1:1 relationship between daily mean and diurnal amplitude of rainfall

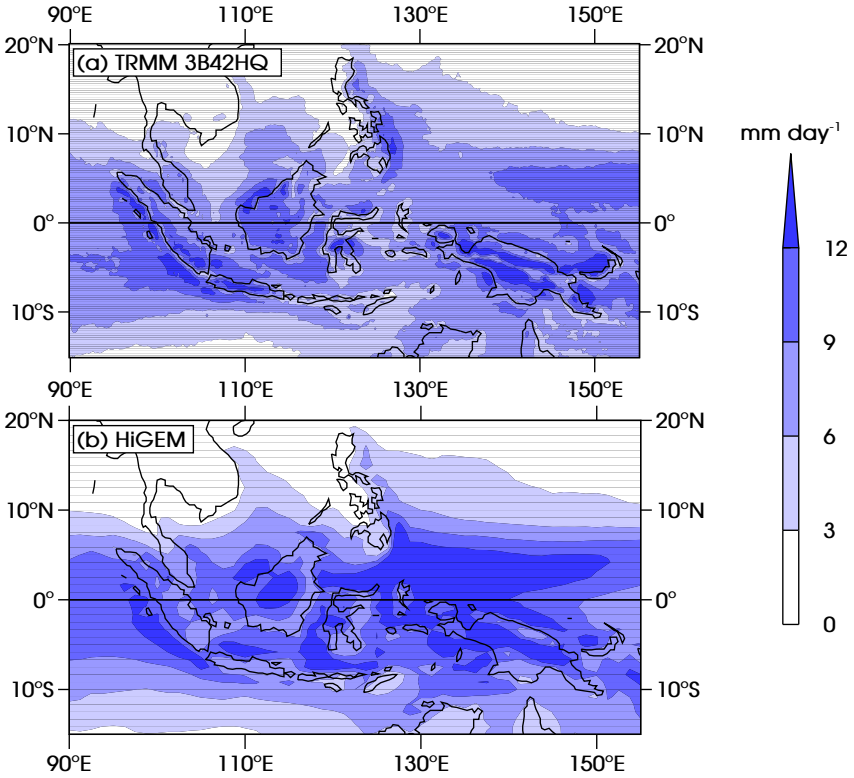

Figure 7.10: Daily mean precipitation in boreal winters from (a) TRMM 3B42HQ and (b) HiGEM.

as the MJO evolves, and the diurnal cycle explains much less of the variance in daily mean precipitation.

7.3.2 Relative MJO phases

As in figure 5.11 (page 94), we now compare the MJO signals of OLR, daily mean precipitation $\bar{r}$ and diurnal amplitude of precipitation r_d over land and over ocean. Figure 7.11a shows the means over the region 7°S–10°N, 100°–120°E (parts of Sumatra and the Malay Peninsula, Java and Borneo) and figure 7.11b shows the means over 12°S–3°N, 130°–153°E (New Guinea). In panel (a) the OLR signals are similar to those of $\overline{T}_b$ in observations, peaking in phase 4, as expected since OLR is used to define the WH04 phases themselves. (The OLR axis in inverted since lower OLR values correspond to active convection.) In observations the diurnal amplitude of precipitation peaks in phase 3 over both land and ocean, but only over land is it strong enough to make the daily mean precipitation also peak in phase 3. Over ocean the daily mean peaks in phase 4. In the model the diurnal cycle peaks over both land and ocean in phase 3, so it does leap ahead of the OLR envelope as in observations. Since

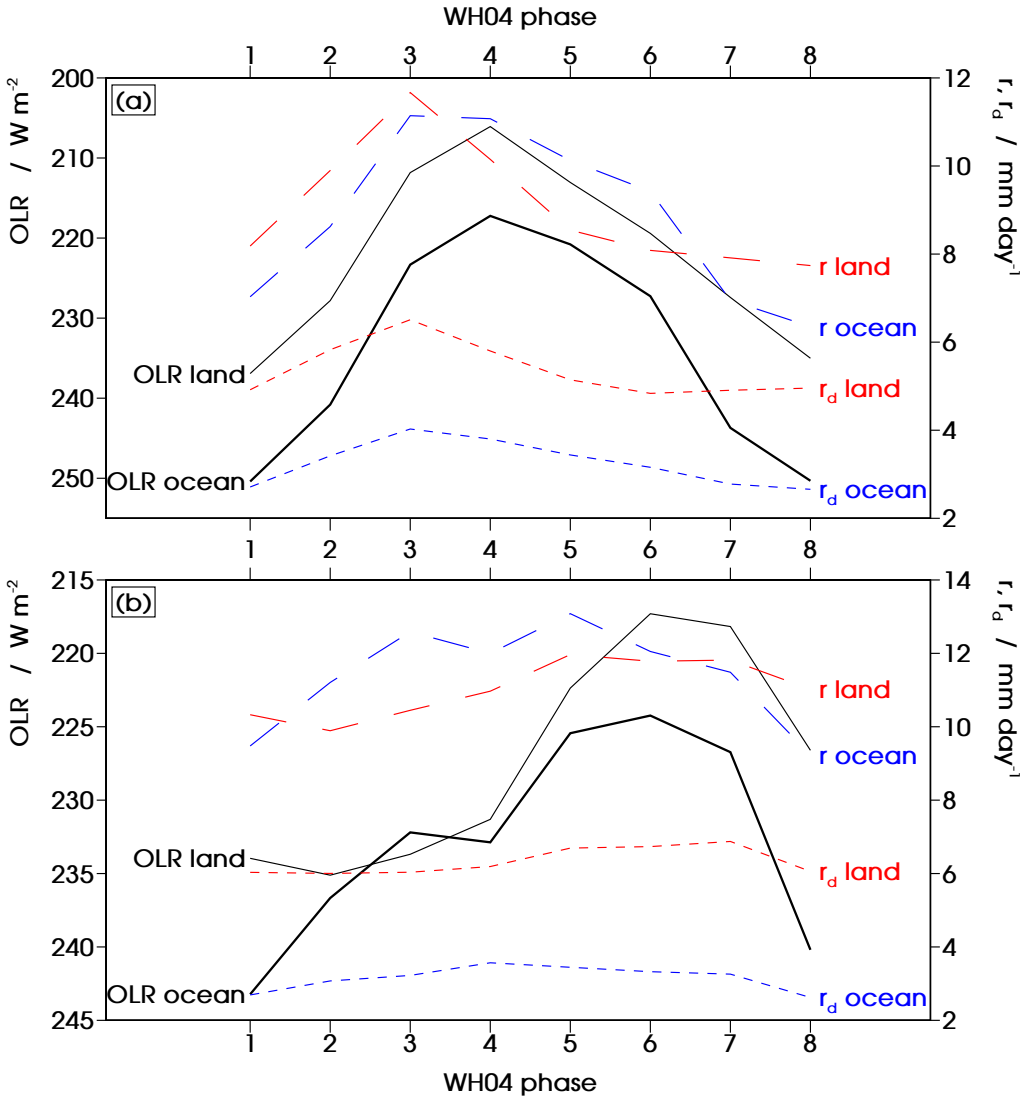

Figure 7.11: Means of daily mean OLR, daily mean precipitation (r) and amplitude of the diurnal harmonic of precipitation (r_d), averaged separately over land and ocean for the same domains used in figure 5.11: (a) 7°S–10°N, 100°–120°E (Borneo and most of Sumatra) and (b) 12°S–3°N, 130°–153°E (New Guinea). Note that the OLR axes are inverted. The equivalent plot for observations is shown in figure 5.11 (page 94).

we have established that this diurnal cycle, which is generally quite weak, accounts for only 51% of the MJO variance in daily mean precipitation even where the diurnal cycle is strongest, we do not expect it to affect the timing of the daily mean signal to a very great extent. However, the modelled daily mean precipitation does nevertheless leap ahead of OLR by one MJO phase over land as in the observations, and leaps ahead by the same amount over ocean, which did not happen in observations.

In panel (b) the picture is more complex. In observations $\overline{T}_b$ peaks in phase 5 but OLR does not peak until phase 6 in the model. As seen in figure 6.9, the

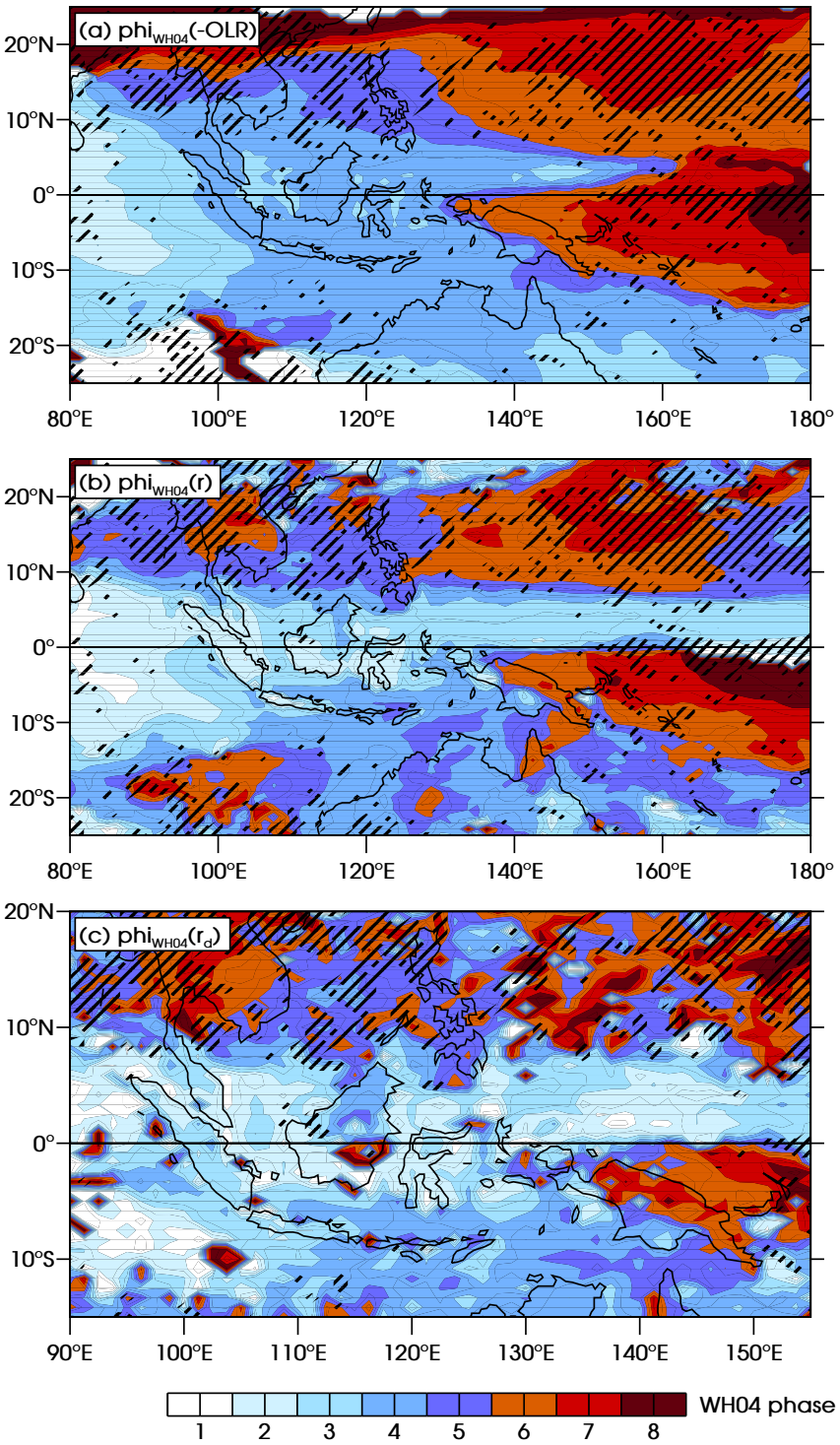

Figure 7.12: Phase of the "MJO harmonic" (see section 5.5.2) of: (a) daily mean negative OLR; (b) daily mean precipitation $\bar{r}$ and (c) diurnal amplitude of precipitation r_d. The phase is measured in MJO phases as defined by WH04. Black hatching indicates regions of low variability of the diurnal cycle during the MJO, defined as the anomaly in figure 7.7 being below 0.4 mm day^{-1} for all eight WH04 phases. The equivalent plots for observations are shown in figure 5.12 (page 96).

propagation from phase 5 to phase 6 is not quite realistic, explaining why the peak OLR signal occurs in the wrong phase. Here there is very little modulation of the diurnal amplitude over either land or ocean, and the daily mean precipitation, while it is modulated somewhat, has no clear MJO peak.

We conclude that the dynamics in the model do cause the diurnal cycle to leap ahead of the active MJO in the western Maritime Continent but the strengthening of the diurnal amplitude is insufficient to determine the phase of the daily mean precipitation. The daily mean does not change in a consistent manner as the MJO evolves. Over the first domain it peaks ahead of the OLR envelope, but over the second it is barely modulated at all. We know that 49% of modelled MJO variability in $\bar{r}$ is caused by phenomena other than the diurnal cycle, and it turns out that the convection parameterisation scheme has these phenomena coupled with the dynamics in such a way that they also leap ahead of the MJO, unlike in observations.

Having compared the large-scale conditions over land and ocean in the MJO, we now compare the timing of OLR and precipitation at each grid point by revisiting the idea of MJO harmonics (section 5.5.2). The phases of the MJO harmonics of $-\overline{\mathrm{OLR}}$, $\bar{r}$ and r_d are shown for HiGEM in figure 7.12. As was noted in section 6.3, even though the WH04 indices are based partially on OLR there are some differences between the MJO composites of brightness temperature $\overline{T}_b$ in observations and of OLR in the model. This can be seen in figure 7.12a with, say, the phase of the harmonic over Sumatra which is predominantly around phase 3 in observations, but in the model the strongest active OLR signal is not until around phase 4. Over New Guinea the most active OLR signal is delayed compared with observations, peaking in phase 6 over the majority of the island. There are similar disparities for panels (b) and (c). The crucial comparison to be made between observations and HiGEM is in the MJO phase lags, shown in figure 5.14 (page 99) for observations and figure 7.13 for the model. Broadly speaking the phase lags in the model are impressively accurate; they are of the correct sign throughout almost all of the domain, and are of approximately the correct magnitude. In panel (a) of each figure ($\Delta\phi\left(-\overline{T}_b, \bar{r}\right)$ for observations, $\Delta\phi\left(-\overline{\mathrm{OLR}}, \bar{r}\right)$ for HiGEM), we see that daily mean rainfall lags behind the brightness temperature or OLR signal over the land by roughly the same amount in the observations and the model. The major difference is over Sumatra, where the lag is about 1 WH04 phase in observations but about 2 phases in HiGEM. The other clear difference is between land and ocean; in reality the precipitation is roughly synchronous with the brightness temperature, but in HiGEM a lag

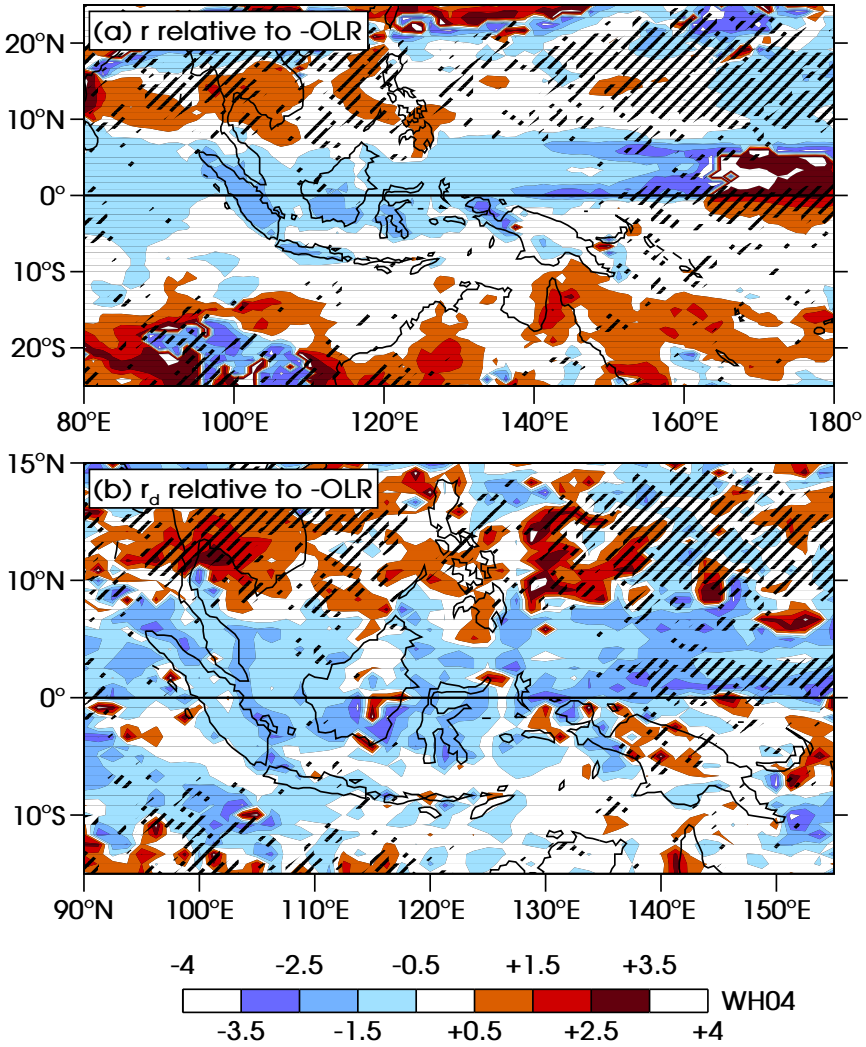

Figure 7.13: MJO phase lags (see section 5.5.2): (a) $\Delta\phi\left(-\overline{\mathrm{OLR}}, \bar{r}\right)$ (i.e., figure 7.12b minus 7.12a); and (b) $\Delta\phi\left(-\overline{\mathrm{OLR}}, r_d\right)$ (7.12c minus 7.12a). As in figure 7.12, the scale is measured in MJO phases as defined by WH04. If $\Delta\phi\left(-\overline{\mathrm{OLR}}, \bar{r}\right)$ is positive (negative) then the maximum in $\bar{r}$ lags (leads) the maximum in $-\overline{\mathrm{OLR}}$, and similarly for $\Delta\phi\left(-\overline{\mathrm{OLR}}, r_d\right)$. Black hatching is used as in figure 7.12. The equivalent plots for observations are shown in figure 5.14 (page 99).

exists just like over land, especially north of the equator within the Maritime Continent. In panel (b), as in observations the signal is generally quite noisy, but there are still clear similarities between HiGEM and TRMM. Over ocean within the Maritime Continent itself the diurnal cycle is consistently ahead of the OLR, as was the case in observations, and over land it peaks ahead of OLR in general but there is a considerable amount of local variability, and this variability does not agree with that in observations. However, it is *a priori* unlikely that a global model, unable to resolve all of the coastal and orographic features of the Maritime Continent, would ever simulate a quantity such as

$\Delta\phi\left(-\overline{\mathrm{OLR}}, r_d\right)$ accurately on small scales. Therefore, the fact that the overall picture of figure 7.13b shows the correct characteristics should be considered a success for the model.

In section 5.6.1 a physical mechanism was proposed for the scale interaction between the MJO and the diurnal cycle in terms of the underlying MJO propagation dynamics. We have seen that the diurnal cycle in the model is modulated by the MJO with approximately the correct MJO phase lag, but that the modulation is weak (and the amplitude of the diurnal cycle is weak in the first place). To investigate the causes of the model errors, we plot the same diagnostics as were used to demonstrate the physical mechanism in a reanalysis earlier (figure 5.15, page 102). This is shown in figure 7.14. Composites are plotted for phase 2 of the MJO, when the MJO is active over the central Indian Ocean. The pressure field in panel (a) shows the expected low-pressure trough extending along the equator to the east, corresponding to an equatorial Kelvin wave. We also expect to see off-equatorial low pressure regions to the west, associated with an equatorial Rossby wave. There is a broad, weak low pressure region in the southern hemisphere, and to the north of the equator the signal is even weaker, but the features are clearly present. However, the stream function contours in panel (a) and the wind vectors in (b) show very little cyclonic flow where the Rossby gyres are expected to be. On the other hand, the flow associated with the Kelvin wave is much more realistic with strong easterly flow on and around the equator to the east of the convective centre. It was also stated in section 5.6.1 that the previous suppressed MJO envelope has an associated Rossby wave response, with positive off-equatorial pressure anomalies to the west of the active convection. In HiGEM these are more clear than the Rossby wave structure from the active envelope, especially in the northern hemisphere. (These positive pressure anomalies are centred to the east of the domain shown here, but extend far enough west still to be visible in panel (a).)

In observations, the strong diurnal cycle being triggered ahead of the advancing active MJO envelope was attributed to convergence over the Maritime Continent islands which was able to sustain any convection there (and the main form of convection is the diurnal cycle). Three sources of this convergence were identified: ageostrophic flow into the equatorial Kelvin wave pressure trough due to friction with the surface, giving a negative contribution to divergence from $\partial v/\partial y$; easterly equatorial flow which grows stronger to the east, due to the equatorial Rossby wave from the previous suppressed MJO envelope, giving a negative contribution to divergence from $\partial u/\partial x$; and easterly

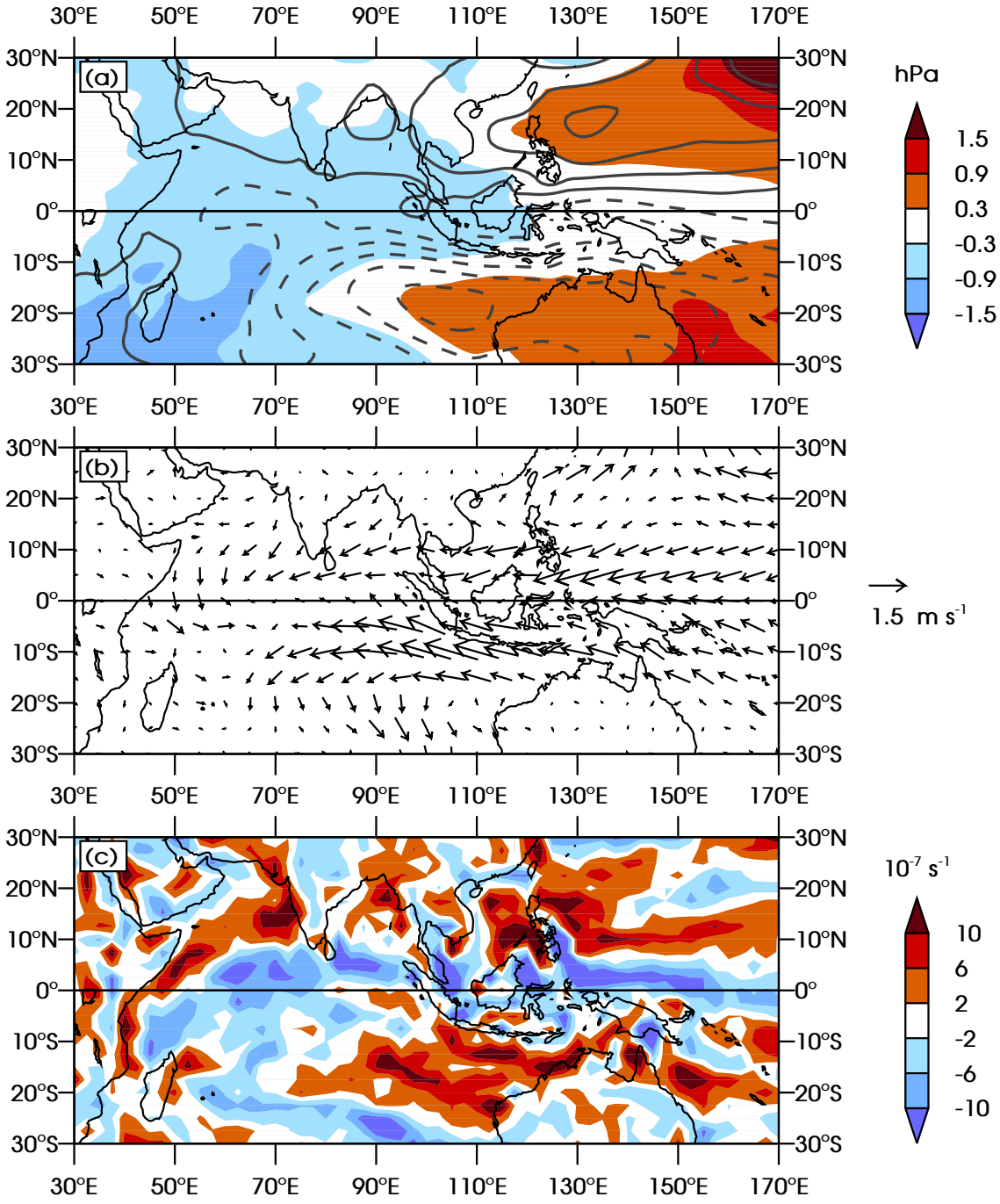

Figure 7.14: MJO phase 2 anomalies of: (a) mean sea level pressure with stream function contours at 10 m; contours are drawn every 4×10^5 m^2 s^{-1} with the smallest contours at $\pm 2 \times 10^5$ m^2 s^{-1}; positive (negative) contours are solid (dashed); (b) wind at 10 m (regridded to 5° resolution for clarity); (c) divergence at 10 m. The equivalent plot for reanalysis data is shown in figure 5.15 (page 102).

anomalies impinging on the orography of the Maritime Continent islands themselves, giving a further negative contribution from $\partial u/\partial x$. The first of these contributions is clearly present in HiGEM, with an equator-ward component of the flow appearing in the region 10°S–10°N, 90°–170°E in panel (b), causing

convergence just north of the equator. This band of convergence is seen in panel (c), mainly around 0°–5°N, 125°–155°E. In the reanalysis this band of convergence followed the islands of the Maritime Continent, reaching from Borneo across to Sulawesi and then down over the length of New Guinea. In HiGEM, however, the region of convergence does not follow the shape of the land, and instead forms the ITCZ (oriented entirely zonally, stretching into the Pacific Ocean). This explains why the enhancement of the diurnal cycle is not nearly as strong as in observations, and why the ITCZ appears so strongly ahead of the active MJO in the composites in figures 6.9 and 6.10.

7.4 Conclusions

In chapter 6 it was shown that HiGEM has a very realistic representation of the MJO, but for a few inaccurate features. In this chapter the scale interaction between the MJO and the diurnal cycle has been investigated and compared with the interaction found in observations (chapter 5).

The diurnal cycle of precipitation has an accurate spatial structure, with a stronger diurnal cycle over land than over ocean, although the amplitude is a little too weak. The gravest error is that the diurnal phase of the rainfall, whilst accurate over ocean, is several hours too early over land. The phase is locked to the phase of incoming solar radiation, with precipitation forming very suddenly as the sun warms the land. The coarseness of the model resolution (although the resolution is high by GCM standards) does not allow most of the coastal or orographic features to be resolved, with the result that some of the small-scale features of the diurnal cycle are not simulated by the model. For example, the model does not have precipitation forming at convex coastal regions then moving inland; rather, the precipitation tends to form homogeneously across land areas. Offshore propagation of gravity waves is simulated in some Maritime Continent locations but is often weak, and from other locations is missing entirely.

The daily mean wind field is generally very accurate in HiGEM, and there is also an accurate diurnal cycle. Winds around the coastline are almost always found to be more onshore in the evening and more offshore during the morning. There are some errors in the Maritime Continent, with the strength and spatial extent of regions of large diurnal difference being too small in places.

As in observations the MJO does modulate the strength of the diurnal cycle.

This modulation is generally of the correct sign but is too weak. This is true even when taking into account the weakness of the climatological diurnal amplitude. Over regions of strong ($r_d > 3$ mm day^{-1}) diurnal cycle, the mean strength of the modulation is 30.3% of the climatology for TRMM 3B42HQ but only 18.2% for HiGEM. The weak modulation, combined with the fact that over the land the daily mean precipitation is of about the right magnitude, means that only 51% of the MJO variability in $\bar{r}$ is explained by the MJO variability in r_d. In observations it was 81%. However, the sign of the diurnal amplitude anomaly is usually correct, suggesting that the correct mechanism for the modulation may be present over the Maritime Continent islands but with a smaller effect than it should have.

When averaging separately over land and ocean, and when comparing variables at each grid point using MJO harmonics, it is seen that the diurnal cycle, certainly over and around Sumatra and Borneo, does leap ahead of the advancing MJO OLR envelope as in observations. We know that the diurnal cycle is not strong enough to control the timing of the daily mean precipitation, and yet the daily mean does also leap ahead of the OLR. Indeed, the daily mean leaps ahead over both land and ocean, whereas in observations this occurred over land only. Whatever is responsible for the 49% of MJO variance in $\bar{r}$ that is not caused by the diurnal cycle must also be coupled to the model's dynamics in such a way that it is most strong just to the east of the active MJO.

In observations it appeared that the scale interaction between the MJO and the Maritime Continent diurnal cycle was caused by convergence on and around the equator ahead of the active MJO. In HiGEM it has been shown that an equivalent region of convergence does exist due to flow into the Kelvin wave pressure trough, but that it does not affect the Maritime Continent islands. Instead, it is this region of convergence which appears to cause the ITCZ to become too strong in the model, as identified in chapter 6.

Chapter 8

Conclusions and further work

The motivation for this research (see section 1.1) was the importance of precipitation over the Maritime Continent in the context of the tropical and global climate, and the fact that the diurnal cycle and the Madden-Julian Oscillation (MJO) are two of the most important sources of variability in determining the Maritime Continent's rainfall distribution. High-resolution satellite data and ever-improving climate models provide an opportunity to investigate these phenomena, and the relationship between them, in great detail.

8.1 Results from observations

8.1.1 Diurnal cycle

The diurnal cycle of precipitation from TRMM 3B42HQ was composited (figure 4.5, page 55), with times in local solar time (LST; all times hereafter are given in LST). This means that the composites are false in the sense that they do not provide a real view of the diurnal cycle at any single instant in time. For example, if the rainfall peaks at the same LST at two different locations, one at 100°E and one at 140°E, then in reality these peaks occur 2 hours 40 minutes apart, not simultaneously as the composites imply. However, the forcing behind the diurnal cycle of precipitation is the diurnal cycle of insolation, and we are more interested in how the precipitation varies in relation to this than how different parts of the Maritime Continent vary in relation to one another.

The diurnal harmonic was fitted to the composites at each grid point, allowing us to plot the amplitude and phase (figure 4.6, page 56). The amplitude

is considerably stronger over land than over ocean and peaks later, confirming previous studies. Over the islands the precipitation occurs earliest (15:00) over convex regions of the coastline, where onshore breezes first converge as the land warms faster than the ocean. The precipitation spreads inland until almost all of the land area is experiencing rainfall by late evening; the convection then decays overnight. Over ocean the main feature of the diurnal cycle is just offshore from regions of strong land-based convection. Here, gravity waves propagate away from the land overnight, triggering further rainfall along their path.

Derived from QuikSCAT data, the diurnal difference (18:00 wind minus 06:00 wind; figure 4.9, page 60 and figure 4.10, page 61) can be thought of as a characteristic amplitude of the diurnal cycle. The daily mean was also composited (figure 4.7, page 58 and figure 4.8, page 59). The composites are successful at showing the well-known aspects of the daily mean wind field throughout the tropics. For example, the trade winds and the inter-tropical convergence zone (ITCZ) are clear in figure 4.7. The diurnal difference shows the morning-evening change in direction of the land-sea breeze circulation, with winds blowing more onshore in the evening and more offshore in the morning. The high resolution of these composites means they are very detailed, and would be a very useful tool in verifying the daily mean and diurnal difference of wind in climate models. Future work will involve comparing these QuikSCAT composites with the output from runs of the HadGEM model, to investigate the effect on the diurnal cycle of having convection either parameterised or explicitly resolved. It was noted in section 4.5.2 that the QuikSCAT composites have streaks in them, which are probably artefacts caused by errors at the swath edges. These composites could be improved in future by neglecting a few pixels at both edges of the swath when processing the data.

8.1.2 Madden-Julian Oscillation and scale interaction

In order to track the stages of the MJO, several researchers have developed sets of indices (section 3.3). Some focus on the convective aspect of the MJO's structure while others focus on its associated atmospheric circulation anomalies. The indices of Wheeler and Hendon (2004; WH04) are used in this research since they attempt to diagnose both aspects, and because they are by far the most widely used indices in MJO research. MJO composites were made by averaging together the data for all days on which the RMM (Real-time Multivariate MJO) amplitude is greater than 1, for both $\overline{T}_b$ (figure 4.11, page 63) and daily mean

precipitation $\bar{r}$ (figure 4.12, page 64). This allowed us to study the MJO's structure in a high level of detail, in particular noting the manner of the MJO's propagation over the Maritime Continent. In both composites, but especially in the composite of $\bar{r}$, the MJO anomalies over the islands are often far smaller than or even of the opposite sign to those over the surrounding ocean. Such regions tend to be spatially quite coherent and cover almost all of, but only, the land. Therefore, the Maritime Continent islands are a special place in the MJO's domain.

This feature of the MJO was attributed in chapter 5 to a scale interaction between the MJO (larger-scale) and the diurnal cycle (smaller-scale). The amplitude r_d of the diurnal cycle is modulated by as much as ~10 mm day^{-1} in opposite phases of the MJO (figure 5.2, page 80), which is similar in magnitude to the modulation of $\bar{r}$ itself. Hence, the MJO has a very significant role in determining the strength of the diurnal cycle. Furthermore, it turns out that this modulation of r_d does not occur exactly in phase with the active-suppressed cycle of the MJO as defined by the $\overline{T}_b$ composites. Figure 5.11 (page 94) showed that the diurnal cycle over both land and ocean peaks sooner in the MJO cycle than the most active $\overline{T}_b$, by about 1 WH04 phase. Over land the daily mean precipitation also peaks ahead of $\overline{T}_b$ by about the same amount, but over ocean it is synchronised with $\overline{T}_b$. The relationship between $\bar{r}$ and r_d throughout the MJO, at each grid point, was shown in figure 5.8 (page 90). Over regions where the diurnal cycle is strong, the gradient of the linear regression between the two was on the order of 1, and the correlation coefficient tended to be about 0.9 or even more, which is statistically significant (95% confidence level). Therefore, the changes in $\bar{r}$ and r_d throughout an MJO cycle are almost in a 1:1 relationship, with 81% of the variance in daily mean precipitation being attributed to the diurnal cycle. Hence, the "leaping ahead" of the daily mean precipitation over land can be attributed to the fact that the diurnal cycle itself leaps ahead of the main MJO envelope; the fact that the same does not happen over ocean can be attributed to the fact that r_d is not strong enough to have an effect there.

The fact that, over land, daily mean precipitation peaks ahead of $\overline{T}_b$ means that $\overline{T}_b$ (or OLR) is not a good proxy for rainfall. Figure 5.11 involved averaging over areas of the Maritime Continent, but the disparity between $\overline{T}_b$ and precipitation was also shown at each individual grid point by figures 5.12 (page 96) and 5.14 (page 99). These were generated by computing the "MJO harmonic", a sine wave fitted through the eight WH04 composites of the MJO. The MJO phase lags in figure 5.14 show that, if OLR is used as a proxy for peak

MJO rainfall, it would estimate the daily mean rainfall 1 phase too late over most of the land. The phase lag between $\overline{T}_b$ and r_d is far more spatially noisy; over both land and ocean there are regions where the lag is non-zero, but even the sign of the phase lag tends to be quite spatially incoherent, so OLR does not give a good indication of the strength of the diurnal cycle either.

In order to investigate why the diurnal cycle leaps ahead of the main MJO envelope, the dynamics of the MJO propagation itself were considered (figure 5.15, page 102). It is known that the atmosphere's response to diabatic heating at the equator is an eastward-propagating equatorial Kelvin wave and a westward-propagating equatorial Rossby wave, and equivalent waves of opposite sign exist as a response to a region of suppressed convection. Figure 5.15 shows that these wave dynamics give rise to low-level convergence just to the east of the active MJO, through frictional convergence and within the Maritime Continent through the easterly flow impinging on topography. This convergence is able to sustain any convection that is present. Over the Maritime Continent islands, due to the land's low thermal inertia, the convection exists as a strong diurnal cycle. Hence, the diurnal cycle is strongest when the active MJO is just to the west, giving the phase lag of about 1 WH04 phase.

It should be noted that this mechanism, whilst consistent with all the observational results presented in this research, remains speculative. To show that a hypothesised physical mechanism is consistent with observations is not the same as demonstrating causality. In general in science, hypotheses can be tested by experiment by varying a single parameter in the physical set-up and noting how the system reacts in comparison with a control. Of course, meteorologists cannot vary the parameters of the real planet Earth, but such experiments can be performed in models. Future modelling studies could attempt to find evidence for a causal link between the MJO dynamics and the scale interaction. For example, a high-resolution model could be run over a limited domain, perhaps just covering one or two of the Maritime Continent islands. The Cascade project used high-resolution versions of the Met Office Unified Model with approximately 40 km, 12 km, 4 km and 1 km grid spacings (using the set-up described by Lean et al., 2008) to investigate scale interactions in the tropics. The same model could be employed here, using a version with explicit convection (probably at either 12 km or 4 km resolution). One approach would be to construct the MJO life cycle by taking the typical MJO length to be 48 days, so that each phase lasts nominally for 6 days. By linear interpolation between the eight phase climatologies the state of the MJO would be found

for each of the 48 days, and model runs could be initialised for each of these 48 days (it is unlikely that the MJO would be sustained for the duration of a full 48-day cycle). Throughout the run, the model would be forced daily at the boundaries of the domain. This would allow us to examine the day-by-day evolution of the Matsuno-Gill dynamics resulting from the MJO convection, the regions of convergence and divergence which form as a result, and whether this can be shown to be the main forcing behind the strength of the diurnal cycle. In further runs the effect of topography could be tested by flattening all of the Maritime Continent islands and comparing with the full-topography versions (for example, all land regions within the Maritime Continent could be given an altitude of 1 m; this retains the islands as regions of low thermal inertia whilst removing any mountains).

The analysis over the Maritime Continent was extended to the entire tropics (section 5.7). Although a detailed investigation into locations beyond the Maritime Continent is outside the scope of this project, it is still interesting to note whether a similar scale interaction occurs elsewhere. Of course the MJO's active and suppressed convective anomalies are confined to the eastern hemisphere around the equator, where there is very little land other than the Maritime Continent, and over ocean the diurnal cycle is very weak, so there are unlikely to be many locations where an MJO-diurnal cycle interaction can be observed in precipitation data. Indeed, in figure 5.18 (page 109) grid points are masked out in grey if the climatological diurnal amplitude is less than 3 mm day^{-1} or the amplitude of the MJO harmonic is less than 2 mm day^{-1}, and almost all of the tropics are masked out. The two locations outside the Maritime Continent which are unmasked and show both a strong gradient and correlation coefficient between $\overline{r}$ and r_d are Sri Lanka and Lake Victoria. It is a reasonable prediction that the mechanism behind this interaction over Sri Lanka is similar to that over the Maritime Continent, since it is another island within the MJO convection region. However, the MJO envelopes are very weak over Lake Victoria, and this is an area of water within a region of land, the reverse of the Maritime Continent and Sri Lanka. A diurnal breeze circulation is likely to exist at the lake edge, similar to the Maritime Continent coasts, but determining whether the mechanism of the interaction is the same as over the Maritime Continent requires further research. As mentioned in section 5.8, this result could be crucial to understanding storms over Lake Victoria which are often life-threatening to fishermen, and are the subject of modelling studies designed to improve forecasting.

The nocturnal offshore propagation of gravity waves from the Maritime Continent islands, and the relationship with the MJO, were also investigated using composites created from 3B42HQ. Three case study regions were chosen (figure 5.3, page 82): south-west of Sumatra, north-east of Borneo and north-north-east of New Guinea. The composites of these convectively-coupled gravity waves (figure 5.4, page 84) show that throughout the MJO their propagation speeds change considerably off the coasts of Sumatra and, to a lesser extent, Borneo and New Guinea. In general, faster speeds were found during more active MJO phases. This modulation was shown to be consistent with three possible causes. First, the heating profiles change throughout the MJO which, as demonstrated by Love et al. (2011), can affect which gravity wave modes are triggered with deeper, lower-order, faster modes associated with the presence of deeper convection. Second, the static stability of the atmosphere changes throughout the MJO cycle and has a direct impact on gravity wave speed. The more stable the atmosphere, the higher the frequency and faster the propagation speed of a gravity wave, since the buoyant restoring force is stronger. As the static stability decreases during the suppressed phase of the MJO the gravity waves tend to propagate more slowly, whereas during the active phase, when moist convection returns the atmosphere to a more stable state, the waves tend to propagate faster. Third, changes to the background flow in the upper troposphere arising from the MJO are consistent with the changes in propagation speed off the coats of Sumatra and Borneo. Also, there is a suggestion that the wind may have a particular effect if the vertical shear throughout the troposphere is minimal so the wind is quasi-barotropic. A further effect which was observed was the speeding up of wave propagation away from the coast of Borneo. This is also dependent on the phase of the MJO.

8.2 Modelling

Despite the importance of the MJO, it is frequently simulated badly by climate models, as discussed in section 3.4.1. Common errors include a lack of eastward-propagating variability on intra-seasonal time scales, an MJO with an incorrect spatial distribution and a failure to couple convection to the atmospheric dynamics. The main causes of these errors include unrealistic convective parameterisation schemes, a resolution that is too coarse (either horizontally or vertically), biases in the mean state and a failure to represent coupled processes between the atmosphere and the ocean.

The interaction with the diurnal cycle is an important feature of the MJO since it determines the way in which the MJO behaves over the Maritime Continent, one of the areas of strongest rainfall in the world (figure 1.2, page 6). Therefore, even if a model is broadly successful at simulating the MJO it is important to study the Maritime Continent region specifically, to determine whether the model is able to simulate the scale interaction. Errors in simulating the deep convection over the Maritime Continent, for example having the strongest convection at the wrong time of day or at the wrong time in the MJO, will cause errors in the radiation budget since clouds have a high albedo and thus reflect a lot of incoming solar radiation back to space. Since the scale interaction appears to arise as a direct result of the dynamics associated with the diurnal cycle and the MJO, a study into the accuracy of its simulation is likely to amount to a study into whether the diurnal cycle and the MJO themselves are correctly simulated in the first place. The model used in this study was the High-resolution Global Environmental Model (HiGEM). All of the diagnostics used for observations can also be used in the model also to verify how realistic the diurnal cycle, MJO and their scale interaction are.

8.2.1 Madden-Julian Oscillation

In chapter 6 it was shown that HiGEM has a well simulated MJO. A Hovmöller diagram of bandpass-filtered OLR (figure 6.2b, page 116) clearly showed alternating active and suppressed anomalies propagating eastwards over the eastern hemisphere with a frequency similar to that of the real MJO. This Hovmöller diagram was just a case study, illustrating one particular year, but the existence of MJO-like variability in general was shown by the Wheeler-Kiladis diagram in figure 6.4 (page 118). MJO variability is eastward-propagating with frequency below around 1/30 cycles per day. Such variability does exist but over a larger range of zonal wavenumbers than in the reanalysis used in figure 4.14 (page 68), implying an inconsistent zonal scale to the MJO's OLR envelopes. However, by the standards of current state-of-the-art GCMs the MJO signal is highly impressive. A strong peak exists in the correct region of the Wheeler-Kiladis diagram, and it is considerably stronger than the corresponding westward-propagating region on the left-hand side of the figure. Even before we examined the detailed spatial structure of the MJO and the nature of its propagation (e.g., how sporadic it is), this result indicated that HiGEM simulates the MJO with a greater degree of fidelity than most existing GCMs.

Ideally, we would like to examine the propagation of HiGEM's MJO using the same indices as are used for observations, the WH04 RMM indices. Given the widespread use of these indices in MJO research, using them to investigate the MJO in HiGEM would provide consistency with other studies. However, it would not be very meaningful to project the model output onto the WH04 EOFs if they do not accurately represent the structure of the modelled MJO. Therefore, the same process used by WH04 was applied to the model, to compare the EOFs from HiGEM to those used for diagnosing the real-life MJO. It was shown (equations 6.5 and 6.6) that WH04's leading two EOFs are degenerate as they explain 12.8$\pm$0.68% and 12.2$\pm$0.65% of the total variance each. Therefore, when investigating the representation of the MJO in any model, what is important is to find that each of the leading two EOFs correspond closely to one or other of the leading two WH04 EOFs. If they are ordered differently from WH04 this does not indicate an error in the MJO's simulation. In HiGEM the EOFs do indeed happen to be ordered the other way round from WH04, with the first EOF in HiGEM having a similar zonal structure to the second EOF in WH04 and *vice versa* (figure 6.6, page 123). Peaks and troughs in the EOFs occur at almost the same longitudes in both OLR and zonal wind. There is only one clear difference between WH04 and HiGEM, which is the existence of a fairly deep trough in the OLR part of HiGEM's EOF1, over the eastern Maritime Continent; the equivalent trough in the WH04 EOF2 is very shallow.

The Hovmöller diagrams, Wheeler-Kiladis diagram and WH04-style EOFs all involve averaging over latitude and considering the zonal structure only, so none of the analysis up to this point considered the full horizontal structure. To see this full structure, composites were created of OLR (figure 6.9, page 128) and daily mean precipitation (figure 6.10, page 129) for each WH04 phase (using the real WH04 EOFs rather than those generated from HiGEM). Although the eastward propagation is broadly realistic, as it must be by definition for OLR because of the way in which the WH04 phases are defined, there is a clear error in that the ITCZ peaks strongly in the wrong phase. This has the effect of splitting the MJO's active and suppressed envelopes into two, interrupting the MJO structure considerably. This error in the ITCZ is consistent with the unrealistic feature in EOF1 generated from HiGEM (figure 6.6d) over the eastern Maritime Continent. Since EOFs are generated so as to maximise the variability in the principal components (hence, EOF1 here is generated so as to maximise the variability in RMM1) this feature exists because the erroneous ITCZ in the OLR data projects strongly onto it, positively in some phases and negatively in

others.

The new diagnostics presented in section 4.6.3 to investigate the nature of MJO propagation were applied to the model to see whether any significant similarities or differences exist compared with observations. First, the number of days and mean amplitude of the MJO in each phase were plotted (figure 6.11, page 131). The significant result was that there is a tendency for the model to favour RMM2 being stronger than RMM1 (i.e., the distribution of number of days is skewed towards phases 2, 3, 6 and 7). This is also consistent with the strong ITCZ error. In the WH04 EOFs, which were used for these RMM time series, the feature corresponding to the ITCZ is in EOF2 but, as mentioned above, is very weak. Therefore, when the HiGEM data are projected onto these EOFs there will be a tendency for them to have a large principal component of EOF2. Hence, there is a tendency for |RMM2| to be large, so that phases 2, 3, 6 and 7 are favoured. The mean RMM amplitude for each phase, when days with an amplitude of less than 1 are neglected, is strongest in phase 3 in observations (mean amplitude 1.88) but is weakest in the same phase in HiGEM (mean amplitude 1.56), whereas for all other phases the model mean amplitudes are approximately accurate. The reason for this is unclear and merits further study. The first fact to be established would be whether any of OLR, u_{850} or u_{200} are chiefly responsible for the weak projection onto the EOFs in HiGEM, or whether it is due to a combination of the three, which would indicate whether the error is in the convection, the circulation or both.

A histogram indicating the frequency of propagation events was presented in figure 6.13 (page 133). A propagation event is defined as the MJO moving from one phase into the next (e.g. 4 to 5, or 8 to 1), where days with an RMM amplitude of less than 1 are labelled as "phase 0" so never count as a propagation event. There is a tendency in the model for MJO propagation to cease once it reaches phase 3 (there are significantly many events ending at phase 3 in the histogram). This is consistent with the fact that the mean amplitude is weak in phase 3, since an MJO that is quite weak on one day is presumably more likely to "die" (i.e., have its amplitude dip below 1) during the following few days, before it reaches the next phase. Also, the model does not have a significantly small number of events ending at phase 2, whereas this is the case in the real-life MJO (figure 4.17, page 72). The reason for this is also unknown and needs further investigation. A further discrepancy in the model is the amount of MJO "inertia" – that is, the tendency for the MJO to remain in the same phase for consecutive days (figure 6.12, page 131 – cf. figure 4.16,

page 70). In observations the MJO is more likely to remain in the same phase for just one day than for any other particular number of consecutive days, and the probability decreases with an increasing number of consecutive days. In the model, however, the MJO is most likely to remain in the same phase for three consecutive days. Again, to determine the reason for this bias in the model requires further research.

8.2.2 Diurnal cycle and scale interaction

The diurnal cycle of precipitation was composited and linearly interpolated to the same times of day as TRMM, for ease of comparison (figure 7.1, page 138) and the same harmonic analysis was performed as for observations, giving us the amplitude and phase (figure 7.2, page 139). It is well known that models tend to have the diurnal phase over land occurring far too early in the day (section 2.2.3) and HiGEM does have this problem, with precipitation tending to peak around the middle of the day, in time with the diurnal solar cycle. This indicates an error in the convective parameterisation scheme and is likely to be causing further model errors since it means there is a high cloud albedo at the wrong time of day. As mentioned at the start of this section, this is likely to be affecting the radiation budget in the model, since less solar radiation reaches the ground around midday than is realistic, and more solar radiation reaches the ground than is realistic later in the day. In observations the precipitation was seen to begin at the coastlines and move inwards throughout the afternoon. A first glance at the diurnal phase in HiGEM (figure 7.2b) suggests that the same effect occurs, since the diurnal phase is earliest at the coasts and latest in the middle of the islands. However, this was attributed to the fact that the precipitation decays later inland, generally over high topography, whereas the initiation happens almost homogeneously.

The amplitude of the diurnal cycle is considerably more accurate than the phase, with the strongest and weakest diurnal amplitudes occurring in approximately the correct locations. In particular, the land correctly has a much stronger amplitude than the ocean. However, the amplitude is in general too weak. For example, over high orography the observed diurnal amplitude is over 9 mm day^{-1} (Sumatra) or over 12 mm day^{-1} (Java and New Guinea), whereas in the model it is generally below 9 mm day^{-1}. This may be partly due to the fact that the orography in HiGEM fails to capture most of the high mountain peaks of the Maritime Continent (figure 6.1, page 114). In observations there were

regions where gravity waves could clearly be seen, which trigger precipitation as they propagate. In HiGEM gravity waves appear to propagate south-west from Sumatra and north-north-east from New Guinea, albeit more weakly than in observations. Over other regions there is no clear propagation signal.

The daily mean (figure 7.3, page 142 and figure 7.4, page 143) and 18:00 minus 06:00 diurnal difference (figure 7.5, page 144 and figure 7.6, page 145) of wind were also composited. Both the daily mean and diurnal difference were extremely accurate, with all of the large-scale features seen in observations also present in the model. There are some model errors in diurnal difference over the Maritime Continent, but they are relatively minor. For example, the diurnal difference is too weak just north of Java, and off the south-west coast of Sumatra the change in wind between morning and evening is almost entirely zonal rather than at a 45° angle to the equator. The region over which the diurnal difference in u off the south-west coast of Sumatra exceeds 0.5 m s^{-1} is far smaller than in observations. Conversely, the region over which the diurnal difference in v off the north coast of New Guinea exceeds 0.5 m s^{-1} is far greater than in observations. It is impossible to tell from the snapshots we have of the observed diurnal cycle whether something like the modelled diurnal difference does occur in reality but at a different time of day. Hence, we cannot tell whether errors in the model are biases in diurnal phase or amplitude. Overall, however, the diurnal cycle is very accurate even though, as we have already seen, the diurnal phase of precipitation is not. Since the dynamical fields of the diurnal cycle are realistic, this suggests that the error in the convection scheme is a failure to couple convection to the dynamics. This may also explain the lack of gravity wave propagation seen in the precipitation data.

A key result of chapter 5 was that the diurnal amplitude of precipitation is significantly modulated by the MJO. In HiGEM, this modulation also exists but is much weaker (figure 7.7, page 146). The sign of the r_d anomaly tends to be accurate, so the correct interaction between the diurnal cycle and MJO does exist. However, even when the weakness of the climatological diurnal cycle in the model is taken into account, this interaction is too weak (figure 7.8, page 147). The average modulation of the diurnal amplitude, across the eight phases of the MJO, is 30.3% in 3B42HQ but only 18.2% in HiGEM. It is quite possible, however, that the weakness of the climatological r_d and the weakness of its modulation are both manifestations of the same error in the model, especially given that the sign of the modulation tends to be correct. If, as suggested above, the main error in the convective parameterisation scheme is that convection is not properly

coupled to dynamics, and given that we believe the MJO propagation dynamics to be responsible for the scale interaction, it could be that this is the underlying cause of both errors.

It was also shown in chapter 5 that the most enhanced diurnal cycle does not occur quite in phase with the MJO but 1 WH04 phase ahead of the most active large-scale MJO conditions, and that over land the diurnal cycle is so strong that the daily mean also peaks 1 phase ahead of the large-scale MJO. However, in the model the modulation of r_d is weaker so the diurnal cycle cannot itself determine the timing of the daily mean precipitation (figure 7.9, page 148). Where the diurnal cycle is strong it accounts for only 51% of the MJO variability in $\overline{r}$; the equivalent figure in observations was 81%. Hence, whatever the timing of the daily mean precipitation in the modelled MJO it cannot be attributed to the diurnal cycle alone. And yet, over Sumatra and Borneo it was shown that $\overline{r}$ does peak 1 phase ahead of OLR (figure 7.11a, page 151) over land, and also over ocean. The same phase lag relative to OLR exists for r_d as well, so the diurnal cycle does realistically leap ahead of the MJO, but whatever precipitative systems account for the remaining 49% of MJO variability in $\overline{r}$ must also leap ahead of the MJO by about 1 phase, over ocean as well as over land. The relationships between OLR, $\overline{r}$ and r_d at each grid point were compared using the difference in phase between their MJO harmonics (figure 7.13, page 154). In observations the daily mean precipitation was out of phase with $\overline{T}_b$ over land, but in the model the same is true over the ocean also. Over Sumatra, the MJO phase lag is 2 WH04 phases (that is, $\overline{r}$ peaks a quarter of an MJO cycle ahead of the most active OLR), so OLR acts as an even worse proxy for rainfall over that location. Overall, however, the phase lag is reasonable, both for $\overline{r}$ and r_d. Thus, one aspect of the convection scheme is very accurate – the strongest OLR signal does not coincide with the heaviest precipitation. The reason for this is not certain since the relationship between precipitation and OLR is complex. A strong negative OLR anomaly may be caused by, say, high cirrus anvils forming at the top of deep convective cloud, but a more positive OLR signal does not necessarily imply a lack of such anvils. For example, it may instead arise from there being significant gaps between clouds so that the infra-red instrument is seeing right down to the ground, especially when the size of each cloud is much smaller than the grid point spacing.

This all raises some more questions for further study. First, what type of weather systems are present in the MJO precipitation in the model? In addition to the short-lived diurnal cycle convection, the active MJO envelope presumably

consists of more persistent weather systems. A further question, then, is why the model has so much MJO variability in the form of these other weather systems and why they, like the observed diurnal cycle, do not have precipitation peaking in phase with OLR.

The scale interaction in observations is consistent with there being a region of convergence over the Maritime Continent resulting from the MJO's associated equatorial wave dynamics when the active envelope is over the eastern Indian Ocean. In HiGEM the MJO dynamics are quite accurate, but the region of convergence lies in the wrong location (figure 7.14, page 156). There is a low-pressure trough on the equator to the east of the active MJO envelope as a result of an equatorial Kelvin wave and, as in reality, there is frictional inflow contributing to the meridional ($\partial v/\partial y$) component of convergence. However, in reality there also appear to be contributions to the zonal ($\partial u/\partial x$) component of convergence, in part from the easterly low-level wind anomalies which impinge on topography. The resulting region of convergence roughly follows the shape of the Maritime Continent islands from Borneo across to New Guinea. However, in the model the resulting convergence is in a zonal band over the ocean in the eastern Maritime Continent, just north of the equator, where the ITCZ is found. The convergence being in the wrong location is consistent with both the ITCZ peaking at the wrong time in the MJO and the diurnal cycle's modulation being weak over the islands. Further model runs could be designed to investigate why this error occurs. For example, the effect of artificially introducing extra topography could be investigated, to see whether this causes the strongest convergence to exist over the land rather than over the ITCZ region.

8.2.3 Implications for modelling studies

Despite the errors in HiGEM which have been detailed here, fundamentally the MJO is highly accurate by current model standards. This research has not attempted to determine what aspect of the model is responsible for this. One possible explanation is that the sea surface temperature and atmosphere-ocean coupled processes are both represented particularly accurately in HiGEM. (As stated in section 3.4.2, several studies have indicated that realistic coupling between the atmosphere and ocean can directly improve the simulation of the MJO in GCMs.) These processes, and others, may also indirectly improve the MJO by improving the mean state of the atmosphere and ocean. Some of the skill in representing the MJO might also be attributable to the model's high

resolution or to the particular way in which the convection parameterisation scheme operates (even though we have seen that the parameterisation gives rise to significant errors on diurnal time scales).

The most obvious error still to be fixed in the MJO is the ITCZ peaking in the wrong phase. However, it is encouraging that many of the model biases identified appear to be linked to this one error, so it is quite possible that an improvement in this one respect could also improve other aspects of the MJO's representation. Given that errors in the MJO and diurnal cycle must cause errors in the energy and radiation budgets of the model, for example through inaccurately modifying the global-mean albedo, the model will have been tuned in some way to offset these biases. For example, other values of albedo are likely to have been changed elsewhere in the model such that the mean state of the simulation as a whole remains as accurate as possible. This means that one process may be inaccurately represented in order to cancel out the errors caused by another process. Therefore, any improvement to the simulation of the MJO or the diurnal cycle may have unexpected side effects which could even reduce the model's overall accuracy in the first instance. However, retuning the model to take account of these changes should, ultimately, allow the model set-up to take more realistic values for all its parameters, improving the simulation of climate processes in general. The results of this particular research could turn out to have only a small effect in this regard, but are still part of the important overall process of making the model as close an analogue to the real climate as possible.

All of the diagnostics used for analysing observations in this thesis could be applied to any climate model, obviously provided that it is set up to output data at sufficiently small time intervals to be able to analyse the diurnal cycle. This research has shown that a comprehensive study of the MJO in any given model requires a broad range of diagnostics to be used. This in contrast to the approach of studies such as Crueger et al. (2013) in which a model's ability to simulate the MJO is measured by a single metric. Such an approach could be used as a first indication of whether a model has any feature resembling an MJO, but it is emphatically not sufficient to use one metric alone.

One type of diagnostic commonly used by researchers is a frequency-wavenumber diagram such as the Wheeler-Kiladis diagram, to identify whether there is MJO-like variability in a model (e.g., Hung et al., 2013; Zhang, 2005). However, the complexity of the MJO's structure over the Maritime Continent means that, in order to demonstrate the MJO's accuracy, full composites of

fields such as precipitation should be used, else important aspects of the MJO life cycle are never studied. Given the role of the diurnal cycle in the nature of the MJO over the Maritime Continent, it is suggested that the analysis of the scale interaction described in chapter 5 should also be considered an important aspect of MJO verification. Composites do not indicate how frequently each of the MJO phases occurs, nor how quickly the MJO propagates between them. Therefore, the diagnostics showing the distributions of MJO phase, amplitude, inertia and propagation events (which demonstrate the MJO's episodic nature) should also be included in any MJO modelling study. However, given the range of MJO indices which have been developed, a better analysis of the MJO would make use of more than just the WH04 indices, as suggested by Straub (2013). A comprehensive study should use the WH04 indices and at least two others, at least one which focuses on the convection in the MJO and at least one which focuses on the planetary-scale circulation. A prerequisite for using any indices, however, should be that EOFs generated from the model output should be similar to those used in creating the indices. If they are not similar it is not very meaningful to apply the existing indices, since the model is likely just to project weakly onto the EOFs on most days which will hide any propagation which exists. In such circumstances EOFs from the model itself should be used, effectively creating a set of bespoke MJO indices. If this is necessary it would indicate major errors in the model but would still be useful to analyse any MJO-like propagation that does exist.

In section 1.2 it was suggested that a better understanding of the MJO and the diurnal cycle could, in principle, improve our ability to forecast the weather, in particular precipitation, over the Maritime Continent. We know that the chief contributor to the Maritime Continent precipitation is the diurnal cycle and we have seen the phase and amplitude of the mean diurnal cycle at every TRMM 3B42 grid point in each of the WH04 phases. It must be remembered that localised effects do exist, so the principle that precipitation will leap ahead of the active MJO may not hold equally well for all locations. (For an example of the effect of the MJO on precipitation at a very local scale, see Matthews et al. 2013.) However, in order to develop a forecasting system from this it would be necessary to carry out further research into the consistency of the diurnal cycle within each phase. Measuring the variance of precipitation within each phase would give a first indication of whether reliable statistical forecasts could be produced on the basis of knowing the current MJO phase. Other factors influencing the precipitation are likely to include the season (boreal

winter versus boreal summer – recall that the composites here were for boreal winters only) and the phase of the El Niño–Southern Oscillation. Of course, the presence of other weather systems such as tropical cyclones would not be accounted for by these methods at all. The use of the MJO to forecast precipitation would also, of course, require accurate forecasts of the evolution of the MJO itself. Experiments could be performed with HiGEM to discover whether it has skill at forecasting real-life MJO cycles. For example, the model could be initialised with the conditions from a particular day of a real MJO to see whether the ensuing propagation around the WH04 phase diagram follows reality, or whether it follows a completely different (albeit realistic-looking) track. For some particular case study in which the MJO makes at least one whole circuit around the WH04 phase diagram, model runs could be initialised with the conditions on each day to find the average number of days before a HiGEM integration diverts significantly from the real MJO. Similarly, the model could be initialised 1, 2, 3, ... days before the onset of the MJO convection to determine how far in advance, if at all, it is able to forecast MJO initiation.

8.3 Concluding remarks

The key finding of this thesis is the two-way interaction between the Madden-Julian Oscillation and the diurnal cycle of precipitation over the Maritime Continent. The MJO acts to enhance the diurnal amplitude slightly to the east of the active convection envelope. Most of the MJO's propagation is over open ocean where the diurnal cycle is weak, but over the Maritime Continent the low thermal inertia of the land means the diurnal cycle is much stronger. The diurnal precipitation peaks about one-eighth of an MJO cycle ahead of the arrival of the most active large-scale MJO conditions, and over land this is so strong that it is the chief contributor to the mean MJO signal, so that the structure of the MJO is modified by the presence of the Maritime Continent. The HiGEM model, which represents the MJO especially accurately by current model standards, does simulate the diurnal cycle and its modulation by the MJO, but weakly. These findings have significant implications for anyone wishing to produce forecasts for the Maritime Continent.

References

Ajayamohan RS, Khouider B, Majda AJ: Realistic Initiation and Dynamics of the Madden-Julian Oscillation in a Coarse Resolution Aquaplanet GCM. *Geophys. Res. Lett.*, **40**, 6252–6257 (2013).

Ambaum MHP: Thermal physics of the atmosphere. *Wiley-Blackwell*, Chichester, 256 pp. (2010).

Batstone CP, Matthews AJ, Stevens DP: Coupled ocean-atmosphere interactions between the Madden-Julian Oscillation and synoptic-scale variability over the warm pool. *J. Climate*, **18**, 2004–2020 (2005).

Benedict JJ and Randall DA: Impacts of Idealized Air-Sea Coupling on Madden-Julian Oscillation Structure in the Superparameterized CAM. *J. Atmos. Sci.*, **68**, 1990–2008 (2011).

Bessafi M and Wheeler MC: Modulation of south Indian Ocean tropical cyclones by the Madden-Julian oscillation and convectively coupled equatorial waves. *Mon. Wea. Rev.*, **134**, 638–656 (2006).

Biasutti M, Yuter SE, Burleyson CD, Sobel AH: Very High Resolution Rainfall Patterns Measured by TRMM Precipitation Radar: Seasonal and Diurnal Cycles. *Clim. Dyn.*, **39**, 239–258 (2012).

Chamberlain JM, Bain CL, Boyd DFA, McCourt K, Butcher T, Palmer S: Forecasting Storms over Lake Victoria using a High Resolution Model. *Meteorol. Appl.*, **21**, 419–430 (2014).

Charnock H, Francis JRD, Sheppard PA: An Investigation of Wind Structure in the Trades: Anegada 1953. *Phil. Trans. R. Soc. A*, **249**, 179–234 (1956).

Chen SS and Houze RA: Diurnal Variation and Life-Cycle of Deep Convective Systems over the Tropical Pacific Warm Pool. *Q. J. R. Meteorol. Soc.*, **123**, 357–388 (1997).

Collier JC and Bowman KP: Diurnal Cycle of Tropical Precipitation in a General Circulation Model. *J. Geophys. Res.*, **109**, D17105 (2004).
doi: 10.1029/2004JD004818

Cravatte S, Delcroix T, Zhang D, McPhaden M, Leloup J: Observed Freshening and Warming of the Western Pacific Warm Pool. *Clim. Dyn.*, **33**, 565–589 (2009).

Crueger T, Stevens B, Brokopf R: The Madden-Julian Oscillation in ECHAM6 and the Introduction of an Objective MJO Metric. *J. Climate*, **26**, 3241–3257 (2013).

Dayem KE, Noone DC, Molnar P: Tropical Western Pacific Warm Pool and Maritime Continent Precipitation Rates and their Contrasting Relationships with the Walker Circulation. *J. Geophys. Res.*, **112**, D06101 (2007).
doi: 10.1029/2006JD007870

Del Genio AD and Wu J: The Role of Entrainment in the Diurnal Cycle of Continental Convection. *J. Climate*, **23**, 2722–2738 (2010).

Deser C and Smith CA: Diurnal and Semidiurnal Variations of the Surface Wind Field over the Tropical Pacific Ocean. *J. Climate*, **11**, 1730–1748 (1998).

Dexter RV: The Diurnal Variation of Warm-Frontal Precipitation and Thunderstorms. *Q. J. R. Meteorol. Soc.*, **70**, 129–137 (1944).

Dirmeyer PA, Cash BA, Kinter JL, Jung T, Marx L, Satoh M, Stan C, Tomita H, Towers P, Wedi N, Achuthavarier D, Adams JM, Altshuler EL, Huang B, Jin EK, Manganello J: Simulating the Diurnal Cycle of Rainfall in Global Climate Models: Resolution Versus Parameterization. *Clim. Dyn.*, **39**, 399–418 (2012).

Drosdowsky W and Chambers LE: Near-global sea surface temperature anomalies as predictors of Australian seasonal rainfall. *J. Climate*, **14**, 1677–1687 (2001).

Duchon CE: Lanczos filtering in one and two dimensions. *J. Appl. Meteor.*, **18**, 1016–1022 (1979).

Flatau M and Kim Y-J: Interaction between the MJO and Polar Circulations. *J. Climate*, **26**, 3562–3574 (2013).

Fujita M, Yoneyama K, Mori S, Nasuno T, Satoh M: Diurnal Convection Peaks over the Eastern Indian Ocean off Sumatra during Different MJO Phases. *J. Meteor. Soc. Japan*, **89A**, 317–330 (2011).

Gill AE: Some Simple Solutions for Heat-Induced Tropical Circulation. *Q. J. R. Meteorol. Soc.*, **106**, 447–462 (1980).

Gill AE: Atmosphere-Ocean Dynamics. *Academic Press*, London, 662 pp. (1982).

Gille ST, Llewellyn Smith SG, Lee SM: Measuring the Sea Breeze from QuikSCAT Scatterometry. *Geophys. Res. Lett.*, **30**, 1114 (2003).
doi: 10.1029/2002GL016230

Gille ST, Llewellyn Smith SG, Statom NM: Global Observations of the Land Breeze. *Geophys. Res. Lett.*, **32**, L05605 (2005).
doi: 10.1029/2004GL022139

Godfrey JS: The Effect of the Indonesian Throughflow on Ocean Circulation and Heat Exchange with the Atmosphere: A Review. *J. Geophys. Res.*, **101**, 12217–12237 (1996).

Gray WM and Jacobson RW: Diurnal Variation of Deep Cumulus Convection. *Mon. Wea. Rev.*, **105**, 1171–1188 (1977).

Guy N and Jorgensen DP: Kinematic and Precipitation Characteristics of Convective Systems Observed by Airborne Doppler Radar during the Life Cycle of a Madden-Julian Oscillation in the Indian Ocean. *Mon. Wea. Rev.*, **142**, 1385–1402 (2014).

Haertel P, Straub K, Fedorov A: Lagrangian Overturning and the Madden-Julian Oscillation. *Q. J. R. Meteorol. Soc.* (in press).
doi: 10.1002/qj.2216

Hall JD, Matthews AJ, Karoly DJ: The modulation of tropical cyclone activity in the Australian region by the Madden-Julian oscillation. *Mon. Wea. Rev.*, **129**, 2970–2982 (2001).

Hara M, Yoshikane T, Takahashi HG, Kimura F, Noda A, Tokioka T: Assessment of the Diurnal Cycle of Precipitation over the Maritime Continent Simulated by a 20 km Mesh GCM Using TRMM PR Data. *J. Meteor. Soc. Japan*, **87A**, 413–424 (2009).

Hendon HH and Liebmann B: Organization of Convection within the Madden-Julian Oscillation. *J. Geophys. Res.*, **99**, 8073–8083 (1994).

Hendon HH and Salby ML: The Life Cycle of the Madden-Julian Oscillation. *J. Atmos. Sci.*, **51**, 2225–2237 (1994).

Hirata FE, Webster P,J, Toma VE: Distinct Manifestations of Austral Summer Tropical Intraseasonal Oscillations. *Geophys. Res. Lett.*, **40**, 3337–3341 (2013).

Hirons LC, Inness P, Vitart F, Bechtold P: Understanding Advances in the Simulation of Intraseasonal Variability in the ECMWF Model. Part I: The Representation of the MJO. *Q. J. R. Meteorol. Soc.*, **139**, 1417–1426 (2013).

Hoffman RN and Leidner SM: An Introduction to the Near-Real-Time QuikSCAT Data. *Wea. Forecasting*, **20**, 476–493 (2005).

Hsu H-H and Lee M-Y: Topographic Effects on the Eastward Propagation and Initiation of the Madden-Julian Oscillation. *J. Climate*, **18**, 795–809 (2005).

Huffman GJ, Bolvin DT, Nelkin EJ, Wolff DB, Adler RF, Gu G, Hong Y, Bowman KP, Stocker EF: The TRMM Multisatellite Precipitation Analysis (TMPA): Quasi-Global, Multiyear, Combined-Sensor Precipitation Estimates at Fine Scales. *J. Hydrometeor.*, **8**, 38–55 (2007).

Hung M-P, Lin J-L, Wang W, Kim D, Shinoda T, Weaver SJ: MJO and Convectively Coupled Equatorial Waves Simulated by CMIP5 Climate Models. *J. Climate*, **26**, 6185–6214 (2013).

Ichikawa H and Yasunari T: Time-Space Characteristics of Diurnal Rainfall over Borneo and Surrounding Oceans as Observed by TRMM-PR. *J. Climate*, **19**, 1238–1260 (2006).

Ichikawa H and Yasunari T: Intraseasonal Variability in Diurnal Rainfall over New Guinea and the Surrounding Oceans during Austral Summer. *J. Climate*, **21**, 2852–2868 (2008).

Inness PM and Slingo JM: Simulation of the Madden-Julian Oscillation in a Coupled General Circulation Model. Part I: Comparison with Observations and an Atmosphere-Only GCM. *J. Climate*, **16**, 345–364 (2003).

Inness PM, Slingo JM, Guilyardi E, Cole J: Simulation of the Madden-Julian Oscillation in a Coupled General Circulation Model. Part II: The Role of the Basic State. *J. Climate*, **16**, 365–382 (2003).

Inness PM, Slingo JM, Woolnough SJ, Neale RB, Pope VD: Organization of Tropical Convection in a GCM with Varying Vertical Resolution; Implications for the Simulation of the Madden-Julian Oscillation. *Clim. Dyn.*, **17**, 777–793 (2001).

Jin F and Hoskins B: The Direct Response to Tropical Heating in a Baroclinic Atmosphere. *J. Atmos. Sci.*, **52**, 307–319 (1995).

Jury MR, Pathack B, Waliser D: Satellite OLR and Microwave Data as a Proxy for Summer Rainfall over Sub-Equatorial Africa and Adjacent Oceans. *Int. J. Climatol.*, **13**, 257–269 (1993).

Kanamitsu M, Ebisuzaki W, Woollen J, Yang S-K, Hnilo JJ, Fiorino M, Potter GL: NCEP-DOE AMIP-II Reanalysis (R-2). *Bull. Amer. Meteor. Soc.*, **83**, 1631–1643 (2002).

Kieffer HH and Wildey RL: Establishing the Moon as a Spectral Radiance Standard. *J. Atmos. Oceanic Technol.*, **13**, 360–375 (1996).

Kikuchi K and Wang B: Diurnal Precipitation Regimes in the Global Tropics. *J. Climate*, **21**, 2680–2696 (2008).

Kiladis GN, Dias J, Straub KH, Wheeler MC, Tulich SN, Kikuchi K, Weickmann KM, Ventrice MJ: A Comparison of OLR and Circulation-Based Indices for Tracking the MJO. *Mon. Wea. Rev.*, **142**, 1697–1715 (2014).

Kiladis GN, Wheeler MC, Haertel PT, Straub KH, Roundy PE: Convectively coupled equatorial waves. *Rev. Geophys.*, **47**, RG2003 (2009).
doi: 10.1029/2008RG000266

Kim D, Kug J-S, Sobel AH: Propagating versus non-propagating Madden-Julian Oscillation Events. *J. Climate*, **27**, 111–125 (2014).

Kim H-M, Hoyos CD, Webster PJ, Kang I-S: Ocean-Atmosphere Coupling and the Boreal Winter MJO. *Clim. Dyn.*, **35**, 771–784 (2010).

Klingaman NP and Woolnough SJ: Using a Case-Study Approach to Improve the Madden-Julian Oscillation in the Hadley Centre Model. *Q. J. R. Meteorol. Soc.* (in press *a*).
doi: 10.1002/qj.2314

Klingaman NP and Woolnough SJ: The Role of Air-Sea Coupling in the Simulation of the Madden-Julian Oscillation in the Hadley Centre Model. *Q. J. R. Meteorol. Soc.* (in press *b*).
doi: 10.1002/qj.2295

Krishnamohan KS, Mohanakumar K, Joseph PV: The influence of Madden-Julian oscillation in the genesis of north Indian Ocean tropical cyclones. *Theor. Appl. Climatol.*, **109**, 271–282 (2012).

Krishnamurti TN and Subrahmanyam D: The 30–50 Day Mode at 850 mb during MONEX. *J. Atmos. Sci.*, **39**, 2088–2095 (1982).

Kubota H and Nitta T: Diurnal Variations of Tropical Convection Observed During the TOGA-COARE. *J. Meteor. Soc. Japan*, **79**, 815–830 (2001).

Kummerow C, Barnes W, Kozu T, Shiue J, Simpson J: The Tropical Rainfall Measuring Mission (TRMM) Sensor Package. *J. Atmos. Oceanic Technol.*, **15**, 809–817 (1998).

Lau K-M and Chan PH: Short-Term Climate Variability and Atmospheric Teleconnections from Satellite-Observed Outgoing Longwave Radiation. Part I: Simultaneous Relationships. *J. Atmos. Sci.*, **40**, 2735–2750 (1983).

Lau K-M and Chan PH: Aspects of the 40–50 Day Oscillation during the Northern Summer as Inferred from Outgoing Longwave Radiation. *Mon. Wea. Rev.*, **114**, 1354–1367 (1986).

Lavender SL and Matthews AJ: Response of the west African monsoon to the Madden-Julian oscillation. *J. Climate*, **22**, 4097–4116 (2009).

Lean HW, Clark PA, Dixon M, Roberts NM, Fitch A, Forbes R, Halliwell C: Characteristics of High-Resolution Versions of the Met Office Unified Model for Forecasting Convection over the United Kingdom. *Mon. Wea. Rev.*, **136**, 3408–3424 (2008).

Li J and Nakamura K: Characteristics of the Mirror Image of Precipitation Observed by the TRMM Precipitation Radar. *J. Atmos. Oceanic Technol.*, **19**, 145–158 (2002).

Lin J-L, Kiladis GN, Mapes BE, Weickmann KM, Sperber KR, Lin W, Wheeler MC, Schubert SD, Del Genio A, Donner LJ, Emori S, Gueremy J-F, Hourdin F, Rasch PJ, Roeckner E, Scinocca JF: Tropical Intraseasonal Variability in 14 IPCC AR4 Climate Models. Part I: Convective Signals. *J. Climate*, **19**, 2665–2690 (2006).

Lindfors AV, MacKenzie IA, Tett SFB, Shi L: Climatological Diurnal Cycles in Clear-Sky Brightness Temperatures from the High-Resolution Infrared Radiation Sounder (HIRS). *J. Atmos. Oceanic Technol.*, **28**, 1199–1205 (2011).

Ling J and Zhang C: Structural Evolution in Heating Profiles of the MJO in Global Reanalyses and TRMM Retrievals. *J. Climate*, **24**, 825–842 (2011).

Ling J, Zhang C, Bechtold P: Large-Scale Distinctions between MJO and Non-MJO Convective Initiation over the Tropical Indian Ocean. *J. Atmos. Sci.*, **70**, 2696–2712 (2013).

Liu C and Zipser EJ: Diurnal Cycles of Precipitation, Clouds, and Lightning in the Tropics from 9 Years of TRMM Observations. *Geophys. Res. Lett.*, **35**, L04819 (2008).
doi: 10.1029/2007GL032437

Lorenz DJ and Hartmann DL: The effect of the MJO on the North American monsoon. *J. Climate*, **19**, 333–343 (2006).

Love BS, Matthews AJ, Lister GMS: The diurnal cycle of precipitation over the Maritime Continent in a high-resolution atmospheric model. *Q. J. R. Meteorol. Soc.*, **137**, 934–947 (2011).

Madden RA and Julian PR: Detection of a 40–50 day oscillation in the zonal wind in the tropical Pacific. *J. Atmos. Sci.*, **28**, 702–708 (1971).

Madden RA and Julian PR: Description of global-scale circulation cells in the tropics with a 40–50 day period. *J. Atmos. Sci.*, **29**, 1109–1123 (1972).

Madden RA and Julian PR: Observations of the 40–50 day tropical oscillation. *Mon. Wea. Rev.*, **122**, 814–837 (1994).

Majda AJ and Stechmann SN: The Skeleton of Tropical Intraseasonal Oscillations. *Proc. Natl. Acad. Sci. USA*, **106**, 8417–8422 (2009).

Maloney ED and Hartmann DL: Frictional Moisture Convergence in a Composite Life Cycle of the Madden-Julian Oscillation. *J. Climate*, **11**, 2387–2403 (1998).

Martin GM, Ringer MA, Pope VD, Jones A, Dearden C, Hinton TJ: The Physical Properties of the Atmosphere in the New Hadley Centre Global Environmental Model (HadGEM1). Part I: Model Description and Global Climatology. *J. Climate*, **19**, 1274–1301 (2006).

Matsuno T: Quasi-Geostrophic Motions in the Equatorial Area. *J. Meteor. Soc. Japan*, **44**, 25–43 (1966).

Matthews AJ: Propagation mechanisms for the Madden-Julian Oscillation. *Q. J. R. Meteorol. Soc.*, **126**, 2637–2651 (2000).

Matthews AJ, Hoskins BJ, Masutani M: The global response to tropical heating in the Madden-Julian oscillation during the northern winter. *Q. J. R. Meteorol. Soc.*, **130**, 1991-2011 (2004).

Matthews AJ: Primary and successive events in the Madden-Julian Oscillation. *Q. J. R. Meteorol. Soc.*, **134**, 439–453 (2008).

Matthews AJ, Pickup G, Peatman SC, Clews P, Martin J: The Effect of the Madden-Julian Oscillation on Station Rainfall and River Level in the Fly River System, Papua New Guinea. *J. Geophys. Res.*, **118**, 10926–10935 (2013).

Moss RH, Edmonds JA, Hibbard KA, Manning MR, Rose SK, van Vuuren DP, Carter TR, Emori S, Kainuma M, Kram T, Meehl GA, Mitchell JFB, Nakicenovic N, Riahi K, Smith SJ, Stouffer RJ, Thomson AM, Weyant JP, Wilbanks TJ: The Next Generation of Scenarios for Climate Change Research and Assessment. *Nature*, **463**, 747–756 (2010).

Nakazawa T: Tropical Super Clusters within Intraseasonal Variations over the Western Pacific. *J. Meteor. Soc. Japan*, **66**, 823–839 (1988).

Neale R and Slingo J: The Maritime Continent and its Role in the Global Climate: A GCM Study. *J. Climate*, **16**, 834–848 (2003).

Nesbitt SW and Zipser EJ: The Diurnal Cycle of Rainfall and Convective Intensity According to Three Years of TRMM Measurements. *J. Climate*, **16**, 1456–1475 (2003).

North GR, Bell TL, F. CR, Moeng FJ: Sampling Errors in the Estimation of Empirical Orthogonal Functions. *Mon. Wea. Rev.*, **110**, 699–706 (1982).

Oh J-H, Kim K-Y, Lim G-H: Impact of MJO on the Diurnal Cycle of Rainfall Over the Western Maritime Continent in the Austral Summer. *Clim. Dyn.*, **38**, 1167–1180 (2012).

Pai DS, Bhate J, Sreejith OP, Hatwar HR: Impact of MJO on the intraseasonal variation of summer monsoon rainfall over India. *Clim. Dyn.*, **36**, 41–55 (2011).

Pearson KJ, Lister GMS, Birch CE, Allan RP, Hogan RJ, Woolnough SJ: Modelling the diurnal cycle of tropical convection across the 'grey zone'. *Q. J. R. Meteorol. Soc.*, **140**, 491–499 (2014).

Peatman SC, Matthews AJ, Stevens DP: Propagation of the Madden-Julian Oscillation through the Maritime Continent and Scale Interaction with the Diurnal Cycle of Precipitation. *Q. J. R. Meteorol. Soc.*, **140**, 814–825 (2014).

Pedgley DE: Diurnal Variation of the Incidence of Monsoon Rainfall over the Sudan. *Meteor. Mag.*, **98**, 97–107,129–134 (1969).

Ploshay JJ and Lau N-C: Simulation of the Diurnal Cycle in Tropical Rainfall and Circulation during Boreal Summer with a High-Resolution GCM. *Mon. Wea. Rev.*, **138**, 3434–3453 (2010).

Qian J-H: Why Precipitation is Mostly Concentrated over Islands in the Maritime Continent. *J. Atmos. Sci.*, **65**, 1428–1441 (2008).

Ramage C: Role of a Tropical "Maritime Continent" in the Atmospheric Circulation. *Mon. Wea. Rev.*, **96**, 365–370 (1968).

Raymond DJ: A New Model of the Madden-Julian Oscillation. *J. Atmos. Sci.*, **58**, 2807–2819 (2001).

Rauniyar SP and Walsh KJE: Scale Interaction of the Diurnal Cycle of Rainfall over the Maritime Continent and Australia: Influence of the MJO. *J. Climate*, **24**, 325–348 (2011).

Riehl H: Diurnal Variation of Cloudiness over the Subtropical Atlantic Ocean. *Bull. Amer. Meteor. Soc.*, **28**, 37–40 (1947).

Ringer MA, Martin GM, Greeves CZ, Hinton TJ, James PM, Pope VD, Scaife AA, Stratton RA, Inness PM, Slingo JM, Yang G-Y: The Physical Properties of the Atmosphere in the New Hadley Centre Global Environmental Model (HadGEM1). Part II: Aspects of Variability and Regional Climate. *J. Climate*, **19**, 1302–1326 (2006).

Saito K, Keenan T, Holland G, Puri K: Numerical Simulation of the Diurnal Evolution of Tropical Island Convection over the Maritime Continent. *Mon. Wea. Rev.*, **129**, 378–400 (2001).

Sandeep S and Stordal F: Use of Daily Outgoing Longwave Radiation (OLR) Data in Detecting Precipitation Extremes in the Tropics. *Remote Sens. Lett.*, **4**, 570–578 (2013).

Sato T, Miura H, Satoh M, Takayabu YN, Wang Y: Diurnal Cycle of Precipitation in the Tropics Simulated in a Global Cloud-Resolving Model. *J. Climate*, **22**, 4809–4826 (2009).

Schneider N: The Indonesian Throughflow and the Global Climate System. *J. Climate*, **11**, 676–689 (1998).

Seo K-H and Kim K-Y: Propagation and initiation mechanism of the Madden-Julian oscillation. *J. Geophys. Res.*, **108**, 4384–4405 (2003).

Shaffrey LC, Stevens I, Norton WA, Roberts MJ, Vidale PL, Harle JD, Jrrar A, Stevens DP, Woodage MJ, Demory ME, Donners J, Clark DB, Clayton A, Cole JW, Wilson SS, Connolley WM, Davies TM, Iwi AM, Johns TC, King JC, New AL, Slingo JM, Slingo A, Steenman-Clark L, Martin GM: U.K. HiGEM: The New U.K. High-Resolution Global Environment Model – Model Description and Basic Evaluation. *J. Climate*, **22**, 1861–1896 (2009).

Simpson J, Keenan TD, Ferrier B, Simpson RH, Holland GJ: Cumulus Mergers in the Maritime Continent Region. *Meteorol. Atmos. Phys.*, **51**, 73–99 (1993).

Simpson J, Kummerow C, Tao W-K, Adler RF: On the Tropical Rainfall Measuring Mission (TRMM). *Meteorol. Atmos. Phys.*, **60**, 19–36 (1996).

Slingo A, Hodges KI, Robinson GJ: Simulation of the Diurnal Cycle in a Climate Model and its Evaluation Using Data from Meteosat 7. *Q. J. R. Meteorol. Soc.*, **130**, 1449–1467 (2004).

Slingo JM, Sperber KR, Boyle JS, Ceron J-P, Dix M, Dugas B, Ebisuzaki W, Fyfe J, Gregory D, Gueremy J-F, Hack J, Harzallah A, Inness P, Kitoh A, Lau WK-M, McAvaney B, Madden R, Matthews AJ, Palmer TN, Park C-K, Randall D, Renno N: Intraseasonal Oscillations in 15 Atmospheric General Circulation Models: Results from an AMIP Diagnostic Subproject. *Clim. Dyn.*, **12**, 325–357 (1996).

Sobel AH, Burleyson CD, Yuter SE: Rain on Small Tropical Islands. *J. Geophys. Res.*, **116**, D08102 (2011).
doi: 10.1029/2010JD014695

Sperber KR, Slingo JM, Inness PM, Lau WK-M: On the Maintenance and Initiation of the Intraseasonal Oscillation in the NCEP/NCAR Reanalysis and the GLA and UKMO AMIP Simulations. *Clim. Dyn.*, **13**, 769–795 (1997).

Stratton RA and Stirling AJ: Improving the Diurnal Cycle of Convection in GCMs. *Q. J. R. Meteorol. Soc.*, **138**, 1121–1134 (2012).

Straub KH: MJO initiation in the Realtime Multivariate MJO index. *J. Climate*, **26**, 1130–1151 (2013).

Sui C-H and Lau K-M: Multiscale Phenomena in the Tropical Atmosphere over the Western Pacific. *Mon. Wea. Rev.*, **120**, 407–430 (1992).

Sui C-H, Li X, Lau K-M, Adamec D: Multiscale Air-Sea Interactions During TOGA COARE. *Mon. Wea. Rev.*, **125**, 448–462 (1997).

Suzuki T: Diurnal Cycle of Deep Convection in Super Clusters Embedded in the Madden-Julian Oscillation. *J. Geophys. Res.*, **114**, D22102 (2009).
doi: 10.1029/2008JD011303

Takayabu YN: Spectral Representation of Rain Profiles and Diurnal Variations Observed with TRMM PR over the Equatorial Area. *Geophys. Res. Lett.*, **29**, 1584–1587 (2002).

Taylor KE, Stouffer RJ, Meehl GA: An Overview of CMIP5 and the Experiment Design. *Bull. Amer. Meteor. Soc.*, **93**, 485–498 (2012).

Teo C-K, Koh T-Y, Lo JC-F, Bhatt BC: Principal Component Analysis of Observed and Modelled Diurnal Rainfall in the Maritime Continent. *J. Climate*, **24**, 4662–4675 (2011).

Thual S, Majda AJ, Stechmann SN: A Stochastic Skeleton Model for the MJO. *J. Atmos. Sci.*, **71**, 697–715 (2014).

Tian B, Waliser DE, Fetzer EJ: Modulation of the Diurnal Cycle of Tropical Deep Convective Clouds by the MJO. *Geophys. Res. Lett.*, **33**, L20704 (2006).
doi: 10.1029/2006GL027752

Ventrice MJ, Wheeler MC, Hendon HH, Schreck III CJ, Throncroft CD, Kiladis GN: A Modified Multivariate Madden-Julian Oscillation Index using Velocity Potential. *Mon. Wea. Rev.*, **141**, 4197–4210 (2013).

Virts KS, Wallace JM, Hutchins ML, Holzworth RH: Diurnal Lightning Variability over the Maritime Continent: Impact of Low-Level Winds, Cloudiness, and the MJO. *J. Atmos. Sci.*, **70**, 3128–3146 (2013).

Wang B, Zhou L, Hamilton K: Effect of Convective Entrainment/Detrainment on the Simulation of the Tropical Precipitation Diurnal Cycle. *Mon. Wea. Rev.*, **135**, 567–585 (2007).

Webber BGM, Matthews AJ, Heywood KJ, Stevens DP: Ocean Rossby Waves as a Triggering Mechanism for Primary Madden-Julian Events. *Q. J. R. Meteorol. Soc.*, **138**, 514–527 (2012).

Weickmann KM, Lussky GR, Kutzbach JE: Intraseasonal (30–60 Day) Fluctuations of Outgoing Longwave Radiation and 250 mb Streamfunction during Northern Winter. *Mon. Wea. Rev.*, **113**, 941–961 (1985).

Weller RA and Anderson SP: Surface Meteorology and Air-Sea Fluxes in the Western Equatorial Pacific Warm Pool during the TOGA Coupled Ocean-Atmosphere Response Experiment. *J. Climate*, **9**, 1959–1990 (1996).

Wheeler MC and Hendon HH: An All-Season Real-Time Multivariate MJO Index: Development of an Index for Monitoring and Prediction. *Mon. Wea. Rev.*, **132**, 1917–1932 (2004).

Wheeler MC and Kiladis GN: Convectively Coupled Equatorial Waves: Analysis of Clouds and Temperature in the Wavenumber-Frequency Domain. *J. Atmos. Sci.*, **56**, 374–399 (1999).

Wilks DS: Statistical methods in the atmospheric sciences, 3rd Ed. *Academic Press*, Oxford, 676 pp. (2011).

Williams M and Houze RA: Satellite-Observed Characteristics of Winter Monsoon Cloud Clusters. *Mon. Wea. Rev.*, **115**, 505–519 (1987).

Wu C-H and Hsu H-H: Topographic Influence on the MJO in the Maritime Continent. *J. Climate*, **22**, 5433–5448 (2009).

Yan X-H, Ho C-R, Zheng Q, Klemas V: Temperature and Size Variabilities of the Western Pacific Warm Pool. *Science*, **258**, 1643–1645 (1992).

Yang G-Y and Slingo J: The diurnal cycle in the tropics. *Mon. Wea. Rev.*, **129**, 784–801 (2001).

Yang S and Smith EA: Mechanisms for Diurnal Variability of Global Tropical Rainfall Observed from TRMM. *J. Climate*, **19**, 5190–5226 (2006).

Zhang C: Madden-Julian oscillation. *Rev. Geophys.*, **43**, RG2003 (2005).
doi: 10.1029/2004RG000158

Zhao C, Li T, Zhou T: Precursor Signals and Processes Associated with MJO Initiation over the Tropical Indian Ocean. *J. Climate*, **26**, 291–307 (2013).

Zhou L and Wang Y: Tropical Rainfall Measuring Mission Observation and Regional Model Study of Precipitation Diurnal Cycle in the New Guinean Region. *J. Geophys. Res.*, **111**, D17104 (2006).
doi: 10.1029/2006JD007243

Zhou L, Neale R, Jochum M, Murtugudde R: Improved Madden-Julian Oscillations with Improved Physics: the Impact of Modified Convection Parameterizations. *J. Climate*, **25**, 1116–1136 (2012).